

REPORT DOCUMENTATION PAGE				Form Approved OMB No. 0704-0188		
<small>The public reporting burden for this collection of information is estimated to average 1 hour per response, including the time for reviewing instructions, searching existing data sources, gathering and maintaining the data needed, and completing and reviewing the collection of information. Send comments regarding this burden estimate or any other aspect of this collection of information, including suggestions for reducing the burden, to Department of Defense, Washington Headquarters Services, Directorate for Information Operations and Reports (0704-0188), 1215 Jefferson Davis Highway, Suite 1204, Arlington, VA 22202-4302. Respondents should be aware that notwithstanding any other provision of law, no person shall be subject to any penalty for failing to comply with a collection of information if it does not display a currently valid OMB control number.</small> <b>PLEASE DO NOT RETURN YOUR FORM TO THE ABOVE ADDRESS.</b>						
1. REPORT DATE (DD-MM-YYYY) 03-23-2009		2. REPORT TYPE Biannual Technical Report		3. DATES COVERED (From - To) 7/1/2008 - 12/31/2008		
4. TITLE AND SUBTITLE  Bi-annual (7/1/2008-12/31/2008) Performance/Technical Report for ONR Award under Grant N00014-07-1-0395 MARSnet: Mission-aware Autonomous Radar Sensor Network for Future Combat Systems				5a. CONTRACT NUMBER		
				5b. GRANT NUMBER N00014 - 07 -1 -0395		
				5c. PROGRAM ELEMENT NUMBER		
				5d. PROJECT NUMBER		
6. AUTHOR(S) Liang, Qilian				5e. TASK NUMBER		
				5f. WORK UNIT NUMBER		
7. PERFORMING ORGANIZATION NAME(S) AND ADDRESS(ES) University of Texas at Arlington Office of Sponsored Projects PO Box 19145 Arlington, TX 76019				B. PERFORMING ORGANIZATION REPORT NUMBER		
9. SPONSORING/MONITORING AGENCY NAME(S) AND ADDRESS(ES) Office of Naval Research 875 N. Randolph St. One Liberty Center Arlington, VA 22203-1995				10. SPONSOR/MONITOR'S ACRONYM(S) ONR		
				11. SPONSOR/MONITOR'S REPORT NUMBER(S)		
12. DISTRIBUTION/AVAILABILITY STATEMENT Approved for Public Release; Distribution is Unlimited.						
13. SUPPLEMENTARY NOTES						
14. ABSTRACT  During the period of 7/1/2008 - 12/31/2008, we performed the following studies on radar sensor network and other related areas: 1. Radar Sensor Network Using A New Triphase Coded Waveform: Theory and Application; 2. Sense-Through-Wall Channel Modeling Using UWB Noise Radar; 3. Orthogonal Pulse Compression Codes for MIMO Radar System; 4. Optimized Punctured ZCZ Sequence-pair Set: Design, Analysis and Application to Radar System; 5. A Triphase Coded Waveform: Design, Analysis and Application to Radar System; 6. Combined-Jamming Interference Analysis for FH/MFSK Multi-Radio Wireless Mesh Networks; 7. Passive Geolocation of RF Emitters by Neteentric Small Unmanned Aerial Systems (SUAS).						
15. SUBJECT TERMS  Radar Sensor Network, UWB Radar, tri-phase coded waveforms, UWB channel, geolocation, sense-through-wall, MIMO Radar.						
16. SECURITY CLASSIFICATION OF:			17. LIMITATION OF ABSTRACT		18. NUMBER OF PAGES	
a. REPORT	b. ABSTRACT	c. THIS PAGE	UU		19a. NAME OF RESPONSIBLE PERSON Qilian Liang	
U	U	U			19b. TELEPHONE NUMBER (Include area code) 817-272-1339	

Bi-annual (7/1/2008–12/31/2008) Performance/Technical Report  
for ONR Award under Grant N00014-07-1-0395  
MARSnet: Mission-aware Autonomous Radar Sensor Network for  
Future Combat Systems

Qilian Liang  
Department of Electrical Engineering  
University of Texas at Arlington  
Arlington, TX 76019-0016 USA  
Phone: 817-272-1339, Fax: 817-272-2253  
E-mail: liang@uta.edu

**Abstract**

During the period of 7/1/2008 – 12/31/2008, we performed the following studies on radar sensor network and other related areas:

1. Radar Sensor Network Using A New Triphase Coded Waveform: Theory and Application;
2. Sense-Through-Wall Channel Modeling Using UWB Noise Radar;
3. Optimized Punctured ZCZ Sequence-pair Set: Design, Analysis and Application to Radar System;
4. A Triphase Coded Waveform: Design, Analysis and Application to Radar System;
5. Combined-Jamming Interference Analysis for FH/MFSK Multi-Radio Wireless Mesh Networks;
6. Passive Geolocation of RF Emitters by Netcentric Small Unmanned Aerial Systems (SUAS).

## **1 Radar Sensor Network Using A New Triphase Coded Waveform: Theory and Application**

In radar sensor network (RSN), interferences among radars can be effectively reduced when waveforms are properly designed. In [1][5], we firstly performed some theoretical studies on coexistence of phase coded waveforms in RSN. Then we gave the definition of new kind of triphase coded waveform-optimized punctured Zero Correlation Zone sequence-Pair Set (ZCZPS) and analyze their properties especially their optimized cross correlation property of any two sequencepairs in the set. Besides, we applied our newly provided triphase coded waveforms and equal gain combination technique to the system simulation and study the performances versus different number of radars in RSN under the condition of either Doppler shift or time delay. Simulation results showed that detection performances of RSN (applying our optimized punctured ZCZPS and equal gain combination) with or without Doppler shift are superior to those of singler radar. In [9], similarly to the RSN, we extended our design to underwater sonar sensor networks.

## 2 Sense-Through-Wall Channel Modeling Using UWB Noise Radar

Sensing-through-wall will benefit various applications such as emergence rescues and military operations. In order to add more signal processing functionality, it is vital to understand the characterization of sense-through-wall channel. In [2], we proposed a statistical channel model on a basis of real experimental data using UWB noise radar. We employ CLEAN algorithm to obtain the multipath channel impulse response (CIR) and observe that the amplitude of channel coefficient at each path can be accurately characterized as  $\chi^2$  location-scale distribution. We also analyzed that the multipath contributions arrive at the receiver are grouped into clusters. The time of arrival of clusters can be modeled as a Poisson arrival process, while within each cluster, subsequent multipath contributions or rays also arrive according to a Poisson process. However, these arrival rates are much smaller than those of indoor UWB channels.

## 3 Optimized Punctured ZCZ Sequence-pair Set: Design, Analysis and Application to Radar System

Based on the zero correlation zone (ZCZ) concept, in [3] we presented the definition and properties of a set of new triphase coded waveforms ZCZ sequence-pair set (ZCZPS) and propose a method to use the optimized punctured sequence-pair along with Hadamard matrix in the zero correlation zone in order to construct the optimized punctured ZCZ sequence-pair set (optimized punctured ZCZPS). According to property analysis, the optimized punctured ZCZPS has good autocorrelation and cross correlation properties when Doppler shift is not large. We apply it to radar target detection. The simulation results showed that optimized punctured ZCZ sequence-pairs (optimized punctured ZCZPs) outperform other conventional pulse compression codes, such as the well known polyphase codeP4 code.

## 4 A Triphase Coded Waveform: Design, Analysis and Application to Radar System

In [4], we presented new developed triphase code punctured binary sequence-pair. The definitions and the autocorrelation properties of the proposed code are given. Doppler shift performance is also investigated. The significant advantages of punctured binary sequencepair over conventional pulse compression codes, such as the widely used Barker codes, are zero autocorrelation sidelobes and the longer length of the code which can be as long as 31 so far. Applying the codes in the radar target detection system simulation, punctured binary sequencepair also outperforms other conventional pulse compression codes. Therefore, our proposed code can be used as good candidates for pulse compression code.

## 5 Combined-Jamming Interference Analysis for FH/MFSK Multi-Radio Wireless Mesh Networks

For the past decades, the performances of frequency-hopping systems under various jamming strategies have been investigated. In [6], we considered the performance of the noncoherent slow frequency-hopping system with M-ary frequencyshift-keyed modulation (NC-FH/MFSK) under independent multitone jamming (IMTJ) and under partial-band jamming (PBJ). The exact BER expressions of the system under each jamming strategy are derived. Then, we combine the two

expressions together to develop a new interference model for multi-radio frequency-hopping wireless mesh networks (MR-FH WMN). Because it takes into account both the cochannel and the coexisting-network interferences, the new interference model thus reflects a very realistic interference situation and it can be incorporated to the channel assignment (CA) algorithms to assign appropriate channels (or hopping pattern, in our case) to interfaces of the routers in the mesh network. In addition, we also compare the performances of NC-FH/4FSK system under the two jamming strategies, the numerical results have illustrated that PBJ is more effective jamming strategy than IMTJ. In [7], we applied this result to wireless mesh networks.

## 6 Passive Geolocation of RF Emitters by Netcentric Small Unmanned Aerial Systems (SUAS)

Conventional geolocation of RF emitters has adopted active triangulation methodology. One successful commercial example is satellite-based global positioning system (GPS). However the active localization in some cases can be extremely vulnerable especially for battlefield. In [8], we designed a netcentric Small Unmanned Aerial System (SUAS) for passive geolocation of RF emitters. Each small UAV is equipped with multiple Electronic Surveillance (ES) sensors to provide local mean distance estimation based on received signal strength indicator (RSSI). Fusion center will determine the location of the target through UAV triangulation. Different with previous existing studies, our method is on a basis of an empirical path loss and log-normal shadowing model, from a wireless communication and signal processing vision to offer an effective solution. The performance degradation between UAVs and fusion center is taken into consideration other than assume lossless communication. We analyzed the geolocation error and the error probability of distance based on the proposed system. The result showed that this approach provides robust performance for high frequency RF emitters.

## References

- [1] L. Xu, Q. Liang, "Radar Sensor Network Using A New Triphase Coded Waveform: Theory and Application," submitted to *IEEE Trans on Vehicular Technology*.
- [2] J. Liang, Q. Liang, "Sense-Through-Wall Channel Modeling Using UWB Noise Radar," submitted to *IEEE Globecom*, Nov 2009.
- [3] L. Xu, Q. Liang, "Optimized Punctured ZCZ Sequence-pair Set: Design, Analysis and Application to Radar System," submitted to *IEEE Trans on Aerospace and Electronic Systems*.
- [4] L. Xu, Q. Liang, T. Jing "A Triphase Coded Waveform: Design, Analysis and Application to Radar System," submitted to *IET Proc on Radar, Sonar, and Navigation*.
- [5] L. Xu, Q. Liang, "Radar Sensor Network Using a New Triphase Coded Waveform: Theory and Application," accepted by *IEEE ICC 2008*, Dresden, Germany, June 2009.
- [6] D. Kirachaiwanich, Q. Liang, "Combined-Jamming Interference Analysis for FH/MFSK Multi-Radio Wireless Mesh Networks," submitted to *IEEE Trans on Mobile Computing*.
- [7] D. Kirachaiwanich, Q. Liang, "Interference Analysis for FH-Based Multi-Radio Wireless Mesh Networks," submitted to *IEEE SENCON*, June 2009.

- [8] J. Liang, Q. Liang, "Passive Geolocation of RF Emitters by Netcentric Small Unmanned Aerial Systems (SUAS)," submitted to *IEEE Trans on Vehicular Technology*.
- [9] L. Xu, Q. Liang "Waveform design for underwater sonar sensor networks," submitted to *IEEE Globecom*, Nov 2009.

# RADAR SENSOR NETWORK USING KIND OF NEW TRIPHASE CODED WAVEFORM: THEORY AND APPLICATION

Lei Xu and Qilian Liang

Department of Electrical Engineering

University of Texas at Arlington

416 Yates Street Nedderman Hall, Rm 501

Arlington, TX 76010

Email: xu@ecn.uta.edu, liang@uta.edu

## Abstract

*In radar sensor network(RSN), interference with each radar can be effectively reduced when waveforms are properly designed. In this paper, we firstly perform some theoretical studies on co-existence of phase coded waveforms in RSN. Then we give the definition of new kind of triphase coded waveforms-optimized punctured Zero Correlation Zone(ZCZ) sequence-pair set and analyze their properties especially their optimized cross correlation property of any two sequence-pairs in the set. Also, we study the performances versus different number of radars in RSN under the condition of either doppler shift or not by applying our newly provided triphase coded waveforms and equal gain combination technique in the system simulation. Simulation results show that performances of detection of multiradars(applying our optimized punctured ZCZ sequence-pair set and equal gain*

combination) either under the doppler shift condition or not are superior to those of singler radar. Therefore, applying our optimized punctured ZCZ sequence-pair set as a bank of phase coded waveforms in RSN can effectively satisfy higher demands criterion for detection accuracy in modern military and security affairs.

## 1 Introduction

A network of multiple radar sensors can be introduced to overcome performance degradation of single radar along with waveform optimization. This network of radar sensors should operate with multiple goals managed by an intelligent platform network that can combine waveform diversity to meet common goals of platform, rather than each radar to operate independently.

Much time and effort have been put in waveform design. Bell [1] who introduced information theory to radar waveform design, concluded that distributing energy is a good choice to better detect targets. Sowelan and Tewfik [2] applied a sequential experiment design procedure to select signal for radar target classification. In their work, each waveform selected maximizes the KullbackLeibler information number that measures the dissimilarity between the observed target and the alternative targets in order to minimize the decision time. However, all the above researches only focused on a single active radar. In [3], Liang studied constant frequency (CF) pulse waveform design and proposed maximum-likelihood (ML) automatic target recognition (ATR) approach for both nonfluctuaing and fluctuating targets in a network of multiple radar sensors. In [4], RSN design based on linear frequency modulation (LFM) waveform was studied and LFM waveform design was applied to RSN with application to ATR with delay-doppler uncertainty by Liang as well. J.Liang [5] provided an orthogonal waveform model for RSN, which eliminates interference when there is no doppler shift. They designed both coherent and noncoherent RSN detection systems which can apply equal gain combination technique performed by clusterhead to take the advantage

of spatial diversity. In [6], binary coded pulses using simulated annealing in RSN are highlighted. Nevertheless, the radar sensor network using phase coded waveforms has not been well studied. In this paper, we firstly theoretically study RSN design based on phase coded waveforms: the conditions for waveforms co-existence. Then we apply our newly proposed triphase code-optimized punctured ZCZ sequence-pair set to RSN. We perform studies on the codes' properties, especially the cross correlation property and analyze the performance of optimized punctured ZCZ sequence-pairs in RSN system under the environment of doppler shift and time delay for each transmitting radar sensor. According to the Monte Carlo simulation results, RSN based on optimized punctured ZCZ sequence-pairs provides promising detection performance much better than that of single radar, in terms of probability of miss and false alarm detection.

The rest of the paper is organized as follows. In Section 2, we study the co-existence of phase coded waveforms. Section 3 introduces the definition and properties of our newly provided triphase coded waveform-optimized punctured ZCZ sequence-pair set, especially the outstanding cross correlation property. In Section 4, we study the performance versus the number of radars in RSN either under the condition of doppler shift or not by applying our triphase coded waveforms and equal gain combination technique in the system simulation. In Section 5, conclusions are drawn on radar sensor network using our optimized punctured ZCZ sequence-pairs.

## 2 CO-EXISTENCE OF PHASE CODED WAVEFORMS IN RSN

In RSN, radar sensors are likely to interfere with each other and the performances may be bad if their waveforms are not properly designed. Orthogonality can be introduced as one criterion for the phase coded waveforms design in RSN to make them co-existence.

The phase coded waveform can be defined as

$$x(t) = \sum_{n=0}^{N-1} x^{(n)}(t - n\tau_c) = \sum_{n=0}^{N-1} \exp(j2\pi\beta^{(n)}(t - n\tau_c)) \quad (1)$$

Here,  $0 < t \leq \tau_c$ .

The periodic autocorrelation property of the phase coded waveform here is

$$\begin{aligned} & \int_{-\frac{T}{2}+\tau}^{\frac{T}{2}} x(t)x^*(t-\tau)dt \\ &= \sum_{n=m}^{N-1} \tau_c \exp[j2\pi[\beta^{(n-m)}(m + \frac{N}{2} + 1) \\ & \quad + \beta^{(n)}(-\frac{N}{2} + 1)]\tau_c] \text{sinc} \left[ \tau_c(\beta^{(n)} - \beta^{(n-m)}) \right] \\ &= \begin{cases} N\tau_c & \tau = 0 \\ 0 & \tau \in \text{ZCZ} \end{cases} \end{aligned} \quad (2)$$

Accordingly, it is easy to see that

$$\pi\tau_c(\beta^{(n)} - \beta^{(n-m)}) = k\pi, \quad k = 1, 2, 3, \dots \quad (3)$$

We assume there are  $N$  radars networking together in a self-organizing fashion in our RSN. The radar  $i$  transmits a waveform as

$$x_i(t) = \sum_{n=0}^{N-1} x_i^{(n)}(t - n\tau_c) = \sum_{n=0}^{N-1} \exp(j2\pi\beta_i^{(n)}(t - n\tau_c)). \quad (4)$$

Here,  $0 < t \leq \tau_c$ .

When the phase coded waveforms are orthogonal to each other, the interference from one waveform to the other can be minimized or even removed. The cross correlation between  $x_i(t)$  and

$x_j(t)$  could be

$$\begin{aligned}
& \int_{-T/2}^{T/2} x_i(t) x_j^*(t) dt \\
&= \sum_{n=0}^{N-1} \int_{-T/2+n\tau_c}^{-T/2+(n+1)\tau_c} \exp(j2\pi\beta_i^{(n)}(t-n\tau_c)) \\
&\quad \exp^*(j2\pi\beta_j^{(n)}(t-n\tau_c)) dt \\
&= \tau_c \sum_{n=0}^{N-1} \exp[j2\pi(-\frac{N}{2} + \frac{1}{2})\tau_c(\beta_i^{(n)} - \beta_j^{(n)})] \\
&\quad \text{sinc}[\tau_c(\beta_i^{(n)} - \beta_j^{(n)})]
\end{aligned} \tag{5}$$

$$\tag{6}$$

The optimized cross correlation is that of orthogonal waveforms

$$\int_{-T/2}^{T/2} x_i(t) x_j^*(t) dt = \begin{cases} N\tau_c & i = j \\ 0 & i \neq j \end{cases} \tag{7}$$

According to the property of biphas coded waveforms whose phase state is either 0 or  $\pi$ , it is easy to see that  $\pi\tau_c(\beta_i^{(n)} - \beta_j^{(n)}) = k\pi, k = 1, 2, 3, \dots$ . So the equation (6) can be easily proved to be zero, when  $i \neq j$ . As a result, biphas coded waveforms which are orthogonal to each other can work well simultaneously in Radar Sensor Network.

Nevertheless, there are time delay and Doppler shift ambiguity that will introduce interference to waveforms in RSN. Ambiguity function (AF) [7] is usually used to succinctly characterize the behavior of a waveform paired with its matched filter. So it is an analytical tool for waveform design especially there are time delay and Doppler shift ambiguity.

The matched filter for waveform  $x(t)$  is  $x^*(-t)$ . Since the property performance we analyzed in this paper is the periodic one, the ambiguity function for a single radar is modified and different

from the one in [7]. The ambiguity function of phase coded waveform here can be

$$\begin{aligned}
& A(\tau, F_D) \tag{8} \\
&= \left| \int_{-\infty}^{\infty} x(t) \exp(j2\pi F_D t) x^*(t - \tau) dt \right| \\
&= \left| \sum_{n=m}^{N-1} \int_{-\frac{T}{2} + n\tau_c}^{-\frac{T}{2} + (n+1)\tau_c} \exp[j2\pi\beta^{(n)}(t - n\tau_c) \right. \\
&\quad \left. - j2\pi\beta^{n-m}(t - n\tau_c + T - m\tau_c) + j2\pi F_D t] dt \right| \\
&= \left| \tau_c \sum_{n=m}^{N-1} \exp[j2\pi[\beta^{(n-m)}(\frac{N}{2} + m - 1)\tau_c \right. \\
&\quad \left. + \beta^{(n)}(-\frac{N}{2} + 1)\tau_c + F_D(-\frac{N}{2} + n + 1)\tau_c \right. \\
&\quad \left. \text{sinc}[\tau_c(\beta^{(n)} - \beta^{(n-m)} + F_D)]] \right|
\end{aligned}$$

When it is satisfied that

$$\pi\tau_c(\beta^{(n)} - \beta^{(n-m)} + F_D) = k\pi, \quad k = 1, 2, 3, \dots \tag{9}$$

the amplitude of ambiguity function turns to be zero. In some other words, based on the result of

(3),  $A(\tau, F_D) = 0$ , when  $F_D = \frac{k}{\tau_c}, k = 0, 1, 2, \dots$

In the RSN, all the radar sensors are transmitting signals, the radar  $i$  not only receives its own back-scattered waveform, but also scattered signals generated by other radars which caused interference to radar  $i$ . Considering interference from another radar  $j$ , if there are time delay and

Doppler shift, the ambiguity function of radar  $i$  is

$$\begin{aligned}
& A(\tau, F_{D_i}, F_{D_j}) \tag{10} \\
& = \left| \int_{-\infty}^{\infty} [x_i(t) \exp(j2\pi F_{D_i} t) \right. \\
& \quad \left. + x_j(t) \exp(j2\pi F_{D_j} t)] x_i^*(t - \tau) dt \right| \\
& = \left| \tau_c \sum_{n=m}^{N-1} \left[ \exp[j2\pi [\beta_i^{(n-m)} (\frac{N}{2} + m - 1)\tau_c \right. \right. \\
& \quad \left. \left. + \beta_i^{(n)} (-\frac{N}{2} + 1)\tau_c + F_{D_i} (-\frac{N}{2} + n + 1)\tau_c]] \right. \right. \\
& \quad \left. \left. \text{sinc}[\tau_c(\beta_i^{(n)} - \beta_i^{(n-m)} + F_{D_i})] \right. \right. \\
& \quad \left. \left. + \exp[j2\pi [\beta_i^{(n-m)} (\frac{N}{2} + m - 1)\tau_c \right. \right. \\
& \quad \left. \left. + \beta_j^{(n)} (-\frac{N}{2} + 1)\tau_c + F_{D_j} (-\frac{N}{2} + n + 1)\tau_c]] \right. \right. \\
& \quad \left. \left. \text{sinc}[\tau_c(\beta_j^{(n)} - \beta_i^{(n-m)} + F_{D_j})] \right] \right|
\end{aligned}$$

The number of radars can be extended to  $M$  in an RSN. Assuming each radar has no time delay,  $t_1 = t_2 = t_M = 0$  and considering interferences from all the other  $M - 1$  radars. Assuming time delay  $\tau$  for receiving radar  $i$ , the ambiguity function of radar  $i$  with phase coded waveform can be

$$\begin{aligned}
& A_i(\tau, F_{D_1}, \dots, F_{D_M}) \tag{11} \\
& = \left| \int_{-\infty}^{\infty} \sum_{j=1}^M x_j(t) \exp(j2\pi F_{D_j} t) x_i^*(t - \tau) dt \right| \\
& = \left| \tau_c \sum_{j=1}^M \sum_{n=m}^{N-1} \left[ \exp[j2\pi [\beta_i^{(n-m)} (\frac{N}{2} + m - 1)\tau_c \right. \right. \\
& \quad \left. \left. + \beta_j^{(n)} (-\frac{N}{2} + 1)\tau_c + F_{D_j} (-\frac{N}{2} + n + 1)\tau_c]] \right. \right. \\
& \quad \left. \left. \text{sinc}[\tau_c(\beta_j^{(n)} - \beta_i^{(n-m)} + F_{D_j})] \right] \right|
\end{aligned}$$

Here,  $0 < i \leq M$ . (11) consists of two parts: useful signal(reflected signal from radar  $i$  waveform),

$j = i$  part in the (11); and interferences from other  $M - 1$  radar waveforms,  $j \neq i$  parts in (11).

### 3 Perfect Punctured ZCZ Sequence-Pair set

Zero correlation zone(ZCZ) is a new concept provided by Fan [8] [9] [10] in which both autocorrelation and cross correlation sidelobes are zero while the time delay is kept within the Zero Correlation Zone instead of the whole period of time domain.

Matsufuji and Torii have provided some methods of constructing ZCZ sequences in [11] [12]. In this section, we apply optimized punctured sequence-pair [13] in zero correlation zone to construct a new kind of triphase code-optimized punctured ZCZ sequence-pair set. The newly provided triphase code which has good autocorrelation and cross correlation properties in ZCZ can be good candidate for phase coded waveforms in RSN.

#### 3.1 The Definition of Optimized Punctured ZCZ Sequence-Pair Set

**Definition 3-1** Assume  $(x_i^{(p)}, y_i^{(p)})$  to be sequence-pair set of length  $N$  and the number of sequence-pairs  $K$ , where  $p = 1, 2, 3, \dots, N - 1, i = 0, 1, 2, \dots, K - 1$ , if all the sequences in the set satisfy the following equation:

$$R_{x^{(p)}y^{(q)}}(\tau) = \sum_{i=0}^{N-1} x_i^{(p)} y_{(i+\tau) \bmod(N)}^{(q)*} = \sum_{i=0}^{N-1} y_i^{(p)} x_{(i+\tau) \bmod(N)}^{(q)*}$$

$$= \begin{cases} \lambda N, & \text{for } \tau = 0, p = q \\ 0, & \text{for } \tau = 0, p \neq q \\ 0, & \text{for } 0 < |\tau| \leq Z_0 \end{cases} \quad (12)$$

where  $0 < \lambda \leq 1$ , then  $(x_i^{(p)}, y_i^{(p)})$  is called ZCZ sequence-pair set,  $ZCZP(N, K, Z_0)$  is a symbol in short.

**Definition 3-2** [13] Sequence  $u = (u_0, u_1, \dots, u_{N-1})$  is the punctured sequence for  $v = (v_0, v_1, \dots, v_{N-1})$ ,

$$u_j = \begin{cases} 0, & \text{if } j \in p \text{ punctured bits} \\ v_j, & \text{if } j \in \text{Non-punctured bits} \end{cases} \quad (13)$$

Where  $p$  is the number of punctured bits in sequence  $v$ , suppose  $v_j = (-1, 1)$ ,  $u$  is  $p$ -punctured binary sequence,  $(u, v)$  is called a punctured binary sequence-pair.

**Theorem 3-1** [13] The autocorrelation of punctured sequence-pair  $(u, v)$  is defined

$$R_{uv}(\tau) = \sum_{i=0}^{N-1} u_i v_{(i+\tau) \bmod N}, 0 \leq \tau \leq N-1 \quad (14)$$

If the punctured sequence-pair has the following autocorrelation property:

$$R_{uv}(\tau) = \begin{cases} E, & \text{if } \tau \equiv 0 \bmod N \\ 0, & \text{others} \end{cases} \quad (15)$$

the punctured sequence-pair is called optimized punctured sequence-pair [13]. Where,  $E = \sum_{i=0}^{N-1} u_i v_{(i+\tau) \bmod N} = N - p$ , is the energy of punctured sequence-pair.

The properties, Fourier spectrum characters, existing necessary conditions and some construction methods with help of already known sequences such as PN code have been proven and given out by Jiang[1]. Many optimized punctured sequence-pairs have been found of length from 7 to 31 so far. If  $(x_i^{(p)}, y_i^{(p)})$  in Definition 3-1 is constructed by optimized punctured sequence-pair and a certain matrix, such as Hadamard matrix or an orthogonal matrix, where

$$x_i^{(p)} \in (-1, 1), \quad i = 0, 1, 2, \dots, N-1$$

$$y_i^{(q)} \in (-1, 0, 1), \quad i = 0, 1, 2, \dots, N-1$$

$$\begin{aligned} R_{x^{(p)}y^{(q)}}(\tau) &= \sum_{i=0}^{N-1} x_i^{(p)} y_{(i+\tau) \bmod N}^{(q)*} = \sum_{i=0}^{N-1} y_i^{(p)} x_{(i+\tau) \bmod N}^{(q)*} \\ &= \begin{cases} \lambda N, & \text{for } \tau = 0, p = q \\ 0, & \text{for } \tau = 0, p \neq q \\ 0, & \text{for } 0 < |\tau| \leq Z_0 \end{cases} \end{aligned} \quad (16)$$

where  $0 < \lambda \leq 1$ , then  $(x_i^{(p)}, y_i^{(p)})$  can be called optimized punctured ZCZ sequence-pair set.

### 3.2 Design for Optimized Punctured ZCZ Sequence-pair Set

Based on odd length optimized punctured binary sequence pairs and a Hadamard matrix, a optimized punctured ZCZ sequence-pair set can be constructed on following steps:

**Step 1:** Considering an odd length optimized punctured binary sequence-pair  $(u, v)$ , the length of each sequence is  $N_1$

$$u = u_0, u_1, \dots, u_{N_1-1}, u_i \in (-1, 1),$$

$$v = v_0, v_1, \dots, v_{N_1-1}, v_i \in (-1, 0, 1),$$

$$i = 0, 1, 2, \dots, N_1 - 1, N_1 \text{ odd}$$

**Step 2:** Consider Walsh sequences set(Hadamard matrix)  $B$ , the length of the sequence is  $N_2$  which is equal to the number of the sequences. In some other words, a Hadamard matrix of order  $N_2$  is considered.

$$B = (b^0, b^1, \dots, b^{N_2-1}),$$

$$b^i = (b_0^i, b_1^i, \dots, b_{N_2-1}^i),$$

$$R_{b^i b^j} = \begin{cases} N_2, & \text{if } i = j \\ 0, & \text{if } i \neq j \end{cases}$$

**Step 3:** Doing bit-multiplication on the optimized punctured binary sequence-pair and each line of Walsh sequences set  $B$ (Hadamard matrix), then sequence-pair set  $(X, Y)$  is obtained,

$$b^i = (b_0^i, b_1^i, \dots, b_{N_2-1}^i), i = 0, 1, \dots, N_2 - 1,$$

$$x_j^i = u_{j \bmod N_1} b_{j \bmod N_2}^i, 0 \leq i \leq N_2 - 1, 0 \leq j \leq N - 1,$$

$$X = (x^0, x^1, \dots, x^{N_2-1}),$$

$$y_j^i = v_{j \bmod N_1} b_{j \bmod N_2}^i, 0 \leq i \leq N_2 - 1, 0 \leq j \leq N - 1,$$

$$Y = (y^0, y^1, \dots, y^{N_2-1})$$

Where  $GCD(N_1, N_2) = 1$ , common divisor of  $N_1$  and  $N_2$  is 1,  $N = N_1 * N_2$ . The sequence-pair set  $(X, Y)$  is optimized punctured ZCZ sequence-pair set and  $N_1 - 1$  is the zero correlation zone  $Z_0$ . The length of each sequence in optimized punctured ZCZ sequence-pair set is  $N = N_1 * N_2$  that depends on the product of length of optimized punctured sequence-pair and the length of Walsh sequence in Hadamard matrix. The number of sequence-pair in optimized punctured ZCZ sequence-pair set rests on the order of the Hadamard matrix. The sequence  $x^i$  in sequence set  $X$  and the corresponding sequence  $y^i$  in sequence set  $Y$  construct an optimized punctured ZCZ sequence-pair  $(x^i, y^i)$  that can be used as a pulse compression code. The phase states for any sequence-pair among  $(x^i, y^i)$  are  $-\pi, 0$  and  $\pi$ . Consequently, our newly provided optimized punctured ZCZ sequence-pair is a new kind of triphase code. And optimized punctured ZCZ sequence-pair set is made up of a set of triphase codes.

The correlation property of the sequence-pair in optimized punctured ZCZ sequence-pair set is:

$$\begin{aligned}
R_{x^j y^j}(\tau) &= R_{x^j y^i}(\tau) = R_{uv}(\tau \bmod N_1) R_{b^i b^j}(\tau \bmod N_2) \\
&= R_{uv}(\tau \bmod N_1) R_{b^i b^i}(\tau \bmod N_2) \\
&= \begin{cases} EN_2, & \text{if } \tau = 0, i = j \\ 0, & \text{if } 0 < |\tau| \leq N_1 - 1, i = j \\ 0, & \text{if } i \neq j \end{cases} \quad (17)
\end{aligned}$$

where  $N_1 - 1$  is the zero correlation zone  $Z_0$ .

Proof:

1) When  $i = j$ ,

$$\tau = 0,$$

$$R_{uv}(0) = E, R_{b'b'}(0) = N_2,$$

$$R_{x^i y^j}(0) = R_{uv}(0)R_{b'b'}(0) = EN_2;$$

$$0 < |\tau| \leq N_1 - 1,$$

$$R_{uv}(\tau) = 0,$$

$$R_{x^i y^j}(\tau) = R_{uv}(\tau \bmod N_1)R_{b'b'}(\tau \bmod N_2) = 0;$$

2) When  $i \neq j$ ,

$$\tau = 0,$$

$$R_{b'b'}(0) = 0,$$

$$R_{x^i y^j}(0) = R_{x^j y^i}(0)$$

$$= R_{uv}(\tau \bmod N_1)R_{b'b'}(\tau \bmod N_2) = 0;$$

$$0 < |\tau| \leq N_1 - 1,$$

$$R_{uv}(\tau) = 0,$$

$$R_{x^i y^j}(\tau) = R_{x^j y^i}(\tau)$$

$$= R_{uv}(\tau \bmod N_1)R_{b'b'}(\tau \bmod N_2) = 0.$$

According to Definition 3-1, the sequence-pair set constructed by the above method is ZCZ sequence-pair set.

### 3.3 Properties of Optimized Punctured ZCZ Sequence-pair set

Considering the optimized punctured ZCZ sequence-pair set that is constructed by the method mentioned in the last part, the autocorrelation and cross correlation properties can be simulated

and analyzed with Matlab. For example, the optimized punctured ZCZ sequence-pair set  $(X, Y)$  is constructed by 31-length optimized punctured binary sequence-pair  $(u, v)$ ,  $u = (1111 - 1 - 1 - 11 - 11 - 1111 - 1 - 1 - 1 - 11 - 1 - 11 - 1 - 1111 - 111 - 1)$ ,  $v = (1111000101011100001001001110110)$  and Hadamard matrix  $H = [1111; 1 - 11 - 1; 11 - 1 - 1; 1 - 1 - 11]$  of order 4. We follow the three steps presented in Section 3 to construct the 124-length optimized punctured ZCZ sequence-pair set. The number of sequence-pair here is 4 and the length of each sequence is  $31 * 4 = 124$ . The first line of each matrix  $X = [x_1; x_2; x_3; x_4]$  and  $Y = [y_1; y_2; y_3; y_4]$  constitute a certain optimized punctured ZCZ sequence-pair  $(x_1, y_1)$ . Similarly, the second line of each matrix  $X$  and  $Y$  constitute

another optimized punctured ZCZ sequence-pair  $(x_2, y_2)$ .

$$x_1 = ( \begin{array}{l} 1111 - 1 - 1 - 11 - 11 - 1111 - 1 - 1 - 1 - 1 \\ 1 - 1 - 11 - 1 - 1111 - 111 - 11111 - 1 - 1 \\ -11 - 11 - 1111 - 1 - 1 - 1 - 11 - 1 - 11 - 1 \\ -1111 - 111 - 11111 - 1 - 1 - 11 - 11 - 111 \\ 1 - 1 - 1 - 1 - 11 - 1 - 11 - 1 - 1111 - 111 - 1 \\ 1111 - 1 - 1 - 11 - 11 - 1111 - 1 - 1 - 1 - 11 \\ -1 - 11 - 1 - 1111 - 111 - 1 \end{array} ),$$

$$y_1 = ( \begin{array}{l} 11110001010111000010010011101101111000 \\ 10101110000100100111011011110001010111 \\ 00001001001110110111100010101110000100 \\ 1001110110 \end{array} );$$

$$x_2 = ( \begin{array}{l} 1 - 11 - 1 - 11 - 1 - 1 - 1 - 1 - 1 - 11 - 1 \\ -11 - 1111 - 1 - 1 - 111 - 1111 - 1 - 1 - 1 \\ 1 - 111 - 1111111 - 111 - 11 - 1 - 1 - 1111 \\ -1 - 11 - 1 - 1 - 1111 - 11 - 1 - 11 - 1 - 1 \\ -1 - 1 - 1 - 11 - 1 - 11 - 1111 - 1 - 1 - 11 \\ 1 - 1111 - 1 - 1 - 11 - 111 - 1111111 - 111 \\ -11 - 1 - 1 - 1111 - 1 - 11 - 1 - 1 - 111 \end{array} ),$$

$$y_2 = ( \begin{array}{l} 1 - 11 - 1000 - 10 - 10 - 11 - 10000100 - 1 \\ 001 - 1101 - 10 - 11 - 1100010101 - 110000 \\ -100100 - 11 - 10 - 1101 - 11 - 1000 - 10 \\ -10 - 11 - 10000100 - 1001 - 1101 - 10 - 1 \\ 1 - 1100010101 - 110000 - 100100 - 11 - 10 \end{array} )$$

Optimized punctured ZCZ sequence-pairs  $(x_1, y_1)$  and  $(x_2, y_2)$  are simulated and investigated in the following parts.

### 3.3.1 Autocorrelation and Cross Correlation Properties

The autocorrelation property and cross correlation property of 124-length optimized punctured ZCZ sequence pair set  $(X, Y)$  are shown in Fig.1 and Fig.2 .

From the Fig.1 and Fig.2, the sidelobe of autocorrelation of ZCZ sequence-pair set can be as low as 0 when the time delay is kept within  $Z_0 = N_1 = 31$  (zero correlation zone) and the cross correlation value is kept as low as 0 during the whole time domain.

As it is known that a suitable criterion for evaluating code of length  $N$  is the peak signal to peak signal sidelobe ratio (PSR) of their aperiodic autocorrelation function, which can be bounded by [14]

$$[PSR]_{dB} \leq 20\log N = [PSR_{max}]_{dB} \quad (18)$$

The only uniform phase codes that can reach the  $PSR_{max}$  are the Barker codes whose length is equal or less than 13. However, the sidelobe of the new code in both Fig.1 and Fig.2 can be as low as 0. In some other words, the peak signal to peak signal sidelobe can be as large as infinite. In addition, it is also obvious that the length of the new code can extend to 31 that is much longer than the length of the Barker code.

### 3.3.2 Ambiguity function

When the transmitted impulse is reflected by a moving target, the reflected echo signal includes a linear phase shift which corresponds to a Doppler shift  $f_d$  [7]. As a result of the Doppler shift  $f_d$ , the main peak of the autocorrelation function is reduced and so as to the SNR degradation shown as following:

$$|d|_{dB} = 10 \log \frac{\int_0^T x(s)x^*(s)ds}{\int_0^T x(s)e^{j2\pi f_d T_c} x^*(s)ds} \quad (19)$$

In addition, the sidelobe structure is changed because of the Doppler shift.

Considering the sequence-pair  $(x, y)$  here, the receiving sequence in ambiguity function is different from the echo signal. Furthermore, the periodic correlation is use here. The ambiguity function listed as (9) can be rewritten as

$$A(\tau, F_D) = \left| \int_{-\frac{T}{2}}^{-\frac{T}{2}+\tau} x(t) \exp(j2\pi F_D t) y^*(t + T - \tau) dt + \int_{-\frac{T}{2}+\tau}^{\frac{T}{2}} x(t) \exp(j2\pi F_D t) y^*(t - \tau) dt \right| \quad (20)$$

Equation (20) can be used to analyze the autocorrelation performance within Doppler shift. Equation (20) is plotted in Fig.3 in a three-dimensional surface plot to analyze the radar performance of optimized punctured ZCZ sequence-pair set within Doppler shift. Here, maximal time delay is 1 unit (normalized to length of the code, in units of NTs) and maximal doppler shift is 3 units for autocorrelation (normalized to the inverse of the length of the code, in units of 1/NTs). In Fig.3, there is relative uniform plateau suggesting low and uninform sidelobes, minimizing target masking effect in zero correlation zone of time domain, where  $Z_0 = 31$ ,  $-31 < \tau < 31$ ,  $\tau \neq 0$ .

### 3.4 Co-existence of Optimized Punctured ZCZ Sequence-pairs

Considering interference from another radar  $j$ , if there are time delay and Doppler shift, the ambiguity function of radar  $i$  can be expressed as

$$\begin{aligned} & A(\tau, F_{D_i}, F_{D_j}) \\ &= \left| \int_{-\infty}^{\infty} (x^i(t) \exp(j2\pi F_{D_i} t) + x^j(t) \exp(j2\pi F_{D_j} t)) \right. \\ & \quad \left. y^{i*}(t - \tau) dt \right| \end{aligned} \quad (21)$$

Fig.4 is three-dimensional surface plot to analyze the ambiguity function of radar  $i$  (considering interference from radar  $j$ ).

Generally speaking, Fig.4 closely resembles Fig.3. There is relative uniform plateau suggesting low and uniform sidelobes, minimizing target masking effect in zero correlation zone of time domain, where  $Z_0 = 31$ ,  $-31 < \tau < 31, \tau \neq 0$ . It is easy to see that even considering the interference from another radar  $j$ , the radar  $i$  may work as well as there is no interference.

Fig.5 is the output of matched filter of radar  $i$  (considering interference from radar  $j$ ) when there is no Doppler shift.

Fig.1 and Fig.5 are similar. There are regular high peaks on multiples of period 31 which is the length of zero correlation zone. And the sidelobe can be as low as 0 when the time delay is kept among zero correlation zone  $-31 < \tau < 31, \tau \neq 0$ . The high peak on zero time delay point can be used to detect targets.

In addition, output of matched filter of radar  $i$  (considering interference from radar  $j$ ), when there is no time delay, is illustrated in Fig.6. Here, the Doppler shift is kept among 5 units (normalized to the inverse of the length of the code, in units of  $1/NT_s$ ). From Fig.6, without time delay, while the Doppler shift is less than 1 unit (normalized to length of the code, in units of  $NT_s$ ), the amplitude decreases sharply. And the amplitude has a downward trend on the whole frequency domain. For some traditional phase coded waveforms, such as the Barker code, when Doppler frequencies equal to multiples of the pulse repetition frequency ( $PRF = 1/PRI = 1/T_s$ ) the ambiguity value turns to be zero. Because of these zeros, such multiples of the pulse repetition frequency will render the radar blind [15] to their velocities. However, in Fig.6, ambiguity values are zero only when Doppler frequencies are equal to odd multiples of the PRF. Therefore, using the optimized punctured ZCZ sequence-pair in the RSN system could, to some extent, improve the blind speed problem in moving target detection system.

## 4 System Simulation in Radar Sensor Network

In RSN of  $M$  radars, the combined received signal for the radar  $i$  is

$$r_i(u, t) = \sum_{j=1}^M x_j(t - t_j) \exp(j2\pi F_{D_j} t) + n(u, t) \quad (22)$$

$F_{D_j}$  is doppler shift of target relative to waveform  $j$ ,  $t_j$  is delay of radar transmitting waveform  $j$ , and  $n(u, t)$  is additive white Gaussian noise(AWGN). Equal gain diversity combination is used in the following simulation, the structure can be constructed as Fig.7.

According to this structure, the combined received signal  $r_i(u, t)$  is processed by its corresponding matched filter  $i$  and the output of branch  $i$  is  $Z_i(u, t)$ . Each  $Z_i(u, t)$  can be equal gain combined to construct the final output  $Z(u, t)$ .

The output of branch  $i$  is

$$\begin{aligned} & |Z_i(u)| \\ = & \left| \int_{-\frac{T}{2}}^{\frac{T}{2}} \left[ \sum_{j=1}^M x_j(t - t_j) \exp(j2\pi F_{D_j} t) + n(u, t) \right] \right. \\ & \left. y_i^*(t - t_i) dt \right| \end{aligned}$$

Where  $n(u) = \int_{-\frac{T}{2}}^{\frac{T}{2}} n(u, t) y_i^*(t - t_i) dt$  can be easily proved to be still an AWGN.

We can also have three special cases for  $|Z_i(u)|$ :

1) When all the radar sensors transmit the signals synchronously, in some other words, there is no time delay for each radar sensor nor doppler shift,  $t_1 = t_2 = \dots = t_M = 0$  and  $F_{D_1} = F_{D_2} = \dots = F_{D_j} = 0$ , then

$$\begin{aligned} & |Z_i(u)| \quad (23) \\ = & \left| \int_{-\frac{T}{2}}^{\frac{T}{2}} \left[ \sum_{j=1}^M x_j(t) + n(u, t) \right] y_i^*(t) dt \right| \\ = & |E + 0 + n(u)| \end{aligned}$$

2) If there are no time delay but Doppler shift,  $t_1 = t_2 = \dots = t_M = 0$ , then

$$\begin{aligned} & |Z_i(u)| \\ &= \left| \int_{-\frac{T}{2}}^{\frac{T}{2}} \left[ \sum_{j=1}^M x_j(t) \exp(j2\pi F_{D_j}) + n(u, t) \right] y_i^*(t) dt \right| \end{aligned} \quad (24)$$

In our work, we assume the doppler shift can be well estimated in the receiving radar sensor, so the doppler shift compensation factor  $\exp^*(j2\pi F_{D_j})$  is introduced here. The equation can be modified as:

$$\begin{aligned} & |Z_i(u)| \\ &= \left| \int_{-\frac{T}{2}}^{\frac{T}{2}} \left[ \sum_{j=1}^M x_j(t) \exp(j2\pi F_{D_j}) + n(u, t) \right] y_i^*(t) \exp^*(j2\pi F_{D_j}, t) dt \right| \\ &\leq |E| + \left| \int_{-\frac{T}{2}}^{\frac{T}{2}} \left[ \sum_{j=1}^M x_j(t) \exp(j2\pi (F_{D_j} - F_{D_j})) y_i^*(t) \right] \right. \\ &\quad \left. + \int_{-\frac{T}{2}}^{\frac{T}{2}} n(u, t) y_i^*(t) \exp^*(j2\pi F_{D_j}, t) dt \right| \end{aligned} \quad (25)$$

According to the the third part of the equation (25), the magnitude of noise is reduced because of the doppler shift compensation factor.

If  $F_{D_1} = F_{D_2} = \dots = F_{D_j} = F_D$ , the equation (25) can be further simplified as

$$\begin{aligned} & |Z_i(u)| \\ &\leq |E| + 0 + \left| \int_{-\frac{T}{2}}^{\frac{T}{2}} n(u, t) y_i^*(t) \exp^*(j2\pi F_D, t) dt \right| \end{aligned} \quad (26)$$

3) If both time delay and doppler shift exist in the RSN, also considering the doppler shift

compensation factor in the receiving sensor,

$$\begin{aligned}
& |Z_i(u)| \\
&= \left| \int_{-\frac{T}{2}}^{\frac{T}{2}} \left[ \sum_{j=1}^M x_j(t-t_j) \exp(j2\pi F_{D_j} t) + n(u, t) \right] \right. \\
&\quad \left. y_i^*(t-\tau) \exp^*(j2\pi F_{D_j} t) dt \right| \\
&\leq |E| + \left| \int_{-\frac{T}{2}}^{\frac{T}{2}} \left[ \sum_{j=1}^M x_j(t-t_j) \exp(j2\pi(F_{D_j} - F_{D_i})) \right] \right. \\
&\quad \left. y_i^*(t-t_i) + \int_{-\frac{T}{2}}^{\frac{T}{2}} n(u, t) y_i^*(t-t_j) \exp^*(j2\pi F_{D_i} t) dt \right|
\end{aligned} \tag{27}$$

Assume  $F_{D_1} = F_{D_2} = \dots = F_{D_j} = F_{D_i}$ ,

$$\begin{aligned}
& |Z_i(u)| \\
&\leq |E| + \left| \int_{-\frac{T}{2}}^{\frac{T}{2}} \left[ \sum_{j \neq i}^M x_j(t-t_j) \right] y_i^*(t-t_i) dt \right| \\
&\quad + \left| \int_{-\frac{T}{2}}^{\frac{T}{2}} n(u, t) y_i^*(t-t_j) \exp^*(j2\pi F_{D_i} t) dt \right|
\end{aligned} \tag{28}$$

Because of the good periodic autocorrelation sidelobe properties of our codes, the frame of receiving data could be modified before the matched filter on the receiving radar sensor to improve the RSN performance. Here is the frame of receiving data illustrated in Fig.8.

The data from  $N+1$  to  $\max(t_j) + N$  are added to data from 1 to  $N$  bit by bit. In this way can we get the periodic correlation of receiving signal and the matched filter.

Therefore,

$$\begin{aligned}
& |Z_i(u)| \\
&\leq |E| + 0 + \left| \int_{-\frac{T}{2}}^{\frac{T}{2}} n(u, t) y_i^*(t) \exp^*(j2\pi F_{D_i} t) dt \right|
\end{aligned} \tag{29}$$

Based on (27) and (29), using frame modification before the matched filter, the performance of case 2) and 3) can be theoretically comparable. In some other words, using our provided codes

and frame modification, the RSN under the condition of time delay for each radar sensor can, to some extent, work as well as the RSN where all the radar sensors transmit signal synchronously.

We apply optimized punctured ZCZ sequence-pair set as a bank of phase coded waveforms together with equal gain combination technique in the simulation in order to study the performance versus different number of radars in RSN under the condition of either doppler shift or not. According to [7],  $P_D$ (Probability of Detection),  $P_{FA}$ (Probability of False Alarm) and  $P_M$ (Probability of Miss) are three probabilities of most interest in the radar system. Note that  $P_M = 1 - P_D$ , thus,  $P_D$  and  $P_{FA}$  suffice to specify all of the probabilities of interest in radar system. Therefore, we respectively simulated the above two probabilities of different number of radars using different number of optimized punctured ZCZ sequence-pairs in single radar system, 4-radar system and 8-radar system together with 1-radar system using Barker code respectively in this section. Three special cases of performances have been simulated. They are detection performance under the condition of no time delay nor doppler shift, no time delay but doppler shift and both time delay for each radar sensor and doppler shift.  $10^6$  times of Monte-Carlo simulation has been run for each SNR value. When multiple radars are working in RSN under the condition of doppler shift, the doppler shift are supposed to be well estimated in the receiving radar sensor and the compensating factors are introduced in the receiving radars. Since equal gain combination is used here, the threshold for detection is chosen to be around 0.5.

The probability of miss detection of the envelope detector in single radar, 4-radar, 8-radar and the single radar system using Barker code under the condition of no time delay nor doppler shift, of no time delay but doppler shift and of both time delay and doppler shift are compared in Fig.9(a), Fig.9(b) and Fig.9(c) respectively. According to the Fig.9(a), to achieve the same  $P_M = 10^{-3}$ , single radar system using Barker code requires about  $2dB$  more SNR than that of 4-radars under the environment of no time delay nor no doppler shift. Fig.9(b) also illustrates that

when  $P_M = 10^{-3}$ , SNR of 8-radars are  $2.2dB$  smaller than that of single radar system using Barker code when there is doppler shift in the simulation system. Considering time delay for each radar in multiple radars system, we only have  $P_M$  of 4-radar and 8-radar system in Fig.9(c). From Fig.10(c), SNR of 8-radar RSN can gain  $1.7dB$  smaller than 4-radar SNR to achieve the same  $P_M = 10^{-3}$ .

The probability of false alarm of envelope detector in different number of radars under the condition of no time delay nor doppler shift, of no time delay but doppler shift and of both time delay and doppler shift are shown in Fig.10(a) Fig.10(b) and Fig.10(c) respectively. Considering doppler shift, Fig.10(a) shows that the SNR of single radar system using Barker code requires about  $5dB$  greater than that of 8-radars to obtain the same  $P_{FA} = 10^{-2}$ . When there is no doppler shift illustrated in Fig.10(b), the SNR of 8-radars can be nearly  $3.8dB$  smaller than that of single radar system using Barker code in order to achieve the same  $P_{FA} = 10^{-2}$ . From Fig.10(c), 4-radar system requires  $1.7dB$  more than that of 8-radar RSN under the condition of both time delay and doppler shift.

However, it is clear to see that, no matter how many radars have been exploited in the RSN, the performances of system without doppler shift are worse than that under doppler shift condition. It is of the reason that doppler shift, assumed to be exactly estimated, is well compensated on the receiving radar in the system under the condition of doppler shift. Besides, the doppler shift compensating part in receiving radar also, to some extent, reduces the magnitude of Gaussian noise of the channel because of the doppler shift factor  $\exp(-j2\pi F_{D_j}t)$  we used to compensate the doppler shift in the receiving radar as shown in quation (25). The above figures also clearly illustrate that whether considering doppler shift in RSN or not, performance of detection of multiradars(applying our optimized punctured ZCZ sequence-pair set and equal gain combination) are superior to that of singler radar. In addition, because of the superior autocorrelation sidelobe property of our codes, the performances of 4-radar and 8-radar RSN under the condition of time delay can be comparable

to those under the condition of no time delay.

Therefore, according to the above results, applying our optimized punctured ZCZ sequence-pair set in RSN, the detection performances are much better than those of applying traditional phase coded waveforms in a single radar network.

## 5 Conclusion

We have studied phase coded waveform design and spatial diversity under the condition of doppler shift in radar sensor networks (RSN). In addition, the definition and properties of optimized punctured ZCZ sequence-pair set, which can be used as phase coded waveforms in RSN, are discussed in this paper. The significant advantage of the optimized punctured ZCZ sequence-pair set is a considerably reduced sidelobe as low as zero in the zero correlation zone and zero mutual cross correlation value in the whole time domain. Because of the orthogonal property of any two optimized punctured ZCZ sequence-pairs among a optimized punctured ZCZ sequence-pair set, they can co-exist in RSN and achieve better detection performance than that of a single radar. Consequently, the general conclusion can be drawn from the results presented in this paper that the optimized punctured ZCZ sequence-pair set, which has much better cross correlation properties than the optimum biphasic codes(longer than 13), whose cross correlation peak value has been found to be approximately  $\sqrt{N}$ , can effectively satisfy higher demands criterion for detection accuracy in modern military and security affairs.

## Acknowledgement

This work was supported by the Office of Naval Research (ONR) Grant N00014-07-1-0395, N00014-07-1-1024, and N00014-03-1-0466.

## References

- [1] M. R. Bell, "Information theory and radar waveform design," *IEEE Trans on Information Theory*, vol. 39, no. 5, pp. 1578-1597, Sept. 1993.
- [2] S. Sowelam and A. Tewfik, "Waveform selection in radar target classification," *IEEE Trans on Information Theory*, vol. 46, no. 3, pp. 1014-1029, 2000.
- [3] Q. Liang, "Waveform Design and Diversity in Radar Sensor Networks: Theoretical Analysis and Application to Automatic Target Recognition," *Sensor and Ad Hoc Communications and Networks*, vol. 2, no. 28, pp. 684-689, Sep. 2006.
- [4] Q. Liang, "Radar Sensor Networks for Automatic Target Recognition with Delay-Doppler Uncertainty," *Military Communications Conference, 2006. MILCOM 2006* 23-25, pp. 1-7, Oct. 2006.
- [5] J. Liang, and Q. Liang, "Orthogonal Waveform Design and Performance Analysis in Radar Sensor Networks," *Military Communications Conference, 2006. MILCOM 2006* 23-25, pp. 1-6, Oct. 2006.
- [6] H. Deng, "Synthesis of binary sequences with good correlation and cross-correlation properties by simulated annealing," *IEEE Trans on Aerospace and Electronic systems*, vol. 32, no. 1, Jan 1996.
- [7] M. A. Richards, *Fundamentals of Radar Signal Processing*, McGraw-Hill, 2005.
- [8] P. Z. Fan, N. Suehiro, N. Kuroyanagi and X. M. Deng, "A class of binary sequences with zero correlation zone," *IEE Electron.Letter*, 35 (10): 777-779, 1999.
- [9] P. Z. Fan and L. Hao, "Generalized Orthogonal Sequences and Their Applications in Synchronous CDMA Systems," *IEICE Trans.Fundamentals*, E832A(11): 1 16, 2000.

- [10] P. Z. Fan, "New Direction in Spreading Sequence Design and the Related Theoretical Bounds," *International Conference of Communications , Circuits and Systems*, June 29-July 1, 2002, PRC.
- [11] S. Matsufuji, N Suehiro , N Kuroyanagi and P Z Fan, "Two types of polyphase sequence set for approximately synchronized CDMA systems," *IEICE Trans. Fundamentals*, E862A(1): 229-234, Jan. 2003.
- [12] H. Torii, M. Nakamura and N. Suehiro, "A new class of zero correlation zone sequences," *Tran. Inform.Theory*, 50: 559-565, Mar. 2004.
- [13] T. Jiang, *Research on Quasi-Perfect Binary Signal Pair and Perfect Punctured Binary Signal Pair Theory*, Ph.D Dissertation: Yanshan University, 2003.
- [14] M. I. Skolnik, *Radar Handbook*, New York: McGraw-Hill, 1970.
- [15] S. Ariyavisitakul, N. Sollenberger, and L. Greenstein, *Introduction to Radar System*, Tata McGraw-Hill, 2001.
- [16] X.Lei and L. Qilian, "Perfect punctured ZCZ sequence-pair set: design, analysis and application to radar," *submitted to Milcom 2008*

## List of Figures

1	Periodic autocorrelation property of optimized punctured ZCZ sequence-pair set . . .	26
2	Periodic cross correlation property of optimized punctured ZCZ sequence-pair set . . .	26
3	Ambiguity function of 124-length ZCZ sequence-pair set: autocorrelation . . . . .	27
4	Ambiguity function of radar $i$ (considering interference from radar $j$ ) . . . . .	27
5	Output of matched filter of radar $i$ (considering interference from radar $j$ ) with no Doppler shift . . . . .	27
6	Output of matched filter of radar $i$ (considering interference from radar $j$ ) with no time delay . . . . .	28
7	Waveform diversity combining in RSN . . . . .	28
8	Received Signal Frame . . . . .	28
9	Probability of miss detection in RSN under the condition of: (a)No time delay nor doppler shift (b)No time delay but doppler shift (c)Time delay and doppler shift . . .	29
10	Probability of false alarm in RSN under the condition of: (a)No time delay nor doppler shift (b)No time delay but doppler shift (c)Time delay and doppler shift . . .	30

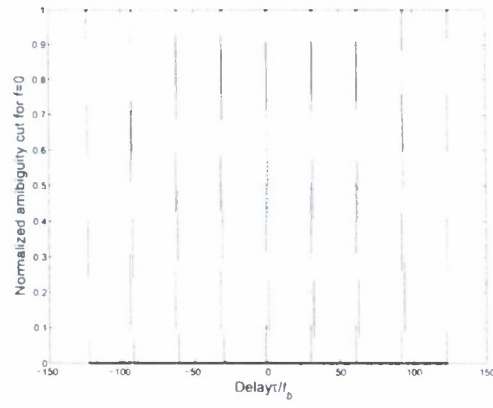


Figure 1: Periodic autocorrelation property of optimized punctured ZCZ sequence-pair set

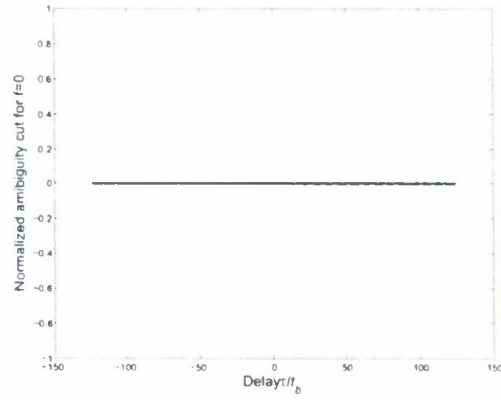


Figure 2: Periodic cross correlation property of optimized punctured ZCZ sequence-pair set

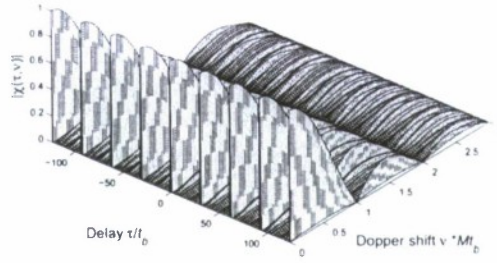


Figure 3: Ambiguity function of 124-length ZCZ sequence-pair set: autocorrelation

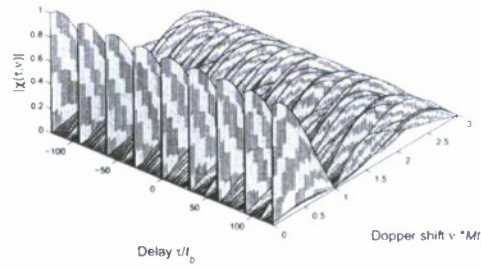


Figure 4: Ambiguity function of radar  $i$  (considering interference from radar  $j$ )

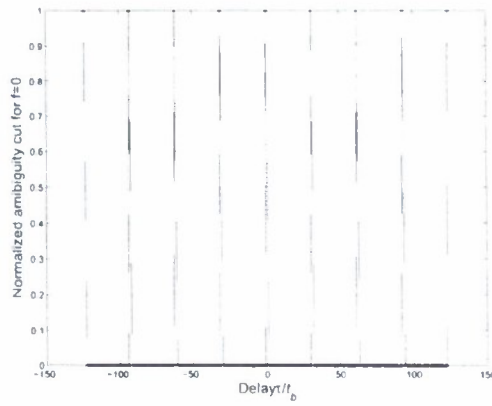


Figure 5: Output of matched filter of radar  $i$  (considering interference from radar  $j$ ) with no Doppler shift

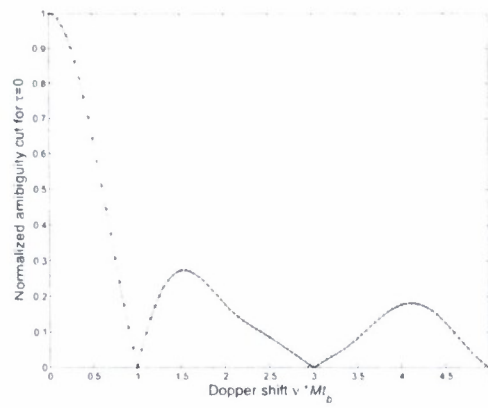


Figure 6: Output of matched filter of radar  $i$  (considering interference from radar  $j$ ) with no time delay

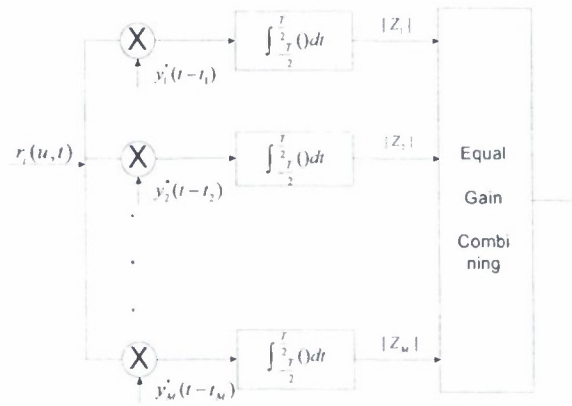
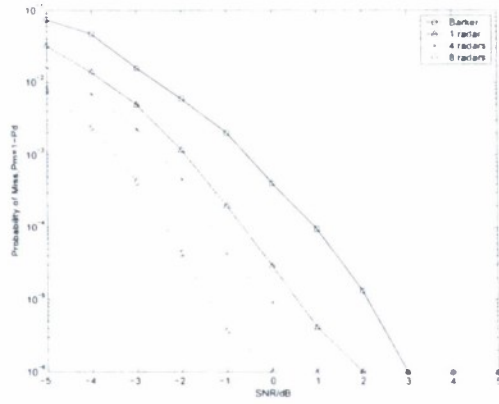


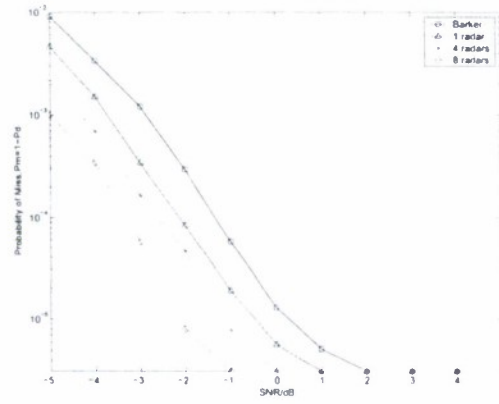
Figure 7: Waveform diversity combining in RSN



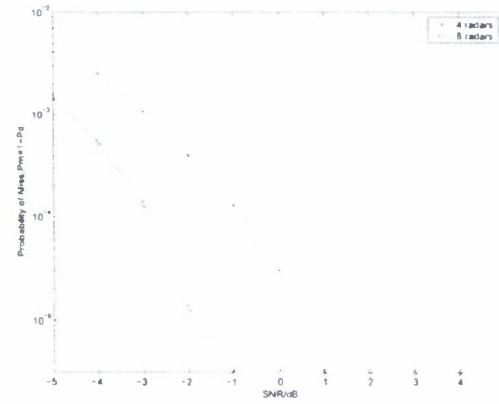
Figure 8: Received Signal Frame



(a)

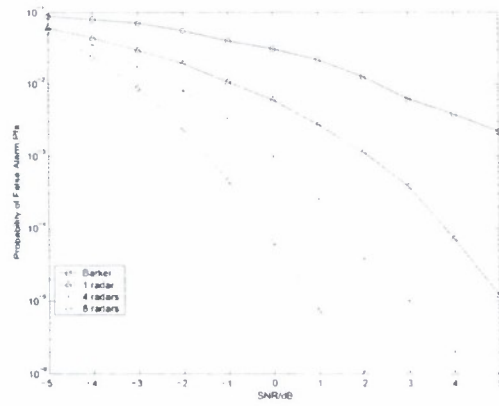


(b)

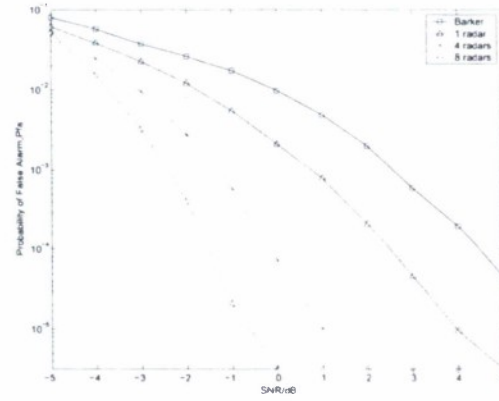


(c)

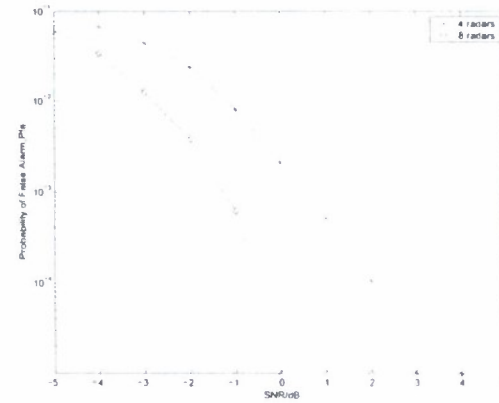
Figure 9: Probability of miss detection in RSN under the condition of: (a) No time delay nor doppler shift (b) No time delay but doppler shift (c) Time delay and doppler shift



(a)



(b)



(c)

Figure 10: Probability of false alarm in RSN under the condition of: (a) No time delay nor doppler shift (b) No time delay but doppler shift (c) Time delay and doppler shift

# Sense-Through-Wall Channel Modeling Using UWB Noise Radar

Jing Liang and Qilian Liang  
Department of Electrical Engineering  
University of Texas at Arlington  
E-mail: jliang@ecn.uta.edu, liang@uta.edu

**Abstract**—Sensing-through-wall will benefit various applications such as emergence rescues and military operations. In order to add more signal processing functionality, it is vital to understand the characterization of sense-through-wall channel. In this paper, we propose a statistical channel model on a basis of real experimental data using UWB noise radar. We employ CLEAN algorithm to obtain the multipath channel impulse response (CIR) and observe that the amplitude of channel coefficient at each path can be accurately characterized as  $T$  location-scale distribution. We also analyze that the multipath contributions arrive at the receiver are grouped into clusters. The time of arrival of clusters can be modeled as a Poisson arrival process, while within each cluster, subsequent multipath contributions or rays also arrive according to a Poisson process. However, these arrival rates are much smaller than those of indoor UWB channels.

## I. INTRODUCTION

Sensing-through-wall techniques have attracted great interest due to a broad range of military and civilian applications. During detection, it is more likely that signal processing occurs at one side of the wall and the interior space to be exploited is on the other and it can not be seen through conventional measures. Therefore it is desirable that the wall penetration sensing provide following information: building layouts like rooms and inner objects; identification of humans and their positions; the composition and structure of the wall. These characterizations will be of great use in locating weapon caches during military operations, searching and rescuing people from natural disasters such as earthquakes and providing sustainability assessment of bridges and buildings.

In recent years UWB waveforms are frequently employed for indoor wireless propagation systems due to the exceptional range resolution and strong penetrating capability. There has been a great amount of research on statistical modeling of UWB indoor multipath channels [1]–[3] and IEEE [4] has standardized it on a basis of Saleh and Valenzuela (S-V) channel model [5]. There have been some efforts investigating sensing-through-wall using UWB waveforms. [6] uses finite difference time-domain (FDTD) method to simulate reflected UWB pulses for three different types of walls. [7] proposes UWB transmission pulses for walls with different thickness and conductivity. However, these reports only describe about transmitted or reflected waveforms based on simulation, sense-through-wall channel has not yet been touched on. Imaging techniques have also been employed to show objects behind the wall in [8] and [9]. [8] uses wideband synthetic aperture

radar and incorporates wall thickness and dielectric constant to generate the indoor scene through image fusion. [9] discusses the advantages of using thermally generated noise as a probing signal and analyzes the basic concepts of synthetic aperture radar image formation using noise waveforms. Nevertheless these studies haven't provide any insight into any property of through-wall radio channel.

In this paper, we propose a statistical multipath model of through-wall radio channel based on real measurement. The UWB noise waveform presented in [9] has been adopted in our work. This is due to the inherently low probability of intercept (LPI) and low probability of detection (LPD). These characterizations provide immunity from detection, jamming, and interference. We investigate the model based on channel impulse response (CIR) obtained through CLEAN processing method. It is observed that the amplitude of channel coefficient at each path can be accurately characterized by  $T$  location-scale distribution. It is also observed that the multipath contributions arrive at the receiver are grouped into clusters. The time of arrival of clusters can be modeled as a Poisson arrival process, while within each cluster, subsequent multipath contributions or rays also arrive according to a Poisson process.

The rest of this paper is organized as follows. In Section II, we summarize the measurement and collection of the data. In Section III, we apply CLEAN algorithm to extract CIR. Section IV presents the channel model in terms of amplitude and temporal characterizations. Conclusion and future work is given in Section V.

## II. MEASUREMENT SETUP

A UWB noise radar system was set up in the Radar Imaging Lab at Villanova University. Fig. 1 illustrates the layout of the experiment room. The wall segment, constructed utilizing solid concrete blocks with a dielectric constant of 7.66, is 0.14m thick 2.8m long and 2.3m high. The room behind this wall is empty.

A horn antenna, model ETS-Lindgren 3164-04, with an operational bandwidth from 0.7 to 6 GHz, was used as the transceiver. The antenna was placed only 1cm to the front wall, which is illustrated in Fig. 2. Therefore the through-wall propagation from antenna front edge to the backside of the wall is 15cm. 37 times of measurements are collected at different but equally spaced positions along the wall with step size 5cm. An Agilent network analyzer, model ENA 5071B, was used for signal synthesis and data collection.

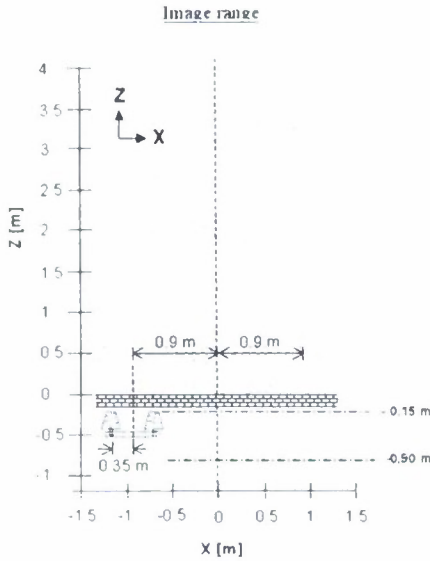


Fig. 1. Experiment Setup

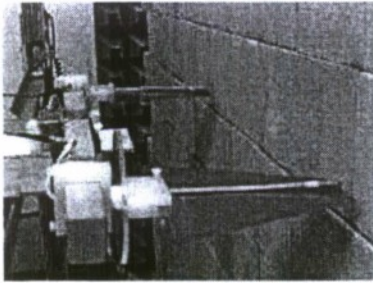
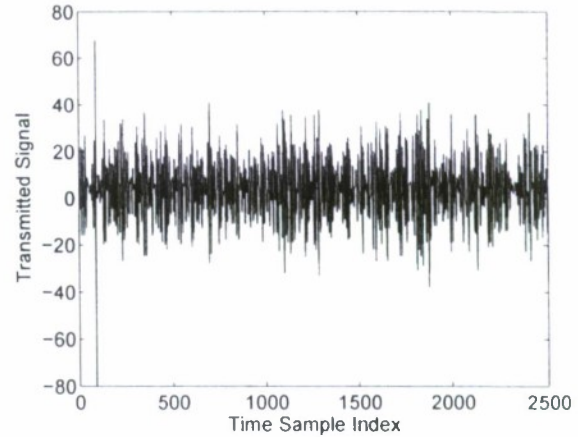


Fig. 2. Radar antenna and wall in the experiment

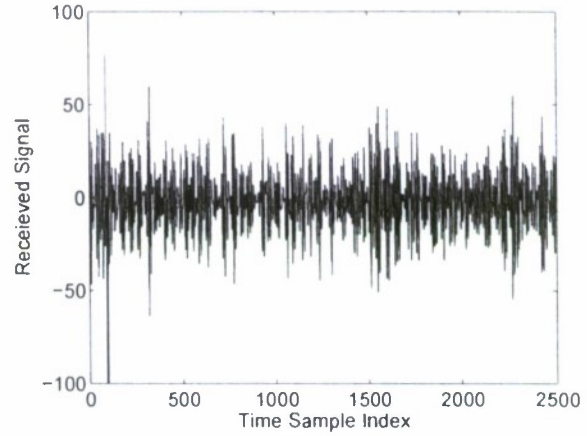
### III. CHANNEL IMPULSE RESPONSE BASED ON THE MEASURED DATA AND CLEAN ALGORITHM

The transmitted noise waveform and received echoes of one measurement are plotted in Fig. 3. It shows that UWB noise waveform has a very good sensing-through-wall capability. During 37 experiments, the frequency of the transmitted signal is 400 – 720 MHz and sampling rate is 1.5GHz/s. The tremendously large amplitude at around sample 100 is due to the antenna coupling [10]. Note that at a different position the measurement result will be slightly different but the characterization of the signals are quite similar. Thus the illustration of pulses collected at one position is sufficient to describe the property.

Fig. 4 shows the histogram of transmitted and received waveform amplitude. It is very interesting to see that after sensing-through-the wall, the back scattered signal still roughly follows Gaussian distribution. This conclusion applies to all other 36 measurements. Assume the mean and variance are  $\mu$  and  $\sigma^2$  respectively, Table 1 shows the detail of these parameters.



(a)



(b)

Fig. 3. UWB noise waveforms: (a) transmitted pulse (b) received echoes

Since the transmitted and received signals have been known, the CLEAN algorithm can be used to extract channel impulse response (CIR). This method was initially introduced in [11] to enhance radio astronomical maps of the sky, and has been frequently employed in UWB channel characterization problems [12]-[14]. The CLEAN algorithm is an iterative, high-resolution, subtractive deconvolution procedure that is capable resolving dense multipath components which are usually irresolvable by conventional inverse filtering [16].

Our steps involved [15] are:

- 1) Calculate the autocorrelation of the transmitted signal  $R_{ss}(t)$  and the cross-correlation of the transmitted with the received waveform  $R_{sy}(t)$ .
- 2) Find the largest correlation peak in  $R_{sy}(t)$ , record the normalized amplitudes  $\alpha_k$  and the relative time delay  $\tau_k$  of the correlation peak.
- 3) Subtract  $R_{ss}(t)$  scaled by  $\alpha_k$  from  $R_{sy}(t)$  at the time delay  $\tau_k$ .
- 4) If a stopping criterion (a minimum threshold) on the

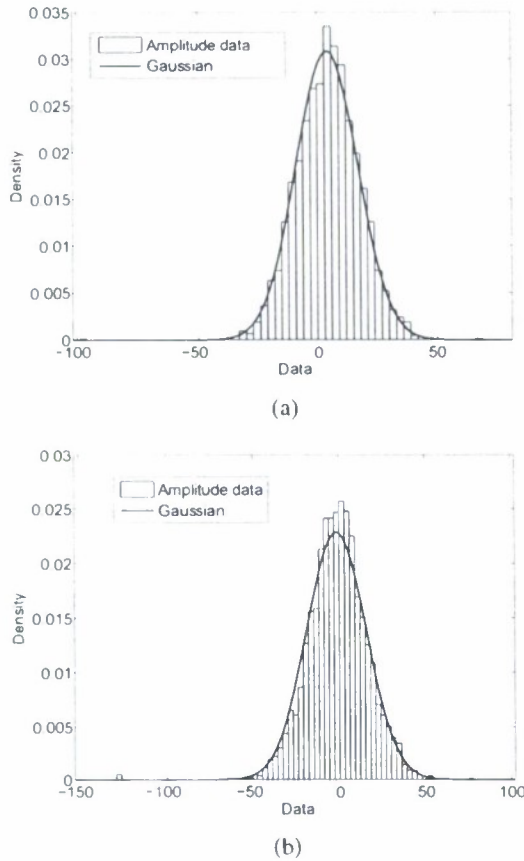


Fig. 4. Amplitude density: (a) transmitted pulse (b) received echoes

TABLE I  
ESTIMATED STATISTICAL PARAMETERS OF TRANSMITTED AND RECEIVED SIGNALS

parameter	transmitted signal	received signal
$\mu$	4.0512	-1.6756
STD Error of $\mu$	0.258655	0.348318
$\sigma$	12.9328	17.4159
STD Error of $\sigma$	0.182952	0.246372

peak correlation is not met, go step 2. otherwise stop.

Fig. 4 illustrated the absolute value of through-wall CIR at one position by clean algorithm. We can see that the channel consists of multipaths that arrive in clusters. Each cluster is made up of subsequent rays. This is very similar to the multipath rays in S-V channel model. However, in S-V model, the largest scattering, i.e., the highest magnitude always appears at the first path. It is obvious to see this is not the general case in the through-wall channel. On a basis of CIR, the channel can be represented as

$$r(t) \approx \sum_n a_n p_n(t - \tau_n) \quad (1)$$

where  $a_n$  and  $\tau_n$  is referred to as the amplitude and delay of the  $n^{\text{th}}$  propagation path. In the next Section we shall analyze

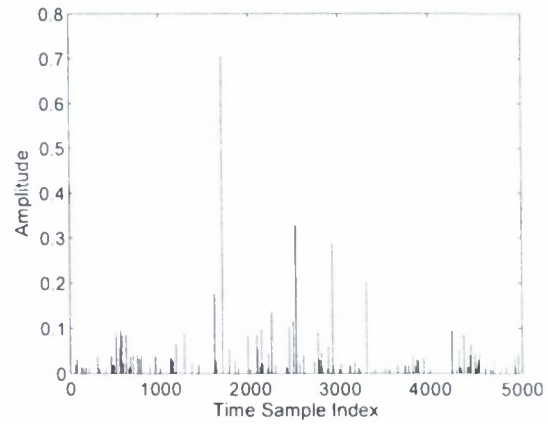


Fig. 5. Normalized CIR by CLEAN algorithm

them in detail.

#### IV. SENSE-THROUGH-WALL CHANNEL MODELING

##### A. Temporal Characterization

Like in S-V model, multipath contributions arrive at the receiver grouped into clusters and therefore similar methodology used in S-V model studies may be also applied to sensing-through-wall CIR. The time of arrival of clusters can be modeled as a Poisson arrival process with a rate  $\Lambda$ , while within each cluster, subsequent multipath contributions or rays also arrive according to a Poisson process with a rate  $\lambda$ .

We define:

- $T_l$ : the arrival time of the first path of the  $l$ -th cluster;
- $\tau_{k,l}$ : the delay of the  $k$ -th path within the  $l$ -th cluster relative to the first path arrival time  $T_l$ ;
- $\Lambda$ : the cluster arrival rate;
- $\lambda$ : the ray arrival rate, i.e., the arrival rate of the paths within each cluster;
- $\bar{\tau}$ : the mean excess delay;
- $\sigma_\tau$ : the rms delay spread

By definition, we have  $\tau_{0l} = T_l$ . The distributions of the cluster arrival time and the ray arrival time are given by

$$p(T_l|T_{l-1}) = \Lambda \exp(-\Lambda(T_l - T_{l-1})), l > 0$$

$$p(\tau_{k,l}|\tau_{(k-1),l}) = \lambda \exp(-\lambda(\tau_{k,l} - \tau_{(k-1),l})), k > 0 \quad (2)$$

$\bar{\tau}$ ,  $\sigma_\tau$  are defined by

$$\bar{\tau} \equiv \frac{\sum_n a_n^2 \tau_n}{\sum_n a_n^2} \quad (3)$$

$$\sigma_\tau \equiv \sqrt{\bar{\tau}^2 - \bar{\tau}^2} \quad (4)$$

where

$$\bar{\tau}^2 \equiv \frac{\sum_n a_n^2 \tau_n^2}{\sum_n a_n^2} \quad (5)$$

We analyze these parameters based on 37 experiments and show the result in Table II.

TABLE II  
TEMPORAL PARAMETERS FOR SENSE-THROUGH-WALL CHANNEL  
MODEL

parameter	$\Lambda(1/ns)$	$\lambda(1/ns)$	$\tau(\mu s)$	$\sigma_\tau$
value	0.002	0.0224	1.8153	0.0827

We may compare the  $\Lambda$  and  $\lambda$  in Table II with the same parameters for indoor UWB, which are 0.0667 and 2.1 respectively with unit  $1/ns$  [17]. The parameters for through-wall channel is much smaller due to the resistance of wireless propagation in wall.

#### B. Statistical Distribution of Channel Amplitude

In the S-V model, the amplitude follows rayleigh distribution. In the IEEE UWB indoor channel model [4], log-normal distribution was introduced for representing the fluctuations of the total multipath gain. In this Section we propose that the amplitude of sensing-through-wall channel follows T location-scale distribution. Its probability density function (PDF) is

$$f(x) = \frac{\Gamma(\frac{\nu+1}{2})}{\phi\sqrt{\nu\pi} \cdot \Gamma(\frac{\nu}{2})} \left[ \frac{\nu + (\frac{x-\delta}{\phi})^2}{\nu} \right]^{-\frac{(\nu+1)}{2}}, \phi > 0, \nu > 0 \quad (6)$$

where  $\delta$  is the location parameter,  $\phi$  is scale parameter,  $\nu$  is shape parameter and  $\Gamma(\cdot)$  denotes gamma function. Note that if define  $y \equiv \frac{x-\delta}{\phi}$ , then  $y$  follows student's T distribution with  $\nu$  degrees of freedom. As  $\nu$  goes to infinity, the T location-scale distribution approaches the standard Gaussian distribution.

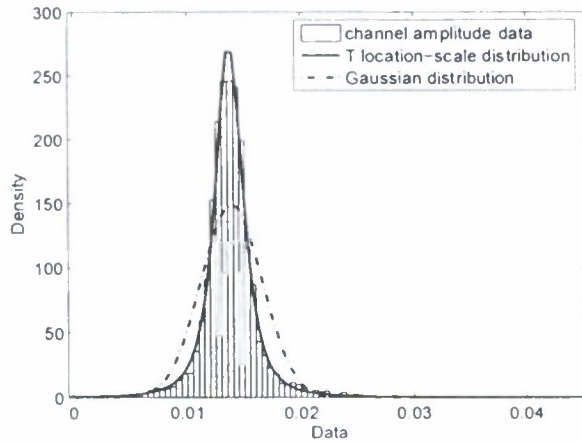


Fig. 6. Goodness-of-fit

Fig. 6 clearly illustrates to what extent does the CIR amplitude match the PDF curve of the statistic model. The absolute amplitudes of CIR have been plotted in terms of histogram. We compare T location-scale distribution with Gaussian distribution. Although the transmitted and received signal amplitude follows Gaussian model, this is not the case for the channel. It can be easily seen that T location-scale model provides perfect goodness-of-fit.

On a basis of CIR amplitudes from 37 different positions, we apply Maximum Likelihood Estimation (MLE) approach to estimate the parameters [18] [19]. It is generalized as follows:

Let  $y_1, y_2, \dots, y_N$  be  $N$  independent samples drawn from a random variable  $\mathbf{Y}$  with  $m$  parameters  $\theta_1, \theta_2, \dots, \theta_m$ , where  $\theta_i \in \theta$ , then the joint PDF of  $y_1, y_2, \dots, y_N$  is

$$L_N(\mathbf{Y}|\theta) = f_{Y|\theta}(y_1|\theta_1, \dots, \theta_m) \dots f_{Y|\theta}(y_N|\theta_1, \dots, \theta_m) \quad (7)$$

When expressed as the conditional function of  $\mathbf{Y}$  depends on the parameter  $\theta$ , the likelihood function is

$$L_N(\mathbf{Y}|\theta) = \prod_{k=1}^N f_{Y|\theta}(y_k|\theta_1, \theta_2, \dots, \theta_m) \quad (8)$$

The maximum likelihood estimate of  $\theta_1, \theta_2, \dots, \theta_m$  is the set of values  $\hat{\theta}_1, \hat{\theta}_2, \dots, \hat{\theta}_m$  that maximize the likelihood function  $L_N(\mathbf{Y}|\theta)$ .

As the logarithmic function is monotonically increasing, maximizing  $L_N(\mathbf{Y}|\theta)$  is equivalent to maximizing  $\ln(L_N(\mathbf{Y}|\theta))$ . Hence, it can be shown that a necessary but not sufficient condition to obtain the ML estimate  $\hat{\theta}$  is to solve the likelihood equation

$$\frac{\partial}{\partial \theta} \ln(L_N(\mathbf{Y}|\theta)) = 0 \quad (9)$$

We obtain  $\hat{\delta}$ ,  $\hat{\phi}$  and  $\hat{\nu}$  for t location-scale distribution,  $\hat{\mu}$  and  $\hat{\sigma}$  for Gaussian distribution. These are shown in table III. We also explore the standard deviation (STD) error of each parameter. These descriptions are also shown in table III in the form of  $\epsilon_x$ , where  $x$  denotes different parameter for each model. It can be seen that T location-scale provides smaller STD errors than those of Gaussian distribution.

TABLE III  
STATISTICAL AMPLITUDE PARAMETERS FOR SENSE-THROUGH-WALL  
CHANNEL MODEL

PDF	T location-scale	Gaussian
Parameters	$\hat{\delta} = 0.0136836$	$\hat{\mu} = -0.0138875$
	$\hat{\phi} = 0.00129967$	$\hat{\sigma} = 0.00267908$
	$\hat{\nu} = 2.18286$	
	$\epsilon_\delta = 2.35418e-005$	$\epsilon_\mu = 3.78917e-005$
	$\epsilon_\phi = 2.50893e-005$	$\epsilon_\sigma = 2.67975e-005$
	$\epsilon_\nu = 0.0821753$	
RMSE	9.8983	25.5854

We may also observe the goodness-of-fit by root mean square error (RMSE). Let  $i (i=1, 2, \dots, n)$  be the sample index of CIR amplitude in Fig. 6,  $c_i$  is the corresponding density value.  $\hat{c}_i$  is the density value of the statistical model with estimated parameters by means of MLE. RMSE is obtained through

$$RMSE = \sqrt{\frac{1}{n} \sum_{i=1}^n (c_i - \hat{c}_i)^2} \quad (10)$$

where  $n$  is the total amount of sample index. The RMSE for T location-scale and Gaussian distributions have been listed

in Table III also. It demonstrates that T location-scale is the model that fits the channel amplitude data very well.

## V. CONCLUSION

From our investigation, we would draw following conclusions: 1)UWB noise waveform may have a very good sensing-through-wall capability for walls composed of solid concrete blocks. 2)Sense-through-wall channels are made up of multipath components and the highest magnitude does not always appear at the first path. 3)The multipath contributions arrive at the receiver are grouped into clusters. The time of arrival of clusters can be modeled as a Poisson arrival process, while within each cluster, subsequent multipath contributions or rays also arrive according to a Poisson process. However, these arrival rates are much smaller than those of indoor UWB channels. 4) The amplitude of channel coefficient at each path can be more accurately characterized as T location-scale distribution other than Gaussian distribution due to better goodness-of-fit and smaller root-mean-square-error (RMSE).

## ACKNOWLEDGEMENT

This work was supported in part by Office of Naval Research (ONR) under Grant N00014-07-1-0395 and N00014-07-1-1024, and National Science Foundation (NSF) under Grant CNS-0721515 and CNS-0831902.

## REFERENCES

- [1] D. Cassioli, M. Z. Win, and A. F. Molisch, "The ultra-wide bandwidth indoor channel: From statistical study to simulations", *IEEE J. Select. Areas Commun.*, vol. 20, pp. 1247C1257, Aug. 2002.
- [2] S. S. Ghassemzadeh, R. Jana, C. W. Rice, W. Turin, and V. Tarokh, "Measurement and modeling of an ultra-wide bandwidth indoor channel", *IEEE Trans. Commun.*, vol. 52, pp. 1786C1796, Oct. 2004.
- [3] B. M. Donlan, D. R. McKinstry and R. M. Buehrer, "The UWB Indoor Channel: Large and Small Scale Modeling", *IEEE Trans. on Wireless Commun.*, vol. 5, pp. 2863C2873, Oct. 2006.
- [4] IEEE 802.15.SG3a, "Channel modeling sub-committee report final", *IEEE P802.15-02/490r1-SG3a*, Feb. 2003.
- [5] A. A. Saleh and R. A. Valenzuela, "A statistical model for indoor multipath propagation", *IEEE Journal on Selected Areas in Communications*, vol. 5, no.2, pp. 128C137, Feb. 1987.
- [6] Z. Yun and M. F. Iskander, "UWB Pulse Propagation through Complex Walls in Indoor Wireless Communications Environments", *International Conference on Wireless Networks, Communications and Mobile Computing, 2005*, vol.2, pp. 1358C1361, June 2005.
- [7] N. Noori, A. Abolghasemi and M. Fardis, "Modeling of ultra wideband transmission through building walls", *International Conference on Microwaves and Millimeter Wave Technology, 2008, ICMMT 2008*, vol.2, pp. 982C985.
- [8] F. Ahmad and M.G.Amin, "Multi-location wideband synthetic aperture imaging for urban sensing applications", *Journal of the Franklin Institute*, 345 (6), pp.618C639, Sep 2008.
- [9] R. M. Narayanan, "Through-wall radar imaging using UWB noise waveforms", *Journal of the Franklin Institute*, 345 (6), pp.659C678, Sep 2008.
- [10] J. A. Henning, "Design and Performance of An Ultra-Wideband Foliage Penetrating Noise Radar", Masters Thesis, University of Nebraska, May 2001.
- [11] J. A. Högbom, "Aperture Synthesis with a non-regular distribution of interferometer baselines", *Astronomy and Astrophysics Supplement Ser.*, vol. 15, pp. 417-426, 1974.
- [12] R. J. -M. Cramer, R. A. Scholtz and M. Z. Win, "Evaluation of an ultra-wide-band propagation channel", *IEEE Transactions on Antennas and Propagation*, vol. 50, pp. 561 - 570, May 2002.
- [13] P. C. Richardson, W. Xiang and W. Stark, "Modeling of ultra-wideband channels within vehicles", *IEEE Journal on selected areas in communications*, vol. 24, pp. 906-912, Apr. 2006.
- [14] W. Yang and Z. Naitong, "A new multi-template CLEAN algorithm for UWB channel impulse response characterization", in *Proc. Int. Conf. Commun. Technol.*, Nov. 2006, pp. 1-4.
- [15] J. H. Reed, *An introduction to Ultra Wideband Communication Systems*, Prentice Hall, 2005.
- [16] A. F. Molisch, "Ultrawideband propagation channels: Theory, measurement and modeling", *IEEE Transactions on Vehicular Technology*, vol. 54, Sept. 2005, pp. 1528-1545.
- [17] M. -G. Di Benedetto and G. Giancola, *Understanding ultra wideband Radio Fundamentals*, Prentice Hall, 2004.
- [18] Devore, *Probability and Statistics for Engineering and the Sciences*, Monterey, CA: Brooks/Cole, 1982.
- [19] M. Barkat, *Signal detection and estimation*, 2nd, London: Artech house, 2005.

# WAVEFORM DESIGN FOR UNDERWATER SONAR SENSOR NETWORK

Lei Xu and Qilian Liang  
Department of Electrical Engineering  
University of Texas at Arlington  
Arlington, TX 76019-0016  
Email: xu@wcn.uta.edu, liang@uta.edu

## ABSTRACT

*In this paper, we study the underwater sonar sensor network which is more complicated because of the time-variant and energy costing underwater environment. Since it is known that interference with each sonar could be effectively reduced when waveforms are appropriately designed, we provide a new set of triphase coded waveforms called optimized punctured Zero Correlation Zone sequence-pair set (optimized punctured ZCZPS) and provide a method to construct such a kind of code. We also study codes' properties especially using the useful ambiguity function to analyze the nature of the output of the matched filter when there are both time delay and Doppler shift. Then we apply our provided triphase waveforms to the underwater sensor network, provide a system structure and simulate the target detection performance of the system. Comparing with the classical periodic Gold sequences, our codes could improve the system detection performance to a certain extent.*

**Keywords:** Zero correlation zone; Optimized punctured ZCZ sequence-pair set; Sonar sensor network.

## I. INTRODUCTION

Much time and effort have been put in radar waveform design for radar sensor networks [1] [2] [3], since multiple radar sensors could be combined to form a multiradar system to overcome performance degradation of single radar. Though underwater sonar system is more complicated than the radar system because of many unique channel characteristics such as fading, extended multipath and refractive properties of the sound, multiple sonar sensors could construct a underwater sonar sensor network so that the detection performance could be improved.

The long-range bistatic sound transmission through the ocean sound channel, such as in ocean acoustic tomography [4] [5], in acoustic thermometry of ocean climate (ATOC) [6], used the signal that allows sufficient sound energy delivery into the ocean so that the signal received at long range, perhaps several megameters, has a sufficiently high signal-to-noise energy ratio but low signal-to-noise power ratio. Consequently, precision measurements of sound travel time could be made and good time resolution should be allowed after signal processing.  $m$  sequences, successfully

used in previous experiments [4] [7] [8], satisfy the long-range transmission requirement and the same time resolution as a monopulse or periodic pulse system whose pulse width is one digit duration achievable at high power. In other words, high signal energy is provided by transmitting over a long time (large  $T$ ) and good time resolution is achieved by using a sequence of short pulse (large  $W$ ), therefore having a large  $TW$  product [9]. This is called the phase coded waveform technique which is a widely used in radar system.

Therefore, family of  $m$  sequences could be applied to the underwater sonar sensor network to achieve better targets detection performance. Nevertheless, the autocorrelation and cross correlation properties of family of  $m$  sequences or even Gold sequences are not optimized. Based on the ZCZ [10] concept, we propose triphase coded waveforms called ZCZ sequence-pair set (ZCZPS), which can reach zero autocorrelation sidelobe during ZCZ, as well as zero mutual cross correlation peak and sidelobe during ZCZ. We propose and demonstrate a method that optimized punctured sequence-pair joins together with orthogonal matrix to construct the triphase coded waveforms called optimized punctured ZCZ sequence-pairs set (optimized punctured ZCZPS), and subsequently apply them to an underwater sonar sensor network. In addition, a frame structure of the underwater sonar sensor network is provided and used in the simulation. According to the simulation results, the target detection performance is well improved by using our proposed codes in the provided system structure comparing with the system using Gold codes.

The rest of the paper is organized as follows. In Section 2, the definition of ZCZPS and optimized punctured ZCZPS is proposed. A method using optimized punctured sequence-pair and orthogonal matrix to construct ZCZPS is given and proved. In Section 3, we analyze the properties and ambiguity function of optimized punctured ZCZPS. We investigate the performance of optimized punctured ZCZPS in targets detection simulation of underwater sonar sensor network comparing with Gold code in Section 4. In Section 5, we draw some final conclusions on optimized punctured ZCZPS.

## II. DESIGN FOR OPTIMIZED PUNCTURED ZCZ SEQUENCE-PAIR SET

Since it has been well studied that it is almost impossible to find or construct sequences which have ideal autocorrelation

sidelobes and cross correlation peaks at the same time, zero correlation zone (ZCZ) is a new concept provided by Fan [11] in which both autocorrelation and cross correlation sidelobes are zero while the time delay is kept within the ZCZ instead of the whole period of time domain.

Matsufuji and Torii have provided some methods of constructing ZCZ sequences in [12] [13]. In this section, we apply optimized punctured sequence-pair [14] in ZCZ together with the orthogonal matrix to construct optimized punctured ZCZ sequence-pair set.

#### A. The Definition of Optimized Punctured ZCZ Sequence-Pair Set

**Definition 3-1** Assume  $(x^{(p)}, y^{(p)})$  to be a sequence-pair of set  $(X, Y)$  of length  $N$  and the number of sequence-pairs  $K$ , where  $p = 0, 1, \dots, K-1$ ,  $i = 0, 1, \dots, N-1$ , if sequences in the set satisfy the following equation:

$$R_{x^{(p)}y^{(q)}}(\tau) = \sum_{i=0}^{N-1} x_i^{(p)} y_{(i+\tau) \bmod N}^{(q)*} = \sum_{i=0}^{N-1} y_i^{(p)} x_{(i+\tau) \bmod N}^{(q)*} = \begin{cases} \lambda N, & \text{for } \tau = 0, p = q \\ 0, & \text{for } 0 < |\tau| \leq Z_0 \end{cases} \quad (1)$$

where  $0 < \lambda \leq 1$ ,  $(x^{(p)}, y^{(p)})$  is called a ZCZ sequence-pair,  $ZCZP(N, K, Z_0)$  is an abbreviation.  $(X, Y)$  is called a ZCZ sequence-pair set,  $ZCZPS(N, K, Z_0)$  is an abbreviation.

**Definition 3-2** [14] Sequence  $u = (u_0, u_1, \dots, u_{N-1})$  is the punctured sequence for  $v = (v_0, v_1, \dots, v_{N-1})$ ,

$$u_j = \begin{cases} 0, & \text{if } j \in P \text{ punctured bits} \\ v_j, & \text{if } j \in \text{Non-punctured bits} \end{cases} \quad (2)$$

Here,  $P$  is the number of punctured bits in sequence  $v$ . Suppose  $v_j \in (-1, 1)$ ,  $u$  is  $P$ -punctured binary sequence that  $u_j \in (-1, 0, 1)$ ,  $(u, v)$  is called a punctured binary sequence-pair.

**Theorem 3-1** [14] The autocorrelation of punctured sequence-pair  $(u, v)$  is defined

$$R_{uv}(\tau) = \sum_{i=0}^{N-1} u_i v_{(i+\tau) \bmod N}, 0 \leq \tau \leq N-1 \quad (3)$$

If the punctured sequence-pair has the following autocorrelation property:

$$R_{uv}(\tau) = \begin{cases} E, & \text{if } \tau \equiv 0 \bmod N \\ 0, & \text{others} \end{cases} \quad (4)$$

the punctured sequence-pair is called optimized punctured sequence-pair [14]. Where,  $E = \sum_{i=0}^{N-1} u_i v_{(i+\tau) \bmod N} = N - p$ , is the energy of punctured sequence-pair.

The properties, existing necessary conditions and some construction methods of punctured binary sequence-pair have been well studied by Jiang [14]. Many optimized punctured sequence-pairs have been found of length from 7 to 31 so far.

**Definition 3-3** If  $(x^{(p)}, y^{(p)})$  in Definition 3-1 is constructed by optimized punctured sequence-pair and a certain matrix, such as Hadamard matrix or an orthogonal matrix, where

$$x_i^{(p)} \in (-1, 1), \quad i = 0, 1, 2, \dots, N-1 \\ y_i^{(q)} \in (-1, 0, 1), \quad i = 0, 1, 2, \dots, N-1$$

$$R_{x^{(p)}y^{(q)}}(\tau) = \sum_{i=0}^{N-1} x_i^{(p)} y_{(i+\tau) \bmod N}^{(q)*} = \sum_{i=0}^{N-1} y_i^{(p)} x_{(i+\tau) \bmod N}^{(q)*} = \begin{cases} \lambda N, & \text{for } \tau = 0, p = q \\ 0, & \text{for } 0 < |\tau| \leq Z_0 \end{cases} \quad (5)$$

where  $0 < \lambda \leq 1$ , then  $(x^{(p)}, y^{(p)})$  can be called an optimized punctured ZCZP.

#### B. A Method to Construct Optimized Punctured ZCZ Sequence-pair Set

An optimized punctured ZCZ sequence-pair set can be constructed from the following steps:

**Step 1:** Given an optimized punctured binary sequence-pair  $(u, v)$ , the length of each sequence is  $N_1$

$$u = u_0, u_1, \dots, u_{N_1-1}, u_i \in (-1, 1), \\ v = v_0, v_1, \dots, v_{N_1-1}, v_i \in (-1, 0, 1),$$

**Step 2:** Given orthogonal matrix  $B$ , the length of the sequence is  $N_2$  which is equal to the number of the sequences.

$$B = (b^0; b^1; \dots, b^{N_2-1}), b^i = \frac{1}{\sqrt{N_2}} (b_0^i, b_1^i, \dots, b_{N_2-1}^i)$$

**Step 3:** Process the optimized punctured binary sequence-pair with each row of the orthogonal matrix  $B$ ,

$$x_j^i = u(((N_1/d) * j + \lfloor j/d \rfloor) \bmod N_1) b_{j \bmod N_2}^i, \\ X = (x^0; x^1; \dots; x^{N_2-1}), x^i = (x_0^i, x_1^i, \dots, x_{N_2-1}^i), \\ 0 \leq i \leq N_2-1, 0 \leq j \leq N-1, \\ y_j^i = v(((N_1/d) * j + \lfloor j/d \rfloor) \bmod N_1) b_{j \bmod N_2}^i, \\ 0 \leq i \leq N_2-1, 0 \leq j \leq N-1, \\ Y = (y^0; y^1; \dots; y^{N_2-1}), y^i = (y_0^i, y_1^i, \dots, y_{N_2-1}^i)$$

Where  $d = \text{GCD}(N_1, N_2)$ ,  $N = N_1 * N_2$  and  $\lfloor j/d \rfloor$  means to get the integer of  $\lfloor j/d \rfloor$ . The three steps make the sequence-pair set  $(X, Y)$  an optimized punctured ZCZPS, where ZCZ  $Z_0 = N_1 - 1$  or  $Z_0 = N_1 - 2$  which depend on the value of  $d$ . The length of each sequence in optimized punctured ZCZPS is  $N = N_1 * N_2$  that depends on the product of length of optimized punctured sequence-pair and the length of a row in Orthogonal matrix. The number of sequence-pairs in optimized punctured ZCZPS rests on the order of the Orthogonal matrix. The sequence  $x^{(i)}$  in  $X$  and the corresponding sequence  $y^{(i)}$  in  $Y$  construct an optimized punctured ZCZP  $(x^{(i)}, y^{(i)})$  that can be used as a phase coded waveform, such as  $x^{(i)}$  for radar transmitter and  $y^{(i)}$  for radar receiver. The phase states for any sequence-pair among  $(x^{(i)}, y^{(i)})$  are only of three options, so

our newly provided optimized punctured ZCZPS is a new set of triphase codes.

Then we will prove that the sequence-pair set constructed by the above steps are optimized punctured ZCZPS. Proof:

$$\begin{aligned}
R_{x^{(i)}y^{(j)}}(\tau) &= \sum_{k=0}^{N_1N_2-1} u_k^{(i)} v_{(k+\tau) \bmod N_1N_2}^{(j)} \\
&= \sum_{k=0}^{N_1N_2-1} u((N_1/d)k + \lfloor k/d \rfloor) \bmod N_1 b_{i,k \bmod N_2} \cdot \\
&\quad v^*((N_1/d)(k+\tau) + \lfloor (k+\tau)/d \rfloor) \bmod N_1 b_{j,(k+\tau) \bmod N_2}^* \\
&= \sum_{m=0}^{N_1-1} \sum_{r=0}^{N_2-1} b_{i,(mN_2+r) \bmod N_2} b_{j,(mN_2+r+\tau_0d+\tau_1) \bmod N_2}^* \\
&\quad u((N_1/d)(mN_2+r) + \lfloor (mN_2+r)/d \rfloor) \bmod N_1 \\
&\quad v^*((N_1/d)(mN_2+r+\tau_0d+\tau_1) \\
&\quad + \lfloor (mN_2+r+\tau_0d+\tau_1)/d \rfloor) \bmod N_1 \\
&= \sum_{r=0}^{N_2-1} b_{i,r} b_{j,(r+\tau_0d+\tau_1) \bmod N_2}^* \sum_{m=0}^{N_1-1} \\
&\quad u((N_1/d)r + mN_2/d + \lfloor r/d \rfloor) \bmod N_1 \\
&\quad v^*((N_1/d)(r+\tau_1) + mN_2/d + \tau_0 + \lfloor (r+\tau_1)/d \rfloor) \bmod N_1
\end{aligned}$$

Here,  $k = mN_2 + r$ ,  $\tau = \tau_0d + \tau_1$ ,  $0 \leq m \leq N_1 - 1$ ,  $0 \leq r \leq N_2 - 1$ ,  $0 \leq \tau_1 \leq d - 1$ . If  $T_{m,r} = ((N_1/d)r + mN_2/d + \lfloor r/d \rfloor) \bmod N_1$ ,  $T_{m,r+\tau} - T_{m,r}$  is unrelated to  $m$ . Then we can have that

$$\begin{aligned}
t_{r,\tau} &= T_{m,r+\tau} - T_{m,r} \\
&= ((N_1/d) \cdot \tau_1 + \tau_0 + \lfloor (r+\tau_1)/d \rfloor) - \lfloor r/d \rfloor \bmod N_1
\end{aligned} \quad (7)$$

So  $R_{x^{(i)}y^{(j)}}$  could be abbreviated to

$$R_{x^{(i)}y^{(j)}} = \sum_{r=0}^{N_2-1} b_{i,r} b_{j,(r+\tau_0d+\tau_1) \bmod N_2}^* R_{uv}(t_{r,\tau}) \quad (8)$$

(1) If  $d = 1$ ,  $\tau = \tau_0d + \tau_1$ ,  $0 \leq \tau_1 \leq d - 1$ ,  $\tau_1 = 0$ ,  $t_{r,\tau} = \tau$ . According to (8), we have  $R_{x^{(i)}y^{(j)}}(\tau) = \sum_{r=0}^{N_2-1} b_{i,r} b_{j,(r+\tau_0d+\tau_1) \bmod N_2}^* R_{uv}(\tau)$ . Also  $(u, v)$  is the optimized punctured binary sequence-pair.

When  $i = j$ ,

$$\begin{aligned}
\tau &= 0, \\
R_{x^{(i)}y^{(j)}}(0) &= R_{xy}(0) = \sum_{r=0}^{N_2-1} b_{i,r} b_{i,r \bmod N_2}^* R_{uv}(0) = N_2 E; \\
0 < |\tau| &\leq N_1 - 1, R_{uv}(\tau) = 0, \\
R_{x^{(i)}y^{(j)}}(\tau) &= \sum_{r=0}^{N_2-1} b_{i,r} b_{i,r \bmod N_2}^* R_{uv}(\tau) = 0;
\end{aligned}$$

When  $i \neq j$ ,

$$\tau = 0,$$

$$R_{x^{(i)}y^{(j)}}(0) = R_{xy}(0) \sum_{r=0}^{N_2-1} b_{i,r} b_{i,r \bmod N_2}^*,$$

$$(6) \quad \text{since } \sum_{r=0}^{N_2-1} b_{i,r} b_{i,r \bmod N_2}^* = 0, R_{x^{(i)}y^{(j)}}(0) = 0;$$

$$0 < |\tau| \leq N_1 - 1, R_{uv}(\tau) = 0,$$

$$R_{x^{(i)}y^{(j)}}(\tau) = \sum_{r=0}^{N_2-1} b_{i,r} b_{i,(r+\tau) \bmod N_2}^* R_{xy}(\tau) = 0;$$

Similarly,  $R_{x^{(j)}y^{(i)}}$  could be proved.

(2) If  $d > 1$ ,

When  $\tau_0 \leq N_1/d - 2$  and  $0 \leq \tau_1 \leq d - 1$ ,

$$\begin{aligned}
t_{r,\tau} &= ((N_1/d) \cdot \tau_1 + \tau_0 + \lfloor (r+\tau_1)/d \rfloor) \bmod N_1 \\
&\leq ((N_1/d)(d-1) + N_1/d - 2 + 1) \bmod N_1 \\
&= N_1 - 1
\end{aligned}$$

When  $\tau_0 \leq N_1/d - 1$ ,  $\tau_1 \leq d - 2$ ,

$$\begin{aligned}
t_{r,\tau} &= (N_1/d)\tau_1 + \tau_0 + \lfloor (r+\tau_1)/d \rfloor + \lfloor r/d \rfloor \bmod N_1 \\
&\leq ((N_1/d)(d-2) + N_1/d - 1 + 1) \bmod N_1 \\
&= N_1 - N_1/d \leq N_1 - 1
\end{aligned}$$

As a result, when  $0 < \tau \leq N_1 - 2$ , then  $1 \leq t_{r,\tau} \leq N_1 - 1$ .  $(u, v)$  is the optimized punctured binary sequence-pair, so we could get  $R_{uv}(\tau) = 0$  and  $R_{x^{(i)}y^{(j)}}(\tau) = 0$ . Similarly, when  $i \neq j$ ,  $R_{x^{(i)}y^{(j)}}(0) = R_{uv}(0) \sum_{r=0}^{N_2-1} b_{i,r} b_{j,r \bmod N_2}^*$ . Since  $\sum_{r=0}^{N_2-1} b_{i,r} b_{j,r \bmod N_2}^* = 0$ ,  $R_{x^{(i)}y^{(j)}}(-\tau) = R_{x^{(j)}y^{(i)}}(\tau)$ . It is also easy to prove that when  $-(N_1 - 2) \leq \tau < 0$ ,  $R_{x^{(i)}y^{(j)}}(\tau) = 0$ . Similarly,  $R_{x^{(j)}y^{(i)}} = 0$ .

**Theorem 3-2** The optimized punctured binary sequence-pair  $(u, v)$  and the  $N_2$  order orthogonal matrix  $B$  constructed an optimized punctured ZCZPS  $(X, Y)$ ,  $d = \text{GCD}(N_1, N_2)$ , in some other words,  $N_1/d$  is relatively prime to  $N_2$ , then (1)  $d = 1$ , the ZCZPS could be expressed as  $\text{ZCZPS}(N_1N_2, N_2, N_1 - 1)$ , and

$$R_{x^{(i)}y^{(j)}}(\tau) = \begin{cases} EN_2, & \text{if } \tau = 0, i = j \\ 0, & \text{if } 0 < |\tau| \leq N_1 - 1, i = j \\ 0, & \text{if } 0 < |\tau| \leq N_1 - 1, i \neq j \end{cases}$$

(2)  $d > 1$ , the ZCZPS could be expressed as  $\text{ZCZPS}(N_1N_2, N_2, N_1 - 2)$ , and

$$R_{x^{(i)}y^{(j)}}(\tau) = \begin{cases} \epsilon N_1N_2, & \text{if } \tau = 0, i = j \\ 0, & \text{if } 0 < |\tau| \leq N_1 - 2, i = j \\ 0, & \text{if } 0 < |\tau| \leq N_1 - 2, i \neq j \end{cases}$$

where  $0 < \epsilon < 1$ . If the punctured sequence-pair has the following autocorrelation property:

$$R_{uv}(\tau) = \begin{cases} E, & \text{if } \tau \equiv 0 \bmod N \\ 0, & \text{others} \end{cases} \quad (9)$$

the punctured sequence-pair is called optimized punctured sequence-pair [14]. Where,  $E = \sum_{i=0}^{N-1} u_i v_{(i+\tau) \bmod N} = N - p$ , is the energy of punctured sequence-pair.

### III. PROPERTIES OF OPTIMIZED PUNCTURED ZCZ SEQUENCE-PAIR SET

An example is given to analyze the autocorrelation and cross correlation properties of the optimized punctured ZCZPS constructed by the method mentioned above. The 144-length optimized punctured ZCZPS  $(X, Y)$  is constructed by 12-length optimized punctured binary sequence-pair  $(u, v)$ ,  $u = [++++- - - - + - + -]$ ,  $v = [0 + + + - 0 0 + - + + 0]$  (using '+' and '-' symbols for '1' and '-1') and orthogonal matrix  $B$  of order 12. Each row of matrix  $X = [x^{(1)}; x^{(2)}; \dots; x^{(12)}]$  and  $Y = [y^{(1)}; y^{(2)}; \dots; y^{(12)}]$  constitute a certain optimized punctured ZCZP  $(x^{(i)}, y^{(i)})$ .

1) *Autocorrelation and Cross Correlation Properties:* The autocorrelation property  $R(x^{(1)}, y^{(1)})$  and cross correlation property  $R(x^{(1)}, y^{(2)}) = R(y^{(1)}, x^{(2)})$  of 144-length optimized punctured ZCZPS  $(X, Y)$ , are shown in Fig.1.

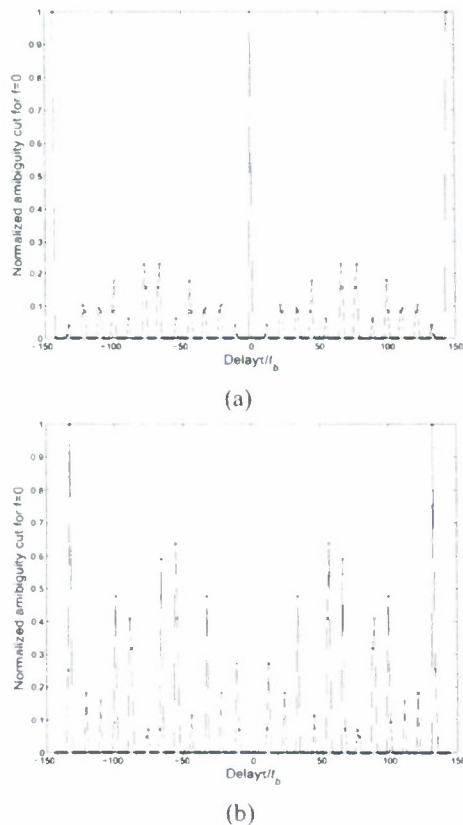


Fig. 1. (a) Periodic autocorrelation property of 144-length optimized punctured ZCZ sequence-pair  $(x^{(1)}, y^{(1)})$  (b) Periodic cross correlation property of 144-length optimized punctured ZCZ sequence-pair  $(x^{(1)}, y^{(2)})$

According to Fig. 1(a), the sidelobe of autocorrelation of ZCZPS can be as low as 0 when the time delay is kept within  $Z_0 = N_1 - 2 = 10$ , as well as the peak and sidelobe of the cross correlation value, since  $d > 1$ . The only uniform phase code that can reach the theoretical maximum peak signal sidelobe ratio (PSR) [15] is the Barker code whose length is equal or less than 13. The sidelobe of the new code shown in

Fig.1 can be as low as 0 during ZCZ, and the PSR can be as large as infinite. Besides, the length of the new code is various and much longer than the length of the Barker code.

2) *Ambiguity function:* Because of the Doppler shift  $f_d$  [15], the main peak of the autocorrelation function is reduced and so as to the SNR degradation. Focusing on the sequence-pair  $(x, y)$  here, the receiving sequence in ambiguity function is different from the echo signal and the periodic correlation is used instead of aperiodic correlation here. The ambiguity function can be rewritten as

$$A(\tau, F_D) = \left| \int_{-\frac{T}{2}}^{-\frac{T}{2}+\tau} x_i(t) \exp(j2\pi F_D t) y_i^*(t + T - \tau) dt + \int_{-\frac{T}{2}+\tau}^{\frac{T}{2}} x_i(t) \exp(j2\pi F_D t) y_i^*(t - \tau) dt \right| \quad (10)$$

In order to analyze the autocorrelation performance of an optimized punctured ZCZP with delay-Doppler shift, equation (10) is plotted in Fig.2 in a three-dimensional surface plot. In

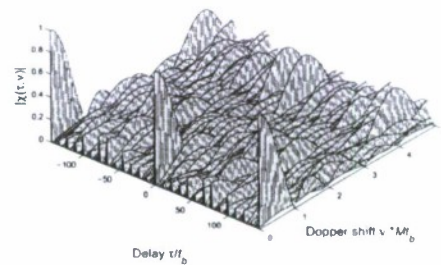


Fig. 2. Ambiguity function of a 144-length ZCZ sequence-pair  $(x^{(1)}, y^{(1)})$

Fig.2, there is relative uniform plateau suggesting low and uniform sidelobes. This low and uniform sidelobes minimize target masking effect in ZCZ of time domain, where  $Z_0 = 10$ ,  $-10 \leq \tau \leq 10$ ,  $\tau \neq 0$ . When Doppler shift is well controlled, there are peaks on period of 12 and sharp peaks on period of 144 in time domain which could be used to detect the targets.

### IV. ZCZ OPTIMIZED PUNCTURED SEQUENCE-PAIR WAVEFORM CODING IN SONAR SYSTEM

$M$  denotes the number of essentially different ZCZ optimized punctured sequence-pairs. The receiver is pictured as  $M$  cross correlators; and each calculates the cross correlation function of the received signal  $\tau(t)$  and the corresponding sequence  $(y^{(i)}(t), i = 1, 2, \dots, M)$ .

Suppose that the transmission was the summation of the  $M$  outputs of the transmitter  $s_i(\tau_i T_c)$ , which is a baseband sequence-controlled phase-modulated signal from the  $i$ th sequence with  $\tau_i T_c$  time delay. Let  $Z_i(u)$  be the output from the

$i$ th correlator, and  $Z$  is the final output after the equal gain combination is used. The sample output is

$$Z = \sum_{i=1}^M Z_i(u) \quad (11)$$

The transmission signal is

$$S = \sum_{i=1}^M s_i(t - \tau_i T_c) \quad (12)$$

In the underwater sonar sensor network of  $M$  radars, the combined received signal for the radar  $i$  is

$$r(u, t) = \sum_{j=1}^M x_j(t - t_j) \exp(j2\pi F_{D_j} t) + n(u, t) \quad (13)$$

$F_{D_j}$  and  $t_j$  are Doppler shift of target and time delay relative to waveform  $j$ , and  $n(u, t)$  is additive white Gaussian noise (AWGN). The structure can be constructed as Fig.3.

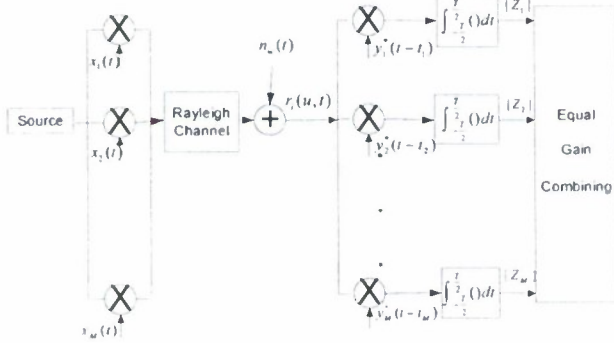


Fig. 3. Waveform diversity combining in RSN

According to this structure, the combined received signal  $r(u, t)$  is processed by the matched filter  $i$  and the output of branch  $i$  is  $Z_i(u)$ . Each  $Z_i(u)$  can be equal gain combined to construct the final output  $Z(u)$ .

The output  $|Z_i(u)|$  of branch  $i$  is

$$\left| \int_{-\frac{T}{2}}^{\frac{T}{2}} \left[ \sum_{j=1}^M x_j(t - t_j) \exp(j2\pi F_{D_j} t) + n(u, t) \right] y_i^*(t - t_i) dt \right| \quad (14)$$

Where  $n(u) = \int_{-\frac{T}{2}}^{\frac{T}{2}} n(u, t) y_i^*(t - t_i) dt$  can be easily proved to be still an AWGN.

We can also have two special cases for  $|Z_i(u)|$ :

1) If there is Doppler shift but no time delay, all the radar sensors transmit signals synchronously,  $|Z_i(u)|$  turns to be:

$$\left| \int_{-\frac{T}{2}}^{\frac{T}{2}} \left[ \sum_{j=1}^M x_j(t) \exp(j2\pi F_{D_j} t) + n(u, t) \right] y_i^*(t) dt \right| \quad (15)$$

Assuming that the Doppler shift can be well estimated in the receiving radar sensor, so the Doppler shift compensation

factor  $\exp^*(j2\pi F_{D_j})$  is introduced here.

$$\begin{aligned} |Z_i(u)| \leq & |E| + \left| \int_{-\frac{T}{2}}^{\frac{T}{2}} \left[ \sum_{j=1, j \neq i}^M x_j(t) \exp(j2\pi (F_{D_j} - F_{D_i}) t) y_i^*(t) \right] \right. \\ & \left. + \int_{-\frac{T}{2}}^{\frac{T}{2}} n(u, t) y_i^*(t) \exp^*(j2\pi F_{D_i} t) dt \right| \end{aligned} \quad (16)$$

If  $F_{D_1} = F_{D_2} = \dots = F_{D_j} = F_{D_i}$ , further simplified as

$$|Z_i(u)| \leq |E| + 0 + \left| \int_{-\frac{T}{2}}^{\frac{T}{2}} n(u, t) y_i^*(t) \exp^*(j2\pi F_{D_i} t) dt \right| \quad (17)$$

2) If both time delay and Doppler shift exist in the RSN, assuming  $F_{D_1} = F_{D_2} = \dots = F_{D_j} = F_{D_i}$ , considering the Doppler shift compensation factor in the receiving sensor,

$$\begin{aligned} |Z_i(u)| \leq & |E| + \left| \int_{-\frac{T}{2}}^{\frac{T}{2}} \left[ \sum_{j=1, j \neq i}^M x_j(t - t_j) y_i^*(t - t_i) \right] \right. \\ & \left. + \int_{-\frac{T}{2}}^{\frac{T}{2}} n(u, t) y_i^*(t - t_j) \exp^*(j2\pi F_{D_i} t) dt \right| \end{aligned} \quad (18)$$

Because of the good properties of our proposed codes, we modify the frame of receiving data before the matched filter on the receiver to improve the performance. The data from  $N + 1$  to  $\max(t_j) + N$  are added to data from 1 to  $\max(t_j)$ , bit by bit, where  $N$  is the original data length and  $t_j$  is the time delay for  $j$ th transmitting radar sensor. In this way can we get the output of the matched filter

$$|Z_i(u)| \leq |E| + 0 + \left| \int_{-\frac{T}{2}}^{\frac{T}{2}} n(u, t) y_i^*(t) \exp^*(j2\pi F_{D_i} t) dt \right| \quad (19)$$

According to (16) and (18), it is easy to see that using our provided codes and frame modification the underwater sonar sensor network under the condition of time delay for each radar sensor can, to some extent, theoretically work as well as the network where all the sonar sensors transmit signals synchronously.

According to [15],  $P_D$  (Probability of Detection),  $P_{FA}$  (Probability of False Alarm) and  $P_M$  (Probability of Miss) suffice to specify all of the probabilities of interest in a sonar system. Therefore, we apply optimized punctured ZCZPS to the underwater sonar sensor network, together with equal gain combination technique in the simulation. We respectively simulated  $P_M$  and  $P_{FA}$  of underwater sonar sensor network using our optimized punctured ZCZ sequence-pairs comparing with Gold codes of comparative length. Two special cases of performances have been simulated. They are performances under the condition of no time delay but Doppler shift, and under the condition of time delay (limited within the ZCZ) for each radar sensor and having Doppler shift.

Fig.4 illustrates that when  $P_M = 10^{-3}$ , SNR of 4-sensor underwater sonar sensor network using Gold codes are 1dB greater than that of 4-sensor system using our proposed codes with Doppler shift but no time delay. Considering time delay for each sensor in Fig.4, SNR of 4-sensor underwater sonar sensor network using our codes can gain 1.5dB smaller than

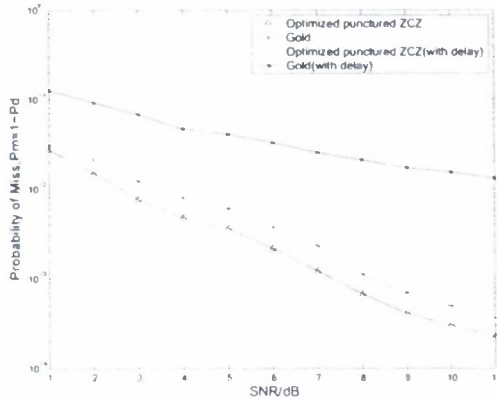


Fig. 4. Probability of miss detection in sonar sensor network under the condition of no time delay but Doppler shift or time delay and Doppler shift

4-sensor system within Gold codes to achieve the same  $P_M = 10^{-1.9}$ .

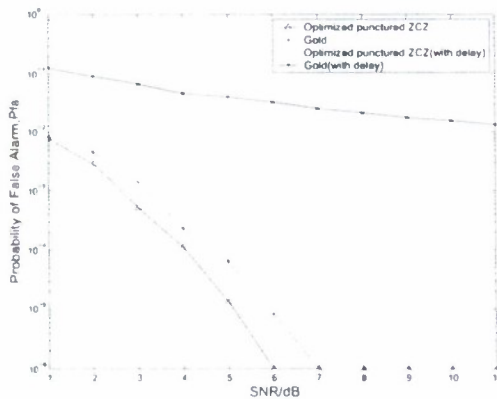


Fig. 5. Probability of false alarm in RSN under the condition of no time delay but Doppler shift or time delay and Doppler shift

According to Fig.5, the SNR of 4-sensor underwater sonar sensor network within our proposed codes can be nearly 0.8dB smaller than that using Gold codes in order to achieve the same  $P_{FA} = 10^{-3}$ . In addition, 4-sensor system requires 1.5dB more than that of 4-sensor system under the condition of both time delay and Doppler shift when  $P_{FA} = 10^{-1.8}$ .

The above figures distinctly illustrate that detection performances of underwater sonar sensor network using our proposed codes are superior to that using Gold codes. The performances of underwater sonar sensor network considering time delay for each transmitting sensor are worse than those under the condition of no time delay, but could be acceptable. Since the time delay estimate in the receiving part may introduce some kind of inaccuracy to the system. In addition, it is easy to assume that the more sensors used, the better performance could be obtained.

## V. CONCLUSION

We propose and investigate a new kind of triphase codes—optimized punctured ZCZPS, provide a constructing method and analyze the codes' properties. The significant advantage of the optimized punctured ZCZ sequence-pair set is a considerably reduced autocorrelation sidelobe and zero mutual cross correlation value as low as zero in ZCZ. Then we apply our optimized punctured ZCZPS to the underwater sonar sensor network, of which the system structure is given and analyzed. A conclusion could be drawn from the simulation results that our proposed optimized punctured ZCZPS, which provide better target detection performance than Gold codes, could satisfy higher demands criterion for detection accuracy in modern military and security affairs for underwater acoustics.

## ACKNOWLEDGEMENT

This work was supported in part by Office of Naval Research (ONR) under Grant N00014-07-1-0395 and N00014-07-1-1024, and National Science Foundation (NSF) under Grant CNS-0721515 and CNS-0831902.

## REFERENCES

- [1] Q. Liang, "Waveform Design and Diversity in Radar Sensor Networks: Theoretical Analysis and Application to Automatic Target Recognition," *Sensor and Ad Hoc Communications and Networks*, vol. 2, no. 28, pp. 684-689, Sep. 2006.
- [2] Q. Liang, "Radar Sensor Networks for Automatic Target Recognition with Delay-Doppler Uncertainty," *Military Communications Conference, MILCOM 2006* 23-25, pp. 1-7, Oct. 2006.
- [3] J. Liang, and Q. Liang, "Orthogonal Waveform Design and Performance Analysis in Radar Sensor Networks," *Military Communications Conference, MILCOM 2006* 23-25, pp. 1-6, Oct. 2006.
- [4] P. F. Worcester, B. D. Cornuelle and R. C. Spindel, "A review of ocean acoustic tomography: 1987-1990," *Re. Geophys.*, suppl., pp. 557-570, Apr. 1991.
- [5] D. Behringer, T. Birdsall, M. Brown, B. Cornuelle, R. Heinmiller, R. Knox, K. Metzger, W. Munk, J. Spiesberger, R. Spindel, D. Webb and P. Worcester, "A demonstration of ocean acoustic tomography," *Nature*, vol. 299, pp. 121-125, Sept. 1982.
- [6] A. Baggeer and W. Munk, "The Heard Island feasibility test," *Phys. Today*, pp. 22-30, Sept. 1982.
- [7] J. L. Spiesberger and K. Metzger, "Basin-scale tomography: A new tool for studying weather and climate," *J. Geophys. Res.*, vol. 96, pp. 4869-4889, Mar. 1991.
- [8] B. Cornuelle et al., "Tomographic maps of the ocean mesoscale-1: Pure acoustics," *J. Phys. Oceanogr.*, vol. 15, pp. 133-152, Feb. 1985.
- [9] T. G. Birdsall and K. Metzger, Jr., "Factor inverse matched filtering," *J. Acoust. Soc. Amer.*, vol. 79, pp. 91-99, Jan. 1986.
- [10] P. Z. Fan, N. Suchiro, N. Kuroyanagi and X. M. Deng, "A class of binary sequences with zero correlation zone," *IEE Electron.Letter*, 35 (10): 777-779, 1999.
- [11] P. Z. Fan, N. Suchiro, N. Kuroyanagi and X. M. Deng, "A class of binary sequences with zero correlation zone," *IEE Electron.Letter*, 35 (10): 777-779, 1999.
- [12] S. Matsufuji, N. Suchiro, N. Kuroyanagi and P. Z. Fan, "Two types of polyphase sequence set for approximately synchronized CDMA systems," *IEICE Trans. Fundamentals*, E862A(1): 229-234, Jan. 2003.
- [13] H. Torii, M. Nakamura and N. Suchiro, "A new class of zero correlation zone sequences," *Trans. Inform.Theory*, 50: 559-565, Mar. 2004.
- [14] T. Jiang, *Research on Quasi-Perfect Binary Signal Pair and Perfect Punctured Binary Signal Pair Theory*, Ph.D Dissertation: Yanshan University, 2003.
- [15] M. A. Richards, *Fundamentals of Radar Signal Processing*, McGraw-Hill, 2005.

# Radar Sensor Network Using a New Triphase Coded Waveform: Theory and Application

Lei Xu and Qilian Liang

Department of Electrical Engineering

University of Texas at Arlington

Arlington, TX 76019-0016

Email: xu@wen.uta.edu, liang@uta.edu

## ABSTRACT

*In radar sensor network (RSN), interference with each radar can be effectively reduced when waveforms are properly designed. In this paper, we firstly perform some theoretical studies on co-existence of phase coded waveforms in RSN. Then we give the definition of a new set of triphase coded waveforms called optimized punctured Zero Correlation Zone sequence-pair set (optimized punctured ZCZPS) and analyze their properties especially their optimized cross correlation property of any two sequence-pairs in the set. Furthermore, we apply our newly provided triphase coded waveforms and equal gain combination technique to the system simulation, and study the performances versus different number of radars in RSN, with Doppler shift or not. Simulation results show that detection performances of multiradars (utilizing our optimized punctured ZCZPS and equal gain combination), either under the Doppler shift condition or not, are superior to those of singler radar.*

**Keywords:** Zero correlation zone; Optimized punctured ZCZ sequence-pair; Radar sensor network.

## I. INTRODUCTION

With recent rapid development in information fusion technology, much time and effort have been put in waveform design. Bell [1] who introduced information theory to radar waveform design, concluded that distributing energy is a good choice to better detect targets. In Sowelam and Tewfik [2]'s work, each waveform selected maximizes the KullbackLeibler information number that measures the dissimilarity between the observed target and the alternative targets in order to minimize the decision time. However, all the above researches only focused on a single active radar.

Multiple radar sensors can be combined to form a multiradar system to overcome performance degradation of single radar along with waveform optimization. In [3], Liang studied constant frequency (CF) pulse waveform design and proposed maximum-likelihood (ML) automatic target recognition (ATR) approach for both nonfluctuating and fluctuating targets in a network of multiple radar sensors. In [4], RSN design based on linear frequency modulation (LFM) waveform was studied and LFM waveform design was applied to RSN with application to ATR with delay-Doppler uncertainty by Liang as well.

J.Liang [5] provided an orthogonal waveform model for RSN, which eliminates interference when there is no Doppler shift.

Phase coded waveform design is one of the widely used waveform design methods for pulse compression which allows a radar to simultaneously achieve the energy of a long pulse and the resolution of a short pulse without the high peak power which is required by a high energy short duration pulse [1]. Nevertheless, the radar sensor network using phase coded waveforms has not been well studied so far. In this paper, we firstly theoretically study RSN design based on phase coded waveforms: the conditions for waveforms co-existence. Then we apply our newly proposed triphase code called optimized punctured ZCZ sequence-pair set to RSN. We perform studies on the codes' properties, especially the cross correlation property and analyze the performance of optimized punctured ZCZ sequence-pairs in RSN system with Doppler shift. According to the Monte Carlo simulation results, RSN based on optimized punctured ZCZ sequence-pairs provides promising detection performance much better than that of single radar, in terms of probability of miss and false alarm detection. The rest of the paper is organized as follows. In Section 2, we study the co-existence of phase coded waveforms. Section 3 introduces the definition and properties of our newly provided triphase coded waveform-optimized punctured ZCZ sequence-pair set. In Section 4, we study the performance versus the number of radars in RSN with Doppler shift. In Section 5, conclusions are drawn on a RSN using our optimized punctured ZCZ sequence-pairs.

## II. CO-EXISTENCE OF PHASE CODED WAVEFORMS IN RSN

In RSN, radar sensors are likely to interfere with each other and the performances may be bad if their waveforms are not properly designed. Orthogonality can be introduced as one criterion for the phase coded waveforms design in RSN to make radar sensors co-existence.

We assume there are  $N$  radars networking together in a self-organizing fashion in our RSN. The radar  $i$  transmits a waveform as

$$x_i(t) = \sum_{n=0}^{N-1} x_i^{(n)}(t - n\tau_c) = \sum_{n=0}^{N-1} \exp(j2\pi f_i^{(n)}(t - n\tau_c)) \quad (1)$$

Here,  $0 < t \leq \tau_c$ .

When the phase coded waveforms are orthogonal to each other, the interference from one waveform to the another can be minimized or even removed. The cross correlation between  $x_i(t)$  and  $x_j(t)$  could be

$$\begin{aligned} & \int_{-T/2}^{T/2} x_i(t)x_j^*(t)dt \\ &= \tau_c \sum_{n=0}^{N-1} \exp[j2\pi(-\frac{N}{2} + \frac{1}{2})\tau_c(\beta_i^{(n)} - \beta_j^{(n)})] \\ & \quad \text{sinc}[\tau_c(\beta_i^{(n)} - \beta_j^{(n)})] \end{aligned} \quad (2)$$

The optimized cross correlation is that of orthogonal waveforms

$$\int_{-T/2}^{T/2} x_i(t)x_j^*(t)dt = \begin{cases} N\tau_c & i = j \\ 0 & i \neq j \end{cases} \quad (3)$$

It is easy to see that when  $\sum_{n=0}^{N-1} \pi\tau_c(\beta_i^{(n)} - \beta_j^{(n)}) = k\pi$ ,  $k = 1, 2, 3, \dots$ , it satisfies the equation (3). In this way can phase coded waveforms be orthogonal to each other and work well simultaneously in Radar Sensor Network. Nevertheless, there are time delay and Doppler shift ambiguity that will introduce interference to waveforms in RSN. Ambiguity function (AF) [6] is usually used to succinctly characterize the behavior of a waveform paired with its matched filter.

The matched filter for waveform  $x_i(t)$  is  $x_i^*(-t)$ . In the RSN of  $M$  radars, the radar  $i$  not only receives its own back-scattered waveform, but also scattered signals generated by other  $M - 1$  radars which caused interference to radar  $i$ .

Assuming each radar transmits signal synchronously,  $t_1 = t_2 = t_M = 0$  and considering interferences from all the other  $M - 1$  radars. Assuming time delay  $\tau = m\tau_c$  for receiving radar  $i$ , the ambiguity function of radar  $i$  could be

$$\begin{aligned} & A_i(\tau, F_{D_1}, \dots, F_{D_M}) \\ &= \left| \int_{-\infty}^{\infty} \left[ \sum_{j=1}^M x_j(t) \exp(j2\pi F_D t) \right] x_i^*(t - \tau) dt \right| \\ &= \left| \tau_c \sum_{j=1}^M \sum_{n=m}^{N-1} \exp[j2\pi(\beta_i^{(n-m)})(\frac{N}{2} + m - 1)\tau_c \right. \\ & \quad \left. + \beta_j^{(n)}(-\frac{N}{2} + 1)\tau_c + F_{D_j}(-\frac{N}{2} + n + 1)\tau_c] \right. \\ & \quad \left. \text{sinc}[\tau_c(\beta_i^{(n)} - \beta_j^{(n-m)} + F_{D_j})] \right| \end{aligned} \quad (4)$$

Here,  $0 < i \leq M$ . (5) consists of two parts: useful signal(reflected signal from radar  $i$  waveform),  $j = i$  part in the (5); and interferences from other  $M - 1$  radar waveforms,  $j \neq i$  parts in (5). Since  $\sum_{n=0}^{N-1} \pi\tau_c(\beta_i^{(n)} - \beta_j^{(n-m)} + F_{D_j}) = k\pi$ ,  $k = 1, 2, 3, \dots$ , it satisfies that  $A(\tau, F_D) = 0$ , when  $F_D = \frac{k}{\tau_c}$ ,  $k = 0, 1, 2, \dots$

### III. OPTIMIZED PUNCTURED ZCZ SEQUENCE-PAIR SET

Zero correlation zone (ZCZ) is a new concept provided by Fan [7] in which both autocorrelation and cross correlation sidelobes are zero while the time delay is kept within the ZCZ instead of the whole period of time domain.

Matsufuji and Torii have provided some methods of constructing ZCZ sequences in [8] [9]. In this section, we apply optimized punctured sequence-pair [10] in ZCZ to construct a new set of triphase code-optimized punctured ZCZ sequence-pair set.

#### A. The Definition of Optimized Punctured ZCZ Sequence-Pair Set

**Definition 3-1** Assume  $(x_i^{(p)}, y_i^{(p)})$  to be a sequence-pair of set  $(X, Y)$  of length  $N$  and the number of sequence-pairs  $K$ , where  $p = 0, 1, \dots, N - 1$ ,  $i = 0, 1, \dots, K - 1$ , if sequences in the set satisfy the following equation:

$$\begin{aligned} R_{x^{(p)}y^{(q)}}(\tau) &= \sum_{i=0}^{N-1} x_i^{(p)} y_{(i+\tau) \bmod N}^{(q)} = \sum_{i=0}^{N-1} y_i^{(p)} x_{(i+\tau) \bmod N}^{(q)} \\ &= \begin{cases} \lambda N, & \text{for } \tau = 0, p = q \\ 0, & \text{for } \tau = 0, p \neq q \\ 0, & \text{for } 0 < |\tau| \leq Z_0 \end{cases} \end{aligned} \quad (5)$$

where  $0 < \lambda \leq 1$ , then  $(x_i^{(p)}, y_i^{(p)})$  is called a ZCZ sequence-pair,  $ZCZP(N, K, Z_0)$  is an abbreviation, and  $(X, Y)$  is called a ZCZ sequence-pair set,  $ZCZPS(N, K, Z_0)$  is an abbreviation.

**Definition 3-2** [10] Sequence  $u = (u_0, u_1, \dots, u_{N-1})$  is the punctured sequence for  $v = (v_0, v_1, \dots, v_{N-1})$ ,

$$u_j = \begin{cases} 0, & \text{if } j \in p \text{ punctured bits} \\ v_j, & \text{if } j \in \text{Non-punctured bits} \end{cases} \quad (6)$$

Where  $p$  is the number of punctured bits in sequence  $v$ . Thus, suppose  $v_j \in (-1, 1)$ ,  $u$  is  $p$ -punctured binary sequence that  $u_j \in (-1, 0, 1)$ ,  $(u, v)$  is called a punctured binary sequence-pair.

**Theorem 3-1** [10] The autocorrelation of punctured sequence-pair  $(u, v)$  is defined

$$R_{uv}(\tau) = \sum_{i=0}^{N-1} u_i v_{(i+\tau) \bmod N}, 0 \leq \tau \leq N - 1 \quad (7)$$

If the punctured sequence-pair has the following autocorrelation property:

$$R_{uv}(\tau) = \begin{cases} E, & \text{if } \tau \equiv 0 \bmod N \\ 0, & \text{others} \end{cases} \quad (8)$$

the punctured sequence-pair is called optimized punctured sequence-pair [10]. Where,  $E = \sum_{i=0}^{N-1} u_i v_{(i+\tau) \bmod N} = N - p$ , is the energy of punctured sequence-pair.

The properties, existing necessary conditions and some construction methods, with help of already known sequences, of punctured binary sequence-pair have been well studied by Jiang [10]. Many optimized punctured sequence-pairs have been found of length from 7 to 31 so far.

**Definition 3-3** If  $(x_i^{(p)}, y_i^{(p)})$  in Definition 3-1 is constructed by optimized punctured sequence-pair and a certain matrix, such as Hadamard matrix or an orthogonal matrix, where

$$\begin{aligned} x_i^{(p)} &\in (-1, 1), \quad i = 0, 1, 2, \dots, N - 1 \\ y_i^{(q)} &\in (-1, 0, 1), \quad i = 0, 1, 2, \dots, N - 1 \end{aligned}$$

$$R_{x^{(p)}y^{(q)}}(\tau) = \sum_{i=0}^{N-1} x_i^{(p)} y_{(i+\tau) \bmod N}^{(q)} = \sum_{i=0}^{N-1} y_i^{(p)} x_{(i+\tau) \bmod N}^{(q)}$$

$$= \begin{cases} \lambda N, & \text{for } \tau = 0, p = q \\ 0, & \text{for } \tau = 0, p \neq q \\ 0, & \text{for } 0 < |\tau| \leq Z_0 \end{cases} \quad (9)$$

where  $0 < \lambda \leq 1$ , then  $(x_i^{(p)}, y_i^{(p)})$  can be called an optimized punctured ZCZP.

### B. Design for Optimized Punctured ZCZ Sequence-pair Set

Based on odd length optimized punctured binary sequence pairs and a Hadamard matrix, an optimized punctured ZCZ sequence-pair set can be constructed from the following steps:

**Step 1:** Given an odd length optimized punctured binary sequence-pair  $(u, v)$ , the length of each sequence is  $N_1$

$$u = u_0, u_1, \dots, u_{N_1-1}, u_i \in (-1, 1),$$

$$v = v_0, v_1, \dots, v_{N_1-1}, v_i \in (-1, 0, 1),$$

**Step 2:** Given Hadamard matrix  $B$ , the length of the sequence is  $N_2$  which is equal to the number of the sequences.

$$B = (b^0; b^1; \dots, b^{N_2-1}), b^i = (b_0^i, b_1^i, \dots, b_{N_2-1}^i)$$

**Step 3:** Processing bit-multiplication on the optimized punctured binary sequence-pair and each row of Hadamard matrix  $B$ , then sequence-pair set  $(X, Y)$  is obtained,

$$x_j^i = u_{j \bmod N_1} b_{j \bmod N_2}^i, 0 \leq i \leq N_2 - 1, 0 \leq j \leq N - 1,$$

$$X = (x^0; x^1; \dots, x^{N_2-1}), x^i = (x_0^i, x_1^i, \dots, x_{N-1}^i),$$

$$y_j^i = v_{j \bmod N_1} b_{j \bmod N_2}^i, 0 \leq i \leq N_2 - 1, 0 \leq j \leq N - 1,$$

$$Y = (y^0, y^1, \dots, y^{N_2-1}), y^i = (y_0^i, y_1^i, \dots, y_{N-1}^i)$$

Where  $GCD(N_1, N_2) = 1$  and  $N = N_1 * N_2$ . The three steps make the sequence-pair set  $(X, Y)$  an optimized punctured ZCZPS, where  $ZCZ Z_0 = N_1 - 1$ . The length of each sequence in optimized punctured ZCZPS is  $N = N_1 * N_2$  that depends on the product of length of optimized punctured sequence-pair and the length of a row in Hadamard matrix. The number of sequence-pairs in optimized punctured ZCZPS rests on the order of the Hadamard matrix. The sequence  $x^i$  in  $X$  and the corresponding sequence  $y^i$  in  $Y$  construct an optimized punctured ZCZP  $(x^i, y^i)$  that can be used as a phase coded waveform, such as  $x^i$  for radar transmitter and  $y^i$  for radar receiver. The phase states for any sequence-pair among  $(x^i, y^i)$  are  $-\pi, 0$  and  $\pi$ , so our newly provided optimized punctured ZCZPS is a new set of triphase codes.

It is easy to prove that the correlation property of the sequence-pairs in the set is:

$$R_{x^i y^j}(\tau) = R_{x^j y^i}(\tau) = R_{uv}(\tau \bmod N_1) R_{b^i b^j}(\tau \bmod N_2)$$

$$= R_{uv}(\tau \bmod N_1) R_{b^i b^j}(\tau \bmod N_2)$$

$$= \begin{cases} EN_2, & \text{if } \tau = 0, i = j \\ 0, & \text{if } 0 < |\tau| \leq N_1 - 1, i = j \\ 0, & \text{if } i \neq j \end{cases} \quad (10)$$

According to Definition 3-1, the sequence-pair set constructed by the above method is a ZCZPS.

### C. Properties of Optimized Punctured ZCZ Sequence-pair set

Considering the optimized punctured ZCZPS that is constructed by the method mentioned in the last part, the autocorrelation and cross correlation properties can be simulated and analyzed with Matlab. For example, the optimized punctured ZCZPS  $(X, Y)$  is constructed by 31-length optimized punctured binary sequence-pair  $(u, v)$ ,  $u = [++++- - - + - + - + + - - - + - - + - - + + - + - +]$ ,  $v = [++++000+0+0++0000+00+00++0+0+0]$  (using '+' and '-' symbols for '1' and '-1') and Hadamard matrix  $H$  of order 4. We follow the three steps presented in Section B to construct the 124-length optimized punctured ZCZPS. The number of sequence-pairs here is 4 and the length of each sequence is  $31 * 4 = 124$ . The first row of each matrix  $X = [x_1; x_2; x_3; x_4]$  and  $Y = [y_1; y_2; y_3; y_4]$  constitute a certain optimized punctured ZCZP  $(x_1, y_1)$ . Similarly, the second row of each matrix  $X$  and  $Y$  constitute another optimized punctured ZCZ sequence-pair  $(x_2, y_2)$  and so on.

**1) Autocorrelation and Cross Correlation Properties:** The autocorrelation property  $R(x_1, y_1)$  and cross correlation property  $R(x_1, y_2) = R(y_1, x_2)$  of 124-length optimized punctured ZCZPS  $(X, Y)$ , are shown in Fig.1.

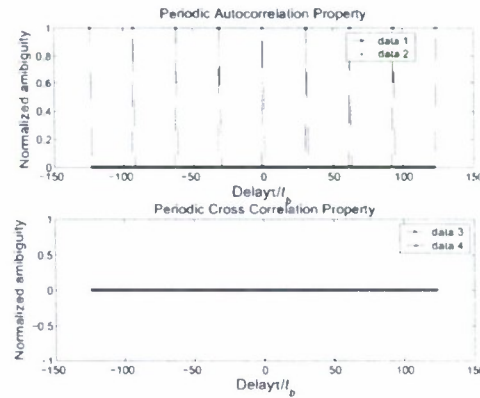


Fig. 1. Periodic autocorrelation property of optimized punctured ZCZ sequence-pair set

From the Fig.1, the sidelobe of autocorrelation of ZCZPS can be as low as 0 when the time delay is kept within  $Z_0 = N_1 = 31$  and the cross correlation value is 0 during the whole time domain.

It is known that a suitable criterion for evaluating code of length  $N$  is ratio of the peak signal divided by peak signal sidelobe ratio (PSR) of their aperiodic autocorrelation function, which can be bounded by [6]

$$[PSR]_{dB} \leq 20 \log N = [PSR_{max}]_{dB} \quad (11)$$

The only uniform phase codes that can reach the  $PSR_{max}$  are the Barker codes whose length is equal or less than 13. The sidelobe of the new code shown in Fig.1 can be as low as 0, and the peak signal to peak signal sidelobe can be as large as infinite. Besides, the length of the new code is various and much longer than the length of the Barker code.

2) *Ambiguity function*: When the transmitted impulse is reflected by a moving target, the reflected echo signal includes a linear phase shift, which comes from the Doppler shift  $f_d$  [6]. Because of the Doppler shift  $f_d$ , the main peak of the autocorrelation function is reduced and so as to the SNR degradation. Focusing on the sequence-pair  $(x, y)$  here, the receiving sequence in ambiguity function is different from the echo signal and the periodic correlation is used instead of aperiodic correlation here. The ambiguity function in [6] can be rewritten as

$$A(\tau, F_D) = \left| \int_{-\frac{T}{2}}^{-\frac{T}{2}+\tau} x(t) \exp(j2\pi F_D t) y^*(t + T - \tau) dt \right. \\ \left. + \int_{-\frac{T}{2}+\tau}^{\frac{T}{2}} x(t) \exp(j2\pi F_D t) y^*(t - \tau) dt \right| \quad (12)$$

In order to analyze the autocorrelation performance of an optimized punctured ZCZP with delay-Doppler shift, Equation (12) is plotted in Fig.2(a) in a three-dimensional surface plot. Here, maximal time delay is 1 unit (normalized to length of the code, in units of NTs) and maximal Doppler shift is 3 units for autocorrelation (normalized to the inverse of the length of the code, in units of 1/NTs). In Fig.2(a), there is relative uniform

uniform sidelobes minimize target masking effect in ZCZ of time domain, where  $Z_0 = 31$ ,  $-31 < \tau < 31$ ,  $\tau \neq 0$ .

#### D. Co-existence of Optimized Punctured ZCZ Sequence-pairs

Considering interference from other radars  $j \neq i$ , with delay-Doppler shift, the ambiguity function of radar  $i$  can be expressed as

$$A(\tau, F_{D1}, \dots, F_{DM}) \quad (13) \\ = \left| \int_{-\infty}^{\infty} \sum_j^M (x_j(t) \exp(j2\pi F_{Dj} t) y_i^*(t - \tau) dt \right|$$

Fig.2(b) is three-dimensional surface plot to analyze the ambiguity function of radar  $i$  (considering interference from other radars). Generally speaking, Fig.2(b) closely resembles Fig.2(a). Without Doppler shift, there are regular high peaks on multipliers of period of 31 which is the length of ZCZ. And the high peak on zero time delay point can be used to detect targets. Hence, even considering the interference from other  $M - 1$  radars, the radar  $i$  may work as well as there is no interference.

When time delay equals repetition of  $Z_0 = 31$ , the figures of amplitude versus Doppler shift are the same. Because of periodic property of our code. Hence, output of matched filter of radar  $i$  (considering interference from other radars), with time delay, is illustrated on right side of Fig.2(b). For some traditional phase coded waveforms, when Doppler frequencies equal to multiples of the pulse repetition frequency ( $PRF = 1/PRI = 1/T_s$ ) the ambiguity value turns to be zero which will render the radar blind [6] to their velocities. Nevertheless, from Fig.2(b), ambiguity values are zero only when Doppler frequencies are equal to odd multiples of the PRF. Therefore, using the optimized punctured ZCZ sequence-pair in the RSN system could, to some extent, improve the blind speed problem in moving target detection system.

#### IV. SYSTEM SIMULATION IN RADAR SENSOR NETWORK

In RSN of  $M$  radars, the combined received signal for the radar  $i$  is

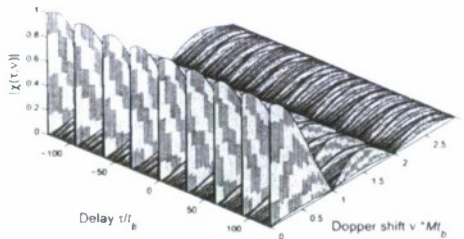
$$r_i(u, t) = \sum_{j=1}^M x_j(t - t_j) \exp(j2\pi F_{Dj} t) + n(u, t) \quad (14)$$

$F_{Dj}$  and  $t_j$  are Doppler shift of target and time delay relative to waveform  $j$ , and  $n(u, t)$  is additive white Gaussian noise(AWGN). The structure can be constructed as Fig.3.

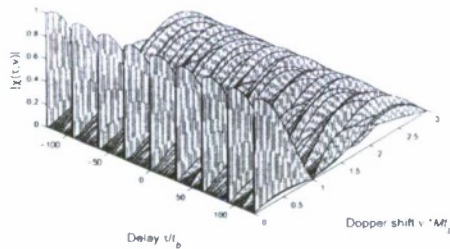
According to this structure, the combined received signal  $r_i(u, t)$  is processed by its corresponding matched filter  $i$  and the output of branch  $i$  is  $Z_i(u, t)$ . Each  $Z_i(u, t)$  can be equal gain combined to construct the final output  $Z(u, t)$ .

The output of branch  $i$  is

$$|Z_i(u)| = \left| \int_{-\frac{T}{2}}^{\frac{T}{2}} \left[ \sum_{j=1}^M x_j(t - t_j) \exp(j2\pi F_{Dj} t) + n(u, t) \right] y_i^*(t - t_i) dt \right| \quad (15)$$



(a)



(b)

Fig. 2. (a) Ambiguity function of a 124-length ZCZ sequence-pair  $(x_i, y_i)$  (b) Ambiguity function of radar  $i$  (considering interference from other radars)

plateau suggesting low and uniform sidelobes. This low and

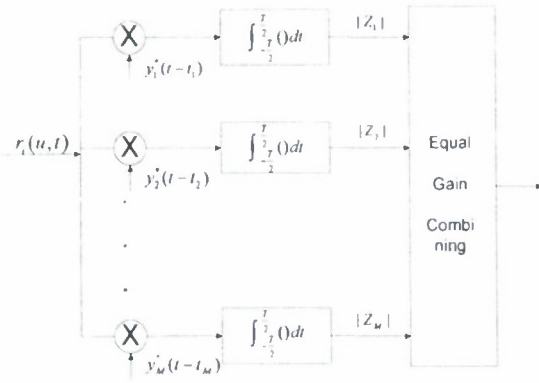


Fig. 3. Waveform diversity combining in RSN

Where  $n(u) = \int_{-\frac{T}{2}}^{\frac{T}{2}} n(u, t) y_i^*(t - t_i) dt$  can be easily proved to be still an AWGN.

We can also have two special cases for  $|Z_i(u)|$ :

1) If there is Doppler shift but no time delay, all the radar sensors transmit signals synchronously,  $t_1 = t_2 = \dots = t_M = 0$ , then

$$|Z_i(u)| = \left| \int_{-\frac{T}{2}}^{\frac{T}{2}} \left[ \sum_{j=1}^M x_j(t) \exp(j2\pi F_{D_j} t) + n(u, t) \right] y_i^*(t) dt \right| \quad (16)$$

Assuming that the Doppler shift can be well estimated in the receiving radar sensor, so the Doppler shift compensation factor  $\exp^*(j2\pi F_{D_j})$  is introduced here.

$$|Z_i(u)| \leq |E| + \left| \int_{-\frac{T}{2}}^{\frac{T}{2}} \left[ \sum_{j=1}^M x_j(t) \exp(j2\pi (F_{D_j} - F_{D_i}) t) y_i^*(t) \right] + \int_{-\frac{T}{2}}^{\frac{T}{2}} n(u, t) y_i^*(t) \exp^*(j2\pi F_{D_i} t) dt \right|$$

If  $F_{D_1} = F_{D_2} = \dots = F_{D_j} = F_{D_i}$ , further simplified as

$$|Z_i(u)| \leq |E| + 0 + \left| \int_{-\frac{T}{2}}^{\frac{T}{2}} n(u, t) y_i^*(t) \exp^*(j2\pi F_{D_i} t) dt \right| \quad (18)$$

2) If both time delay for each transmitting radar sensor and Doppler shift exist in the RSN, assuming  $F_{D_1} = F_{D_2} = \dots = F_{D_j} = F_{D_i}$ , considering the Doppler shift compensation factor in the receiving sensor,

$$|Z_i(u)| \leq |E| + \left| \int_{-\frac{T}{2}}^{\frac{T}{2}} \left[ \sum_{j=1}^M x_j(t - t_j) y_i^*(t - t_i) \right] + \int_{-\frac{T}{2}}^{\frac{T}{2}} n(u, t) y_i^*(t - t_j) \exp^*(j2\pi F_{D_i} t) dt \right| \quad (19)$$

Because of the good periodic autocorrelation and cross correlation properties of our proposed codes, the frame of receiving data could be modified before the matched filter on

the receiving radar sensor to improve the RSN performance. The data from  $N + 1$  to  $\max(t_j) + N$  are added to data from 1 to  $\max(t_j)$ , bit by bit, where  $N$  is the original data length and  $t_j$  is the time delay for  $j$ th transmitting radar sensor. In this way can we get the output of the matched filter

$$|Z_i(u)| \leq |E| + 0 + \left| \int_{-\frac{T}{2}}^{\frac{T}{2}} n(u, t) y_i^*(t) \exp^*(j2\pi F_{D_i} t) dt \right| \quad (20)$$

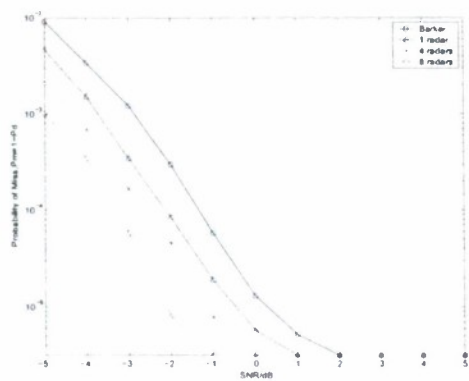
Based on (17) and (20), it is easy to see that using our provided codes and frame modification, the RSN under the condition of time delay for each radar sensor can, to some extent, work as well as the RSN where all the radar sensors transmit signals synchronously.

We apply optimized punctured ZCZPS as a bank of phase coded waveforms together with equal gain combination technique in the simulation in order to study the performance versus different number of radars in RSN with Doppler shift. According to [6],  $P_M$  (Probability of Miss Detection) and  $P_{FA}$  (Probability of False Alarm) suffice to specify all of the probabilities of interest in radar system. Therefore, we respectively simulated the above two probabilities of different number of radars using different number of optimized punctured ZCZ sequence-pairs in single radar system, 4-radar system and 8-radar system together with 1-radar system using Barker code respectively. Two special cases of performances have been simulated. They are performances under one condition of no time delay but having Doppler shift, and under the another condition of time delay for each radar sensor and having Doppler shift.  $10^6$  times of Monte-Carlo simulation has been run for each SNR value. Since equal gain combination is used here, the threshold for detection is chosen to be around 0.5.

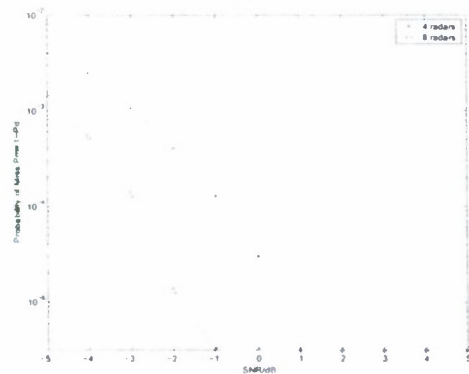
The miss detection probabilities of the envelope detector in RSN under the condition of two special cases mentioned above are compared in Fig.4(a) and Fig.4(b) respectively. Fig.4(a) illustrates that when  $P_M = 10^{-3}$ , SNR of 8-radars are 2.2dB smaller than that of single radar system using Barker code with Doppler shift. Considering time delay for each radar in multiple radars system in Fig.4(b), SNR of 8-radar RSN can gain 1.7dB smaller than 4-radar SNR to achieve the same  $P_M = 10^{-3}$ .

The false alarm probability of envelope detector in different number of radars under the condition of the two special cases are shown in Fig.5(a) and Fig.5(b) respectively. From Fig.5(a), the SNR of 8-radars can be nearly 3.8dB smaller than that of single radar system using Barker code in order to achieve the same  $P_{FA} = 10^{-2}$ . From Fig.6(b), 4-radar system requires 1.7dB more than that of 8-radar RSN under the condition of both time delay and Doppler shift.

The above figures distinctly illustrate that performances of detection of multiradars (utilizing our optimized punctured ZCZPS and equal gain combination) are superior to that of single radar. In addition, the performances of 4-radar and 8-radar RSN considering time delay for each radar transmitting sensor can be comparable to those under the condition of no

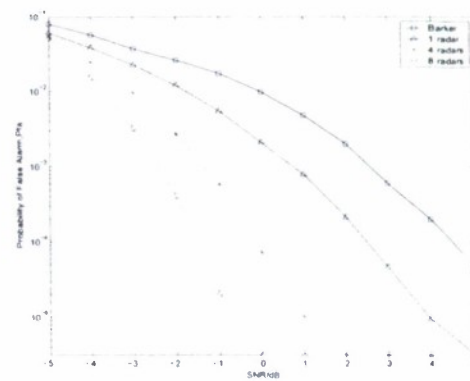


(a)

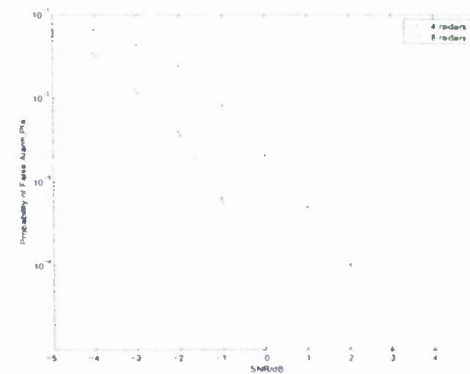


(b)

Fig. 4. Probability of miss detection in RSN under the condition of: (a) No time delay but Doppler shift (b) Time delay and Doppler shift



(a)



(b)

Fig. 5. Probability of false alarm in RSN under the condition of: (a) No time delay but Doppler shift (b) Time delay and Doppler shift

time delay.

## V. CONCLUSION

We have studied phase coded waveform design and spatial diversity under the condition of Doppler shift in RSN. In this paper, we also investigate the definition and properties of optimized punctured ZCZPS, which can be used as a set of phase coded waveforms in RSN. The significant advantage of the optimized punctured ZCZ sequence-pair set is a considerably reduced autocorrelation sidelobe as low as zero in ZCZ and zero mutual cross correlation value in the whole time domain. Because any two optimized punctured ZCZPS among an optimized punctured ZCZPS have the ideal orthogonal property, they can co-exist in RSN and achieve better detection performance than that of a single radar. The general conclusion can be drawn that applying our optimized punctured ZCZPS as a bank of phase coded waveforms to a RSN can effectively satisfy higher demands criterion for detection accuracy in modern military and security affairs..

## ACKNOWLEDGEMENT

This work was supported by the Office of Naval Research (ONR) Grant N00014-07-1-0395, N00014-07-1-1024, and N00014-03-1-0466.

## REFERENCES

- [1] M. R. Bell, "Information theory and radar waveform design," *IEEE Trans on Information Theory*, vol. 39, no. 5, pp. 1578-1597, Sept. 1993.
- [2] S. Sowelam and A. Tewfik, "Waveform selection in radar target classification," *IEEE Trans on Information Theory*, vol. 46, no. 3, pp. 1014-1029, 2000.
- [3] Q. Liang, "Waveform Design and Diversity in Radar Sensor Networks: Theoretical Analysis and Application to Automatic Target Recognition," *Sensor and Ad Hoc Communications and Networks*, vol. 2, no. 28, pp. 684-689, Sep. 2006.
- [4] Q. Liang, "Radar Sensor Networks for Automatic Target Recognition with Delay-Doppler Uncertainty," *Military Communications Conference, 2006. MILCOM 2006* 23-25, pp. 1-7, Oct. 2006.
- [5] J. Liang, and Q. Liang, "Orthogonal Waveform Design and Performance Analysis in Radar Sensor Networks," *Military Communications Conference, 2006. MILCOM 2006* 23-25, pp. 1-6, Oct. 2006.
- [6] M. A. Richards, *Fundamentals of Radar Signal Processing*, McGraw-Hill, 2005.
- [7] P. Z. Fan, N. Suchiro, N. Kuroyanagi and X. M. Deng, "A class of binary sequences with zero correlation zone," *IEE Electron Letter*, 35 (10): 777-779, 1999.
- [8] S. Matsufuji, N. Suchiro, N. Kuroyanagi and P. Z. Fan, "Two types of polyphase sequence set for approximately synchronized CDMA systems," *IEICE Trans. Fundamentals*, E862A(1): 229-234, Jan. 2003.
- [9] H. Torii, M. Nakamura and N. Suchiro, "A new class of zero correlation zone sequences," *Trans. Inform. Theory*, 50: 559-565, Mar. 2004.
- [10] T. Jiang, *Research on Quasi-Perfect Binary Signal Pair and Perfect Punctured Binary Signal Pair Theory*, Ph.D Dissertation: Yanshan University, 2003.

# Interference Analysis for FH-Based Multi-Radio Wireless Mesh Networks

Davis Kirachaiwanich and Qilian Liang  
Department of Electrical Engineering  
University of Texas at Arlington  
Arlington, TX 76019-0016, USA  
E-mail: liang@uta.edu

**Abstract**—In this paper, we study the interference analysis in a Noncoherent Frequency-Hopping (NC-FH) MFSK rural infrastructure Wireless Mesh Networks (WMNs) with each router node being equipped with multiple radio interfaces. Our choice of the FH/MFSK modulation technique here is not just to satisfy the security requirement in military communications but also to provide easy implementation for each router nodes; since FH/MFSK modulation technique has been specified in IEEE 802.11 standard, these router nodes can be implemented also using IEEE 802.11(FH) equipments. The performances of noncoherent slow frequency-hopping system with  $M$ -ary frequency-shift-keyed modulation (NC-FH/MFSK) with AWGN channel and Ricean fading under independent multitone jamming (independent MTJ) are investigated in this paper. The expressions for calculating the exact BER performances of the system under the effect of the jamming strategies are derived. We apply the analyses to channel assignment (CA) in multiradio rural WMNs. We obtain a new interference model combining interference tone and partial band noise, which would be incorporated into the CA algorithm to assign the most appropriate channel (or hopping pattern, in our case) to links in the mesh. Because it takes into account both the intra-network and the coexisting-network interferences, the new interference model thus reflects a very realistic interference situation in WMNs.

## 1. INTRODUCTION

Wireless mesh networks (WMNs) consist of mesh routers and mesh clients, where mesh routers have minimal mobility and form the backbone of WMNs. They provide network access for both mesh and conventional clients. The integration of WMNs with other networks such as the Internet, cellular, IEEE 802.11, IEEE 802.15, IEEE 802.16, sensor networks, etc., can be accomplished through the gateway and bridging functions in the mesh routers. Mesh clients can be either stationary or mobile, and can form a client mesh network among themselves and with mesh routers [1]. The IEEE 802.11b/g and IEEE 802.11a standards define 3 and 12 non-overlapping frequency channels, respectively. Using multiple channels in multi-radio WMNs greatly improves the network throughput [8]. One of the most important design questions for a multi-radio WMN is the channel assignment problem, i.e., how to bind each radio interface to a radio channel [3].

Most of the WMN, nowadays, are deployed using commercial off-the-shelf (COTS) IEEE 802.11 equipment due to its relatively low cost and high performance and, to provide an adequate support for high data traffic, especially in infrastructure networks, the mesh are usually formed by router/gateway nodes that are equipped with multiple IEEE 802.11 radio interfaces. However, it is widely known that, as the size of the WMN increases, mesh routers tend to interfere more with each other; thus, the capacity of the network drops. To achieve the reasonable throughput from WMN, therefore, several publications ([11]–[14]) have proposed algorithms, which are focused to reduce such intra-network interference by carefully managing how each node accesses to the media. And, as a part of their studies, numerous attempts were devoted to acquire the interference models, which can provide as accurate interference estimation as possible. In [11], an interference-aware channel assignment (CA) algorithm has been proposed for multiradio IEEE 802.11 WMN. The centralized CA algorithm was designed by taking into account both the interferences among router nodes and the external interference from co-existing network. To estimate the two types of interferences, the author developed the Multiradio Conflict Graph (MCG) and used it for modelling the interferences among router nodes while, for the co-existing network interference, the inherited IEEE 802.11 radio-sensing mechanism was adopted to periodically monitor for unrecognized radios. Also, in [7], the author has proposed an interference model for partially overlapped channels and, to illustrate its benefit, the model was thus used to enhance the performance of two previously proposed CA algorithms. In [6], a hybrid channel assignment scheme is proposed where some radios are statically assigned a channel while the remaining radios can dynamically change their frequency channel. In [4], throughput improvements was studied by replacing CSMA/CA with an STDMA scheme where transmissions are scheduled according to the physical interference model. In [3], a centralized channel assignment and routing algorithm is developed for multi-radio WMNs aiming to maximize the network throughput. An integer linear programming (ILP) model was used to evaluate the performance. Recently, a seminar work on su-

perimposed code-based channel assignment was proposed for MR-MC WMNs [19].

In this paper, we will study the channel assignment in an Noncoherent Frequency-Hopping (NC-FH) MFSK rural infrastructure WMN with each router node being equipped with multiple radio interfaces. Our choice of the FH modulation technique here is not just to satisfy the security requirement in military communications but also to provide easy implementation for each router nodes; since FH/MFSK modulation technique has been specified in IEEE 802.11 standard, these router nodes can be implemented also using IEEE 802.11(FH) equipments. Generally, these IEEE standard FH equipments uses 83.5MHz of ISM frequency bandwidth (2.4GHz-2.4835GHz) as the operational bandwidth and divide it into 79 FH bands, each with 1 MHz, to support the FH modulation technique. Subsequently, to enable multiple transmissions, three non-colliding hopping patterns are established, each with 26 FH bands [5]. We have observed that if we can assign different hopping patterns to the radio interfaces of router nodes properly, simultaneous transmissions will be allowed throughout the mesh, consequently increase the mesh capacity. Should we consider hopping patterns as radio channels, hence, the assignment of hopping patterns is equivalent to the assignment of channels to radio interfaces and the channel assignment (CA) algorithm can then be used for assigning the hopping patterns.

The rest of this paper is organized as follows. In Section II, the BER expressions for NC-FH/MFSK system with AWGN channel and Rician fading under independent multi-tone jamming (MTJ) will be derived. Section III will be devoted for the study of the channel assignment in rural NC-FH/MFSK WMN. Section IV will conclude the paper.

## II. NC-FH/MFSK UNDER INDEPENDENT MULTITONE JAMMING

In this paper the FH system is assumed to be slow hopping over  $N$  non-overlapping FH bands, i.e. a hop period is a multiple of symbol period ( $T_h = kT_s$ , where  $k=1,2,3,\dots$ ). Each FH band is comprised of  $M = 2^K$  signal frequencies of the  $M$ -ary FSK modulation. Hence, there are  $NM$  possible frequency bins for a signal tone to be transmitted. If all FH bands are contiguous, the total communication bandwidth thus equals to  $B_T = NM/T_s$ . Also, we will assume that the transmission bit rate of the system is  $R_b = KR_s = K/T_s$ , where  $R_s = 1/T_s$  denotes the symbol rate. And, the average received power for every symbol transmitted, regardless of the channels effect, is assumed to be  $P_s$  or an average symbol energy of  $E_s = P_s T_s$ . Therefore, the received bit energy can be calculated by  $E_b = E_s / \log_2 M$ .

The jamming source of interest is assumed to possess the complete description of the signal transmitted from the NC-FH/MFSK system and able to transmit multiple signal-like interference tones simultaneously within one symbol time,  $T_s$ . Also it is assumed that the power source

in the jammer is an ideal source and can supply the power constantly at all time. While  $q$ ,  $1 \leq q \leq NM$ , is the number of simultaneously transmitted interference tones, which are distinct and uniformly distributed over the entire bandwidth  $B_T$ , if we assume that the total interference tone power at the receiver is  $P_{jT}$  and that each interference tone equally shares this power, the received power for each interference tone is therefore equal to  $P_j = P_{jT}/q$  or the received energy of  $E_j = P_j T_s = P_{jT} T_s / q$ .

The transmitted signal and interference tones are assumed to undergo an independent fading channel before arriving at the receiver with noncoherent detection scheme and all fading channels in this study are modeled as slow fading, frequency non-selective Rician processes, whose PDF are of the form

$$f_{X_k}(x_k) = \frac{x_k}{\sigma_k^2} \exp\left(-\frac{x_k^2 + \alpha_k^2}{2\sigma_k^2}\right) I_0\left(\frac{\alpha_k x_k}{\sigma_k^2}\right) u(x_k) \quad (1)$$

where  $I_0(\cdot)$  denotes the zero<sup>th</sup> order modified Bessel function and  $u(\cdot)$  is the unit step function.  $\alpha^2$  and  $2\sigma^2$  are the average power of the LOS (Line-Of-Sight) and the scattering rays of the fading channel. We can also define another parameter to determine the Rician fading channel by using the ratio of  $\alpha^2$  and  $2\sigma^2$ . This ratio is called the Rician K factor,  $K_k = \alpha_k^2 / 2\sigma_k^2$  where  $k=1,2$  is used for signal tone and interference tone respectively. It is used to determine how severe the multipath effect is.

At the receiver, the received signal will be noncoherently detected and it is assumed that each symbol of the  $M$ -ary FSK is equally likely. The receive signal can be represented as

$$r_i(u, t) = x_k \sqrt{2P_i} \cos(\omega_m t + \phi_i) + n(u, t) \quad (2)$$

where  $x_k$  is a Rician random variable representing the envelope of the fading channel and its PDF can be represented as (1).  $P_i$  is the average received power of the tone if the effect of fading channel is not accounted. The subscript  $i=s,j$  denotes signal tone and interference tone respectively.  $\omega_m$ ,  $m=1,2,\dots,M$ , is angular frequency for an MFSK symbol and  $\phi$  is unknown phase.  $n(u, t)$  is AWGN, Gaussian-process thermal noise, with total power  $\sigma_n^2 = N_0/T_s$ .

Since the interferers are distinct and uniformly distributed, in any hop there can be as few as none and as many as  $\min(q, M)$  interference tones. Hence, the probability of symbol error (or symbol error rate, SER) of the system can be calculated by

$$\begin{aligned} P_s(e) &= P_0 \cdot P_{s0}(e|no \text{ int. tone}) \\ &+ \sum_{n=1}^{\min(q, M-1)} P_n \cdot P_{sn}(e|n \text{ int. tones}) \\ &+ P_M \cdot P_{sM}(e|M \text{ int. tones}) \cdot u(q - M) \end{aligned} \quad (3)$$

where  $P_s(e)$  is the probability of symbol error.  $P_0$ ,  $P_M$ , and  $P_n$  are the probabilities that a hop is jammed by zero,  $M$ , and  $n$  interference tones, where  $1 \leq n \leq \min(q, M -$

1).  $P_{s0}(e)$ ,  $P_{sM}(e)$  and  $P_{sn}(e)$  are the probabilities of symbol error corresponding to the specified number of interference tones in the hop. It should be noted that  $u(\cdot)$  in the last term on RHS is the unit step function included to account for the fact that the probability of having  $M$  interference tones in a hop is equal to zero if the total number of interference tones in the entire spectrum bandwidth is less than  $M$ , i.e.  $q < M$ .

Finally, for MFSK system, the probability of bit error can be calculated from the probability of symbol error by

$$P_b(e) = \frac{M/2}{M-1} P_s(e) \quad (4)$$

#### A. Probability of Symbol Error with No Interference Tone

If  $q$  equal power interference tones are transmitted simultaneously in  $NM$  possible frequency bins, the probability that the transmitted signal band does not contain any interference tone can be given by

$$P_0 = \prod_{k=0}^{M-1} \left(1 - \frac{q}{NM-k}\right) \quad (5)$$

Generally for noncoherent detection scheme, the output of the envelope detector in the branch where signal tone, or interference tone (or both) is present will have its PDF followed a Rician distribution while that of the other output branches with AWGN only, are known to follow just Rayleigh distribution, which can be expressed by replacing  $\alpha_s$  in (1) with zero. The probability of symbol error conditioned on no interference and the signal Rician channel gain can thus be calculated using [9] [10],

$$\begin{aligned} P_{s0}(e|no\ int.\ tone, x_1) &= P(|S + n(u)| < |n(u)| |x_1)^{M-1} \\ &= \sum_{v=1}^{M-1} \frac{(-1)^{v+1}}{v+1} \binom{M-1}{v} \exp \left[ \frac{-v P_s x_1^2}{(v+1) \sigma_n^2} \right] \end{aligned} \quad (6)$$

where  $|\cdot|$  represents an envelope and  $n(u)$  is AWGN.

Multiplying the Rician PDF in (1) to (6) and integrating the resulting product with respect to  $x_1$ , we can obtain the probability of symbol error conditioned on no interference in the form of [9],

$$\begin{aligned} P_{s0}(e|no\ int.\ tone) &= \sum_{v=1}^{M-1} \frac{(-1)^{v+1}}{1+v(1+\frac{2\sigma_s^2}{\sigma_n^2})} \binom{M-1}{v} \\ &\quad \cdot \exp \left[ \frac{-v \frac{\alpha_s^2}{\sigma_n^2}}{1+v(1+\frac{2\sigma_s^2}{\sigma_n^2})} \right] \end{aligned} \quad (7)$$

where  $\alpha_s^2$  and  $2\sigma_s^2$  are the average LOS power and the average scattering power of the signal symbol. These parameter can be expressed in general as

$$\begin{aligned} \alpha_i^2 &= P_i \alpha_k^2 \\ \sigma_i^2 &= P_i \sigma_k^2 \end{aligned} \quad (8)$$

with the subscript  $i=s,j$ , and  $\alpha_k^2$  and  $2\sigma_k^2$ , where  $k=1,2$ , are averaged LOS and scattering powers of the channel for signal and interference tones respectively.

#### B. Probability of Symbol Error with $n$ Interference Tones Given The Signal Branch Is Jammed

With total  $q$  interference tones simultaneously transmitted from the jammer, if a hop is actually jammed, the possible number of interference tones in the hop can range from 1 up to  $\min(q, M)$ . For an NC-FH/MFSK system with  $NM$  possible frequency bins, the probability that a hop will be jammed by  $n$  interference tones, where  $1 \leq n \leq \min(q, M-1)$  is given as

$$P_n = \prod_{k=0}^{n-1} \left( \frac{q-k}{NM-k} \right) \prod_{j=n}^{M-1} \left( 1 - \frac{q-n}{NM-j} \right) \quad (9)$$

Given that a hop is interfered by  $n$  interference tones, the probability of symbol error can further be divided into two subcases. First is the case when the signal tone is jammed by one of  $n$  interference tones in the hop and the probability that one out of  $n$  interference tones will jam the signal tone is  $n/M$ . Second is when none of  $n$  interference tones is located in the same frequency bin as the signal, i.e. the signal tone is not jammed. The probability of the second case is  $1 - n/M = (M-n)/M$ . Hence, the probability of symbol error given a hop is interfered by  $n$  interference tones can be expressed as

$$\begin{aligned} P_{sn}(e|n\ int.\ tones) &= \left( \frac{n}{M} \right) P_{sn}(e|signal\ is\ jammed) \\ &\quad + \left( \frac{M-n}{M} \right) P_{sn}(e|signal\ is\ not\ jammed) \end{aligned} \quad (10)$$

To evaluate the probability of symbol error when the signal branch is jammed, [15] has provided a computational-efficient method based on the use of phasor representations and nonecentral chi-squared PDF's. It can be shown for any two Rician random variables, say  $R_{01}$  and  $R_{02}$ , that  $P(R_{01} > R_{02}) = P(R_{01}^2 > R_{02}^2)$ . In (3) of [15], the probability is given as

$$\begin{aligned} P(R_{01} > R_{02}) &= P(R_{01}^2 > R_{02}^2) \\ &= Q \left( \sqrt{\frac{2K_{01}}{b+1}}, \sqrt{\frac{2K_{02}b}{b+1}} \right) \\ &\quad - \left( \frac{b}{b+1} \right) \exp \left( -\frac{K_{01} + K_{02}b}{b+1} \right) \\ &\quad \cdot I_0 \left( \frac{\sqrt{4K_{01}K_{02}b}}{b+1} \right) \end{aligned} \quad (11)$$

where  $K_l = \alpha_l^2 / 2\sigma_l^2$ ,  $l = 01, 02$ , are Rician factor for  $R_{01}$  and  $R_{02}$  respectively,  $b = \sigma_{02}^2 / \sigma_{01}^2$ , and  $Q(x,y)$  is the Marcum's Q function. Without loss of generality we can assume that the signal is present in the first output branch of the detector, as well as one of the  $n$  interference tones that jam the signal tone. And we will assume also that

the rest  $n-1$  interference tones are in the next consecutive branches. Therefore,  $1^{st}$  to  $n^{th}$  output branches of the envelope detector will have their PDF follow Rician distributions and the output of the rest  $M-n$  branches will follow just a Rayleigh distribution. Furthermore, when the signal tone in the first output branch is jammed by an interference tone, the averaged LOS power in the output branch can be expressed as

$$\alpha_{sj}^2 = \alpha_s^2 + \alpha_j^2 + 2\alpha_s\alpha_j \cos \varphi \quad (12)$$

$\varphi$  is the random phase difference between received signal tone and interference tone and assumed to uniformly distributed between 0 to  $2\pi$ . So, the probability of symbol error given the signal tone is jammed can be calculated by

$$\begin{aligned} P_{sn}(e| \text{signal is jammed}) &= 1 - P(R_{01} > R_{02} \cap R_{01} > R_{03} \cap R_{01} > R_{04} \dots) \\ &= 1 - \prod_{k=2}^n P(R_{01} > R_{0k}) \prod_{j=n+1}^M P(R_{01} > R_{0j}) \\ &= 1 - P(R_{01} > R_{02})^{n-1} \cdot P(R_{01} > R_{0M})^{M-n} \quad (13) \end{aligned}$$

The second equality in (13) is obtained by using the fact that each output of the detector branches is independent of each other. Now, we will consider separately the first product term on RHS of the third equality in (13). For given  $\varphi$ , the conditional probability  $P(R_{01} > R_{02}|\varphi)$  can be evaluated easily by substituting the following parameters into (11)

$$\begin{aligned} K_{01} &= \frac{\alpha_{sj}^2}{2\sigma_s^2 + 2\sigma_j^2 + \sigma_n^2} \\ K_{02} &= \frac{\alpha_j^2}{2\sigma_j^2 + \sigma_n^2} \\ b &= \frac{2\sigma_j^2 + \sigma_n^2}{2\sigma_s^2 + 2\sigma_j^2 + \sigma_n^2} \quad (14) \end{aligned}$$

In the same manner, if we treat a Rayleigh random variable only as a special case for Rician random variable, we can also obtain the probability for the second product term with a condition on  $\varphi$  as

$$\begin{aligned} P(R_{01} > R_{0M}|\varphi) &= 1 - \frac{\sigma_n^2}{2(\sigma_s^2 + \sigma_j^2 + \sigma_n^2)} \\ &\quad \cdot \exp \left[ -\frac{\alpha_{sj}^2}{2(\sigma_s^2 + \sigma_j^2 + \sigma_n^2)} \right] \quad (15) \end{aligned}$$

Substituting (14) in (11) to obtain the conditional probability of the first product term, using (15) for the conditional probability of the second product term, and integrating (13) over  $\varphi$ , we then obtain the complete

expression for the symbol error probability for the case.

$$\begin{aligned} P_{sn}(e| \text{signal is jammed}) &= 1 - \frac{1}{2\pi} \int_0^{2\pi} \left\{ Q \left( \sqrt{\frac{\alpha_{sj}^2}{\sigma_T^2 + \sigma_j^2}}, \sqrt{\frac{\alpha_j^2}{\sigma_T^2 + \sigma_j^2}} \right) \right. \\ &\quad \left. - \frac{2\sigma_j^2 + \sigma_n^2}{2(\sigma_T^2 + \sigma_j^2)} \exp \left[ -\frac{\alpha_{sj}^2 + \alpha_j^2}{2(\sigma_T^2 + \sigma_j^2)} \right] \right. \\ &\quad \left. \cdot I_0 \left( \frac{2\alpha_{sj}\alpha_j}{\sigma_T^2 + \sigma_j^2} \right) \right\}^{n-1} \\ &\quad \cdot \left\{ 1 - \frac{\sigma_n^2}{2\sigma_T^2} \exp \left( -\frac{\alpha_{sj}^2}{2\sigma_T^2} \right) \right\}^{M-n-1} d\varphi \quad (16) \end{aligned}$$

where

$$\sigma_T^2 = \sigma_s^2 + \sigma_j^2 + \sigma_n^2 \quad (17)$$

### C. Probability of Symbol Error with $n$ Interference Tones Given The Signal Branch Is Not Jammed

When all  $n$  interference tones in the hop are not in signal branch,  $n+1$  output branches of the envelope detector will follow Rician distribution and the rest  $M-n-1$  branches will follow a Rayleigh distribution. Similarly, we will assume that the signal tone is present in the first output branch and each of the  $n$  interference tones is in the next consecutive branches. In this case the probability of symbol error can be expressed as

$$\begin{aligned} P_{sn}(e| \text{signal is not jammed}) &= 1 - P(R_{01} > R_{02} \cap R_{01} > R_{03} \cap R_{01} > R_{04} \dots) \\ &= 1 - \prod_{k=2}^{n+1} P(R_{01} > R_{0k}) \prod_{j=n+2}^M P(R_{01} > R_{0j}) \\ &= 1 - P(R_{01} > R_{02})^n \cdot P(R_{01} > R_{0M})^{M-n-1} \quad (18) \end{aligned}$$

Once again, the probability  $P(R_{01} > R_{02})$  for the third equality of (18) can be calculated by substituting the following parameters into (11)

$$\begin{aligned} K_{01} &= \frac{\alpha_s^2}{2\sigma_s^2 + \sigma_n^2} \\ K_{02} &= \frac{\alpha_j^2}{2\sigma_j^2 + \sigma_n^2} \\ b &= \frac{2\sigma_j^2 + \sigma_n^2}{2\sigma_s^2 + \sigma_n^2} \quad (19) \end{aligned}$$

and, by the same mean, the conditional probability for the second product term is found to be

$$\begin{aligned} P(R_{01} > R_{0M}) &= 1 - \frac{\sigma_n^2}{2(\sigma_s^2 + \sigma_n^2)} \exp \left[ -\frac{\alpha_s^2}{2(\sigma_s^2 + \sigma_n^2)} \right] \quad (20) \end{aligned}$$

To obtain the complete expression for the symbol error probability for the case, we then substitute (19) in (11) to obtain the probability of the first product term of (18) and use (20) for the probability of the second product term.

Finally, the symbol error probability for the case when signal branch is not jammed can be shown as follow, where  $\sigma_T^2$  is given in (17).

$$\begin{aligned}
P_{sn}(e| \text{signal is not jammed}) \\
= 1 - \left\{ Q \left( \sqrt{\frac{\alpha_s^2}{\sigma_T^2}}, \sqrt{\frac{\alpha_j^2}{\sigma_T^2}} \right) - \frac{2\sigma_j^2 + \sigma_n^2}{2\sigma_T^2} \right. \\
\left. \cdot \exp \left( -\frac{\alpha_s^2 + \alpha_j^2}{2\sigma_T^2} \right) I_0 \left( \frac{2\alpha_{sj}\alpha_j}{\sigma_T^2} \right) \right\}^n \\
\left\{ 1 - \frac{\sigma_n^2}{2(\sigma_s^2 + \sigma_n^2)} \exp \left[ -\frac{\alpha_s^2}{2(\sigma_s^2 + \sigma_n^2)} \right] \right\}^{M-n-1} \quad (21)
\end{aligned}$$

#### D. Probability of Symbol Error with $M$ Interference Tones

Once  $q \geq M$ , it is possible that we can have all  $M$  branches jammed by the interference tones and the probability of having  $M$  interference tones in a hop can be calculated easily by

$$P_M = \prod_{k=0}^{M-1} \left( \frac{q-k}{NM-k} \right) \quad (22)$$

With  $M$  interference tones, every output branch of the envelope detector will have their PDF's now followed only Rician distributions with the averaged LOS power equal to  $\alpha_j^2$ . An exception is made only for the branch where signal tone is also present, in which the averaged LOS power is equal to the summation of  $\alpha_s^2$  and  $\alpha_j^2$ , as shown previously in (12). Without loss of generality, we will also assume in here that the first detector output branch is one where the signal tone is present. Thus, the first output branch will have both the signal and an interference tone. In this case, the probability of symbol error can be found by

$$\begin{aligned}
P_{sM}(e|M \text{ int. tones}) \\
= 1 - P(R_{01} > R_{02} \cap R_{01} > R_{03} \cap R_{01} > R_{04} \dots) \\
= 1 - \prod_{k=2}^M P(R_{01} > R_{0k}) \\
= 1 - P(R_{01} > R_{0M})^{M-1} \quad (23)
\end{aligned}$$

The conditional probability  $P(R_{01} > R_{0M}|\varphi)$  of the squared term in the equation can be computed by applying same parameters in (14) to (11) and, in the end, we can obtain the probability of symbol error given  $M$  interference tones in the hop as

$$\begin{aligned}
P_{sM}(e|M \text{ int. tones}) \\
= 1 - \frac{1}{2\pi} \int_0^{2\pi} \left\{ Q \left( \sqrt{\frac{\alpha_{sj}^2}{\sigma_T^2 + \sigma_j^2}}, \sqrt{\frac{\alpha_j^2}{\sigma_T^2 + \sigma_j^2}} \right) \right. \\
\left. - \frac{2\sigma_j^2 + \sigma_n^2}{2(\sigma_T^2 + \sigma_j^2)} \exp \left[ -\frac{\alpha_{sj}^2 + \alpha_j^2}{2(\sigma_T^2 + \sigma_j^2)} \right] \right. \\
\left. I_0 \left( \frac{2\alpha_{sj}\alpha_j}{\sigma_T^2 + \sigma_j^2} \right) \right\}^{M-1} d\varphi \quad (24)
\end{aligned}$$

where  $\sigma_T^2$  can be calculated from (17). Finally, we can combine together every equation we have derived so far to compute for the total probability of symbol error. The probability of symbol error given  $n$  interference tones can be obtained first by substituting (16) and (21) into (10). Then, using the substitution result together with (9), (7), (5), (24), and (22) in (3), we will obtain the complete analysis for the probability of symbol error for FH/MFSK system with the independent multitone interference. And, we can easily convert it to the probability of bit error (BER) using (4).

### III. DEVELOPMENT OF A COMBINED INTERFERENCE MODEL FOR RURAL WIRELESS MESH NETWORK UNDER INFLUENCE OF A CO-EXISTING DSSS NETWORK

In this paper, we take on an example of the channel assignment for an NC-FH/MFSK rural infrastructure WMN with each router node being equipped with multiple radio interfaces. As previously suggested, these router nodes can also be implemented cost-efficiently using commercial IEEE 802.11 equipment whose cost is relatively low nowadays. In spite of how they are implemented, however, to establish the network, we assume that the router nodes are uniformly deployed over a rural region. So, the distances between nodes and their surrounding neighbors are not so different and, because they are rurally deployed, each node will have only a few neighbors surrounding them. Also, each node are assumed to be perfectly aware of its own coordinate position, which can be retrieved at any time from the memory inside the node. Furthermore, it is also assumed that the transmission powers and the gain of the antenna of each router node are known and these parameters are homogeneous for every node. Each node will be comprised of at least two different radio interfaces, one for a control channel and all the others for information channels. For an enhanced security during information transmissions, every interface designated for information are specifically chosen to be NC-FH/MFSK radio system while, for the controlling purpose, the interface can be of any radio systems other than the NC-FH/MFSK. Only important thing is that the two channel types must be operating on different frequency ranges so that they do not interfere with each other when simultaneously active.

In the entire communication bandwidth  $B_T$ , we assume that there are  $N$  FH bands available and, to achieve the greatest benefit of having multiple interfaces on nodes, we will divide the FH bands into  $b$  interleaving and non-colliding hopping patterns to enable concurrent links. Each hopping pattern thus contains equal number of  $N_p = N/b$  FH bands, each with  $M$  possible signal frequency bins. So, there will be the total of  $N_p M$  possible signal frequencies on any link. And, because these patterns are interleaving and non-colliding, a link in one hopping pattern will not interfere with that on the others. Hence, it is possible for the nodes with multiple NC-FH/MFSK interfaces to

support concurrent information links without having them interfering with each other, if the links are performed using different hopping patterns.

It can be observed that the hopping patterns here is, in fact, very similar to the radio channels in IEEE 802.11 a/b/g. Hence, the decision as to which hopping pattern is suitable for a specific link can also be determined by the CA algorithm similar to those in [11]-[14] at the setup phase of the network. Usually, the number of available hopping patterns is relatively low when compared to total number of possible links in the mesh, thus some of the links may need to be assigned to the same pattern and they will interfere with each other if being active simultaneously. It thus depends on the CA algorithm to recursively search for the most appropriate pattern for each link, i.e. the pattern that make the link less likely to interfere with the others. An ideal algorithm will therefore require to consider each link individually and evaluate the level of severity of the interference if the link is assigned with a pattern by taking into account the number of links previously assigned that pattern and possibly interfering with the current link. At the end, it should come across with the list of hopping patterns to be assigned to each link in order to reduce the amount of interferences in the entire mesh, i.e. increasing network capacity.

Because the main interest of this section is to propose an alternative application for the interference models we have previously derived, much of our attention is thus pointed toward the development for an appropriate interference model, which will be served in the CA algorithm to evaluate how severe links are interfered, and not the algorithm itself. Therefore, we will assume that the CA algorithm is already developed, such as the one proposed in [11], and we enhance it by introducing an appropriate interference model for estimating the link's BER. Note should be taken also that we have just defined the BER as a metric for measuring the severity of the interferences in our study.

We can observe that the transmission range is determined mainly by the BER requirement system and it will be the same for each router node because every node uses NC-FH/MFSK radio system for information links (same BER requirement) and the transmission power and the antenna gain are assumed homogeneous from node to node. At this point, we will assume that the BER requirement has already been specified and the transmission range covers approximately the distance of one hop. Besides, it is also assumed that the interference range is twice as far as the transmission range; it is, hence, equal to a two hop distance.

Since each mesh router is previously assumed to have a control channel, it is further assumed that the control channels of every router node are, by default, set to an encrypted common channel. So, after the router nodes are setup, they can instantly forward all their information (node IDs, coordinate locations, transmission powers, number of interfaces) to a pre-assigned center router node (PAC), who

will gather all the information and construct a map of the network and the Multiradio Conflict Graph (MCG) as defined in (for this paper, we assume any two links will interfere if they are within two-hop interference range). Then, PAC will execute the CA algorithm to assign hopping patterns to links of each routers starting from PAC itself then moving outward to those surrounding PAC within the first hop, the second hop, and so on (among those within the same hop distance from PAC, the algorithm will start at the closest node to PAC first). Once the assignment is ended, PAC then notifies all router nodes to set their radios accordingly.

After nodes receive the hopping patterns from the PAC, instead of applying them directly as the hopping sequence for each of the assigned link, nodes will randomly shuffle the FH bands within each hopping pattern again to acquire a new hopping sequence that is distinct. But, because one link involves two nodes, obviously only one node on the link should be performing the shuffling process, otherwise the hopping sequence between two nodes will not match and the link will never be formed. For our study, we assume the node with lower ID on the link will execute the shuffling process and then inform the new hopping sequence to other node via the control channel. At the completion of the process, the mesh is then formed and nodes will communicate accordingly. Thus far, we have already picked up some ideas about how the network operates and how the CA algorithm is used to assigned the hopping patterns. As an illustration of how interferences should be taken into account in the algorithm, let us consider an example scenario shown in Fig. 1.

In Fig. 1, six router nodes were used to setup a simple mesh network and each node is labeled corresponding to its name and number of its information interfaces, for example A-2 means node A is equipped with two NC-FH/MFSK interfaces. Here, we assumed that the total of  $N$  FH bands was divided into two hopping patterns and node A was chosen as the PAC node. After information of nodes had been forwarded, node A thus began to create the map and the MCG of the mesh. At the time being, we assumed that node A has already started running the CA algorithm and some of the links have already been assigned with hopping patterns;  $A \leftrightarrow B$  (the link between node A and node B) and  $C \leftrightarrow E$  are assigned to pattern 1 while  $A \leftrightarrow C$  and  $B \leftrightarrow D$  are allocated to pattern 2. The algorithm is now running for  $C \leftrightarrow F$  at node C.

First, let us consider if  $C \leftrightarrow F$  is to be assigned with pattern 1. Because the interference range was defined as the distance of two hop, every link of the two-hop neighbors of node C is thus considered a conflict link to  $C \leftrightarrow F$ ; namely  $A \leftrightarrow B$ ,  $A \leftrightarrow C$ ,  $B \leftrightarrow D$ , and  $C \leftrightarrow E$ . However, should  $C \leftrightarrow F$  be taken on pattern 1, the transmissions on  $A \leftrightarrow C$  and  $B \leftrightarrow D$  in pattern 2 no longer interfere with it; hence, the BER calculation should take into account only  $A \leftrightarrow B$  and  $C \leftrightarrow E$ , which use the same hopping pattern as  $C \leftrightarrow F$ . Let's now assume information is being transmitted as signal tones on

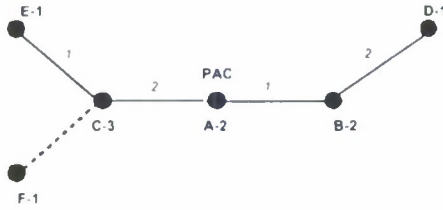


Fig. 1. An Example of Interferences in WMN.

NC-FH/MFSK systems from node F to node C and node A to node B. During the transmissions on the links, node E has also started to transmit information to node C using another interface of node C. Therefore, as a receiver, node C will pickup not only the desired signal tones from node E and F but also undesired interference tones from A. If we consider node C as a reference receiver (the algorithm is run for node C) and node F as a reference transmitter ( $C \leftrightarrow F$  is being considered), every tone transmitted from node F will be regarded as the desired signal tones to node C while the tones from node A and node E are just the interference tones or the jamming tones to the signal from node F to node C. Similarly, if  $C \leftrightarrow F$  is to be assigned with pattern 2,  $A \leftrightarrow C$  and  $B \leftrightarrow D$  is thus its conflict links. Node C is considered a reference receiver, as well as node F as a reference transmitter, and every tones transmitted from node F are desired signal tones, as oppose to those from node A and B, which are regarded as the jamming tones. Because hopping patterns of each link are further shuffled to make hopping sequences of each link distinct and independent from each other, therefore, it appears that the interference model for the independent MTJ in Section II has once again proven useful. Recalling from Section II, however, we can see that the interference model was developed, at that time, mainly based on the assumption that all interference tones are received with equal power and no two interference tones exist on the same frequency bin. But, from the situation in Fig. 1, it is obvious that, when  $C \leftrightarrow F$  is assigned with pattern 2, the interference tones from node A and node B will be received at different power due to their different distances from node C. Besides, the interference tone from node A and node B can also be transmitted on the same frequency bin because their hopping sequences are random and independent of each other.

If we consider the practical system configuration, for example, IEEE 802.11 (FH) equipment with 26 FH bands per pattern and FH/4FSK modulation (or 4-level Gaussian FSK), then it can be observed that the total number of frequency bins per pattern ( $N_p M = 104$ ) is actually quite large; in other word, there will be a lot of frequency bins, in which the interference tones can be transmitted. So, the probability of having interference tones being transmitted on the same frequency bin will be considerably small. Reasonably, we can then assume that no interference tones

are transmitted in the same frequency bins. Thus, the only restriction remaining is the requirement of having interference tones with equal power, with which we can easily cope by using an average of the power of every interference tone received.

As an example, let us consider again the case when  $C \leftrightarrow F$  is assigned with hopping pattern 2. In this case, the total number of independent interference tones ( $q_2$ ) for pattern 2 is equal two since there are two interference tones being received at node C; one from node A and the other from node B. The received powers of the signal tone from node F and the interference tones from node A and node B can be found by using the pathloss model, [12],

$$P_{kl} = K \frac{P_T}{d^2} \quad (25)$$

where  $d$  is the distance between transmitter and receiver node,  $P_{kl}$  is the received power of the signal transmitted from node  $k$  and received at node  $l$ , and  $P_T$  is the transmitted power. The constant  $K$  can be determined by the transmitting and receiving antenna gains and the wavelength of the transmitted signal. Since all these parameters are assumed to be known, therefore we can easily calculate the received power of interference tone from node A, ( $P_{AC}$ ), and node B, ( $P_{BC}$ ), using (25). Then, we can find the average received power of the interference tones at node C,  $P_{jC} = (P_{AC} + P_{BC})/2$ , and substitute necessary parameters as in Table I into the complete BER expression derived in Section II to obtain the estimate BER value. Note that  $K_1$  and  $K_2$  in Table I were set to 100dB, i.e. AWGN channel, since no fading channel was assumed in this section. In fact, fading channels can also be taken into account by changing the Rician factors correspondingly.

Due to the use of average power from various interference sources, clearly the BER resulted from this approach will be less accurate compared to one obtained by taking into account each interference tone individually. Yet, in the scope of this section, the BER is only used as a metric to illustrate how the link quality changes relatively when different subband is allocated. It is not how much, but how does the BER change that is actually matter. Though nearly of no meaning numerically, the result obtained is still proven useful in comparing the performances of the link.

Nevertheless, as an additional source of error, the interference from external network also play an important role in defining the quality of the link. To formulate the complete analysis for a mesh, not only must we consider the interferences among router nodes (intra-network interferences), but we need to account also for the interferences from the external networks. Obviously, the amount and form of the external interferences are different from site to site, depending on the types of radio and the frequency range often used in that area. For this paper, it is assumed that a site survey has been performed prior to the mesh installation and, because the prospective deployment site is in rural area, only one external network is found to be

TABLE I  
INPUT VALUES FOR CALCULATING BER OF WMN IN FIG. 1 (IF C→F  
IS TO BE ASSIGNED WITH PATTERN 2)

Variable	Definition	Value
$N$	Total FH bands in the pattern	$N_p$
$P_s$	Received power of signal tone	$P_{FC}$
$P_j$	Avg. received power of int. tone	$\frac{1}{2}(P_{AC} + P_{BC})$
$q$	Total int. tones in the pattern	$q = 2$
$K_1$	Rician factor for signal fading	100dB
$K_2$	Rician factor for int. fading	100dB

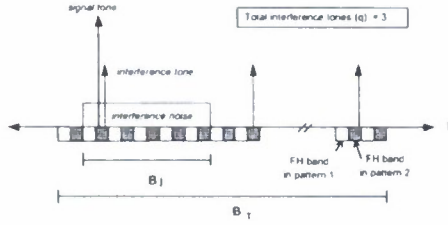


Fig. 2. A frequency-domain illustration of interference tones (intra-network interferences) and interference noise (external interference) of the mesh network with 2 hopping patterns.

co-existing on the site. Further, we assume the external network is a DSSS modulated network and it is occupying the fixed portion of our intended communication bandwidth. For example, if we are to use IEEE 802.11(FH) equipment on our mesh router, this external interfering network could be an IEEE 802.11b wireless local area network (WLAN), which is operating on a channel in 2.4 GHz frequency range. Depending on its location, each router node will receive the interference signal from this network with different received power but, because the site survey has already been performed, the interference power received at each node is assumed to be known to the PAC.

By the above statement, this external interference can then be modeled as an additive white Gaussian interference noise with a power of  $\sigma_{jk}^2$  being received at router node  $k$  of the mesh. If  $B_j$  and  $N_j$  is defined as the portion of the bandwidth and the number of FH bands jammed by the interference noise respectively, the jamming ratio can then expressed as  $\rho = B_j/B_T = N_j/N$ . The  $\sigma_{jk}^2$  for node  $k$  and  $B_j$  are known to the PAC via the site survey. When an FH band is jammed, we will assume that all of its  $M$  frequency bins is jammed. Nevertheless, it should also be noted that, because hopping patterns are established from the interleaving and non-colliding FH bands within the entire bandwidth  $B_T$ , each hopping pattern then share  $N_j$  jammed FH bands equally; therefore, the jamming ratio  $\rho_i$  of hopping pattern  $i$  will be the same as the network jamming ratio  $\rho$ .

Should no interference tone exist, the external interference noise will then be the only source of interference in the mesh and we can calculate the BER of the link easily. However, if the influence of the interference tones

is accounted, using the PBJ interference model alone is, apparently, inadequate. It is necessary that we must consider the interference tones and the interference noise all together. Therefore, a new interference analysis needs to be developed to combine together the errors caused by the interference tones and the interference noise.

For ease of representation, let us first define  $\underline{A}$  as the event that the signal hop is jammed by the interference noise and  $\underline{A}'$  as the complementary event or the event that the signal hop is not jammed by the interference noise. We can calculate the probability of symbol error by

$$P_s(e) = P(\underline{A}) \cdot P_s(e|\underline{A}) + P(\underline{A}') \cdot P_s(e|\underline{A}') \quad (26)$$

With the total of  $q_i$  interference tones from the conflict links using the same pattern  $i$ , the number of interference tones in a hop,  $n$ , can be a value within  $[0, \min(q_i, M)]$ . For ease of representation, we then define  $\underline{B}_0$  as the event when the hop is not jammed by interference tone ( $n = 0$ ),  $\underline{B}_M$  as the event when the hop is jammed by  $M$  interference tone ( $n = M$ ), and  $\underline{B}_n$  as the event when the hop is jammed by  $n$  interference tones where  $n \in [1, \min(q_i, M - 1)]$ . Now, if incorporated the effect of the interference tones, (26) can then be re-written as

$$\begin{aligned} P_s(e) &= P(\underline{A} \cap \underline{B}_0) \cdot P_s(e|\underline{A} \cap \underline{B}_0) \\ &+ P(\underline{A}' \cap \underline{B}_0) \cdot P_s(e|\underline{A}' \cap \underline{B}_0) \\ &+ \sum_{n=1}^L \{ P(\underline{A} \cap \underline{B}_n) \cdot P_s(e|\underline{A} \cap \underline{B}_n) \\ &+ P(\underline{A}' \cap \underline{B}_n) \cdot P_s(e|\underline{A}' \cap \underline{B}_n) \} \\ &+ \{ P(\underline{A} \cap \underline{B}_M) \cdot P_s(e|\underline{A} \cap \underline{B}_M) \\ &+ P(\underline{A}' \cap \underline{B}_M) \cdot P_s(e|\underline{A}' \cap \underline{B}_M) \} u(q_i - M) \\ &= \{ P(\underline{B}_0) \cdot P_s(e|\underline{A} \cap \underline{B}_0) \\ &+ \sum_{n=1}^L P(\underline{B}_n) \cdot P_s(e|\underline{A} \cap \underline{B}_n) \\ &+ P(\underline{B}_M) \cdot P_s(e|\underline{A} \cap \underline{B}_M) \cdot u(q_i - M) \} \cdot P(\underline{A}) \\ &+ \{ P(\underline{B}_0) \cdot P_s(e|\underline{A}' \cap \underline{B}_0) \\ &+ \sum_{n=1}^L P(\underline{B}_n) \cdot P_s(e|\underline{A}' \cap \underline{B}_n) \\ &+ P(\underline{B}_M) \cdot P_s(e|\underline{A}' \cap \underline{B}_M) \cdot u(q_i - M) \} \cdot P(\underline{A}') \end{aligned} \quad (27)$$

where  $u(q_i - M)$  denotes the unit step function and  $L$  equals  $\min(q_i, M - 1)$ . The second equality is obtained from the fact that the interference tones and the interference noise are independent, so event  $\underline{A}$  is independent from event  $\underline{B}_0$ ,  $\underline{B}_n$ , and  $\underline{B}_M$ .

Given a jamming ratio  $\rho_i$  for subband  $i$ ,  $P(\underline{A})$  and  $P(\underline{A}')$  can be calculated as  $\rho_i$  and  $(1 - \rho_i)$ , respectively. Also, using (5), (9), and (22),  $P(\underline{B}_0)$ ,  $P(\underline{B}_n)$ , and  $P(\underline{B}_M)$  can be calculated just by substituting parameters  $N$  and  $q$  with  $N_p$  and  $q_i$ . Now, The only terms to be considered are the probabilities of symbol error with conditions on

difference events, which can be evaluated easily using the analysis in Section II.

Consider first the event  $\underline{A}'$  when there is no interference noise in the hop. Without the external-network interference noise, AWGN will be the only noise corrupting the signal tone and the total noise power  $\sigma_T^2$  is thus equal to just  $\sigma_n^2$ . Therefore,  $P_s(e|\underline{A}' \cap \underline{B}_0)$ ,  $P_s(e|\underline{A}' \cap \underline{B}_n)$ , and  $P_s(e|\underline{A}' \cap \underline{B}_M)$  can be evaluated using exactly the same analysis in Section II. On the other hand, for the case of  $\underline{A}$  when the interference noise does exist, the total noise power in the hop will be the summation of AWGN power and the interference noise power, i.e.  $\sigma_T^2 = \sigma_n^2 + \sigma_{jk}^2$ . It should be noted, however, that, despite the total noise level in the hop, the two cases are very much alike. Consequently, we can use the same analysis in Section II with a simple change of parameter from  $\sigma_n^2$  to  $\sigma_T^2$  to calculate  $P_s(e|\underline{A}' \cap \underline{B}_n)$ , and  $P_s(e|\underline{A}' \cap \underline{B}_M)$ . Again, if no fading channel is assumed, the Rician factor  $K_1$  for the fading channel of the signal tone can be set to a very large value, e.g. 100dB. Otherwise, it must be set correspondingly to reflect the actual characteristic of the fading channel.

Finally, the complete BER value can be calculated just by substituting all the probability terms found into (27) and using (4) to convert the result. Then, based on the BER value, the CA algorithm will decide the most appropriate patterns for links and the mesh network with enhanced capacity will be formed correspondingly.

#### IV. CONCLUSIONS

In this paper, we studied the interference analysis in a NC-FH MFSK rural infrastructure WMNs with each router node being equipped with multiple radio interfaces. Our choice of the FH/MFSK modulation technique here is not just to satisfy the security requirement in military communications but also to provide easy implementation for each router nodes; since FH/MFSK modulation technique has been specified in IEEE 802.11 standard, these router nodes can be implemented also using IEEE 802.11(FH) equipments. The performances of noncoherent slow frequency-hopping system with  $M$ -ary frequency-shift-keyed modulation (NC-FH/MFSK) with AWGN channel and Rician fading under independent multitone jamming (independent MTJ) were investigated in this paper. The expressions for calculating the exact BER performances of the system under the effect of the jamming strategies are derived. We applied the analyses to channel assignment (CA) in multiradio rural WMNs. We obtained a new interference model combining interference tone and partial band noise, which would be incorporated into the CA algorithm to assign the most appropriate channel (or hopping pattern, in our case) to links in the mesh. Because it takes into account both the intra-network and the coexisting-network interferences, the new interference model thus reflects a very realistic interference situation in WMNs.

#### REFERENCES

- [1] I. F. Akyildiz, X. Wang, W. Wang, "Wireless mesh networks: a survey," *Computer Networks*, vol. 47, 2005, pp. 445-487.
- [2] M. Alichery, R. Bhatia, and L. Li, "Joint Channel Assignment and Routing for throughput optimization in Multi-Radio wireless mesh networks," *ACM MobiCom*, 2005.
- [3] S. Avallone, I. F. Akyildiz, "A Channel Assignment Algorithm for Multi-Radio Wireless Mesh Networks," *Computer Communications*, vol. 31, no. 7, May 2008, pp. 1343-1353.
- [4] G. Brar, et al, "Computationally Efficient Scheduling with the Physical Interference Model for Throughput Improvement in Wireless Mesh Networks," *ACM MobiCom*, 2006.
- [5] B. P. Crow, I. Widjaja, J. G. Kim, and P. T. Sakai, "IEEE 802.11 wireless local area networks," *IEEE Comm. Magazine*, vol. 35, no. 9, pp. 116-126, September 1997.
- [6] P. Kyasanur and N. H. Vaidya, Routing and Interface Assignment in Multi-Channel Multi-Interface Wireless Networks, *IEEE WCNC*, 2005, vol. 4, pp. 2051-2056.
- [7] A. Mishra, V. Shrivastava, S. Banerjee, and W. Arbaugh, "Partially overlapped channels not considered harmful," *ACM SIGMETRICS Performance Evaluation Review*, vol. 34, issue. 1, pp. 63-74, June 2006.
- [8] A. Raniwala and T. Chiuch, Architecture and Algorithms for an IEEE 802.11-Based Multi-Channel Wireless Mesh Network, *IEEE INFOCOM*, 2005, vol. 3, pp. 2223-2234.
- [9] R. C. Robertson and J. F. Sheltre, "Multitone interference of frequency-hopped noncoherent MFSK signals transmitted over Rician fading channels," *IEEE Trans Commun.*, vol. 44, no. 7, pp. 867-875, July 1996.
- [10] J. G. Proakis, *Digital Communications*, 2nd ed., New York: McGraw-Hill, 1989.
- [11] K. N. Ramachandran, E. M. Belding, K. C. Almeroth, and M. M. Buddhikot, "Interference-aware channel assignment in multi-radio wireless mesh networks," *Proc. of IEEE INFOCOM 2006*, pp. 1-12, April 2006.
- [12] M. Schwartz, *Mobile Wireless Communications*, Cambridge University Press, 2005.
- [13] A. P. Subramanian, H. Gupta, and S. R. Das "Minimum Interference Channel Assignment in Multi-Radio Wireless Mesh Networks," *IEEE SENCON*, 2007.
- [14] A. P. Subramanian, H. Gupta, S. R. Das, and J. Cao, "Minimum interference channel assignment in multiradio wireless mesh networks," *IEEE Trans. Mobile Computing*, vol. 7, no. 11, November 2008.
- [15] T. T. Tjhung and C. C. Chai, "Multitone jamming of FH/BFSK in Rician channels," *IEEE Trans Commun.*, vol. 47, no. 7, pp. 974-978, July 1999.
- [16] S. Lin and D. J. Castello, *Error Control Coding: Fundamentals and Applications*, Prentice Hall, Englewood Cliffs, NJ, 1983.
- [17] R. Steele, and W. Webb, "Variable rate QAM for data transmission over Rayleigh fading channels," *Wireless*, Calgary, Alberta, Canada: IEEE, 1991, pp. 1-14.
- [18] G. L. Stuber, "Principles of mobile communication" Boston: Kluwer Academic Publishers, 2001.
- [19] K. Xing, X. Cheng, L. Ma, and Q. Liang, "Superimposed code based channel assignment in multi-radio multi-channel wireless mesh networks," *ACM MobiCom '07*, Sept 2007, Montreal, Canada.
- [20] Z. Yu, "Multitone Jamming of FH/BFSK in Rician Channels," *IEEE Trans Commun.*, vol. 47, no. 7, pp. 974-978, July 1999.

# Passive Geolocation of RF Emitters by Netcentric Small Unmanned Aerial Systems (SUAS)

Jing Liang and Qilian Liang, *Senior Member, IEEE*

Department of Electrical Engineering

University of Texas at Arlington

Arlington, TX 76019-0016 USA

E-mail: jliang@wcn.uta.edu, liang@uta.edu

## Abstract

Conventional geolocation of RF emitters has adopted active triangulation methodology. One successful commercial example is satellite-based global positioning system (GPS). However the active localization in some cases can be extremely vulnerable especially for battlefield. In this paper, we design a netcentric Small Unmanned Aerial System (SUAS) for passive geolocation of RF emitters. Each small UAV is equipped with multiple Electronic Surveillance (ES) sensors to provide local mean distance estimation based on received signal strength indicator (RSSI). Fusion center will determine the location of the target through UAV triangulation. Different with previous existing studies, our method is on a basis of an empirical path loss and log-normal shadowing model, from a wireless communication and signal processing vision to offer an effective solution. The performance degradation between UAVs and fusion center is taken into consideration other than assume lossless communication. We analyze the geolocation error and the error probability of distance based on the proposed system. The result shows that this approach provides robust performance for high frequency RF emitters.

**Index Terms :** UAV, fading, geolocation, path-loss, log-normal shadowing

## 1 Introduction and Motivation

The precision geolocation of radio frequency (RF) emitters has been a long-standing subject and is now captured more attention in both electronic warfare and civilian applications, such as targeting military invaders and rescuing airplanes or ships sunk at sea. Among the traditional work of target detection and location, care has been taken on a basis of bearing-only measurements from the aspect of geometry [1]-[5] to determine the position, velocity and direction. There is no doubt that this bearing-based methodology such as Angel of Arrival (AOA) can be adopted in RF emitter geolocation, since RF emitter is in essence a target. On the other hand, RF emitters stand out from conventional targets as they are capable of sending out electromagnetic signals, which suggests the wireless communication and signal processing vision to offer the effective solution.

Conventionally, synthetic aperture radar (SAR), inverse synthetic aperture radar (ISAR) and moving target indicator (MTI) radar have been employed to provide situational awareness picture, such as localization of targets. Due to the principle that radars operate by radiating energy into space and detecting the echo signal reflected from the target [6], the vulnerability of active radars are obvious:

- Given transmitter and receiver, a radar systems is generally bulky, expensive and not easily portable
- Transmitter is easily detectable while in operation, thus draws unwanted attention of adversary
- Detection range is limited by the power of transmitter
- The transmission energy highly reduce the life of battery for MTI radars

Therefore, passive geolocation approaches are preferred.

Currently, there is a developing trend to use unmanned aerial vehicles (UAVs) for geolocation of RF emitters owing to better grazing angles closer to the target than large dedicated manned surveillance platforms [7]. In addition, UAVs are capable of continuous 24-hour surveillance coverage. As a result, they had been developed for battlefield reconnaissance beginning in the 1950s.

During the 1980s, all the major military powers and many of the minor ones acquired a battlefield UAV capability, and they are now an essential component of any modern army. Till now, UAV is not only limited to an unpiloted aircraft, but unmanned aerial systems (UAS) including ground stations and other elements as well.

Small unmanned aerial systems (SUAS) are rapidly gaining popularity due to the miniaturization of RF components and processors. In particular, given the cutting-edge technology in modern remote sensing (RS), SUAS can be equipped with Electronic Surveillance (ES) sensors in place of bulky active radars, which result in smaller, lighter and lower-cost counterparts. These types of SUAS are generally classified as having a wing-span of less than 4 meters [8] and a gross vehicle weight less than 15 pounds [9]. A number of UAV manufacturers have developed low-cost TDMA data links that support the cooperative team work of multiple UAVs, which provides higher mobility, survivability and closer proximity to the targeting emitters.

In the present work, [9] and [10] are based on a team of UAVs working cooperatively with on-board camera systems. The location of an object is determined by the fusion of camera images. However, the visual feature can become vulnerable in the following cases: 1)when telemetry and image streams are not synchronized, the target coordinates read by UAV can be particularly misleading; 2)when weather is severe and visibility is low, the image based geolocation may not provide day-or-night, all-weather surveillance; 3)target is well protected and hidden, such as deeply beneath the foliage.

Besides visual feature, the time difference of arrival (TDOA) technique has been adopted in the current work [11]-[15]. In these work, a network of at least three UAVs has been employed with on-board ES sensors, a global positioning system (GPS) receiver and a precision clock. When the target is detected by the sensor, the time of arrival would be transmitted to a fusion center, which would finally estimate the emitter location based on their TDOA. Also, Kalman filters is used to track the object. However, TDOA, like other methods including Angle of Arrival (AOA), Frequency of Arrival (FOA), Frequency Difference of Arrival (FDOA) and Phase Difference of Arrival (PDOA) etc., is well known for difficult synchronization issues, such as fine synchronization for geolocation algorithms and coarse synchronization for the coordinating data collected within the area of interest

at a common time.

In this paper, we apply netcentric SUAS with on-board multiple ES sensors for RF emitter geolocation. Different from previous work described above, our work describes about a complete system design and analyze the performance in detail. Our method is on a basis of an empirical pass loss and log-normal shadowing model, which has been adopted for reliable high-speed wireless communications for moving users in dynamic environment, but has never been used in the SUAS before, to the best of our knowledge. Also, the performance of multiple ES sensors will be considered for the system as a whole. In addition, we will provide a confidence assessment through error bounding, which has not been seen in the existing approaches.

The rest of paper is organized as follows. Section 2 describes about the system design including the emitter detection, path loss and log-normal shadowing approach and netcentric decision. Section 3 presents simulation results and performance analysis. Finally, section 4 draws the conclusion.

## 2 System Design Based on Path loss and Log-normal shadowing

### 2.1 Target Detection

Before UAVs cooperatively locating the RF emitter, it is necessary for them to understand whether targets are present in the range or not. Due to the randomness of dynamic environment, statistical model can be used to characterize the signal fluctuation. Herein threshold detection based on Bayesian's rule is adopted.

The Rayleigh distribution has been generally applied to describe the fluctuations of the amplitude over a short period of time or travel distance [16]. when there is no any RF emitter, moving UAVs will obtain scattered noise that reach the receiver by multipath, which can be denoted as

$$g(u) = g_I(u) + jg_Q(u) \quad (1)$$

where the envelope of received signal  $r = \sqrt{g_I^2(u) + g_Q^2(u)}$  obeys a Rayleigh distribution.  $g_I(u)$  and  $g_Q(u)$  are two independent quadrature Gaussian random variables with zero mean and variance  $\phi^2$ .

The probability density function (PDF) of the amplitude is

$$f(r) = \frac{r}{\phi^2} e^{-\frac{r^2}{2\phi^2}}, \quad \phi > 0 \quad (2)$$

When a RF emitter is present, its dominant signal component will contribute to a line-of-sight (LOS) propagation path, consequently the envelope in this case follows Rician distribution with PDF

$$f(r) = \frac{r}{\phi^2} e^{-\frac{r^2+s^2}{2\phi^2}} I_0\left(\frac{rs}{\phi^2}\right), \quad \phi > 0 \quad (3)$$

where  $I_0(\cdot)$  is the zero-order modified Bessel function and it is monotonically increasing for positive argument;  $s$  is the averaged RF signal amplitude.

Assume the presence of RF emitter is with probability  $0 < p < 1$ , then Bayesian's decision rule can be designed as

$$\frac{\frac{r}{\phi^2} e^{-\frac{r^2+s^2}{2\phi^2}} I_0\left(\frac{rs}{\phi^2}\right)}{\frac{r}{\phi^2} e^{-\frac{r^2}{2\phi^2}}} \begin{matrix} \text{emitter exists} \\ > \\ \text{no emitter} \end{matrix} \begin{matrix} 1-p \\ < \\ p \end{matrix} \quad (4)$$

Based on 4, the detection threshold turns out to be

$$T = \frac{\phi}{s} I_0^{-1}\left(\frac{1-p}{p}\right) e^{\frac{s^2}{2\phi}} \quad (5)$$

Therefore the probability of detection, i.e., the probability that the RF emitter be detected at its real presence can be expressed as

$$P_d = p\{r \geq T\} = \int_T^\infty \frac{r}{\phi^2} e^{-\frac{r^2+s^2}{2\phi^2}} I_0\left(\frac{rs}{\phi^2}\right) dr \quad (6)$$

The probability of false alarm can be denoted by

$$P_{fa} = p\{r \geq T\} = \int_T^\infty \frac{r}{\phi^2} e^{-\frac{r^2}{2\phi^2}} dr = e^{-\frac{T^2}{2\phi^2}} \quad (7)$$

## 2.2 Path Loss and Log-normal shadowing Approach

In our work, we assume the SUAS is composed of  $R(R \geq 3)$  small UAVs. Each UAV is equipped with  $N(N \geq 1)$  ES sensors, whose task is to provide Received Signal Strength Indicator (RSSI) of RF emitters. A processor is also on-board to compute the current distance from the RF emitter to the sensors based on RSSI. Notice that even though the computation can be achieved in a very fast time on a basis of detected RSSI, estimated distance poses drifts from the real distance due to the relative motion between the UAV and the RF emitter as well as wind gusts during the moment of computation. Thus multiple sensors are employed to provide the receiver diversity. Later we will

show that multiple sensors help reduce the distance error and improve the geolocation performance. The processor also applies Equal Gain Combining (EGC) to average out local spatial variations within a UAV. EGC is adopted due to its simplicity and fast computation. Additionally, each UAV works independently and knows its own position either by a GPS receiver or pre-planned paths. Also, it is capable of communicating with a fusion center, which makes a final geolocation decision based on the information given by multiple UAVs.

Assume an emitter is sending out RF signal and a UAV  $d$  distance away from it detected the signal at this moment. The signal propagating between these two points with no attenuation or reflection follows the free-space propagation law [17]. This commonly adopted path loss model as a function of distance is expressed as

$$\frac{P(d)}{P(d_0)} = \gamma \left( \frac{d}{d_0} \right)^{-\beta} \quad (8)$$

where  $d_0$  is a close-in distance used as a known received power reference point;  $\beta$  is the path-loss exponent depending on the propagation environment.  $\gamma$  is a unitless constant that depends on the antenna characteristics and the average channel attenuation, which can be defined as

$$\gamma_{dB} = 20 \lg \frac{C}{4\pi f d_0} \quad (\lg = \log_{10}) \quad (9)$$

where  $C$  is the speed of light and  $f$  denotes the frequency. This definition is supported by empirical data for free-space path loss at a transmission distance of 100m [18]. Based on this free-space model, the power in dB form is linearly decreasing with the increase of  $\log(d)$ , as illustrated by the straight dash line in Fig. 1.

However, in practice, the reflecting surfaces and scattering objects will typically contribute to the random variation of RF signal transmission. The most common model for this additional attenuation is log-normal shadowing, which has been empirically confirmed to model accurately the variation in received power in both outdoor [19] and indoor [20] environments. In this case, the difference between the value predicted by the path loss model and the actual power is a log-normal random variable, i.e., normally distributed in dB, which is denoted by

$$\left[ \frac{P(d)}{P(d_0)} \right]_{dB} = \left[ \frac{\hat{P}(d)}{P(d_0)} \right]_{dB} + X \quad (10)$$

where  $X$  is a Gaussian random variable, with mean  $m$  and variance  $\sigma^2$ .

We will use the combined path loss and log-normal shadowing model to estimate the distance between RF emitter and a UAV through RSSI. This model is illustrated in Fig. 1 with a dotted curve. The power in dB is given by

$$\left[\frac{P_{ri}}{P(d_0)}\right]_{dB} = 10lg\gamma - 10\beta lg\left(\frac{\hat{d}_i}{d_0}\right) + X \quad (11)$$

where  $P_{ri}$  is the RSSI of ES sensor  $i$ . Based on (11), when  $P_{ri}$  is detected, the processor can easily compute  $\hat{d}_i$  in a dB form, which is

$$\hat{d}_{idB} = \frac{1}{\beta} \{ \gamma_{dB} + \beta d_{0dB} - [\frac{P_{ri}}{P(d_0)}]_{dB} \} + \frac{X}{\beta} \quad (12)$$

Notice that  $d_{idB} = \frac{1}{\beta} \{ \gamma_{dB} + \beta d_{0dB} - [\frac{P_{ri}}{P(d_0)}]_{dB} \}$ , therefore

$$\hat{d}_{idB} - d_{idB} = \frac{X}{\beta} \quad (13)$$

Then it is obvious that the expectation of distance mean square error based on sensor  $i$  is

$$E\{(\hat{d}_{idB} - d_{idB})^2\} = \frac{m^2 + \sigma^2}{\beta^2} \quad (14)$$

$N$  sensors equipped on a UAV are applied to compute the local mean distance that average the local spatial variations. The estimated local mean distance is

$$\hat{D} = \frac{1}{N} \sum_{i=1}^N \hat{d}_{idB} \quad (15)$$

This value is obtained based on dB measurement due to the smaller estimation error compared to the linear form [21].

Notice that  $D = d_{dB}$ . At the detection moment, UAV is  $d$  distance away from the RF target, i.e.,  $d_{idB} = d_{dB}$ . Also, each sensor independently obtains the  $\hat{d}_{idB}$ , i.e.,  $\hat{d}_{idB} - d_{idB}$  can be considered independent for different  $i$ , thus the expectation of *distance mean square error* for each UAV can be expressed as

$$E\{(\hat{D} - D)^2\} = \frac{m^2 + \sigma^2}{N^2 \beta^2} \quad (16)$$

This shows that based on path loss and log-normal model, the larger number of sensor  $N$ , the smaller distance mean square error will be achieved for each UAV.

As each UAV geolocates RF emitter only based on RSSI and there is no any information about phase, in this situation the current detected area at the moment can be denoted by  $a = \pi d^2$ . If  $a$  is denoted by dB form, then  $A = 10\lg\pi + 2D$ , therefore the expectation of *area mean square error* for each UAV is

$$P_A = E\{(A - \hat{A})^2\} = 4E\{(D - \hat{D})^2\} = \frac{4(m^2 + \sigma^2)}{N^2\beta^2} \quad (17)$$

Finally the upper bound of *geolocation area mean square error* of a UAV network can be denoted by

$$P_e = P(\bigcup_{i=1}^R A_i) \leq \sum_{i=1}^R P_{A_i} = \frac{4R(m^2 + \sigma^2)}{N^2\beta^2} \quad (18)$$

We show this upper bound in Fig. 2, where  $R = 3, m = 0, \beta = 2$  are used for illustration.

Apart from geolocation performance, we also define *distance range probability* as the probability that the estimated local mean distance  $\hat{D}$  falls within  $D_1 \leq \hat{D} \leq D_2$ , where  $D_1 < D_2$  and  $D_1, D_2$  are also in dB form. The corresponding linear form of  $\hat{D}, D_1$  and  $D_2$  are  $\hat{d}, d_1$  and  $d_2$  respectively.

In order to simplify the expression, we would like to denote

$$S_i = \frac{1}{\sigma} \{ \gamma_{dB} + [\frac{P(d_0)}{P_r}]_{dB} - \beta D_i + \beta d_{0dB} \}, \quad i = 1, 2 \quad (19)$$

It's obvious that  $S_2 < S_1$ . Therefore the distance range probability turns out to be

$$P(D_1 \leq \hat{D} \leq D_2) = \begin{cases} Q(S_2) - Q(-S_1) = Q(S_2) + Q(S_1) - 1 & \text{if (a) } S_1 \leq 0 \text{ or (b) } 0 < S_1 < -S_2 \\ Q(-S_1) - Q(S_2) = 1 - Q(S_1) - Q(S_2) & \text{if (c) } 0 \leq -S_2 < S_1 \text{ or (d) } S_2 > 0 \end{cases} \quad (20)$$

where the Q-function is defined as the probability that a Gaussian random  $Z$  is greater than  $x$ :

$$Q(x) = p(Z > x) = \int_x^\infty \frac{1}{\sqrt{2\pi}} e^{-\frac{y^2}{2}} dy \quad (21)$$

The (a)-(d) situations are illustrated in the Fig. 3. It's worth mentioning that  $P(D_1 \leq \hat{D} \leq D_2) = P(d_1 \leq \hat{d} \leq d_2)$ . When  $D_1$  and  $D_2$  are set to be values pretty close to  $D$ , (20) turns out to be the probability of correct distance range.

Based on our previous analysis, it's obvious that

$$\hat{D} = D + \frac{X}{N\beta} \quad (22)$$

When the relative motion between UAV and the emitter is very slow, the mean of  $\frac{X}{N\beta}$ , i.e.,  $l = \frac{m}{N\beta}$  can be considered zero because the mean may be considered to describe the average discrepancies in real and estimated distance between the RF emitter and the UAV during the moment of computation. Also, for simplicity and clarity, we use  $\eta$  to denote the variance of  $\frac{X}{N\beta}$ , which is  $\frac{\sigma^2}{N^2\beta^2}$ . Therefore, the probability of estimation that RF emitter locate in the range  $[D_1, D_2]$  by a single UAV becomes

$$\begin{aligned} P_{cs}(D_1, D_2) &= \int_{D_1}^{D_2} P(D_1 \leq \hat{D} \leq D_2) f_N(u) du \\ &= \int_{D_1}^{D_2} P(D_1 \leq \hat{D} \leq D_2) \frac{1}{\sqrt{2\pi\eta}} e^{-\frac{(u-D)^2}{2\eta^2}} d\hat{D} \\ &= P(D_1 \leq \hat{D} \leq D_2) [Q(\frac{D_1 - D}{\eta}) - Q(\frac{D_2 - D}{\eta})] \end{aligned} \quad (23)$$

When the relative motion between the UAV and the RF emitter is obvious, due to the random variation, even the mean can be considered as a variable which follows uniform distribution in the range  $[L_1, L_2]$  (in dB form), where  $L_1 < D_1 - D$  and  $L_2 > D_2 - D$ . In this case, the probability of RF emitter locating in the range  $[D_1, D_2]$  by a single UAV becomes

$$\begin{aligned} P_{cm}(D_1, D_2) &= \int_{D_1}^{D_2} P(D_1 \leq \hat{D} \leq D_2) \int_{L_1}^{L_2} \frac{1}{\sqrt{2\pi\eta}} e^{-\frac{(u-D-v)^2}{2\eta^2}} \cdot \frac{1}{L_2 - L_1} dv du \\ &= \frac{P(D_1 \leq \hat{D} \leq D_2)}{L_2 - L_1} [\int_{L_1}^{L_2} Q(\frac{D_1 - D - v}{\eta}) - \int_{L_1}^{L_2} Q(\frac{D_2 - D - v}{\eta})] dv \end{aligned} \quad (24)$$

### 2.3 Netcentric Decision

As soon as each UAV obtains its distance from the RF emitter, this data will immediately be sent to a fusion center through TDMA data links. The fusion center can be a ground station or even mounted on one of the UAVs. Due to the shadowing and multipath, the signal sent by a UAV will encounter fading before arriving at the fusion center. Assume the instantaneous signal-to-noise ratio (SNR) is  $y$ , the statistical averaging probability of error over the fading distribution [22] is

$$P_{e.m.f} = \int_0^\infty P_m(y) p_f(y) dy \quad (25)$$

where  $P_m(y)$  is the probability of symbol error in AWGN based on a certain modulation scheme and  $p_f(y)$  denotes the PDF of the fading amplitude.

Apply the moment generating function (MGF)  $M_f(s) = \int_0^\infty p_f(y)e^{sy}dy$  and alternate Q-function  $Q(x) = \frac{1}{\pi} \int_0^{\pi/2} e^{-\frac{x^2}{2\sin^2\varphi}} d\varphi$ , we derive the probability of symbol error for the UAV network using 4 most common modulation schemes: phase-shift keying (MPSK), pulse amplitude modulation (MPAM), quadrature amplitude modulation (MQAM) and noncoherent frequent-shit keying (MFSK) respectively as follows:

$$P_{e\_MPSK\_f} = \frac{1}{\pi} \int_0^{\frac{(M-1)\pi}{M}} M_f\left(-\frac{\sin^2(\pi/M)}{\sin^2\varphi}\right) d\varphi \quad (26)$$

$$P_{e\_MPAM\_f} = \frac{2(M-1)}{\pi M} \int_0^{\frac{\pi}{2}} M_f\left(\frac{-3}{\sin^2\varphi(M^2-1)}\right) d\varphi \quad (27)$$

$$P_{e\_MQAM\_f} = \frac{4}{\pi} \left(\frac{\sqrt{M}-1}{\sqrt{M}}\right) \int_0^{\frac{\pi}{2}} M_f\left(-\frac{3}{2(M-1)\sin^2\varphi}\right) d\varphi \\ - \frac{4}{\pi} \left(\frac{\sqrt{M}-1}{\sqrt{M}}\right)^2 \int_0^{\frac{\pi}{4}} M_f\left(-\frac{3}{2(M-1)\sin^2\varphi}\right) d\varphi \quad (28)$$

$$P_{e\_MFSK\_f} = \sum_{n=1}^{M-1} \binom{M-1}{n} \frac{1}{n+1} M_f\left(-\frac{n}{n+1}\right) \quad (29)$$

When the channel is Rician fading with factor  $K$ , after derivation the detailed expression of (26)-(29) are as follows respectively:

$$P_{e\_MPSK\_Rician} = \frac{1+K}{\pi} \int_0^{\frac{(M-1)\pi}{M}} \frac{\sin^2\varphi \cdot \exp\left[-\frac{yK\sin^2(\pi/M)}{y\sin^2(\pi/M) + (1+K)\sin^2\varphi}\right]}{y\sin^2(\pi/M) + (1+K)\sin^2\varphi} d\varphi \quad (30)$$

$$P_{e\_MPAM\_Rician} = \frac{2(1+K)(M-1)}{\pi M} \int_0^{\pi/2} \frac{\sin^2\varphi \cdot \exp\left\{-\frac{3Ky}{(M^2-1)\left[\frac{3y}{M^2-1} + (1+K)\sin^2\varphi\right]}\right\}}{\frac{3y}{M^2-1} + (1+K)\sin^2\varphi} d\varphi \quad (31)$$

$$P_{e\_MQAM\_Rician} = \frac{4(\sqrt{M}-1)(1+K)}{\pi\sqrt{M}} \int_0^{\pi/2} \frac{\sin^2\varphi \cdot \exp\left\{-\frac{3Ky}{2(M-1)\left[\frac{3y}{M^2-1} + (1+K)\sin^2\varphi\right]}\right\}}{\frac{3y}{2(M-1)} + (1+K)\sin^2\varphi} d\varphi \\ - \frac{4(1+K)}{\pi} \left(\frac{\sqrt{M}-1}{\sqrt{M}}\right)^2 \int_0^{\pi/4} \frac{\sin^2\varphi \cdot \exp\left\{-\frac{3Ky}{2(M-1)\left[\frac{3y}{M^2-1} + (1+K)\sin^2\varphi\right]}\right\}}{\frac{3y}{2(M-1)} + (1+K)\sin^2\varphi} d\varphi \quad (32)$$

$$P_{e\_MFSK\_Rician} = \sum_{n=1}^M (-1)^{n+1} \binom{M-1}{n} \frac{1}{n+1} \cdot \frac{1+K}{1+K+\frac{ny}{n+1}} \exp\left\{\frac{-K\frac{ny}{n+1}}{1+K+\frac{ny}{n+1}}\right\} \quad (33)$$

To simplify the (30)-(33), two extreme cases are taken into account. When the Rician fading factor  $K \rightarrow 0$ , it becomes Rayleigh distribution, therefore (30)-(33) can be denoted using following expressions in this case:

$$P_{e\_MPSK\_Ray} = 1 - \sqrt{\frac{y \sin^2(\frac{\pi}{M})}{1 + y \sin^2(\frac{\pi}{M})}} \quad (34)$$

$$P_{e\_MPAM\_Ray} = \frac{M-1}{M} \cdot \left(1 - \sqrt{\frac{\frac{3y}{M^2-1}}{1 + \frac{3y}{M^2-1}}}\right) \quad (35)$$

$$\begin{aligned} P_{e\_MQAM\_Ray} = & \frac{2(\sqrt{M}-1)}{\sqrt{M}} \left(1 - \sqrt{\frac{\frac{3y}{2(M-1)}}{1 + \frac{3y}{2(M-1)}}}\right) - 4\left(\frac{\sqrt{M}-1}{\sqrt{M}}\right)^2 \\ & \cdot \left[\frac{1}{4} - \frac{1}{\pi} \sqrt{\frac{\frac{3y}{2(M-1)}}{1 + \frac{3y}{2(M-1)}}} \arctg \sqrt{\frac{1 + \frac{3y}{2(M-1)}}{\frac{3y}{2(M-1)}}}\right] \end{aligned} \quad (36)$$

$$P_{e\_MFSK\_Ray} = \sum_{n=1}^{M-1} (-1)^{n+1} \binom{M-1}{n} \frac{1}{n+1} \left(1 + \frac{n}{n+1}y\right)^{-1} \quad (37)$$

When  $K \rightarrow \infty$ , the Rician fading channel becomes AWGN channel. In this situation, the probability of symbol error based on above modulation schemes have been well studied and the result is provided in [17], Table 6.1.

According to these performance, the best modulation scheme can be chosen to reduce the probability of error. This will be further illustrated in Section 3 by simulations.

For simplicity and clarity, we assume the RF emitter is on the ground surface. In the case that the relative motion between the RF emitter and UAVs are quite slow, the UAV  $a$  is able to be aware that the RF emitter is somewhere on a circle, of which the center is itself and the radius is  $d_a$ , as illustrated in Fig. 4(a). Another UAV  $b$  can also identify that there is a RF emitter on a circumference with radius  $d_b$ . After combining the information from both  $a$  and  $b$ , the fusion center will be aware that the target either locates at the position A or B. With the help of a third UAV

$c$ , the fusion center will have the knowledge that the RF emitter is at the position  $A$ . Therefore with the triangulation, 3 UAVs are able to locate the RF emitter on the ground. In the case that the target is above the ground, 4 UAVs are necessary with one more member providing altitude geolocation information.

When the relative movement between the target and UAVs are obvious,  $a$  and  $b$  will aware that the RF emitter is moving within a ring area, and the fusion system will understand that the target is within the intersection of 2 rings. Suppose the intersection area is  $\widehat{abc}$  (the intersection can also be 2 independent areas, here we use one case for illustration without loss of generality), shown in Fig. 4(b). When the data from  $c$  is obtained, its detected range ring will intersect with  $\widehat{abc}$  in a line  $\overline{DE}$ . Therefore, the trace of the RF emitter  $DE$  will be successfully obtained. After a few numbers of measurement, the motion speed, acceleration of the target can be calculated based on range and time difference.

Due to the independence of the distance estimation by each UAV and the transmission of data to the fusion center, the probability that a single UAV accurately provides the geolocation information to the fusion center is  $P_{cs}(D_1, D_2) \cdot (1 - P_{e\_MPSK\_f})$  or  $P_{cm}(d_1, d_2) \cdot (1 - P_{e\_MPSK\_f})$  for different relative motion situations, where  $D_1, D_2$  and  $d_1, d_2$  are close to  $D$  and  $d$  respectively. Therefore, the probability of error for the netcentric SUAS made up of 3 UAVs can be denoted as

$$P_{es} \leq 1 - [P_{cs}(D_1, D_2) \cdot (1 - P_{e\_MPSK\_f})]^3 \quad (38)$$

$$P_{em} \leq 1 - [P_{cm}(d_1, d_2) \cdot (1 - P_{e\_MPSK\_f})]^3 \quad (39)$$

The above expressions are error upper bound, this is because the netcentric decision provides much more resilience than a single UAV. For example, in Fig. 4(a) assume UAV  $a$  and  $b$  accurately geolocate the target while  $c$  has a large location error and believes the target is far away from the point  $A$  and  $B$ , the whole system may still provide accurate estimation if  $c$  determines that the target is closer to  $A$  compared with  $B$ . Demanding every UAV to provide accurate information to fusion center is a stringent rule, therefore (38) and (39) are upper bounds.

### 3 Simulation Results and Performance Analysis

Simulations on a basis of mathematical expressions in Section 2 are presented in this Section for better analysis and illustration about SUAS performance. In the simulation, we assume  $d = 100m$ ,  $d_0 = 0.1d$  and  $\beta = 2$ .

Fig. 5 describes about error probability of distance range vs. frequency for a single UAV, where  $d_1 = 0.99d$  and  $d_2 = 1.01d$  have been used. The curves show that given the same  $\sigma$  (see (10)), the error probability of distance range will be reduced as the frequency increases. However, when the frequency is higher than a certain threshold value, such as  $10^8$  for  $\sigma = 10$ , the error probability becomes a constant. This phenomenon is the result of nonlinearity of the Q function. Therefore, this UAV system is more appropriate for geolocate an emitter with higher frequency.

Fig. 6 shows the contribution of another important factor power-rate-to-noise ratio (PRNR) to the correct probability of distance range for a single UAV. We define PRNR as  $\frac{P(d_0)}{\sigma P_r}$ . It is easy to observe that similar to Fig. 5, there is also a threshold value in correct probability of distance range. The larger the  $\eta$  (see (22)), the smaller the threshold value as well as the probability correctness.

Fig. 7-10 illustrate upper bound error probability for netcentric UAVs based on (38) and (39). Fig. 7 and 8 are in the environment of AWGN while Fig. 9 and 10 are for Rayleigh fading. In the case that relative motion between the RF emitter and UAVs are slow,  $d_1 = 0.99d$ ,  $d_2 = 1.01d$  and  $\eta = 1$ ; when the relative motion is obvious we apply  $l_1 = -0.1d$ ,  $l_2 = 0.1d$  and  $\eta = 1$ , therefore  $P_{cs}(D_1, D_2) = 0.9876$  and  $P_{cm}(D_1, D_2) = 0.94$ . In Figs. 7 and 9, modulation schemes MFSK, MPAM, MPSK and MQAM with  $M = 4$  are applied for illustration. This does not mean  $M = 2$  can not be used. Actually, the smaller  $M$ , the smaller probability of symbol error rate for the same modulation scheme. That partially contributes to the smaller probability of error in Fig. 8. Moreover, the resilience of netcentric design makes the probability of error using BFSK and BPSK much smaller compared to that of 4-FSK and QPSK. This is the same situation while comparing Fig. 10 with 9.

These figures show that no matter the wireless radio channel between UAVS and fusion center is AWGN or Rayleigh, MQAM will provide the smallest probability of error at low SNR while MPSK will provide the smallest probability of error at moderate to high SNR. Therefore MQAM

and MPSK can be applied for adaptive modulation for data fusion depending on how large is the SNR at the receiver of fusion center.

## 4 Conclusions

In this work, we propose a passive geolocation approach to locate RF emitter using a netcentric small UAV systems (SUAS) equipped with ES sensors. This approach is based on log-normal shadowing model, which has been empirically confirmed to model accurately the variation in received power in propagation environments. We show that the geolocation error is essentially a log-normal random variable. The larger number of ES sensors, the smaller geolocation area upper bound error. We also analyze the error probability of distance range for the system. We demonstrate that when the emitter frequency is higher than a certain threshold value, the error probability becomes a constant. The situation is similar for power-rate-to-noise ratio (PRNR). Regardless what the wireless radio channel between UAVS and fusion center is, for example AWGN, Rayleigh or Rician, at low SNR MQAM modulation is applied while MPSK will be chosen at moderate to high SNR due to the smallest performance error of the whole system.

## Acknowledgement

This work was supported in part by Office of Naval Research (ONR) under Grant N00014-07-1-0395, N00014-07-1-1024, and National Science Foundation (NSF) under Grant CNS-0721515.

## References

- [1] A. G. Lindgren and K. F. Gong, "Position and velocity estimation via bearing-only observations", *IEEE Trans. Aerosp. Electron. Syst.*, vol. 14, pp. 564-577, July 1978.
- [2] S. C. Nardone, A.G. Lindgren and K.F. Gong, "Fundamental properties and performance of conventional bearing-only target motion analysis", *IEEE Trans. Automat. Contr.*, vol. 29, pp. 775-787, Sept. 1984.

- [3] M. Gavish and A. J. Weiss, "Performance analysis of bearing-only target location algorithm", *IEEE Trans. Aerosp. Electron. Syst.*, vol. 26, pp. 22-26, Oct. 1992.
- [4] V. J. Aidala and S. E. Hammel, "Utilization of modified polar coordinates for bearing-only tracking", *IEEE Trans. Automat. Contr.*, vol. 28, pp. 283-294, March 1983.
- [5] J. P. Le Cadre and C. Jauffret, "On the convergence of iterative methods for bearing-only tracking", *IEEE Trans. Aerosp. Electron. Syst.*, vol. 34, pp. 179-193, Jan. 1998.
- [6] M. I. Skolnik, *Introduction to Radar Systems*, 3rd ed, New York, McGraw Hill, 2001.
- [7] K. C. Overman, K. A. Leahy, T. W. Lawrence and R. J. Fritsch, "The future of surface surveillance - revolutionizing the view of the battlefield", *IEEE International Radar Conf.*, pp.1-6, May 2000.
- [8] D. Ledger, "Electronic warfare capabilities of mini UAVs", [http://aerosonde.com.au/downloads/electronic\\_warfare\\_ledger.doc](http://aerosonde.com.au/downloads/electronic_warfare_ledger.doc)
- [9] R. Madison, P. DeBitetto, A. R. Olean and M. Peebles, "Target Geolocation from a Small Unmanned Aircraft System", *2008 IEEE Aerospace Conference*, pp. 1-19, March 2008.
- [10] M. Wheeler, B. Schrick, W. Whitacre, M. Campbell, R. Rysdyk and R. Wise, "Cooperative Tracking of Moving Targets by a Team of Autonomous UAVs", *2006 IEEE/AIAA 25th Digital Avionics Systems Conference*, pp. 1-9, Oct. 2006.
- [11] N. Okello, "Emitter Geolocation with Multiple UAVs", *2006 9th International Conference on Information Fusion*, pp. 1-8, July, 2006.
- [12] N. Okello and D. Musicki, "Measurement Association for emitter geolocation with two UAVs", *2007 10th International Conference on Information Fusion*, pp. 1-8, July 2007.
- [13] L. Marsh, D. Gossink, S. P. Drake and G. Calbert, "UAV Team Formation for Emitter Geolocation", *Information, Decision and Control, 2007, IDC'07*, pp. 176-181, Feb. 2007.

- [14] A. Mikhalev and R. F. Ormondroyd, "comparison of hough transform and particle filter methods of emitter geolocation using fusion of TDOA Data", *4th Workshop on Positioning, Navigation and Communication 2007, WPNC'07*, pp.121-127.
- [15] F. Fletcher, B. Ristic, D. Musicki, "Recursive estimation of emitter location using TDOA measurements from two UAVs", *2007 10th International Conference on Information Fusion*, pp. 1-8, July 2007.
- [16] T. S. Rappaport, *Wireless Communications: Principles and Practice*, 2nd ed., Upper Saddle River, NJ: Prentice-Hall, 2002.
- [17] A. Goldsmith, *Wireless Communications*, Cambridge University Press, NJ 2001.
- [18] V. Erceg, L. J. Greenstein, S. Y. Tjandra, S. R. Parkoff, A. Gupta, B. Kulic, A. A. Julius, and R. Bianchi, "An empirically based path loss model for wireless channels in suburban environments", *IEEE J. Sel. Areas Commun.*, pp. 1205-11, July 1999.
- [19] V. Erceg, L. J. Greenstein, S. Y. Tiandra, S. R. Parkoff, A. Gupta, B. Kulic, A. A. Julius, and R. Bianchi, "An empirically based path loss model for wireless channels in suburban environments", *IEEE J. Sel. Areas Commun.*, pp. 1205-1211, July 1999.
- [20] S. S. Ghassemzadeh, L. J. Greenstein, A. Kavcic, T. Sveinsson, and V. Tarokh, "Indoor path loss model for residential and commercial buildings", *Proc. IEEE Veh. Tech. Conf.*, pp. 3115-3119, Oct. 2003.
- [21] A. J. Goldsmith, L. J. Greenstein and G. J. Foschini, "Error statistics of real-time power measurements in cellular channels with multipath and shadowing", *IEEE Trans. Veh. Tech.*, pp. 439-446, August, 1994.
- [22] M. K. Simon and M.-S. Alouini, *Digital Communication over Fading Channels*, 2nd, Wiley, New Jersey, 2005.

## List of Figures

1	Path loss, shadowing vs. distance. . . . .	17
2	Upper bound of geolocation area mean square error for a UAV network. . . . .	17
3	Distance range probability illustration based on Q function: (a) $S_1 \leq 0$ (b) $0 < S_1 < -S_2$ (c) $0 \leq -S_2 < S_1$ (d) $S_2 > 0$ . . . . .	18
4	RF emitter Geolocation by SUAS (a) Relative movement between RF emitter and UAVs are slow (b) Relative movement between RF emitter and mini UAVs are obvious. . . . .	18
5	Error probability of distance range vs. frequency for a single UAV. . . . .	19
6	Correct probability of distance range vs. power-rate-to-noise ratio (PRNR) for a single UAV. . . . .	19
7	Upper error bound of the netcentric UAVs in AWGN when relative movement between the RF emitter and UAVs are slow. . . . .	20
8	Upper error bound of the netcentric UAVs in AWGN when relative movement between the RF emitter and UAVs are obvious. . . . .	20
9	Upper error bound of the netcentric UAVs in Rayleigh fading when relative movement between the RF emitter and UAVs are slow. . . . .	21
10	Upper error bound of the netcentric UAVs in Rayleigh fading when relative movement between the RF emitter and UAVs are obvious. . . . .	21

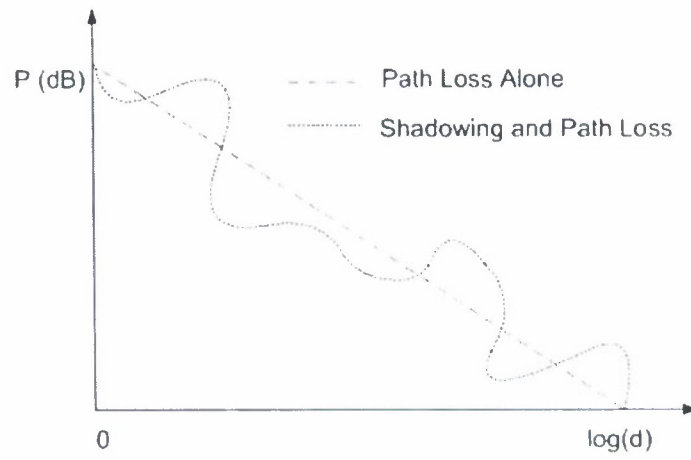


Figure 1: Path loss, shadowing vs. distance.

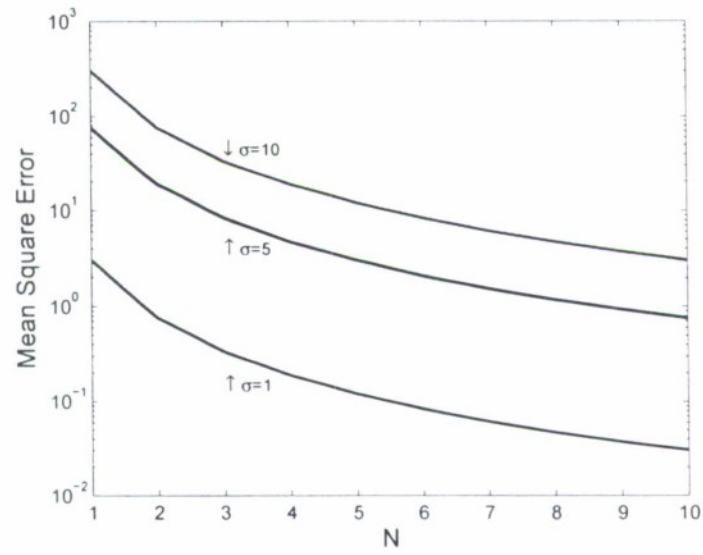


Figure 2: Upper bound of geolocation area mean square error for a UAV network.

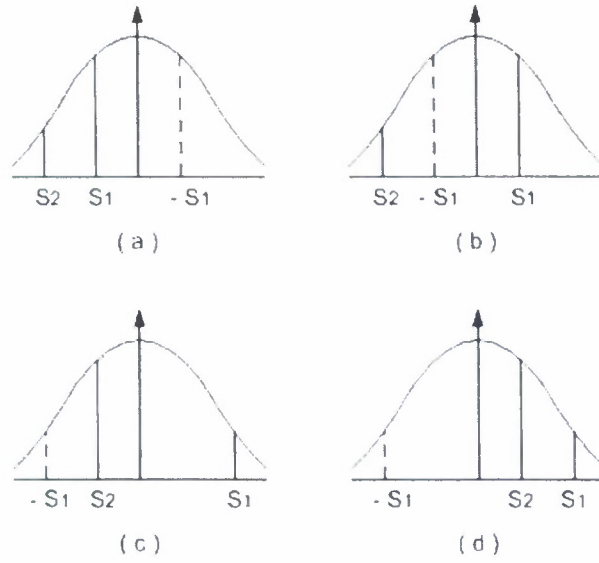


Figure 3: Distance range probability illustration based on Q function: (a)  $S_1 \leq 0$  (b)  $0 < S_1 < -S_2$  (c)  $0 \leq -S_2 < S_1$  (d)  $S_2 > 0$ .

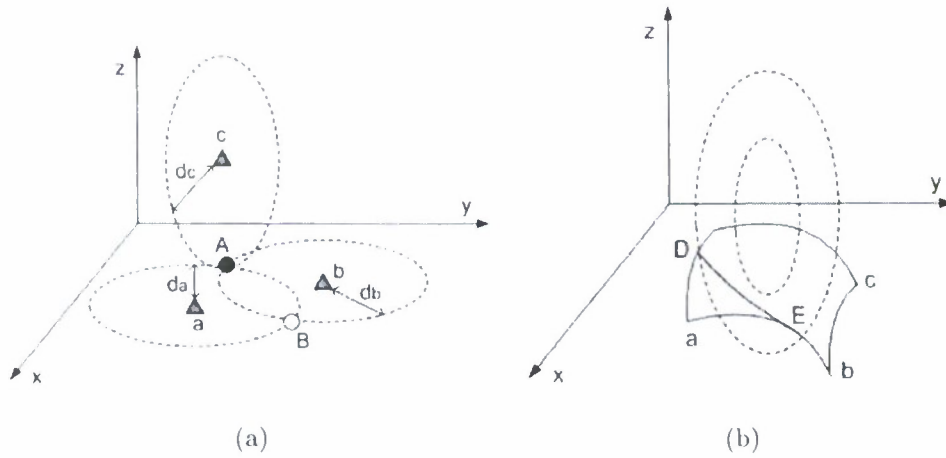


Figure 4: RF emitter Geolocation by SUAS (a) Relative movement between RF emitter and UAVs are slow (b) Relative movement between RF emitter and mini UAVs are obvious.

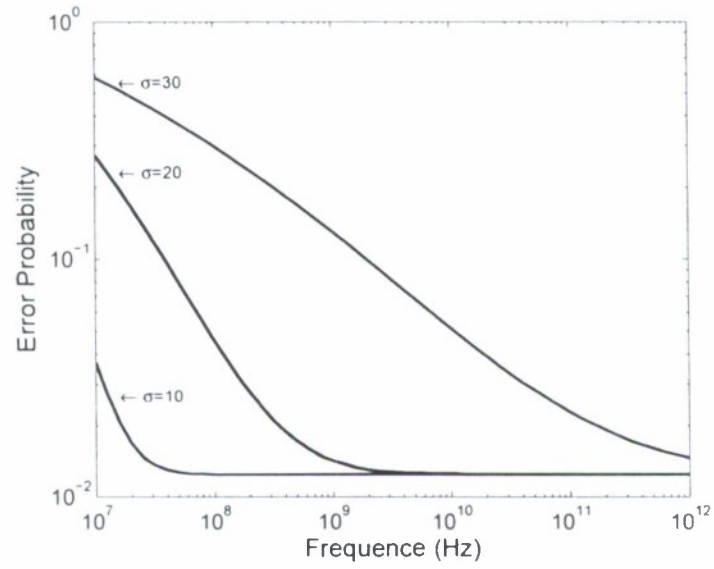


Figure 5: Error probability of distance range vs. frequency for a single UAV.

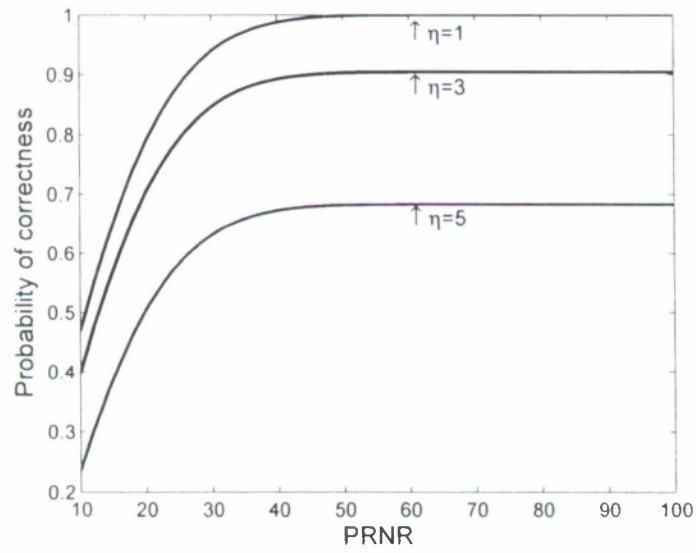


Figure 6: Correct probability of distance range vs. power-rate-to-noise ratio (PRNR) for a single UAV.

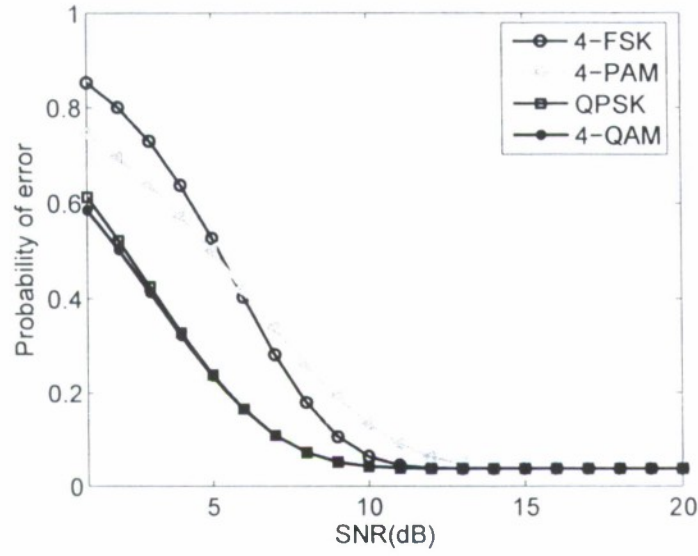


Figure 7: Upper error bound of the netcentric UAVs in AWGN when relative movement between the RF emitter and UAVs are slow.

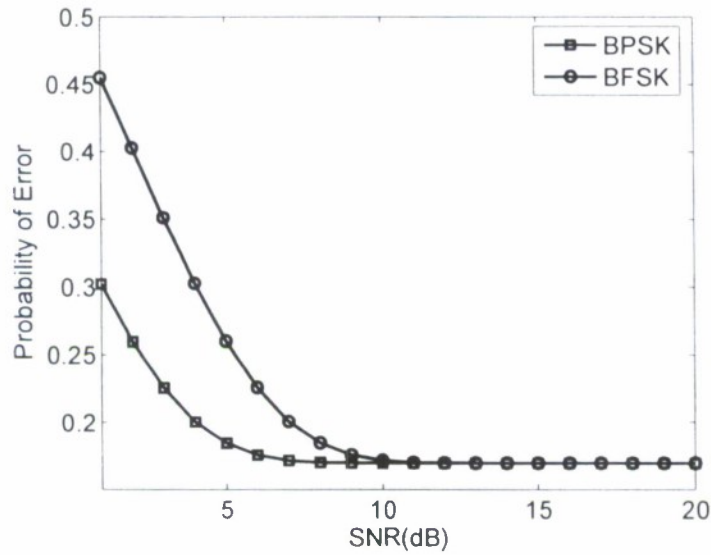


Figure 8: Upper error bound of the netcentric UAVs in AWGN when relative movement between the RF emitter and UAVs are obvious.

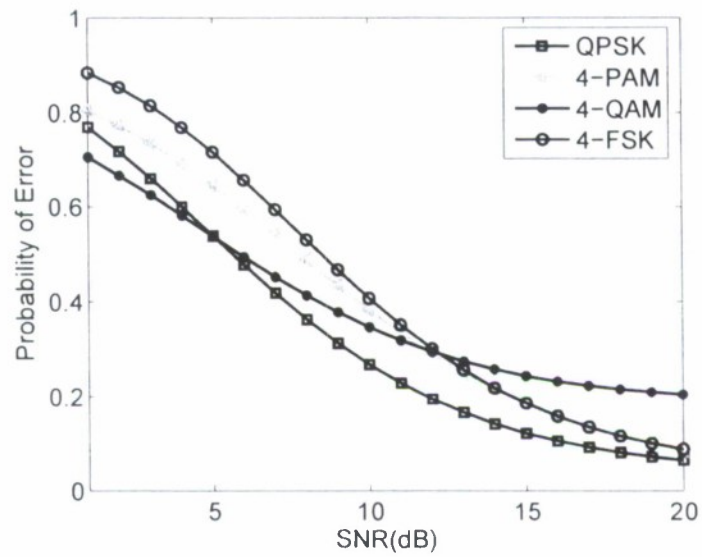


Figure 9: Upper error bound of the netcentric UAVs in Rayleigh fading when relative movement between the RF emitter and UAVs are slow.

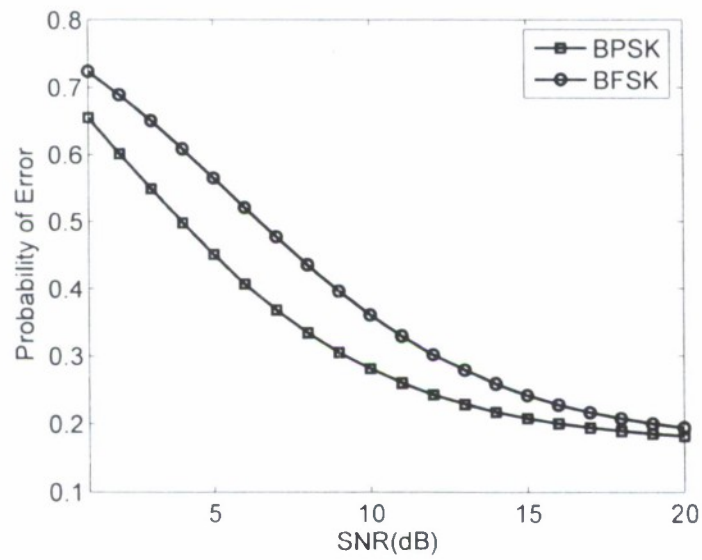


Figure 10: Upper error bound of the netcentric UAVs in Rayleigh fading when relative movement between the RF emitter and UAVs are obvious.

# Orthogonal Pulse Compression Codes for MIMO Radar System

Lei Xu and Qilian Liang, *Senior Member, IEEE*

Department of Electrical Engineering

University of Texas at Arlington

Arlington, TX 76010-0016 USA

Email: xu@ecn.uta.edu, liang@uta.edu

## Abstract

Inspired by recent advances in MIMO radar, we introduce orthogonal pulse compression codes to MIMO radar system in order to gain better target direction finding performance. We propose the concept and the design methodology for the optimized triphase phase coded waveforms that is the optimized punctured Zero correlation Zone (ZCZ) sequence-Pair Set (ZCZPS). The method is to use the optimized punctured sequence-pair along with Hadamard matrix in the ZCZ. According to codes property analysis, our proposed phase coded waveforms could provide optimized autocorrelation and cross correlation properties in ZCZ. Then we present a generalized MIMO radar system model using our proposed codes and simulate the target direction finding performance in the system. The simulation results show that diversity gain could be obtained using our orthogonal pulse compression codes for MIMO radar system. The more antennas used, the better target direction finding performance provided.

**Index Terms :** MIMO radar, orthogonal, optimized punctured ZCZ sequence-pair, phase coded waveform

## 1 Introduction

The previous work [1] [2] [3] showed that processing data from a radar network with spatially distributed nodes could offer significant performance improvement, as a result, there has been considerable interest in MIMO radars which employ multiple antennas both at the transmitter and at the receiver. The present important research of MIMO radar includes all kinds of techniques, such as waveform design [4] [5] [6], ambiguity function [8], patternform syntheses [9][10], detection and localization performance analysis [4]-[10], space-time adaptive signal processing, direction finding, etc. In [5], the authors design covariance matrix of the probing signal vector transmitted by the radar to achieve the desirable features of a MIMO radar system. The desirable features could be to choose freely the probing signals transmitted via its antennas to maximize the power around the locations of the targets of interest, more generally to approximate a given transmit beam pattern, and also to minimize the cross-correlation of the signals reflected back to the radar by the targets of interest. In [6], they also propose a cyclic optimization algorithm for the synthesis of a given optimal covariance matrix  $R$  under various practical constraints to construct signals which also have good auto- and cross- correlation properties in time. In addition, based on investigating target detection and parameter estimation techniques for a multiple-input multiple-output (MIMO) radar system, the authors [11] propose an alternative estimation procedure, referred to as the combined Capon and approximate maximum likelihood (CAML) method which can provide excellent estimation accuracy of both target locations and target amplitudes. In [12], the authors provide a review of some recent work on computing the Cramer-Rao lower bound (CRLB) on the achievable localization accuracy by using the geometric dilution of precision (GDOP) as a tool for assessing and illustrating the localization accuracy of the Best Linear Unbiased Estimator (BLUE).

Apart from the work mentioned above, direction finding [13] [14] is such a technology that a well known waveform is transmitted by an omnidirectional antenna, and a target reflects some of the

transmitted energy toward an array of sensors that is used to estimate some unknown parameters, e.g. bearing, range, or speed. Also, beamforming [15] is another important process generally used in direction finding process that an array of receivers can steer a beam toward any direction in space. The advantages of using an array of closely spaced sensors at the receiver are the lack of any mechanical elements in the system, the ability to use advanced signal processing techniques for improving performance, and the ability to steer multiple beams at once. In this paper, we will focus on the direction finding performance of the MIMO radar system.

MIMO radars, unlike phased array radars, transmit different waveforms on the different antennas of the transmitter, which makes it necessary to do the waveform design for the system. Some researchers have already done some work on the MIMO radar using orthogonal waveforms [16], partial correlation waveforms [10] or the more general non-orthogonal set of waveforms [17][18][19]. Nevertheless, in this paper, we design a set of new triphase orthogonal waveforms for the MIMO radar system using the pulse compression technology. To the best of our knowledge, it is the first time to introduce pulse compression codes to MIMO radar system to improve the direction finding performance. Pulse compression, known as a technique to raise the signal to maximum sidelobe (signal-to-sidelobe) ratio to improve the target detection and range resolution abilities of the radar system, allows a radar to simultaneously achieve the energy of a long pulse and the resolution of a short pulse without the high peak power [28]. A generalized MIMO radar signal model using our triphase orthogonal pulse compression codes is analyzed and the simulation results show that better performance could be obtained by combining MIMO radar and pulse compression codes together.

The rest of the paper is organized as follows. Section 2 introduces the definition and properties of ZCZPS as well as a set of specific ZCZPS which is the optimized punctured ZCZPS. A method using optimized punctured sequence-pair and Hadamard matrix to construct ZCZPS is also given and proved. Section 3 presents and analyzes a generalized MIMO radar system for our proposed

codes. In section 4, some simulation results are provided by using specific examples with different number of uniform linear antennas at the transmitter and receiver of MIMO radar system. In Section 6, conclusions are drawn on our newly provided orthogonal pulse compression codes and MIMO radar system.

## 2 Orthogonal Pulse Compression Codes

A set of orthogonal pulse compression codes could be used in the MIMO radar system to gain the diversity and improve the direction finding performance. In this section, we will propose and analyze the concept and design methodology for a new triphase coded waveforms which could be applied to MIMO radar system.

### 2.1 The Definition and Properties of ZCZ sequence-Pair Set

Here, we introduce sequence-pair into the ZCZ concept to construct ZCZPS. We consider ZCZPS  $(\mathbf{X}, \mathbf{Y})$ ,  $\mathbf{X}$  to be a set of  $K$  sequences of length  $N$  and  $\mathbf{Y}$  to be a set of  $K$  sequences of the same length  $N$ :

$$\mathbf{x}^{(p)} \in \mathbf{X} \quad p = 0, 1, 2, \dots, K-1 \quad (1)$$

$$\mathbf{y}^{(q)} \in \mathbf{Y} \quad q = 0, 1, 2, \dots, K-1 \quad (2)$$

The autocorrelation function for sequence-pair  $(\mathbf{x}^p, \mathbf{y}^p)$  is defined by:

$$R_{\mathbf{x}^{(p)}\mathbf{y}^{(p)}}(\tau) = \sum_{i=0}^{N-1} x_i^{(p)} y_{(i+\tau) \bmod N}^{(p)*}, 0 \leq \tau \leq N-1 \quad (3)$$

The cross correlation function for sequence-pair  $(\mathbf{x}^p, \mathbf{y}^q)$ ,  $p \neq q$  is defined by:

$$C_{\mathbf{x}^{(p)}\mathbf{y}^{(q)}}(\tau) = \sum_{i=0}^{N-1} x_i^{(p)} y_{(i+\tau) \bmod N}^{(q)*}, 0 \leq \tau \leq N-1 \quad (4)$$

$$C_{\mathbf{x}^{(q)}\mathbf{y}^{(p)}}(\tau) = \sum_{i=0}^{N-1} x_i^{(q)} y_{(i+\tau) \bmod N}^{(p)*}, 0 \leq \tau \leq N-1 \quad (5)$$

For pulse compression sequences, some properties are of particular concern in the optimization for any design in engineering. They are the peak sidelobe level, the energy of autocorrelation sidelobes and the energy of their mutual cross correlation [26]. Therefore, the peak sidelobe level which represents a source of mutual interference and obscures weaker targets can be presented as  $\max_K |R_{x^p y^p}(\tau)|, \tau \in Z_0$  (zero correlation zone) for ZCZPS. Another optimization criterion for the set of sequence-pair is the energy of autocorrelation sidelobes joined together with the energy of cross correlation. By minimizing the energy, it can be distributed evenly, and the peak autocorrelation level can be minimized as well [26]. Here, the energy of ZCZPS can be employed as:

$$E = \sum_{p=0}^{K-1} \sum_{\tau=1}^{Z_0} R_{\mathbf{x}^{(p)} \mathbf{y}^{(p)}}^2(\tau) + \sum_{p=0}^{K-1} \sum_{q=0}^{K-1} \sum_{\tau=0}^{N-1} C_{\mathbf{x}^{(p)} \mathbf{y}^{(q)}}(\tau) \quad (6)$$

$(p \neq q)$

According to (6), it is obvious to see that the energy can be kept low while minimizing the autocorrelation and cross correlation of the sequence-pair set.

Then, the ZCZPS can be constructed to minimize the autocorrelation and cross correlation of the sequence-pair set and the definition of ZCZPS can be expressed:

**Definition 2-1** Assume  $(\mathbf{x}_i^{(p)}, \mathbf{y}_i^{(p)})$  to be sequence-pair set of length  $N$  and the number of sequence-pair  $K$ , where  $p = 1, 2, 3, \dots, N-1, i = 0, 1, 2, \dots, K-1$ , if all the sequences in the set satisfy the following equation:

$$R_{\mathbf{x}^{(p)} \mathbf{y}^{(q)}}(\tau) = \sum_{i=0}^{N-1} x_i^{(p)} y_{(i+\tau) \bmod(N)}^{(q)*} = \sum_{i=0}^{N-1} y_i^{(p)} x_{(i+\tau) \bmod(N)}^{(q)*}$$

$$= \begin{cases} \lambda N, & \text{for } \tau = 0, p = q \\ 0, & \text{for } \tau = 0, p \neq q \\ 0, & \text{for } 0 < |\tau| \leq Z_0 \end{cases} \quad (7)$$

where  $0 < \lambda \leq 1$ , then  $(x_i^{(p)}, y_i^{(p)})$  is called a ZCZ sequence-Pair,  $ZCZP(N, K, Z_0)$  is an abbreviation, and  $(\mathbf{X}, \mathbf{Y})$  is called a ZCZ sequence-Pair Set,  $ZCZPS(N, K, Z_0)$  is an abbreviation.

## 2.2 Definition and Design for Optimized Punctured ZCZ Sequence-Pair Set

Matsufuji and Torii have provided some methods of constructing ZCZ sequences in [23] [24]. In this section, a novel triphase coded waveform, namely the optimized punctured ZCZ sequence-pair set, is constructed through applying the optimized punctured sequence-pair [25] to the zero correlation zone. In some other words, optimized punctured ZCZPS is a specific kind of ZCZPS.

**Definition 2-2** [25] Sequence  $\mathbf{u} = (u_0, u_1, \dots, u_{N-1})$  is the punctured sequence for  $\mathbf{v} = (v_0, v_1, \dots, v_{N-1})$ ,

$$u_j = \begin{cases} 0, & \text{if } u_j \text{ is punctured} \\ v_j, & \text{if } u_j \text{ is Non-punctured} \end{cases} \quad (8)$$

Where  $p$  is the number of punctured bits in sequence  $\mathbf{v}$ , suppose  $v_j \in (-1, 1)$ ,  $u_j \in (-1, 0, 1)$ ,  $\mathbf{u}$  is  $p$ -punctured binary sequence,  $(\mathbf{u}, \mathbf{v})$  is called a punctured binary sequence-pair.

**Definition 2-3** [25] The autocorrelation of punctured sequence-pair  $(\mathbf{u}, \mathbf{v})$  is defined

$$R_{\mathbf{uv}}(\tau) = \sum_{i=0}^{N-1} u_i v_{(i+\tau) \bmod N}, 0 \leq \tau \leq N-1 \quad (9)$$

If the punctured sequence-pair has the following autocorrelation property:

$$R_{\mathbf{uv}}(\tau) = \begin{cases} E, & \text{if } \tau \equiv 0 \bmod N \\ 0, & \text{otherwise} \end{cases} \quad (10)$$

the punctured sequence-pair is called optimized punctured sequence-pair [25]. Where,  $E = \sum_{i=0}^{N-1} u_i v_{(i+\tau) \bmod N} = N - p$ , is the energy of punctured sequence-pair.

If  $(x_i^{(p)}, y_i^{(p)})$  in Definition 2-1 is constructed by optimized punctured sequence-pair and a certain matrix, such as Hadamard matrix or an orthogonal matrix, where

$$x_i^{(p)} \in (-1, 1), \quad i = 0, 1, 2, \dots, N-1$$

$$y_i^{(q)} \in (-1, 0, 1), \quad i = 0, 1, 2, \dots, N-1$$

$$R_{\mathbf{x}^{(p)}\mathbf{y}^{(q)}}(\tau) = \sum_{i=0}^{N-1} x_i^{(p)} y_{(i+\tau) \bmod N}^{(q)*} = \sum_{i=0}^{N-1} y_i^{(p)} x_{(i+\tau) \bmod N}^{(q)*}$$

$$= \begin{cases} \lambda N, & \text{for } \tau = 0, p = q \\ 0, & \text{for } \tau = 0, p \neq q \\ 0, & \text{for } 0 < |\tau| \leq Z_0 \end{cases} \quad (11)$$

where  $0 < \lambda \leq 1$ , then  $(x_i^{(p)}, y_i^{(p)})$  can be called optimized punctured ZCZ sequence-pair set. Based on odd length optimized punctured binary sequence pairs and a Hadamard matrix, an optimized punctured ZCZPS can be constructed on following steps:

**Step 1:** Considering an odd length optimized punctured binary sequence-pair  $(\mathbf{u}, \mathbf{v})$ , the length of each sequence is  $N_1$

$$\mathbf{u} = u_0, u_1, \dots, u_{N_1-1}, u_i \in (-1, 1),$$

$$\mathbf{v} = v_0, v_1, \dots, v_{N_1-1}, v_i \in (-1, 0, 1),$$

$$i = 0, 1, 2, \dots, N_1 - 1, N_1 \text{ odd}$$

**Step 2:** A Hadamard matrix  $B$  of order  $N_2$  is considered. The length of the sequence of the matrix is  $N_2$  which is equal to the number of the sequences. Here, any Hadamard matrix order is possible and  $\mathbf{b}^i$  is the row vector.

$$\mathbf{B} = [\mathbf{b}^0; \mathbf{b}^1; \dots; \mathbf{b}^{N_2-1}],$$

$$\mathbf{b}^i = (b_0^i, b_1^i, \dots, b_{N_2-1}^i),$$

$$R_{\mathbf{b}^i, \mathbf{b}^j} = \begin{cases} N_2, & \text{if } i = j \\ 0, & \text{if } i \neq j \end{cases}$$

**Step 3:** Perform bit-multiplication on the optimized punctured binary sequence-pair and each

line of Walsh sequences set B (Hadamard matrix), then sequence-pair set  $(X, Y)$  is obtained,

$$\mathbf{b}^i = (b_0^i, b_1^i, \dots, b_{N_2-1}^i), i = 0, 1, \dots, N_2 - 1,$$

$$x_j^i = u_{j \bmod N_1} b_{j \bmod N_2}^i, 0 \leq i \leq N_2 - 1, 0 \leq j \leq N - 1,$$

$$\mathbf{X} = (\mathbf{x}^0, \mathbf{x}^1, \dots, \mathbf{x}^{N_2-1}),$$

$$y_j^i = v_{j \bmod N_1} b_{j \bmod N_2}^i, 0 \leq i \leq N_2 - 1, 0 \leq j \leq N - 1,$$

$$\mathbf{Y} = (\mathbf{y}^0, \mathbf{y}^1, \dots, \mathbf{y}^{N_2-1})$$

Since most of optimized punctured binary sequence-pairs are of odd lengths and the lengths of Walsh sequence are  $2^n, n = 1, 2, \dots$ , most of  $GCD(N_1, N_2) = 1$ , common divisor of  $N_1$  and  $N_2$  is 1,  $N = N_1 * N_2$ . If  $GCD(N_1, N_2) \neq 1$ ,  $N$  should be the least common multiple  $lcm(N_1, N_2)$ . The construction method for the case of  $GCD(N_1, N_2) \neq 1$  should be similar to  $GCD(N_1, N_2) = 1$ , so we would only consider the case of  $GCD(N_1, N_2) = 1$  in this paper. The sequence-pair set  $(\mathbf{X}, \mathbf{Y})$  is optimized punctured ZCZPS and  $N_1 - 1$  is the zero correlation zone  $Z_0$ . The length of each sequence in optimized punctured ZCZPS is  $N = N_1 * N_2$  that depends on the product of length of optimized punctured sequence-pair and the length of Walsh sequence in Hadamard matrix. The number of sequence-pair in optimized punctured ZCZPS rests on the order of the Hadamard matrix. The sequence  $\mathbf{x}^i$  in sequence set  $\mathbf{X}$  and the corresponding sequence  $\mathbf{y}^i$  in sequence set  $\mathbf{Y}$  construct a sequence-pair  $(\mathbf{x}^i, \mathbf{y}^i)$  that can be used as a pulse compression code.

The correlation property of the sequence-pair in optimized punctured ZCZPS is:

$$\begin{aligned} R_{\mathbf{x}^i, \mathbf{y}^j}(\tau) &= R_{\mathbf{x}^j, \mathbf{y}^i}(\tau) = R_{\mathbf{uv}}(\tau \bmod N_1) R_{\mathbf{b}^i, \mathbf{b}^j}(\tau \bmod N_2) \\ &= R_{\mathbf{uv}}(\tau \bmod N_1) R_{\mathbf{b}^j, \mathbf{b}^i}(\tau \bmod N_2) \\ &= \begin{cases} EN_2, & \text{if } \tau = 0, i = j \\ 0, & \text{if } 0 < |\tau| \leq N_1 - 1, i = j \\ 0, & \text{if } i \neq j \end{cases} \end{aligned} \quad (12)$$

where  $N_1 - 1$  is the zero correlation zone  $Z_0$ .

Proof:

1) When  $i = j$ ,

$$\tau = 0,$$

$$R_{\mathbf{uv}}(0) = E, R_{\mathbf{b}^i \mathbf{b}^j}(0) = N_2,$$

$$R_{\mathbf{x}^i \mathbf{y}^j}(0) = R_{\mathbf{uv}}(0) R_{\mathbf{b}^i \mathbf{b}^j}(0) = EN_2;$$

$$0 < |\tau| \leq N_1 - 1,$$

$$R_{\mathbf{uv}}(\tau) = 0,$$

$$R_{\mathbf{x}^i \mathbf{y}^j}(\tau) = R_{\mathbf{uv}}(\tau \bmod N_1) R_{\mathbf{b}^i \mathbf{b}^j}(\tau \bmod N_2) = 0;$$

2) When  $i \neq j$ ,

$$\tau = 0,$$

$$R_{\mathbf{b}^i \mathbf{b}^j}(0) = 0,$$

$$R_{\mathbf{x}^i \mathbf{y}^j}(0) = R_{\mathbf{x}^j \mathbf{y}^i}(0)$$

$$= R_{\mathbf{uv}}(\tau \bmod N_1) R_{\mathbf{b}^i \mathbf{b}^j}(\tau \bmod N_2) = 0;$$

$$0 < |\tau| \leq N_1 - 1,$$

$$R_{\mathbf{uv}}(\tau) = 0,$$

$$R_{\mathbf{x}^i \mathbf{y}^j}(\tau) = R_{\mathbf{x}^j \mathbf{y}^i}(\tau)$$

$$= R_{\mathbf{uv}}(\tau \bmod N_1) R_{\mathbf{b}^i \mathbf{b}^j}(\tau \bmod N_2) = 0.$$

According to Definition 2-1, the sequence-pair set constructed by the above method is ZCZPS.

### 2.3 Properties of Optimized Punctured ZCZ Sequence-pair Set

Considering the optimized punctured ZCZPS that is constructed by the method mentioned in the last part, the autocorrelation and cross correlation properties can be simulated and analyzed with MATLAB. For example, the optimized punctured ZCZPS  $(\mathbf{X}, \mathbf{Y})$  is constructed by 5-bit length optimized punctured binary sequence-pair  $(\mathbf{u}, \mathbf{v})$ ,  $\mathbf{u} = [+ + - + -]$ ,  $\mathbf{v} = [+ + 000]$  (using '+' and '-' symbols for '1' and '-1') and Hadamard matrix  $H$  of order 4. We follow the three steps presented in Section B to construct the 20-bit length optimized punctured ZCZPS. The number of sequence-pairs here is 4, and the length of each sequence is  $5 * 4 = 20$ . The first row of each matrix  $\mathbf{X} = [\mathbf{x}_1; \mathbf{x}_2; \mathbf{x}_3; \mathbf{x}_4]$  and  $\mathbf{Y} = [\mathbf{y}_1; \mathbf{y}_2; \mathbf{y}_3; \mathbf{y}_4]$  constitute a certain optimized punctured ZCZP  $(\mathbf{x}_1, \mathbf{y}_1)$ . Similarly, the second row of each matrix  $\mathbf{X}$  and  $\mathbf{Y}$  constitute another optimized punctured ZCZ sequence-pair  $(\mathbf{x}_2, \mathbf{y}_2)$  and so on.

$$\mathbf{X} = \begin{bmatrix} + & + & - & + & - & + & + & - & + & - & + & + & - & + & - & + & - & + & - \\ + & - & - & - & - & + & + & + & + & - & - & - & - & + & + & + & + & + & + \\ + & + & + & - & - & + & - & + & + & - & - & - & - & + & + & - & + & - & + \\ + & - & + & + & - & - & - & - & + & + & - & + & - & - & + & + & + & + & - \end{bmatrix};$$

$$\mathbf{Y} = \begin{bmatrix} + & + & 000 & + & + & 000 & + & + & 000 & + & + & 000 \\ + & - & 000 & - & + & 000 & + & - & 000 & - & + & 000 \\ + & + & 000 & + & - & 000 & - & - & 000 & - & + & 000 \\ + & - & 000 & - & - & 000 & - & + & 000 & + & + & 000 \end{bmatrix}.$$

The autocorrelation property and cross correlation property of 20-bit length optimized punctured ZCZ sequence pair set  $(\mathbf{X}, \mathbf{Y})$  are shown in Figs. 1 and 2.

From the Figs. 1 and 2, the sidelobe of autocorrelation of ZCZPS can be as low as 0 when the time delay is kept within  $Z_0 = N_1 = 5$  (zero correlation zone) and the cross correlation value is kept as low as 0 during the whole time domain.

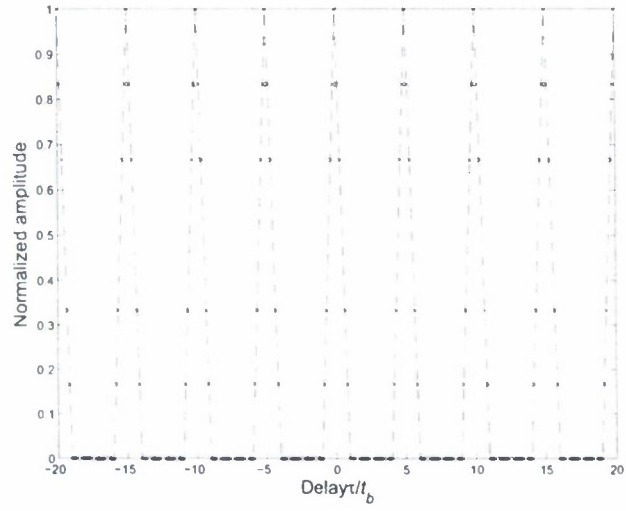


Figure 1: Periodic autocorrelation property of optimized punctured ZCZPS

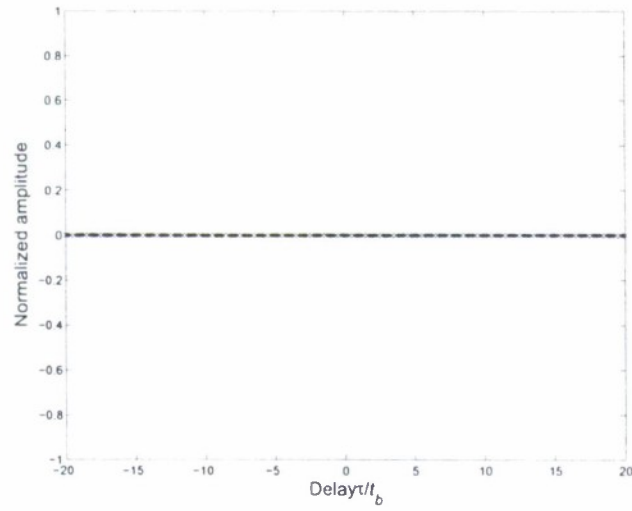


Figure 2: Periodic cross correlation property of optimized punctured ZCZPS

It is known that a suitable criterion for evaluating code of length  $N$  is the ratio of the peak signal divided by the peak signal sidelobe (PSR) of their autocorrelation function, which can be bounded by [27]

$$[PSR]_{dB} \leq 20\log N = [PSR_{max}]_{dB} \quad (13)$$

The only uniform phase codes that can reach the  $PSR_{max}$  are the Barker codes whose length is equal or less than 13. The sidelobe of the new code shown in Fig. 1 can be as low as 0, so the peak signal divided by the peak signal sidelobe can be as high as infinite. Besides, the length of the new code is various and much longer than the length of the Barker code.

### 3 MIMO Radar Signal Model

There has been considerable interest in the use of multiple transmit and receive antennas to offer significant performance improvement in wireless communication. In particular, MIMO radar uses diversity techniques to improve the capacity and performance of the radar systems. In addition, pulse compression, which allows a radar to simultaneously achieve the energy of a long pulse and the resolution of a short pulse without the high peak power required by a high energy short duration pulse [28], is generally used in modern radar systems. In this section, we describe a signal model for the MIMO radar system using orthogonal pulse compression codes. Assume a radar system that utilizes an array with  $M$  antennas at the transmitter, and  $M$  antennas at the receiver. For simplicity, we assume that the target scatters are laid out as a linear array, and the arrays at the transmitter and receiver are parallel. A transmitting linear array made up of  $M$  elements equally spaced a distance  $d$  apart. The elements are assumed to be isotropic radiators in that they have uniform response for signals from all directions. The first antenna will be taken as the reference with zero phase. The signal radiated by the  $m$ -th transmit antenna impinges at angle  $\theta$ . From

simple geometry, the difference in path length between adjacent elements for signals transmitting at an angle  $\theta$  with respect to the normal to the antenna, is  $d\sin\theta$ . This gives a phase difference between adjacent elements of  $\phi = 2\pi(d/\lambda)\sin\theta$ , where  $\lambda$  is wavelength of the received signal. And the phase difference for  $m$ -th transmit antenna is  $\phi_m = 2\pi((m-1)d/\lambda)\sin\theta$ . For convenience, we take the amplitude of the received signal at each element to be unity. A pulse compression code  $C_m = \sum_{p=0}^{P-1} C_m^p(t - p\tau_c)$  is applied to  $m$ -th transmit antenna, and the signal vector induced by the  $m$ -th transmit antenna is given by

$$C_m = [C_m^{(0)} C_m^{(1)} C_m^{(2)} \dots C_m^{(P-1)}], C_m^{(p)} \in [-1, 0, 1]; \quad (14)$$

$$g_m = e^{-j\phi_m} [C_m^{(0)} C_m^{(1)} C_m^{(2)} \dots C_m^{(P-1)}]^T, 1 \leq m \leq M;$$

The signal vectors are organized in the  $M \times P$  transmit matrix  $\mathbf{G} = [g_1 g_2 \dots g_M]^T$ . The transmitted waveforms are listed along the diagonal of the matrix  $\mathbf{S} = \text{diag}(s_1, \dots, s_M)$ . The transmitted waveforms could be normalized such that  $|s_i| = 1/M$ . The normalizing method ensures that transmitted power is not dependent of the number of antennas. Suppose, all antennas transmit the same waveform,  $\mathbf{S} = s\mathbf{I}_M$ , where the subscript denotes the order of the unity matrix.

Similar to the transmitter, the model for the array at the receiver could be developed, resulting in an  $M \times P$  channel matrix  $K$ . Similarly, the first antenna on the receive part will be taken as the reference with zero phase. The signal radiated by the  $n$ -th receive antenna impinges at angle  $\theta_0$ . The phase difference for  $n$ -th transmit antenna is  $\varphi_n = 2\pi((n-1)d_r/\lambda)\sin\theta_0$ . For phase-modulated pulse compression waveforms, the corresponding pulse compression codes  $C'_m = \sum_{p=0}^{P-1} C_m'^p(t - p\tau_c)$  have to be applied to each receive antenna to implement the matched filter. The signal vector arrived at the  $n$ -th receive antenna could be given by

$$C'_n = [C_n^{(0)} C_n^{(1)} C_n^{(2)} \dots C_n^{(P-1)}], C_n^{(p)} \in [-1, 0, 1]; \quad (15)$$

$$k_n = e^{-j\varphi_n} [C_n^{(0)} C_n^{(1)} C_n^{(2)} \dots C_n^{(P-1)}];$$

$$\mathbf{K} = [k_1 k_2 \dots k_M]^T$$

Having the transmit and receive matrix together, the MIMO radar channel model is given by  $M \times M$  matrix

$$\mathbf{H} = \mathbf{K}[\mathbf{G}^H \Sigma] \quad (16)$$

$$= \begin{bmatrix} k_1 \\ k_2 \\ \vdots \\ k_M \end{bmatrix} [g_1^* g_2^* \dots g_M^*] \begin{bmatrix} \lambda_{11} & \lambda_{12} & \dots & \lambda_{1M} \\ \lambda_{21} & \lambda_{22} & \dots & \lambda_{2M} \\ \vdots & & \ddots & \vdots \\ \lambda_{M1} & \lambda_{M2} & \dots & \lambda_{MM} \end{bmatrix}$$

$$= \begin{bmatrix} e^{j(\phi_1 - \varphi_1)} \sum_{p=0}^{P-1} C_1^{(p)} C_1'^{(p)} & e^{j(\phi_2 - \varphi_1)} \sum_{p=0}^{P-1} C_2^{(p)} C_1'^{(p)} & \dots & e^{j(\phi_M - \varphi_1)} \sum_{p=0}^{P-1} C_M^{(p)} C_1'^{(p)} \\ e^{j(\phi_1 - \varphi_2)} \sum_{p=0}^{P-1} C_1^{(p)} C_2'^{(p)} & e^{j(\phi_2 - \varphi_2)} \sum_{p=0}^{P-1} C_2^{(p)} C_2'^{(p)} & \dots & e^{j(\phi_M - \varphi_2)} \sum_{p=0}^{P-1} C_M^{(p)} C_2'^{(p)} \\ \vdots & \vdots & \ddots & \vdots \\ e^{j(\phi_1 - \varphi_M)} \sum_{p=0}^{P-1} C_1^{(p)} C_M'^{(p)} & e^{j(\phi_2 - \varphi_M)} \sum_{p=0}^{P-1} C_2^{(p)} C_M'^{(p)} & \dots & e^{j(\phi_M - \varphi_M)} \sum_{p=0}^{P-1} C_M^{(p)} C_M'^{(p)} \end{bmatrix} \quad (17)$$

$$* \begin{bmatrix} \lambda_{11} & \lambda_{12} & \dots & \lambda_{1M} \\ \lambda_{21} & \lambda_{22} & \dots & \lambda_{2M} \\ \vdots & & \ddots & \vdots \\ \lambda_{M1} & \lambda_{M2} & \dots & \lambda_{MM} \end{bmatrix}$$

Where  $\Sigma$  is the channel matrix.

It is easy to see that if we select orthogonal pulse compression codes for transmit and receive

antennas, so it is satisfied that

$$\sum_{p=0}^{P-1} C_m^p C_n'^{(p)} = \begin{cases} E_s & m = n \\ 0 & m \neq n \end{cases} \quad (18)$$

The  $\mathbf{H}$  matrix turns to be

$$\begin{aligned} \mathbf{H} &= \begin{bmatrix} e^{j(\phi_1 - \varphi_1)} E_s & e^{j(\phi_2 - \varphi_1)} E_s & \dots & e^{j(\phi_M - \varphi_1)} E_s \\ e^{j(\phi_1 - \varphi_2)} E_s & e^{j(\phi_2 - \varphi_2)} E_s & \dots & e^{j(\phi_M - \varphi_2)} E_s \\ \vdots & \vdots & \ddots & \vdots \\ e^{j(\phi_1 - \varphi_M)} E_s & e^{j(\phi_2 - \varphi_M)} E_s & \dots & e^{j(\phi_M - \varphi_M)} E_s \end{bmatrix} \\ &\quad * \begin{bmatrix} \lambda_{11} & \lambda_{12} & \dots & \lambda_{1M} \\ \lambda_{21} & \lambda_{22} & \dots & \lambda_{2M} \\ \vdots & \vdots & \ddots & \vdots \\ \lambda_{M1} & \lambda_{M2} & \dots & \lambda_{MM} \end{bmatrix} \\ &= \begin{bmatrix} \lambda_{11} e^{j(\phi_1 - \varphi_1)} E_s & \lambda_{12} e^{j(\phi_1 - \varphi_1)} E_s & \dots & \lambda_{1M} e^{j(\phi_1 - \varphi_1)} E_s \\ \lambda_{21} e^{j(\phi_2 - \varphi_2)} E_s & \lambda_{22} e^{j(\phi_2 - \varphi_2)} E_s & \dots & \lambda_{2M} e^{j(\phi_2 - \varphi_2)} E_s \\ \vdots & \vdots & \ddots & \vdots \\ \lambda_{M1} e^{j(\phi_M - \varphi_M)} E_s & \lambda_{M2} e^{j(\phi_M - \varphi_M)} E_s & \dots & \lambda_{MM} e^{j(\phi_M - \varphi_M)} E_s \end{bmatrix} \end{aligned}$$

As a result, the signal vector received by the MIMO radar is given by

$$\mathbf{r} = \mathbf{H}\mathbf{S} + \mathbf{n} \quad (19)$$

where the additive white Gaussian noise vector  $\mathbf{n}$  consists of i.i.d, zero-mean complex normal distributed random variables with variance  $1/\text{SNR}$ . The transmitted waveforms are normalized such that  $|\mathbf{s}|^2 = 1/M$ . The normalizing factor ensures that the transmitted power is independent of the number of transmit antennas. In this case that all antennas transmit the same waveform,  $\mathbf{S} = \mathbf{s}\mathbf{I}_M$ .

If receiver antenna uses a beamformer to steer towards direction  $\theta'_0$ ,  $\varphi'_n = 2\pi((n-1)d_r/\lambda)\sin\theta'_0$ , and  $\alpha(\theta'_0) = [e^{-j\varphi'_1}, e^{-j\varphi'_2}, \dots, e^{-j\varphi'_N}]$  and  $\beta(\theta'_0) = [\alpha(\theta'_0); \alpha(\theta'_0); \dots; \alpha(\theta'_0)]$ . The output of the beamformer is

$$\begin{aligned}
 \mathbf{y} &= \mathbf{r}\beta^*(\theta'_0) = \mathbf{H}\mathbf{S}\beta^*(\theta'_0) + \mathbf{n}' \\
 &= \begin{bmatrix} \lambda_{11}e^{j(\phi_1-\varphi_1)}E_{ss} & \lambda_{12}e^{j(\phi_1-\varphi_1)}E_{ss} & \dots & \lambda_{1M}e^{j(\phi_1-\varphi_1)}E_{ss} \\ \lambda_{21}e^{j(\phi_2-\varphi_2)}E_{ss} & \lambda_{22}e^{j(\phi_2-\varphi_2)}E_{ss} & \dots & \lambda_{2M}e^{j(\phi_2-\varphi_2)}E_{ss} \\ \vdots & \vdots & \ddots & \vdots \\ \lambda_{M1}e^{j(\phi_M-\varphi_M)}E_{ss} & \lambda_{M2}e^{j(\phi_M-\varphi_M)}E_{ss} & \dots & \lambda_{MM}e^{j(\phi_M-\varphi_M)}E_{ss} \end{bmatrix}^* \\
 &\quad \begin{bmatrix} e^{j\varphi'_1} & e^{j\varphi'_2} & \dots & e^{-j\varphi'_M} \\ e^{j\varphi'_1} & e^{j\varphi'_2} & \dots & e^{-j\varphi'_M} \\ \vdots & \vdots & \ddots & \vdots \\ e^{j\varphi'_1} & e^{j\varphi'_2} & \dots & e^{-j\varphi'_M} \end{bmatrix} + \mathbf{n}' \\
 &= \begin{bmatrix} \sum_{i=1}^M \lambda_{1i}e^{j(\phi_1-\varphi_1+\varphi'_i)}E_{ss} & \sum_{i=1}^M \lambda_{1i}e^{j(\phi_1-\varphi_1+\varphi'_2)}E_{ss} & \dots & \sum_{i=1}^M \lambda_{1i}e^{j(\phi_1-\varphi_1+\varphi'_M)}E_{ss} \\ \sum_{i=1}^M \lambda_{2i}e^{j(\phi_2-\varphi_2+\varphi'_i)}E_{ss} & \sum_{i=1}^M \lambda_{2i}e^{j(\phi_2-\varphi_2+\varphi'_2)}E_{ss} & \dots & \sum_{i=1}^M \lambda_{2i}e^{j(\phi_2-\varphi_2+\varphi'_M)}E_{ss} \\ \vdots & \vdots & \ddots & \vdots \\ \sum_{i=1}^M \lambda_{Mi}e^{j(\phi_M-\varphi_M+\varphi'_i)}E_{ss} & \sum_{i=1}^M \lambda_{Mi}e^{j(\phi_M-\varphi_M+\varphi'_2)}E_{ss} & \dots & \sum_{i=1}^M \lambda_{Mi}e^{j(\phi_M-\varphi_M+\varphi'_M)}E_{ss} \end{bmatrix} \\
 &\quad + \mathbf{n}'
 \end{aligned} \tag{20}$$

Processing the output of  $\mathbf{y}$ , we obtain the diagonal of the output matrix  $\mathbf{y}$  that  $\mathbf{y}' = \text{diag}(\mathbf{y})$  and change it into a  $M \times 1$  vector  $\mathbf{y}''$ . The output of the beamformer at the receiver antenna is

$$\mathbf{y}'' = \begin{bmatrix} \sum_{i=1}^M \lambda_{i1}e^{j(\varphi'_1-\varphi_1)}E_{ss} \\ \sum_{i=1}^M \lambda_{i2}e^{j(\varphi'_2-\varphi_2)}E_{ss} \\ \vdots \\ \sum_{i=1}^M \lambda_{iM}e^{j(\varphi'_N-\varphi_N)}E_{ss} \end{bmatrix} + \mathbf{n}' \tag{21}$$

Where  $E_s \gg \sigma^2(n')$ . In MIMO radar for direction finding (DF) purpose, the transmit antennas are sufficiently separated, so the phase shifts at the transmitter are set to zero. It is easy to see that when  $\theta = 0$ ,  $\phi_m = 2\pi(d/\lambda)\sin\theta = 0$  and  $g_m = [C_m^{(0)} C_m^{(1)} C_m^{(2)} \dots C_m^{(N-1)}]^T$ . If the beamformer can well estimate the direction  $\theta_0$  at the receiver antenna, in some other words,  $\theta'_0 \cong \theta_0$  and  $\varphi_n = \varphi'_n$ . We can get the result at the MIMO receiver antennas that

$$y = \left[ \sum_{i=1}^M \lambda_{i1} E_s s, \sum_{i=1}^M \lambda_{i2} E_s s, \dots, \sum_{i=1}^M \lambda_{iM} E_s s \right]^T + n' \quad (22)$$

We apply MSE to receiver antennas to estimate direction finding error. Similar to RAKE receiver, we can choose the path which has the best performance before estimate the phase shift error for of the target direction which could be called Selective Combining.

## 4 Simulations and Analysis

In this section, some results are provided using MATLAB simulations. Performance is parameterized by the number of transmitting antennas  $M$ . Since a pair of Optimized punctured ZCZP has been applied as the orthogonal pulse compression codes for transmit and receive antennas correspondingly, the number of receiving antennas has to be the same as the number of transmitting ones, which means  $N = M$ . The transmit antennas are spaced sufficiently to achieve diversity. The target fluctuating model in which the channel fluctuated according to a Rayleigh distribution is also considered in the simulation. Estimation MSE (mean square error) is used as the common figure of merit for comparing the performance of different systems of different number of transmit antennas in the simulation system.

We choose the path which provides the best performance before estimate MSE called Selective Combining method. The MIMO radar systems of 4 and 8 transmit antennas are analyzed and compared in Fig. 3.

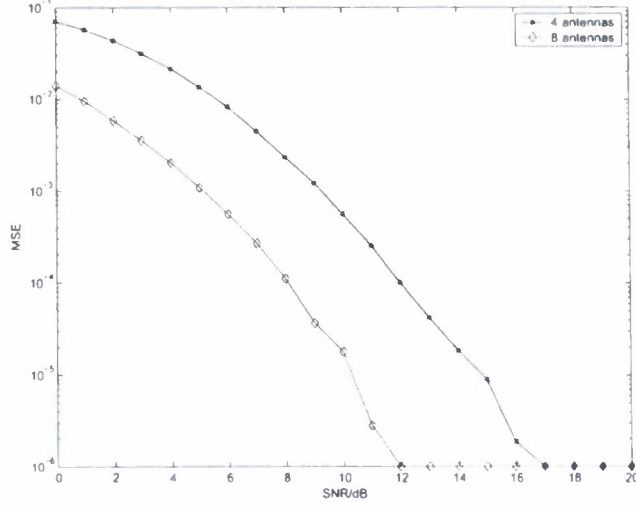


Figure 3: MSE of beamforming at the receiver (select the best path before estimate)

From the Fig. 3, it is easy to see that the 8-antenna system could always achieve about  $2dB$  SNR gain comparing to the 4-antenna system if we select the path which has best performance for estimation. The MSE approaches zero, when the SNR value is larger than  $12dB$  for 8-antenna system and  $17dB$  for 4-antenna system. According to the above results, a general conclusion could be drawn that the more antennas MIMO radar system utilized the better performance could be obtained because of the diversity gain.

## 5 Conclusions

In this paper, we introduced the orthogonal pulse compression codes to the MIMO radar system which has the same number of transmit and receive antennas to improve the radar direction finding performance. We provided a set of new optimized triphase pulse compression codes, gave a specific example and analyzed the codes' properties. We presented and analyzed a generalized MIMO radar system model for our provided framework, in which Beamforming and estimate MSE are also used to find the direction of the target at receive part. Simulation results showed that significant diversity

gain could be obtained in MIMO radar system using orthogonal pulse compression codes. The MIMO radar system using more antennas outperforms the one having less antennas. The paper is only to introduce the basic concept of our newly provided MIMO radar system with orthogonal pulse compression codes to find the direction of fixed targets. In the subsequent work, we may consider the Doppler shift effect for moving targets and some complicate radar channel models for the new approach.

## Acknowledgement

This work was supported by the Office of Naval Research (ONR) under Grant N00014-07-1-0395, N00014-07-1-1024, and N00014-03-1-0466.

## References

- [1] P. F. Sammartino, C. J. Baker, H.D. Griffiths and M. Rangaswamy, "Decentralized detection in radar networks," *IET RADAR 2007, Edinburgh UK*, October 2007.
- [2] P. F. Sammartino, C. J. Baker, and H.D. Griffiths, "A comparison of algorithms for MIMO and netted radar system," *2nd International Waveform Diversity and Design Conference*, Lihue, HI, 22th-27th Jan 2006.
- [3] P. F. Sammartino, C. J. Baker, and H.D. Griffiths, "Target Model Effects On MIMO Radar Performance," *IEEE International Conference on Acoustic, Speech and Signal Processing*, Toulouse, Fr, 14th-19th May 2006.
- [4] L. B. White and P. S. Ray, "Signal Design for MIMO Diversity System," *Conference Record of the 38th Asilomar Conference on Signal, Systems and Computers, 2004.*, pp. 973-977, Nov.2004.

- [5] P. Stoica, Jian Li and Yao Xie, "On Probing Signal Design For MIMO Radar," *IEEE Transactions on Signal Processing*, Vol. 55, pp. 4151-4161, Aug. 2007.
- [6] Jian Li, Petre Stoica and Xumin Zhu, "MIMO Radar Waveform Synthesis," *IEEE Radar Conference, 2008*, pp. 1-6, May. 26-30, 2008.
- [7] Yang Yang and Rick S. Blum, "MIMO Radar waveform Design," *IEEE/SP 14th Workshop on Statistical Signal Processing*, pp. 468-472, Aug. 26-29, 2007.
- [8] G. San Antonio, D. R. Furlhrmann and C. R. Frank, "MIMO radar ambiguity functions", *IEEE Journal of Selected Topics in Signal Processing*, 1(1), pp. 167-177, 2007.
- [9] G. San Antonio and D. R. Furlhrmann, "Beampattern synthesis for wideband MIMO radar systems", *2005 1st IEEE International Workshop on Computational Advances in Multi-Sensor Adaptive Processing*, pp. 105-108, Dec, 2005.
- [10] D. R. Furlhrmann and G. San Antonio, "Transmit beamforming for MIMO radar systems using partial signal correlation", *the 38th Asilomar Conference on Signal, Systems and Computers*, pp. 295-299, Nov. 2004.
- [11] Luzhou Xu, Jian Li and P. Stoica, "Target Detection and Parameter Estimation for MIMO Radar Systems", *IEEE Transactions on Aerospace and Electronic Systems*, Vol.44, no.3, pp. 927-939, July 2008.
- [12] H. Godrich, Alexander M. Haimovich and Rick S. Blum, "Target Localization Techniques and Tools for MIMO Radar", *IEEE Radar Conference, 2008*, pp. 1-6, May. 26-30 2008.
- [13] A. Dogandzic and A. Nehorai, "Cramer-Rao bounds for estimating range, velocity, and direction with an active array," *IEEE Transactions on Signal Processing*, vol.49, no.6, pp. 1122-1137, June 2001.

- [14] S. Pasupathy and A. N. Venetsanopoulos, "Optimum active array processing structure and space-time factorability," *IEEE Trans. Aerosp. Electron. syst.*, vol.10, pp. 770-778, 1974.
- [15] S. Haykin, J. Litva and T. J. Shepherd, *Radar Array Processing*, Springer-Verlag, New York, 1st edition, 1993.
- [16] E. Fishler, A. Haimovich, R. S. Blum, L. J. Cimini, D. Chizhik and R. A. Valenzuela, "Spatial diversity in radars-models and detection performance", *IEEE Trans. on Signal Processing*, 54(3): pp. 823-838, 2006.
- [17] B. Friedlander, "Adaptive waveform design for a multi-antenna radar system", *Proceedings of the Asilomar Conference on Signal, Systems and Computers*, Oct.29-Nov.1, 2006, Pacific Grove, CA.
- [18] B. Friedlander, "Waveform design for MIMO radars", *IEEE Trans. on Aero. Electr. Systems*, Oct., 2007.
- [19] B. Friedlander, "On data-adaptive waveform design for MIMO radar", *Proceedings of the Asilomar Conference on Signal, Systems and Computers*, Nov.4-Nov.7, 2007, Pacific Grove, CA.
- [20] P. Z. Fan, N. Suehiro, N. Kuroyanagi and X. M. Deng, "A class of binary sequences with zero correlation zone," *IEE Electron.Letter*, Vol.35, no.10: pp. 777-779, 1999.
- [21] P. Z. Fan and L. Hao, "Generalized Orthogonal Sequences and Their Applications in Synchronous CDMA Systems," *IEICE Trans.Fundamentals*, E832A(11): 1 16, 2000.
- [22] P. Z. Fan, "New Direction in Spreading Sequence Design and the Related Theoretical Bounds," *International Conference of Communications , Circuits and Systems*, June 29-July 1, 2002, PRC.

- [23] S. Matsufuji, N Suehiro , N Kuroyanagi and P Z Fan, "Two types of polyphase sequence set for approximately synchronized CDMA systems," *IEICE Trans. Fundamentals*, E862A(1): pp. 229-234, Jan. 2003.
- [24] H. Torii, M. Nakamura and N. Suehiro, "A new class of zero correlation zone sequences," *IEEE Tran. Inform.Theory*, Vol 50: pp. 559-565, Mar. 2004.
- [25] T. Jiang, *Research on Quasi-Optimized Binary Signal Pair and Perfect Punctured Binary Signal Pair Theory*, Ph.D Dissertation: Yanshan University, 2003.
- [26] U. Somaini, "Bianry sequences with good autocorrelation and cross correlation properties," *IEEE Transactions on Aerospace and Electronic Systems*, AES-11, 6, pp. 1226-1231, Nov.1975.
- [27] M.A.Richards, *Fundamentals of Radar Signal Processing*, McGraw-Hill, 2005.
- [28] S. Ariyavisitakul, N. Sollenberger, and L. Greenstein, *Introduction to Radar System*, Tata McGraw-Hill, 2001.

# A Triphase Coded Waveform: Design, Analysis and Application to Radar System

Lei Xu and Qilian Liang

Ting Jiang

Department of Electrical Engineering

School of Telecommunications Engineering

University of Texas at Arlington

Beijing University of Posts and Tele.

Arlington, TX 76010, USA

Beijing 100876, China

E-mail: xu@ecn.uta.edu, liang@uta.edu

E-mail: tjjiang@bupt.edu.cn

## Abstract

This paper presents new developed triphase code – punctured binary sequence-pair. The definitions and the autocorrelation properties of the proposed code are given. Doppler shift performance is also investigated. The significant advantages of punctured binary sequence-pair over conventional pulse compression codes, such as the widely used Barker codes, are zero autocorrelation sidelobes and the longer length of the code which can be as long as 31 so far. Applying the codes in the radar target detection system simulation, punctured binary sequence-pair also outperforms other conventional pulse compression codes. Therefore, our proposed code can be used as good candidates for pulse compression code.

**Index Terms :** triphase, phase coded waveform, radar system

## 1 Introduction

Pulse compression, which allows a radar to simultaneously achieve the energy of a long pulse and the resolution of a short pulse without the high peak power required by a high energy short duration

pulse [1], is generally used in modern radar system. The main purpose of this technique is to raise the signal to maximum sidelobe (signal-to-sidelobe) ratio to improve the target detection and range resolution abilities of the radar system. The range sidelobes are harmful because they can mask main peaks caused by small targets situated near large targets. The lower the sidelobes, relative to the mainlobe peak, the better the main peak can be distinguished.

In the industrial world, pulse compression is one of the significant factors to determine the performance of high detection and high resolution radar. For example, a satellite-borne rain radar demands very stringent requirements on range sidelobe level of -60dB [2], a downward looking rain measuring radar requires a range sidelobe of 55dB under the mainlobe level [3] [4], and the air traffic control system demands the sidelobe level lower -55dB [5].

There are two kinds of basic waveform designs suitable for pulse compression: frequency-codes, such as linear frequency modulation (LFM) codes [6] [7] and nonlinear frequency modulation codes(NLFM) [7] [8] [9]; phase-coded waveforms, such as binary phase codes and polyphase codes. For a phase-coded waveform, a long pulse of duration  $T$  is divided into  $N$  subpulses each of width  $T_s$ . Each subpulse has a particular phase, which is selected in accordance with a given code sequence. And the pulse compression ratio equals to the number of subpulses  $N = T/T_s \approx BT$ , where the bandwidth is  $B \approx 1/T_s$ .

A common form of phase coding is *binary phase coding*, in which the phase of each subpulse is selected to be either 0 or  $\pi$  radians. Since the binary phase codes are easy to generate, they are widely used in modern radar system. However, when the selection of the phase is made randomly, the expected maximum sidelobe is only about  $2/N$  of the peak of the compressed pulse. So completely random selection of the phase, is not a good idea, and the criterion for selecting the subpulse phases is that all the time-sidelobe of the compressed pulse should be equal and as low as possible. One family of binary phase code widely used nowadays that can produce compressed

waveforms with constant sidelobe levels equal to unity is the Barker code. It has special features with which its sidelobe structure contains the minimum energy which is theoretically possible for binary codes, and the energy is uniformly distributed among the sidelobes (the sidelobe level of the Barker codes is  $1/N^2$  that of the peak signal) [10]. Unfortunately, the length  $N$  of known binary and complex Barker codes is limited to 13 and 25, respectively [11], which may not be sufficient for the desired radar applications. In [12] [13] [14], polyphase codes, with better Doppler tolerance and lower range sidelobes such as the Frank and P1 codes, the Butler-matrix derived P2 code and the linear-frequency derived P3 and P4 codes were intensively analyzed. However, the low range sidelobe of the polyphase codes can not reach the level zero either, what is more, the structure of polyphase codes is more complicated and is not easy to generate comparing with binary codes. Therefore, we propose and analyze a new kind of triphase code-punctured binary sequence-pair, whose sidelobe level is as low as zero and the longest length of which is 31 in this paper, and subsequently apply it to radar system. According to the simulation results, the new code can be a good alternative for the current used pulse compression codes in radar system.

The rest of the paper is organized as following. Section 2 introduces the basic concept and properties of our proposed code. In Section 3, an example of punctured binary sequence-pair is given and its properties are investigated. In Section 4, the performance of our proposed code is also simulated and analyzed in radar targets detection system. In Section 5, some conclusions are drawn about the punctured binary sequence-pair.

## 2 Design of Punctured Binary Sequence-pair

First of all, there are some relating definitions listed here.

**Definition 1** A sequence-pair  $(x, y)$  is made up of two  $N$ -length sequences  $\mathbf{x} = (x_0, x_1, \dots, x_{N-1})$  and  $\mathbf{y} = (y_0, y_1, \dots, y_{N-1})$ ,

$$R_{xy}(\tau) = \sum_{j=0}^{N-1} x_j y_{(j+\tau) \bmod N}^*, 0 \leq \tau \leq N-1 \quad (1)$$

is called the periodic autocorrelation function of the sequence pair, while  $x = y$ , the sequence-pair  $(x, y)$  turns to be a one-sequence code.

**Definition 2** [15] Sequence  $y = (y_0, y_1, \dots, y_{N-1})$  is the punctured sequence for  $x = (x_0, x_1, \dots, x_{N-1})$ ,

$$y_j = \begin{cases} 0 & j \in p\text{-punctured bits} \\ x_j & j \in \text{Non-punctured bits} \end{cases} \quad (2)$$

Where  $p$  is the number of punctured bits in sequence  $x$ , suppose  $x = [-1, 1]$ ,  $y$  is  $p$ -punctured binary sequence,  $y = [-1, 0, 1]$ ,  $(x, y)$  is called a punctured binary sequence-pair. It is easy to see that there are only three possible choices for the phase state, typically  $-\pi, 0$  and  $\pi$  for the punctured binary sequence-pair. The punctured binary sequence-pair can be referred as a new kind of triphase code.

**Definition 3** The periodic autocorrelation of punctured sequence-pair  $(x, y)$  is defined

$$R_{xy}(\tau) = \sum_{j=0}^{N-1} x_j y_{(j+\tau) \bmod N}^*, 0 \leq \tau \leq N-1$$

When punctured sequence-pair has the following autocorrelation property

$$R_{xy}(\tau) = \begin{cases} E & \tau \equiv 0 \bmod N \\ 0 & \text{otherwise} \end{cases} \quad (3)$$

it is called optimized punctured sequence-pair [15]. Here,  $E = \sum_{j=0}^{N-1} x_j y_j = N - p$ , is the energy of punctured sequence-pair. Then binary sequence-pair  $(x, y)$  is called a  $p$ -punctured sequence-pair.

The energy efficiency of the sequence-pair is defined as

$$\eta = \frac{E}{N} = \frac{N-p}{N} \quad (4)$$

**Definition 4** The balance of the sequence  $x$  is defined as  $I = \sum_{j=0}^{N-1} x_j = n_p - n_n$ , while  $n_p, n_n$  are the number of  $' + 1'$  and  $' - 1'$  in  $x$  separately.

**Theorem 1** Mapping property, if  $x_1(i) = x(-i), y_1(i) = y(-i)$ , then sequence-pair  $(x_1, y_1)$  is optimized punctured binary sequence-pair.

**Theorem 2** Opposite to element symbol property, if  $x_1(i) = -x(i), y_1(i) = -y(i)$ , then sequence-pair  $(x_1, y_1)$  is optimized punctured binary sequence-pair.

**Theorem 3** Cyclic shift property, if  $x_1(i) = -x(i+u), y_1(i) = -y(i+u)$ , then sequence-pair  $(x_1, y_1)$  is optimized punctured binary sequence-pair.

**Theorem 4** Periodically sampling property, if  $x_1(i) = -x(ki), y_1(i) = -y(ki)$ ,  $k$  and  $N$  are relatively prime, then sequence-pair  $(x_1, y_1)$  is optimized punctured binary sequence-pair.

In [15], the optimized punctured binary sequence-pairs of length from 3 to 31 are presented in the Table 1.

### 3 Properties

#### 3.1 Autocorrelation Properties

The autocorrelation function is one of the most important properties that represents the compressed pulse in an ideal pulse compression system, because it is proportional to the matched filter response in the noise-free condition. As presented in the equation (4) in the last section, the periodic autocorrelation function of the punctured binary sequence-pair is

$$R_{xy}(\tau) = \sum_{j=0}^{N-1} x_j y_{(j+\tau) \bmod N}^* = \begin{cases} E & \tau \equiv 0 \bmod N \\ 0 & \text{otherwise} \end{cases}$$

### EXAMPLE 1

The autocorrelation property of 13-length punctured binary sequence pair  $(x, y)$ , ( $x = (+ + + - + + - - - - + + -)$  and  $y = (+0 + 0 + +0000 + +0)$ ), and that of 31-length punctured binary sequence-pair  $(x, y)$ , ( $x = (+ + + + - - - + - + - + + - - - - + - - + - - + + + - + + -)$  and  $y = (+ + + + 000 + 0 + 0 + + + 0000 + 00 + 00 + + + 0 + +0)$ ) ('+' for '1' and '-' for '-1') are shown in the Figs.1 and 2.

It is known that a suitable criterion for evaluating code of length  $N$  is the peak signal to peak signal sidelobe ratio (PSR) of their aperiodic autocorrelation function, which can be bounded by [16]

$$[PSR]_{dB} \leq 20 \log N = [PSR_{max}]_{dB} \quad (5)$$

The only uniform phase codes that can reach the  $PSR_{max}$  are the Barker codes whose length is equal or less than 13. However, the sidelobe of the new code in both Figs.1 and 2 can be as low as 0. In some other words, the peak signal to peak signal sidelobe can be as large as infinite. In addition, it is also obvious that the length of the new code can expend to 31 that is much longer than the length of the Barker code.

### 3.2 Ambiguity Function

When the transmitted impulse is reflected by a moving target, the reflected echo signal includes a linear phase shift which corresponds to a Doppler shift  $f_d$  [17]. As a result of the Doppler shift  $f_d$ , the main peak of the autocorrelation function is reduced:

$$[d]_{dB} = 10 \log \frac{\int_0^T x(s)x^*(s)ds}{\int_0^T x(s)e^{j2\pi f_d T_c} x^*(s)ds} \quad (6)$$

In addition, the SNR degraded and the sidelobe structure is changed because of the Doppler shift.

The ambiguity function which is usually used to analyze the radar performance of Doppler shift and time delay can be found in [17]

$$y(t, F_D) = \int_{-\infty}^{\infty} x(s)e^{j2\pi F_D s} x^*(s-t)ds \equiv \hat{A}(t, F_D) \quad (7)$$

where  $t$  is the time delay and  $F_D$  is the Doppler shift.

An equivalent definition can be given in terms of the signal spectrum by applying basic Fourier transform properties

$$\hat{A}(t, F_D) = \int_{-\infty}^{\infty} X^*(F)X(F-F_D)e^{j2\pi Ft}dF \quad (8)$$

The *ambiguity function* is defined as the magnitude of  $\hat{A}(t, F_D)$  [17]

$$A(t, F_D) \equiv |\hat{A}(t, F_D)| \quad (9)$$

However, we focus on the sequence-pair in this paper, so the transmitting code and the receiving code are not the same. The ambiguity function can be obtained as following:

$$y_{pair}(t, F_D) = \int_{-\infty}^{\infty} x(s)e^{j2\pi F_D s} y^*(s-t)ds \quad (10)$$

$$\hat{A}_{pair}(t, F_D) = \int_{-\infty}^{\infty} X^*(F)Y(F-F_D)e^{j2\pi Ft}dF \quad (11)$$

The *ambiguity function* is defined as the magnitude of  $\hat{A}_{pair}(t, F_D)$

$$A_{pair}(t, F_D) \equiv |\hat{A}_{pair}(t, F_D)| \quad (12)$$

Since the periodic correlation is used instead of aperiodic correlation in this paper. The  $\hat{A}_{pair}(t, F_D)$  in one period of length  $NT_s$  can be expressed as

$$A_{pair}(t, F_D) = \left| \int_0^t x(s)y^*(s + (NT_s - t)) e^{(j2\pi F_D s)} ds + \int_t^{(N-1)T_s} x(s)y^*(s - t) e^{(j2\pi F_D s)} ds \right| \quad (13)$$

## EXAMPLE 2

Ambiguity functions of the punctured binary sequence-pair within length of 13 and 31 used in the last section are simulated, where maximal time delay is 1 unit (normalized to length of the code, in units of  $NT_s$ ) and maximal Doppler shift is 5 units (normalized to the inverse of the length of the code, in units of  $1/NT_s$ ). The ambiguity functions of 13-length long Barker code and 31-length long P4 code are presented in Figs.2 and 3 in order to compare with the punctured binary sequence-pairs of the same length.

Figs.2 and 3 show that the sidelobe improvement of the punctured binary sequence-pair is obvious comparing with those of Barker code and P4 code when there is no Doppler shift. The sidelobe of punctured binary sequence-pair can reach as low as zero. Nevertheless, when there are Doppler shift and time delay, the ambiguity functions of punctured binary sequence-pair is not as flat as those of Barker code or P4 code. In some other words, punctured binary sequence-pair is, to some extent, less tolerant of Doppler shifts than P4 code. One of the reasons why the proposed code is not tolerant of large Doppler shift is that periodic correlation property is used for punctured binary sequence-pair instead of the aperiodic correlation property which is used for the other two codes. However, comparing with P4 code, punctured binary sequence-pair made up of only three different phases, is more simple and easy to obtain in the industrial world.

### 3.3 Doppler Shift Performance without Time Delay

The ambiguity function can be simplified when there is no time delay:

$$A_{pair}(0, F_D) = \left| \int_0^{NT_s} x(s)y^*(s)e^{j2\pi F_D s} ds \right| \quad (14)$$

However, in Figs. 2 and 3, it is not obvious to see the Doppler shift performance of punctured binary sequence-pair and the other two codes when there is no time delay. The Doppler shift performance without time delay is presented in Figs.4 and 5.

Without time delay, while the Doppler shift is less than 1 unit (normalized to length of the code, in units of  $NT_s$ ), punctured binary sequence-pair has the similar performance of Barker and P4 code that the amplitude has a sharp downward trend. Furthermore, amplitude of punctured binary sequence-pair decreases more quickly than amplitude of the other two codes. However, when the Doppler shift is larger than 1 unit (normalized to length of the code, in units of  $NT_s$ ), the performances of these codes are distinguished. On one hand, the trend presented by punctured binary sequence-pair is not as regular as the other two kinds of code when the Doppler shift is larger than 1. On the other hand, for Barker and P4 code, when Doppler frequencies equal to multiples of the pulse repetition frequency ( $PRF = 1/PRI = 1/T_s$ ) the ambiguity value turns to be zero. Because of these zeros, such multiples of the pulse repetition frequency will render the radar blind [1] to their velocities. Nevertheless, referring to punctured binary sequence-pair, ambiguity values do not go to zero when Doppler frequencies are equal to multiples of the PRF. Therefore, using the punctured binary sequence-pair as the compression code could, to some extent, improve the blind speed problem in moving target detection system.

## 4 Application to Radar System

According to [17], the following probabilities are of most interest in the Radar system.

1. Probability of Detection,  $P_D$ : The probability that a target is declared when a target is in fact present.
2. Probability of False Alarm,  $P_{FA}$ : The probability that a target is declared when a target is in fact *not* present.
3. Probability of Miss,  $P_M$ : The probability that a target is *not* declared when a target is in fact present.

Note that  $P_M = 1 - P_D$ , thus,  $P_D$  and  $P_{FA}$  suffice to specify all of the probabilities of interest in radar system. The above three probabilities of the newly provided thiphase code-punctured binary sequence-pairs in radar system are simulated using Matlab, as shown in Figs. 6 and 7. In addition, the performance of the 13-length Barker code and 31-length P4 code are provided in order to compare with the performance of punctured binary sequence-pairs of corresponding lengths. In the simulation model, we ran Monte-Carlo simulation for  $10^5$  times at each SNR value, the Doppler shift frequency which is kept less than 1 unit (normalized to the inverse of the length of the code, in units of  $1/NT_s$ ) is randomly determined by Matlab, and the time delay is assumed to be zero. We use threshold detection in coherent system and the threshold is adaptively determined in the simulation.

In Fig. 6(a), we plotted the miss detection probabilities  $P_M$  of 13-length punctured binary sequence-pair and the same length Baker code. Observe Fig. 6(a), the miss detection probability  $P_M$  of the system using 13-length punctured binary sequence-pair is lower than 13-length Barker code especially when the SNR is not large. It is in accordance with the result shown in Fig. 4 that when Doppler shift is kept less than 1 and the time delay is zero, the amplitude of punctured binary sequence-pair falls more sharply than Barker code. In Fig. 6(b), we plotted the miss targets

detection probabilities of 31-length punctured binary sequence-pair and those of the same length P4 code. The miss targets detection probability of the system using 31-length punctured binary sequence-pair is less than 31-length P4 code especially when the SNR is not large. When SNR is larger than 17 dB, both probabilities of miss targets detection of the system approach zero. However, the probability of miss targets of P4 code is lower than punctured binary sequence-pair. Comparing both Figs.6(a) and 6(b), longer punctured code performs better especially when the SNR is not very large.

In addition, we also plotted the probability of detection versus probability of false alarm of the coherent receiver in Fig. 7.

Fig. 7(a) illustrates performance of 13-length punctured binary sequence-pair and the same length Baker code when the SNR is 10dB and 14dB. Having the same SNR value such as 10dB or 14dB in the figure, the  $P_D$  of 13-length punctured binary sequence-pair is larger than  $P_D$  of 13-length Barker code while the  $P_{FA}$  of the first code is also smaller than  $P_{FA}$  of the latter code. In some other words, 13-length punctured binary sequence-pair has much higher target detection probability while keeping a lower false alarm probability. Furthermore, observe Fig. 7(a), 13-length punctured binary sequence-pair even has much better performance at 10dB SNR value than 13-length Barker code at 14dB SNR value. Similarly, Fig. 7(b) shows that the performance of 31-length punctured binary sequence-pair is much better than the P4 code of same length. According to the above results, it is easy to see that our newly provided punctured binary sequence-pair is very promising to be an alternative pulse compression code in the Radar system.

## 5 Conclusion

A new triphase code-punctured binary sequence-pair and its properties have been investigated in this paper. The significant advantage of the new triphase code over conventional phase compression

code is the considerably reduced sidelobe as low as zero and correspondingly the significantly improved PSR of the autocorrelation function. In addition, the length of punctured binary sequence-pair known can be as long as 31. The disadvantage of the new sequence-pair is that it is not so tolerant of Doppler shift when the Doppler shift is larger than 1. We also apply the punctured binary sequence-pair to the target detection simulation in the radar system. According to the simulation results, it is easy to observe that 13-length punctured binary sequence-pair has better performance than 13-length Barker code. Similarly, the 31-length punctured binary sequence-pair performs better than 31-length P4 code when the Doppler shift is kept less than 1 unit (normalized to the inverse of the length of the code, in units of  $1/NT_s$ ) in the radar target detection system. According to the results presented above, the general conclusion could be made that the punctured binary sequence-pair, which has much longer code length and better autocorrelation sidelobe property than the biphasic code such as Barker code, and simpler structure than those polyphase codes such as P4 code, effectively increases the variety of candidates for pulse compression codes especially for long code.

## Acknowledgement

This work was supported by the Office of Naval Research (ONR) Grant N00014-07-1-0395, N00014-07-1-1024, and N00014-03-1-0466.

## References

- [1] S. Ariyavistakul, N. Sollenberger, and L. Greenstein, *Introduction to Radar System*, Tata McGraw-Hill, 2001.

- [2] H. D. Griffiths and L. Vinagre, "Design of low-sidelobe pulse compression waveforms," *Electronics Letters*, vol. 30, no. 12, pp. 1004-1005, Jun. 1994.
- [3] T. Kozu, "Effects of signal decorrelation on pulse compressed waveforms of nadir-looking spaceborne radar," *IEEE Trans. Geosci. Remote Sensing*, vol. 29, no. 5, pp. 786-790, Sep. 1991.
- [4] A. Tanner, S. L. Durden, R. Denning, E. Im, F. K. Li, W. Ricketts, and W. Wilson, "Pulse compression with very low sidelobes in an airborne rain mapping radar," *IEEE Trans. Geosci. Remote Sensing*, vol. 32, no. 1, pp. 211-213, Jan. 1994.
- [5] J. P. Larvor, "Digital pulse compression with low range sidelobes," *Int. Conference Radar*, pp. 391-394, 1992.
- [6] J. R. Klauder, A. C. Price, S. Darlington and W. J. Albersheim, "The theory and design of chirp radars," *Bell System Technical Journal*, vol. 39, 745-808, Jul. 1960.
- [7] C. E. Cook and M. Bernfeld, *Radar Signals, an Introduction to Theory and Application*, New York: Academic Press, 1967.
- [8] J. W. Arthur, "SAW pulse compression in modern multi-channel radar applications", *Microwave Journal*, pp. 159-169, Jan. 1986.
- [9] M. B. N. Butler, "Radar applications of SAW dispersive filters", *IEE Proceedings*, vol. 127, no. 2, pp. 118-124, Apr. 1980.
- [10] J. L. Eaves and E. K. Reedy, *Principles of Modern Radar*, Van Nostrand Reinhold, 1987.
- [11] L. Bomer and M. Antweiler, "Polyphase Barker sequences," *Electronics Letters*, 1577-1579, Dec. 1989.

- [12] R. L. Frank, "Polyphase codes with good nonperiodic correlation properties", *IEEE Transactions on Information Theory*, IT. -9, pp. 43-45, Jan. 1963.
- [13] B. L. Lewis and F. F. Kretschmer, "A new class of polyphase pulse compression codes and techniques", *IEEE Transactions on Aerospace and Electronic Systems*, AES-17, pp. 364-372, May. 1981.
- [14] B. L. Lewis and F. F. Kretschmer, "Linear frequency modulation derived polyphase pulse compression codes", *IEEE Transactions on Aerospace and Electronic Systems*, AES-18, pp. 637-641, Sep. 1982.
- [15] T. Jiang, *Research on Quasi-Perfect Binary Signal Pair and Perfect Punctured Binary Signal Pair Theory*, Ph.D Dissertation: Yanshan University, 2003.
- [16] M. I. Skolnik, *Radar Handbook*, New York: McGraw-Hill, 1970.
- [17] M. A. Richards, *Fundamentals of Radar Signal Processing*, McGraw-Hill, 2005.

## List of Tables

1	Optimum Punctured Binary Sequence-pair:One . . . . .	15
2	Optimum Punctured Binary Sequence-pair:Two . . . . .	16

Table 1: Optimum Punctured Binary Sequence-pair:One

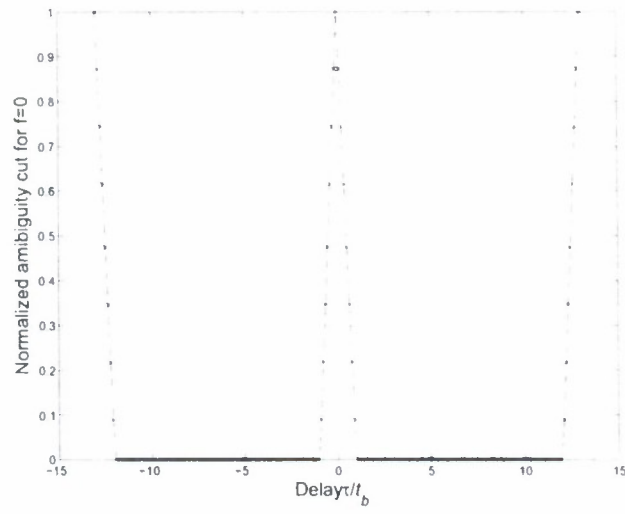
Length	Sequence (octet)	Punctured positions	Energy Efficiency(%)
3	6	3	66.67
5	32	3 4 5	40.00
5	34	2 4 5	40.00
7	162	4 5 7	57.14
7	164	4 6 7	57.014
9	652	1 2 3 4 5 6 7	22.22
9	760	1 2 3 4 6 7 8	22.22
11	3426	4 5 6 8 11	54.54
11	3550	4 7 9 10 11	54.54
12	7426	1 6 7 12	66.67
12	7550	4 5 10 11	66.67
12	7624	3 6 9 12	66.67
13	16606	2 4 7 8 9 10 13	46.15
13	17124	5 6 8 9 10 12 13	46.15
15	74232	5 6 7 9 10 13 15	53.33
15	75310	6 7 10 11 13 14 15	53.33
17	351134	4 6 7 8 9 10 12 16 17	47.06
17	372142	3 6 8 9 10 13 14 15 17	47.06
19	1715412	5 6 9 12 13 14 15 17 19	52.63
19	1724154	5 7 9 10 11 12 15 18 19	52.63
20	3433330	2 5 6 7 8 9 12 15 16 17 18 19	40.00
20	3610556	1 6 7 8 9 10 11 16 17 18 19 20	40.00
21	7405316	2 5 6 7 8 9 11 13 14 16 17 20 21	38.10
21	7563240	3 5 6 9 10 12 13 15 17 18 19 20 21	38.10
23	37024632	6 7 8 9 11 13 14 17 18 21 23	52.17

Table 2: Optimum Punctured Binary Sequence-pair:Two

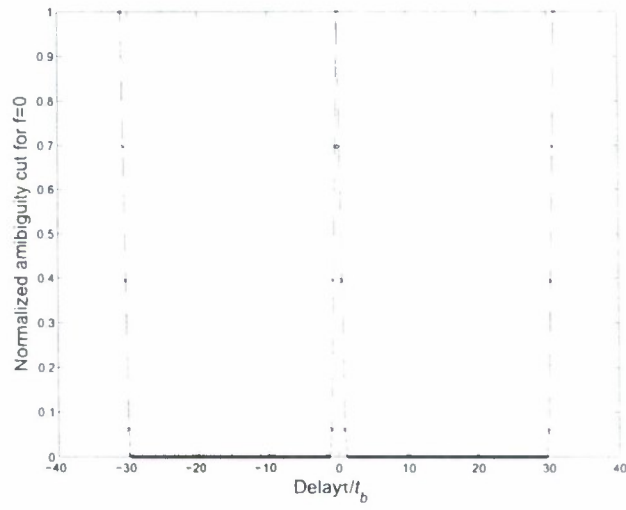
Length	Sequence (octet)	Punctured positions	Energy Efficiency(%)
23	37263120	6 8 11 12 15 16 18 20 21 22 23	52.17
28	1702164566	4 5 6 7 10 11 18 19 20 21 24 25	57.14
28	1734164226	4 5 8 9 10 11 18 19 22 23 24 25	57.14
28	1702164566	4 5 6 7 10 11 18 19 20 21 24 25	57.14
28	1734164226	4 5 8 9 10 11 18 19 22 23 24 25	57.14
28	1740465534	4 6 7 9 10 13 18 20 21 23 24 27	57.14
29	3556415302	4 7 11 13 14 15 16 19 20 21 24 25 26 27 29	48.28
29	3642213634	5 7 8 9 11 12 14 15 16 18 23 24 26 28 29	48.28
31	17053411166	5 6 7 9 11 15 16 17 18 20 21 23 24 28 31	51.61
31	17464412730	6 7 10 12 13 15 16 17 18 20 22 26 29 30 31	51.61

## List of Figures

1	Periodic autocorrelation property of punctured binary sequence-pair: (a) 13 length code (b) 31 length code . . . . .	17
2	Ambiguity function of 13-length codes: (a) Punctured binary sequence-pair (b) Barker code . . . . .	18
3	Ambiguity function of 31-length codes: (a) Punctured binary sequence-pair (b) P4 code . . . . .	19
4	Doppler shift of 13-length codes(time delay=0): (a) Punctured binary sequence-pair (b) Barker code . . . . .	20
5	Doppler shift of 31-length codes(time delay=0): (a) Punctured binary sequence-pair (b) P4 code . . . . .	21
6	Probability of miss targets detection (No time delay, Doppler shift less than 1): (a) 13-length Punctured binary sequence-pair VS. 13-length Barker code(b) 31-length Punctured binary sequence-pair VS. 31-length P4 code . . . . .	22
7	Probability of detection versus probability of false alarm of the coherent receiver(No time delay, Doppler shift less than 1): (a) 13-length Punctured binary sequence-pair VS. 13-length Barker code(b) 31-length Punctured binary sequence-pair VS. 31-length P4 code . . . . .	23



(a)



(b)

Figure 1: Periodic autocorrelation property of punctured binary sequence-pair: (a) 13 length code  
(b) 31 length code

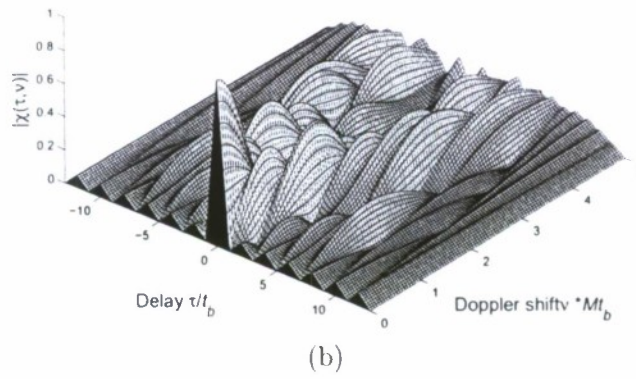
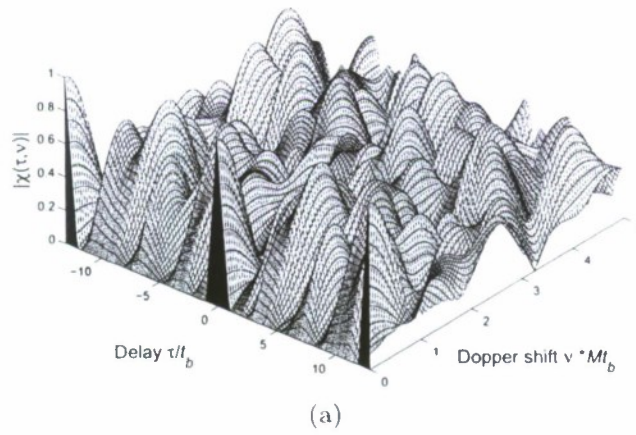


Figure 2: Ambiguity function of 13-length codes: (a) Punctured binary sequence-pair (b) Barker code

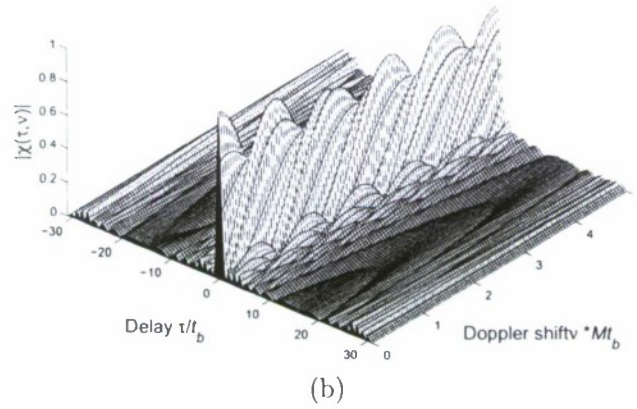
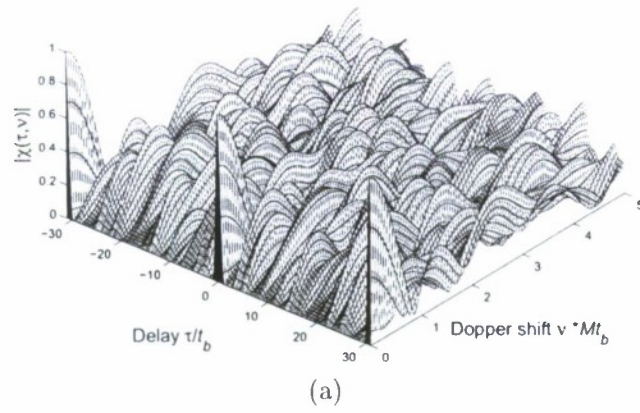
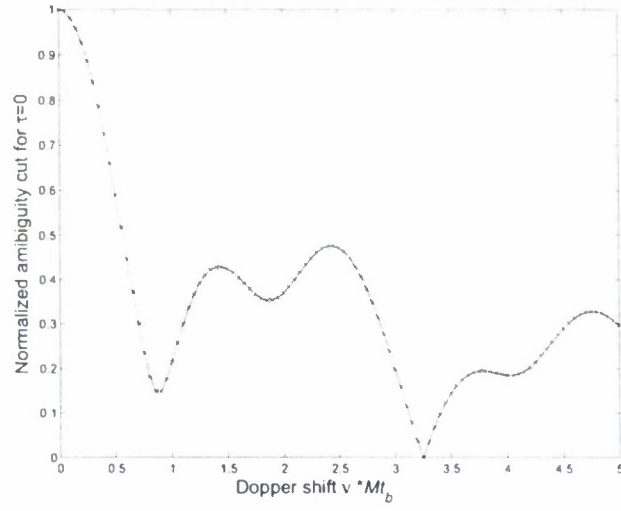
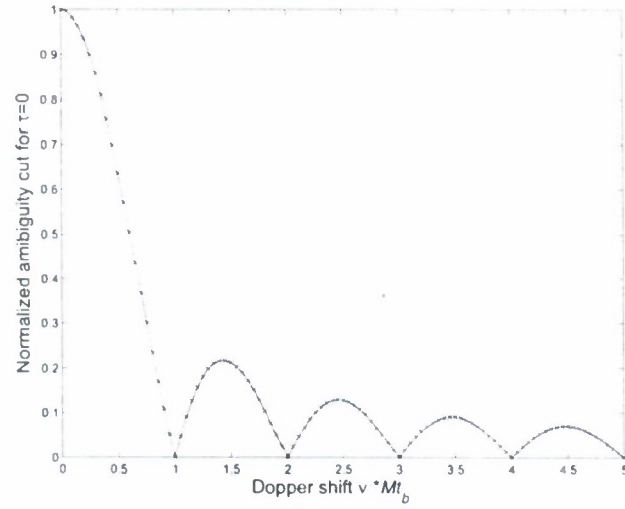


Figure 3: Ambiguity function of 31-length codes: (a) Punctured binary sequence-pair (b) P4 code

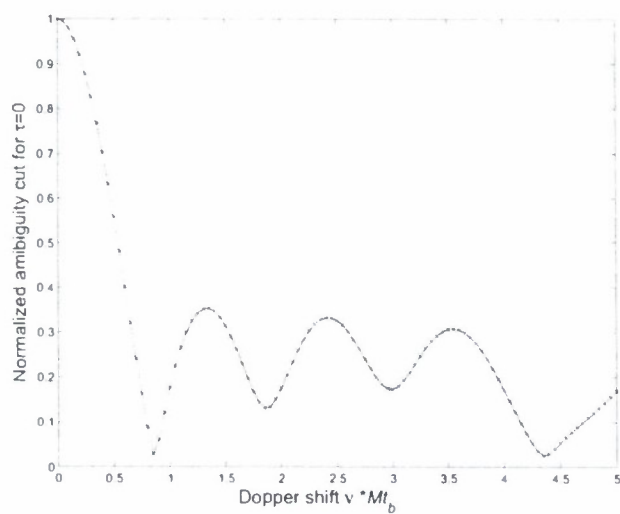


(a)

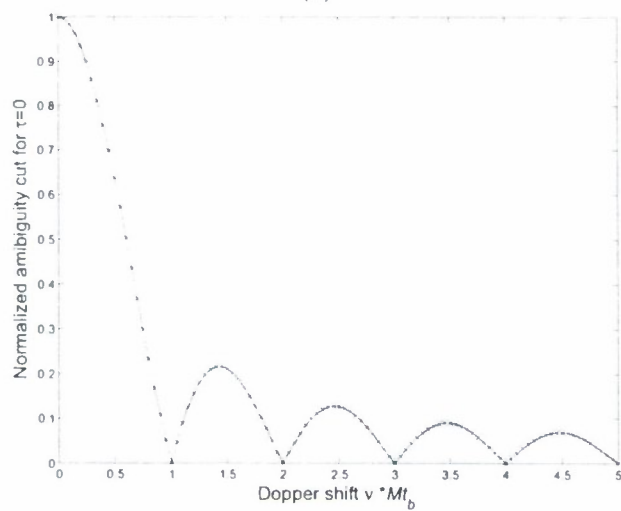


(b)

Figure 4: Doppler shift of 13-length codes(time delay=0): (a) Punctured binary sequence-pair (b) Barker code

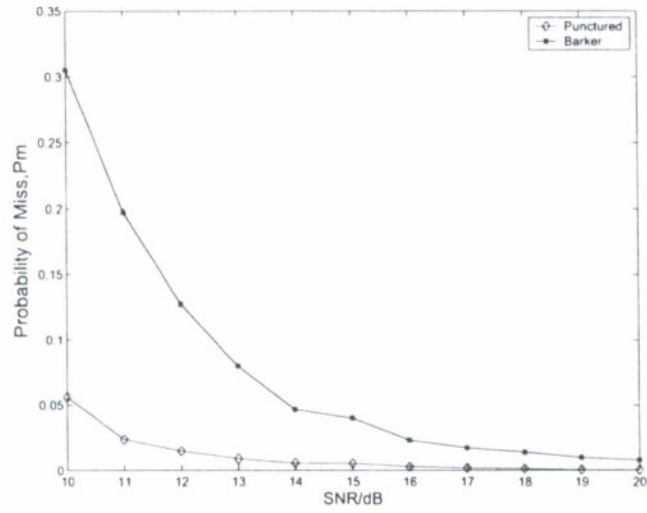


(a)

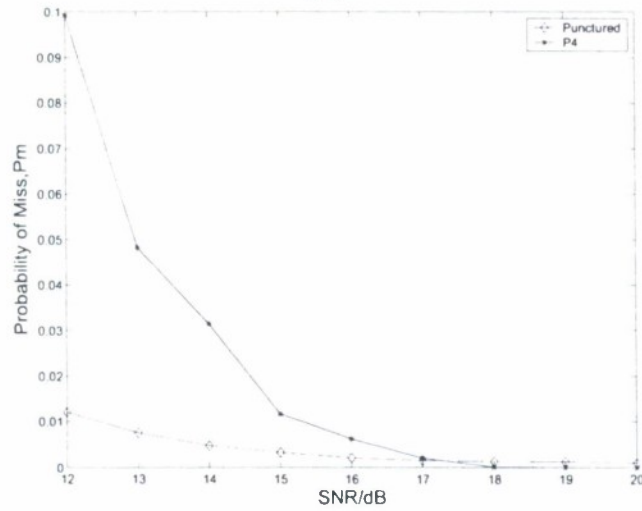


(b)

Figure 5: Doppler shift of 31-length codes(time delay=0): (a) Punctured binary sequence-pair (b) P4 code

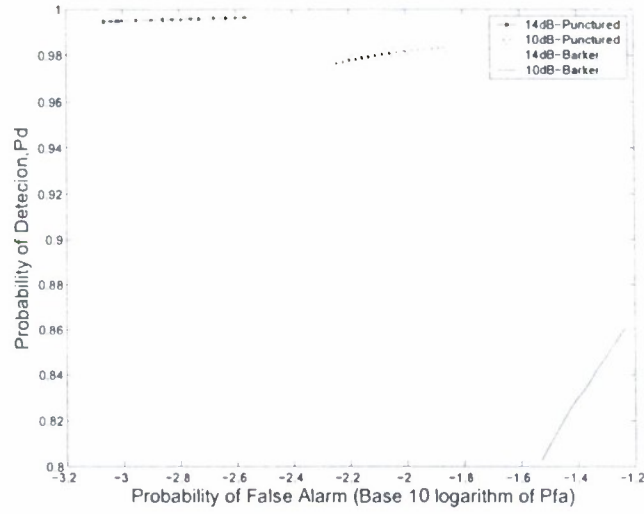


(a)

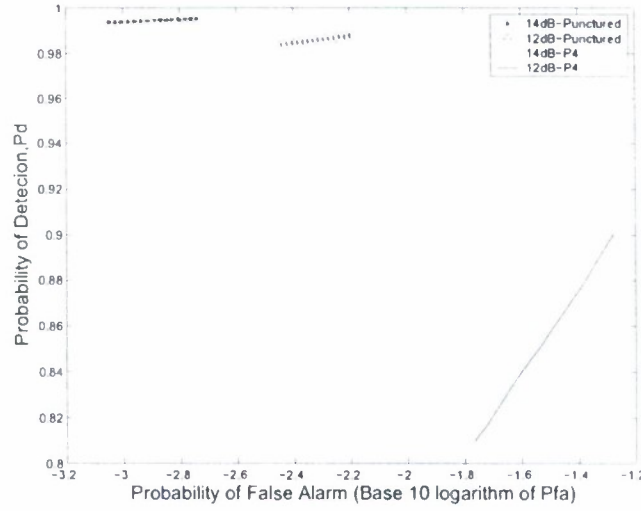


(b)

Figure 6: Probability of miss targets detection (No time delay, Doppler shift less than 1): (a) 13-length Punctured binary sequence-pair VS. 13-length Barker code (b) 31-length Punctured binary sequence-pair VS. 31-length P4 code



(a)



(b)

Figure 7: Probability of detection versus probability of false alarm of the coherent receiver (No time delay, Doppler shift less than 1): (a) 13-length Punctured binary sequence-pair VS. 13-length Barker code (b) 31-length Punctured binary sequence-pair VS. 31-length P4 code

# Optimized Punctured ZCZ Sequence-pair Set: Design, Analysis and Application to Radar System

Lei Xu and Qilian Liang, Senior Member, IEEE

Department of Electrical Engineering

University of Texas at Arlington

Arlington, TX 76010-0016 USA

Email: xu@ecn.uta.edu, liang@uta.edu

## Abstract

Based on the zero correlation zone (ZCZ) concept, in this paper we present the definition and properties of a set of new triphase coded waveforms –ZCZ sequence-pair set (ZCZPS) and propose a method to use the optimized punctured sequence-pair along with Hadamard matrix in the zero correlation zone in order to construct the optimized punctured ZCZ sequence-pair set (optimized punctured ZCZPS). According to property analysis, the optimized punctured ZCZPS has good autocorrelation and cross correlation properties when Doppler shift is not large. We apply it to radar target detection. The simulation results show that optimized punctured ZCZ sequence-pairs (optimized punctured ZCZPs) outperform other conventional pulse compression codes, such as the well known polyphase code-P4 code.

**Index Terms :** triphase, zero correlation zone, optimized punctured ZCZ sequence-pair, phase coded waveform

## 1 Introduction

Pulse compression, known as a technique to raise the signal to maximum sidelobe (signal-to-sidelobe) ratio to improve the target detection and range resolution abilities of the radar system, allows a radar to simultaneously achieve the energy of a long pulse and the resolution of a short pulse without the high peak power which is required by a high energy short duration pulse [1]. One of the waveform designs suitable for pulse compression is phase-coded waveform design that a long pulse of duration  $T$  is divided into  $N$  subpulses each of width  $T_s$ . Each subpulse has a particular phase, which is selected in accordance with a given code sequence. The pulse compression ratio equals the number of subpulses  $N = T/T_s \approx BT$ , where the bandwidth is  $B \approx 1/T_s$ . In general, a phase-coded waveform with longer code word, in some other words, higher pulse compression ratio, can have lower sidelobe of autocorrelation, relative to the mainlobe peak, so its main peak can be better distinguished. The relative lower sidelobe of autocorrelation is very important since range sidelobe are so harmful that they can mask main peaks caused by small targets situated near large targets. In addition, the cross-correlation property of the pulse compression codes should be considered in order to reduce the interference among radars when we choose a set of pulse compression codes, because in the real world, a radar may not work alone, such as in the RSN (Radar Sensor Network).

Much time and effort was put for designing sequences with good autocorrelation and cross correlation properties for radar target ranging and target detection. However, it is known that for most binary sequences of length  $N$  ( $N > 13$ ) the attainable sidelobe levels are approximately  $\sqrt{N}$  [2] [3] and the mutual cross correlation peaks of sequences of the same length are much larger and are usually in the order of  $2\sqrt{N}$  to  $3\sqrt{N}$ . Set of binary sequences of length  $N$  with autocorrelation sidelobes and cross-correlation peak values both of approximately  $\sqrt{N}$  are only achieved in paper [4]. In addition to binary sequences, polyphase codes, with better Doppler

tolerance and lower range sidelobes such as the Frank and P1 codes, the Butler-matrix derived P2 code, the linear-frequency derived P3 and P4 codes were provided and intensively analyzed in [5] [6] [7]. Nevertheless, the range sidelobe of the polyphase codes can not be as low as zero either. The structure of polyphase codes is more complicated and is not easy to generate comparing with binary codes.

Therefore, based on zero-correlation zone (ZCZ) [8] concept, we propose triphase coded waveforms-ZCZ sequence-pair set, which can reach zero autocorrelation sidelobe during zero correlation zone and zero mutual cross correlation peaks during the whole period. We also propose and analyze a method that optimized punctured sequence-pair together with Hadamard matrix are used in the zero correlation zone to construct the triphase coded waveform-optimized punctured ZCZ sequence-pair set called (optimized punctured ZCZPS) and subsequently apply it to radar detection system. For the performance evaluation of the proposed triphase coded waveform, an example is presented, investigated and studied in the radar targets detection simulation system. Because of the outstanding property performance and well target detection performance in simulation system, our proposed new codes can be useful candidate for pulse compression application.

The rest of the paper is organized as follows. Section 2 introduces the definition and properties of ZCZPS. In Section 3, the optimized punctured ZCZPS is introduced, and a method using optimized punctured sequence-pair and Hadamard matrix to construct ZCZPS is given and proved. In Section 4, the properties and ambiguity function of optimized punctured ZCZPS are simulated and analyzed. The performance of optimized punctured ZCZPS is investigated in radar targets detection simulation system comparing with P4 code. In Section 6, conclusions are drawn on optimized punctured ZCZPS.

## 2 The Definition and Properties of ZCZ Sequence-pair Set

Zero correlation zone is a new concept provided by Fan et.al [8] [9] [10] in which the autocorrelation and cross correlation sidelobes are zero while the time delay is kept within the value  $\tau$  instead of the whole period of time domain.

We consider ZCZPS( $X, Y$ ),  $X$  to be a set of  $K$  sequences of length  $N$  and  $Y$  to be a set of  $K$  sequences of the same length  $N$ :

$$x^{(p)} \in X \quad p = 0, 1, 2, \dots, K - 1 \quad (1)$$

$$y^{(q)} \in Y \quad q = 0, 1, 2, \dots, K - 1 \quad (2)$$

The autocorrelation function for sequence-pair  $(x^p, y^p)$  is defined by:

$$R_{x^{(p)}y^{(p)}}(\tau) = \sum_{i=0}^{N-1} x_i^{(p)} y_{(i+\tau) \bmod N}^{(p)*}, 0 \leq \tau \leq N - 1 \quad (3)$$

The cross correlation function for sequence-pair  $(x^p, y^p)$  and  $(x^q, y^q)$ ,  $p \neq q$  is defined by:

$$C_{x^{(p)}y^{(q)}}(\tau) = \sum_{i=0}^{N-1} x_i^{(p)} y_{(i+\tau) \bmod N}^{(q)*}, 0 \leq \tau \leq N - 1 \quad (4)$$

$$C_{x^{(q)}y^{(p)}}(\tau) = \sum_{i=0}^{N-1} x_i^{(q)} y_{(i+\tau) \bmod N}^{(p)*}, 0 \leq \tau \leq N - 1 \quad (5)$$

For pulse compression sequences, some properties are of particular concern in the optimization for any design in engineering field. They are the peak sidelobe level, the energy of autocorrelation sidelobes and the energy of their mutual cross correlation [4]. Therefore, the peak sidelobe level which represents a source of mutual interference and obscures weaker targets can be presented as  $\max_K |R_{x^p y^p}(\tau)|$ ,  $\tau \in Z_0$  (zero correlation zone) for ZCZPS. Another optimization criterion for the set of sequence-pair is the energy of autocorrelation sidelobes joined together with the energy of cross correlation. By minimizing the energy, it can be distributed evenly, and the peak autocorrelation

level can be minimized as well [4]. Here, the energy of ZCZPS can be employed as:

$$E = \sum_{p=0}^{K-1} \sum_{\tau=1}^{Z_0} R_{x^{(p)}y^{(p)}}^2(\tau) + \sum_{p=0}^{K-1} \sum_{q=0}^{K-1} \sum_{\tau=0}^{N-1} C_{x^{(p)}y^{(q)}}(\tau) \quad (6)$$

$(p \neq q)$

According to (6), it is obvious to see that the energy can be kept low while minimizing the autocorrelation and cross correlation of the sequence-pair set.

Then, the ZCZPS can be constructed to minimize the autocorrelation and cross correlation of the sequence-pair set and the definition of ZCZPS can be expressed:

**Definition 2-1** Assume  $(x_i^{(p)}, y_i^{(p)})$  to be sequence-pair set of length  $N$  and number of sequence-pair  $K$ , where  $p = 1, 2, 3, \dots, N-1, i = 0, 1, 2, \dots, K-1$ , if all the sequences in the set satisfy the following equation:

$$R_{x^{(p)}y^{(q)}}(\tau) = \sum_{i=0}^{N-1} x_i^{(p)} y_{(i+\tau) \bmod(N)}^{(q)*} = \sum_{i=0}^{N-1} y_i^{(p)} x_{(i+\tau) \bmod(N)}^{(q)*}$$

$$= \begin{cases} \lambda N, & \text{for } \tau = 0, p = q \\ 0, & \text{for } \tau = 0, p \neq q \\ 0, & \text{for } 0 < |\tau| \leq Z_0 \end{cases} \quad (7)$$

where  $0 < \lambda \leq 1$ , then  $(x_i^{(p)}, y_i^{(p)})$  is called a ZCZ sequence-pair,  $ZCZP(N, K, Z_0)$  is an abbreviation, and  $(X, Y)$  is called a ZCZ sequence-pair set,  $ZCZPS(N, K, Z_0)$  is an abbreviation.

### 3 Optimized Punctured ZCZ Sequence-pair Set

#### 3.1 Definition of Optimized Punctured ZCZ Sequence-pair Set

Matsufuji and Torii have provided some methods of constructing ZCZ sequences in [11] [12]. In this section, we apply optimized punctured sequence-pair [13] in zero correlation zone to construct

our newly provided triphase coded waveform-optimized punctured ZCZPS. In some other words, optimized punctured ZCZPS is a specific kind of ZCZPS.

**Definition 3-1** [13] Sequence  $u = (u_0, u_1, \dots, u_{N-1})$  is the punctured sequence for  $v = (v_0, v_1, \dots, v_{N-1})$ ,

$$u_j = \begin{cases} 0, & \text{if } j \in p \text{ punctured bits} \\ v_j, & \text{if } j \in \text{Non-punctured bits} \end{cases} \quad (8)$$

Where  $p$  is the number of punctured bits in sequence  $v$ , suppose  $v_j = (-1, 1)$ ,  $u$  is  $p$ -punctured binary sequence,  $(u, v)$  is called a punctured binary sequence-pair.

**Theorem 3-1** [13] The autocorrelation of punctured sequence-pair  $(u, v)$  is defined

$$R_{uv}(\tau) = \sum_{i=0}^{N-1} u_i v_{(i+\tau) \bmod N}, 0 \leq \tau \leq N-1 \quad (9)$$

If the punctured sequence-pair has the following autocorrelation property:

$$R_{uv}(\tau) = \begin{cases} E, & \text{if } \tau \equiv 0 \bmod N \\ 0, & \text{others} \end{cases} \quad (10)$$

the punctured sequence-pair is called optimized punctured sequence-pair [13]. Where,  $E = \sum_{i=0}^{N-1} u_i v_{(i+\tau) \bmod N} = N - p$ , is the energy of punctured sequence-pair.

If  $(x_i^{(p)}, y_i^{(p)})$  in Definition 2-1 is constructed by optimized punctured sequence-pair and a certain matrix, such as Hadamard matrix or an orthogonal matrix, where

$$x_i^{(p)} \in (-1, 1), \quad i = 0, 1, 2, \dots, N-1$$

$$y_i^{(q)} \in (-1, 0, 1), \quad i = 0, 1, 2, \dots, N-1$$

$$\begin{aligned} R_{x^{(p)}y^{(q)}}(\tau) &= \sum_{i=0}^{N-1} x_i^{(p)} y_{(i+\tau) \bmod N}^{(q)*} = \sum_{i=0}^{N-1} y_i^{(p)} x_{(i+\tau) \bmod N}^{(q)*} \\ &= \begin{cases} \lambda N, & \text{for } \tau = 0, p = q \\ 0, & \text{for } \tau = 0, p \neq q \\ 0, & \text{for } 0 < |\tau| \leq Z_0 \end{cases} \end{aligned} \quad (11)$$

where  $0 < \lambda \leq 1$ , then  $(x_i^{(p)}, y_i^{(p)})$  can be called optimized punctured ZCZ sequence-pair set.

### 3.2 Design for Optimized Punctured ZCZ Sequence-pair Set

Based on odd length optimized punctured binary sequence pairs and a Hadamard matrix, an optimized punctured ZCZPS can be constructed on following steps:

**Step 1:** Considering an odd length optimized punctured binary sequence-pair  $(u, v)$ , the length of each sequence is  $N_1$

$$u = u_0, u_1, \dots, u_{N_1-1}, u_i \in (-1, 1),$$

$$v = v_0, v_1, \dots, v_{N_1-1}, v_i \in (-1, 0, 1),$$

$$i = 0, 1, 2, \dots, N_1 - 1, N_1 \text{ odd}$$

**Step 2:** Consider Walsh sequences set B, the length of the sequence is  $N_2$  which is equal to the number of the sequences. In some other words, a Hadamard matrix of order  $N_2$  is considered.

$$B = (b^0, b^1, \dots, b^{N_2-1}),$$

$$b^i = (b_0^i, b_1^i, \dots, b_{N_2-1}^i),$$

$$R_{b^i b^j} = \begin{cases} N_2, & \text{if } i = j \\ 0, & \text{if } i \neq j \end{cases}$$

**Step 3:** Doing bit-multiplication on the optimized punctured binary sequence-pair and each line of Walsh sequences set B(Hadamard matrix), then sequence-pair set  $(X, Y)$  is obtained,

$$b^i = (b_0^i, b_1^i, \dots, b_{N_2-1}^i), i = 0, 1, \dots, N_2 - 1,$$

$$x_j^i = u_{j \bmod N_1} b_{j \bmod N_2}^i, 0 \leq i \leq N_2 - 1, 0 \leq j \leq N - 1,$$

$$X = (x^0, x^1, \dots, x^{N_2-1}),$$

$$y_j^i = v_{j \bmod N_1} b_{j \bmod N_2}^i, 0 \leq i \leq N_2 - 1, 0 \leq j \leq N - 1,$$

$$Y = (y^0, y^1, \dots, y^{N_2-1})$$

Where  $GCD(N_1, N_2) = 1$ , common divisor of  $N_1$  and  $N_2$  is 1,  $N = N_1 * N_2$ . The sequence-pair set  $(X, Y)$  is optimized punctured ZCZPS and  $N_1 - 1$  is the zero correlation zone  $Z_0$ . The length of each sequence in optimized punctured ZCZPS is  $N = N_1 * N_2$  that depends on the product of length of optimized punctured sequence-pair and the length of Walsh sequence in Hadamard matrix. The number of sequence-pair in optimized punctured ZCZPS rests on the order of the Hadamard matrix. The sequence  $x^i$  in sequence set  $X$  and the corresponding sequence  $y^i$  in sequence set  $Y$  construct a sequence-pair  $(x^i, y^i)$  that can be used as a pulse compression code.

The correlation property of the sequence-pair in optimized punctured ZCZPS is:

$$\begin{aligned}
R_{x^i, y^j}(\tau) &= R_{x^j, y^i}(\tau) = R_{uv}(\tau \bmod N_1) R_{b^i, b^j}(\tau \bmod N_2) \\
&= R_{uv}(\tau \bmod N_1) R_{b^j, b^i}(\tau \bmod N_2) \\
&= \begin{cases} EN_2, & \text{if } \tau = 0, i = j \\ 0, & \text{if } 0 < |\tau| \leq N_1 - 1, i = j \\ 0, & \text{if } i \neq j \end{cases} \quad (12)
\end{aligned}$$

where  $N_1 - 1$  is the zero correlation zone  $Z_0$ .

Proof:

1) When  $i = j$ ,

$$\tau = 0,$$

$$R_{uv}(0) = E, R_{b^i, b^j}(0) = N_2,$$

$$R_{x^i, y^j}(0) = R_{uv}(0) R_{b^i, b^j}(0) = EN_2;$$

$$0 < |\tau| \leq N_1 - 1,$$

$$R_{uv}(\tau) = 0,$$

$$R_{x^i, y^j}(\tau) = R_{uv}(\tau \bmod N_1) R_{b^i, b^j}(\tau \bmod N_2) = 0;$$

2) When  $i \neq j$ ,

$$\tau = 0,$$

$$R_{b^i b^j}(0) = 0,$$

$$R_{x^i y^j}(0) = R_{x^j y^i}(0)$$

$$= R_{uv}(\tau \bmod N_1) R_{b^i b^j}(\tau \bmod N_2) = 0;$$

$$0 < |\tau| \leq N_1 - 1,$$

$$R_{uv}(\tau) = 0,$$

$$R_{x^i y^j}(\tau) = R_{x^j y^i}(\tau)$$

$$= R_{uv}(\tau \bmod N_1) R_{b^i b^j}(\tau \bmod N_2) = 0.$$

According to Definition 2-1, the sequence-pair set constructed by the above method is ZCZPS.

## 4 Properties of Optimized Punctured ZCZ Sequence-pair set

Considering the optimized punctured ZCZPS that is constructed by the method mentioned in the last part, the autocorrelation and cross correlation properties can be simulated and analyzed with Matlab. For example, the optimized punctured ZCZPS  $(X, Y)$  is constructed by 31-length optimized punctured binary sequence-pair  $(u, v)$ ,  $u = [++++- - - + - + - + + - - - + - - + - - + + - + + -]$ ,  $v = [++++000 + 0 + 0 + + + 0000 + 00 + 00 + + + 0 + + 0]$  (using '+' and '-' symbols for '1' and '-1') and Hadamard matrix  $H$  of order 4. We follow the three steps presented in Section B to construct the 124-length optimized punctured ZCZPS. The number of sequence-pairs here is 4, and the length of each sequence is  $31 * 4 = 124$ . The first row of each matrix  $X = [x_1; x_2; x_3; x_4]$  and  $Y = [y_1; y_2; y_3; y_4]$  constitute a certain optimized punctured ZCZP  $(x_1, y_1)$ . Similarly, the second row of each matrix  $X$  and  $Y$  constitute another optimized punctured

ZCZ sequence-pair  $(x_2, y_2)$  and so on.

$$x_1 = [++++- --+ - + - + + + - - - - + - - + - - + + + - + + - + + + + - - - + \\ - + - + + + - - - - + - - + - - + + + - + + - + + + + - - - + - + - + + + - - - \\ - + - - + - - + + + - + + - + + + + - - - + - + - + + + - - - - + - + - + + + - \\ - + + + + - + + + - +],$$

$$y_1 = [++++000+0+0++++0000+00+00++++0++0++0++000+0+0++++000 \\ 0+00+00++++0++0++++000+0+0++++0000+00+00++++0++0++++ \\ +000+0+0++++0000+00+00++++0++0];$$

$$x_2 = [+ - + - - + - - - - - + - - + - + + + - - - + + - + + + - - - + - + + - + + \\ + + + - + + - + - - - + + + - - + - - - + + + - + - - + - - - - - + - - - + - \\ + + + - - - + + - + + + - - - + - + + - + + + + + + - + + - + - - - + + + - - \\ + - - - + +],$$

$$y_2 = [+ - + - 000-0-0-+-0000+00-00+-+0+-0-+-+000+0+0+-+00 \\ 00-00+00-+-0-+0+-+000-0-0-+-0000+00-+00+-+0+0+-+ \\ 0-++-++000+0+0+-+0000-00+00-+-0-+0].$$

Optimized punctured ZCZ sequence-pairs  $(x_1, y_1)$  and  $(x_2, y_2)$  are simulated and investigated in the following parts.

#### 4.1 Autocorrelation and Cross Correlation Properties

The autocorrelation property and cross correlation property of 124-length optimized punctured ZCZ sequence pair set  $(X, Y)$  are shown in Figs. 1 and 2.

From the Figs. 1 and 2, the sidelobe of autocorrelation of ZCZPS can be as low as 0 when the

time delay is kept within  $Z_0 = N_1 = 31$  (zero correlation zone) and the cross correlation value is kept as low as 0 during the whole time domain.

It is known that a suitable criterion for evaluating code of length  $N$  is the ratio of the peak signal divided by the peak signal sidelobe (PSR) of their autocorrelation function, which can be bounded by [14]

$$[PSR]_{dB} \leq 20 \log N = [PSR_{max}]_{dB} \quad (13)$$

The only uniform phase codes that can reach the  $PSR_{max}$  are the Barker codes whose length is equal or less than 13. The sidelobe of the new code shown in Fig. 1 can be as low as 0, and the peak signal divided by the peak signal sidelobe can be as large as infinite. Besides, the length of the new code is various and much longer than the length of the Barker code.

## 4.2 Ambiguity Function

When the transmitted impulse is reflected by a moving target, the reflected echo signal includes a linear phase shift which corresponds to a Doppler shift  $f_d$  [14]. As a result of the Doppler shift  $f_d$ , the main peak of the autocorrelation function is reduced. At the same time, the SNR degradation occurs as following:

$$[d]_{dB} = 10 \log \frac{\int_0^T x(s)x^*(s)ds}{\int_0^T x(s)e^{j2\pi f_d T_c}x^*(s)ds} \quad (14)$$

In addition, the sidelobe structure is changed because of the Doppler shift.

The ambiguity function which is usually used to analyze the radar performance within Doppler shift can be found in [14] shown as following:

$$y(t, F_D) = \int_{-\infty}^{\infty} x(s)e^{j2\pi F_D s}x^*(s-t)ds \equiv \hat{A}(t, F_D) \quad (15)$$

where  $t$  is the time delay and  $F_D$  is the Doppler shift.

An equivalent definition can be given in terms of the signal spectrum by applying basic Fourier transform properties

$$\hat{A}(t, F_D) = \int_{-\infty}^{\infty} X^*(F)X(F - F_D)e^{j2\pi Ft}dF \quad (16)$$

The *ambiguity function* is defined as the magnitude of  $\hat{A}(t, F_D)$  [14] as following:

$$A(t, F_D) \equiv |\hat{A}(t, F_D)| \quad (17)$$

However, we are focusing on optimized punctured ZCZPS in this research, so the transmitting code and the receiving code are not the same. The ambiguity function for ZCZPS can be rewritten as

$$y_{pair}(t, F_D) = \int_{-\infty}^{\infty} x^{(p)}(s)e^{j2\pi F_D s}y^{(q)*}(s - t)ds$$

where  $p, q = 0, 1, 2, \dots, K - 1$

$$\hat{A}_{pair}(t, F_D) = \int_{-\infty}^{\infty} X^{(p)*}(F)Y^{(q)}(F - F_D)e^{j2\pi Ft}dF$$

$$\text{where } p, q = 0, 1, 2, \dots, K - 1 \quad (18)$$

The *ambiguity function* is defined as the magnitude of  $\hat{A}_{pair}(t, F_D)$  as following:

$$A_{pair}(t, F_D) \equiv |\hat{A}_{pair}(t, F_D)| \quad (19)$$

In addition, assume the ZCZPS are  $(X, Y)$ ,  $x^{(p)} \in X$ ,  $x^{(p)} = \sum_{n=0}^{N-1} x_n^{(p)}(t - nT_s)$  and  $y^{(p)} \in Y$ ,  $y^{(q)} = \sum_{n=0}^{N-1} y_n^{(q)}(t - nT_s)$ , since the periodic correlation is used instead of aperiodic correlation in

this paper. The  $\hat{A}_{pair}(t, F_D)$  in one period of length  $NT_s$  can be expressed as:

$$\begin{aligned}
& |\hat{A}_{pair}(t, F_D)| \\
&= \left| \int_0^t x^{(p)}(s) y^{(q)*}(s + (NT_s - t)) e^{j2\pi F_D s} ds \right. \\
&\quad \left. + \int_t^{(N-1)T_s} x^{(p)}(s) y^{(q)*}(s - t) e^{j2\pi F_D s} ds \right| \\
& p, q = 0, 1, 2, \dots, K - 1
\end{aligned} \tag{20}$$

At the same time, when  $p = q$ , equation (21) can be used to analyze the autocorrelation performance within Doppler shift; and when  $q \neq p$ , equation (21) can be used to analyze the cross correlation performance within Doppler shift. Equation (21) is plotted in Fig. 3 in a three-dimensional surface plot to analyze the radar performance of optimized punctured ZCZPS within Doppler shift. Here, maximal time delay is 1 unit (normalized to length of the code, in units of  $NT_s$ ) and maximal doppler shift is 5 units for cross correlation and 3 units for autocorrelation (normalized to the inverse of the length of the code, in units of  $1/NT_s$ ).

In Fig. 3(a), there is relative uniform plateau suggesting low and uniform sidelobes. This low and uniform sidelobes minimize target masking effect in zero correlation zone of time domain, where  $Z_0 = 31$ ,  $-31 < \tau < 31$ . From Fig. 3(b), considering cross correlation property between any two optimized punctured ZCZ sequence-pairs among the ZCZ sequence-pair set, 124-length optimized punctured ZCZPS is tolerant of Doppler shift when Doppler shift is not large. When the Doppler shift is zero, the range sidelobe of cross correlation of our proposed code is zero in the whole time domain.

As synchronization technology develops exponentially in the industrial world, time delay can, to some extent, be well controlled. Therefore, it is necessary to investigate the performance of our proposed code without time delay. When  $t = 0$ , the ambiguity function can be expressed as:

$$\hat{A}_{pair}(0, F_D) = \int_0^{T_s} x^{(p)}(s) y^{(q)*}(s) e^{j2\pi F_D s} ds \tag{21}$$

And the doppler shift performance without time delay is presented in the Fig. 4.

Fig. 4(a) illustrates that without a time delay and having the Doppler shift less than 1 unit, the autocorrelation value of optimized punctured ZCZPS falls sharply during one unit, and the trend of the amplitude over the whole frequency domain decreases as well. Fig. 4(b) shows that there are some convex surfaces in the cross correlation performance. One should observe Figs.4(a) and 4(b), when Doppler frequencies equal to multiples of the pulse repetition frequency ( $PRF = 1/PRI = 1/T_s$ ), all the ambiguity value turns to zero except when Doppler frequency is equal to 2 PRF for cross correlation. That is the same as many widely used pulse compression binary code such as the Barker code. Overall, the ambiguity function performances of optimized punctured ZCZP can be as efficient as conventional pulse compression binary code.

## 5 Application to Radar System

According to [14],  $P_D$  (Probability of Detection),  $P_{FA}$  (Probability of False Alarm) and  $P_M$  (Probability of Miss) are three probabilities of most interest in the radar system. Note that  $P_M = 1 - P_D$ , thus,  $P_D$  and  $P_{FA}$  suffice to specify all of the probabilities of interest in radar system. Therefore, we simulated the above three probabilities of optimized punctured ZCZ sequence-pair in radar system in this section. The performance of 124-length P4 code is also provided in order to compare with the performance of punctured binary optimized punctured ZCZ sequence-pair of corresponding length. In the simulation model,  $10^5$  times of Monte-Carlo simulation has been run for each SNR value. The Doppler shift frequency that is kept less than 1 unit (normalized to the inverse of the length of the code, in units of  $1/NT_s$ ) is a random variable, and the time delay is assumed zero. Also, the threshold detection is used in this coherent system where the threshold is adaptively adjusted.

In Fig. 5, the probabilities of miss target detection  $P_M$  of the system using 124-length optimized punctured ZCZ sequence-pair are lower than 124-length P4 code especially when the SNR is not

large. When SNR is larger than 18 dB, both probabilities of miss targets of the system approaches zero. However, the probabilities of miss targets of P4 code fall more quickly than optimized punctured ZCZ sequence-pair.

We plotted the detection probability  $P_D$  versus false alarm probability  $P_{FA}$  of the coherent receiver in Fig. 6.

Fig. 6 shows performance of 124-length optimized punctured ZCZ sequence-pair and the same length P4 code when the SNR is 10dB and 14dB. Within the same SNR value either 10dB or 14dB, the detection probabilities of 124-length optimized punctured ZCZ sequence-pair are much larger than detection probabilities of 124-length P4 code, and meanwhile false alarm probabilities of the first code are also smaller than  $P_{FA}$  of the latter code. In some other words, 124-length optimized punctured ZCZ sequence-pair has higher target detection probability while keeping a lower false alarm probability. Furthermore, observe Fig. 6, 124-length optimized punctured ZCZ sequence-pair even has much better performance with 10dB SNR than 124-length P4 code with 14dB SNR.

## 6 Conclusions

The definition and properties of a set of newly provided triphase coded waveforms-ZCZ sequence-pair set were discussed in this paper. Based on optimized punctured sequence-pair and Hadamard matrix, we have investigated a constructing method for the triphase coded waveform-optimized punctured ZCZPS made up of a set of optimized punctured ZCZPs along with studying its properties. The significant advantage of the optimized punctured ZCZPS is a considerably reduced sidelobe as low as zero in the zero correlation zone and zero mutual cross correlation value in the whole time domain. The disadvantage of our proposed code is that the number of the sequences in the set depends on the order of Hadamard matrix that is limited by  $2^k$ , ( $k = 0, 1, \dots$ ). According to the radar system simulation results shown in Figs.5 and 6, it is easy to observe that 124-length

optimized punctured ZCZPS has better performance than 124-length P4 code when the Doppler shift is kept less than 1 unit (normalized to the inverse of the length of the code, in units of  $1/NT_s$ ). A general conclusion can be drawn that the optimized punctured ZCZPs in an optimized punctured ZCZPS can effectively increase the variety of candidates for pulse compression codes if and only if optimized punctured ZCZPS has much better autocorrelation and cross correlation properties than the optimum biphase codes (longer than 13), whose autocorrelation sidelobes and cross correlation peak value have been found to be both approximately  $\sqrt{N}$ . Because of the ideal cross correlation properties of optimized punctured ZCZPS, future work would focus on the application of the optimized punctured ZCZPS in multiple radar systems.

## Acknowledgement

This work was supported by the Office of Naval Research (ONR) Grant N00014-07-1-0395, N00014-07-1-1024, and N00014-03-1-0466.

## References

- [1] S. Ariyavisitakul, N. Sollenberger, and L. Greenstein, *Introduction to Radar System*, Tata McGraw-Hill, 2001.
- [2] A. M. Boehmer, "Binary pulse compression codes," *IEEE Trans. Informaion Theory*, vol.IT-13, pp.156-167, April 1967.
- [3] R. Turyn, "On Barker codes of event length," *Proc. IEEE*, vol.51,9.1256, September 1963.
- [4] U. Somaini, "Bianry sequences with good autocorrelation and cross correlation properties," *IEEE Transactions on Acrospace and Electronic Systems*, AES-11, 6, 1226-1231, Nov.1975.

- [5] R. L. Frank, "Polyphase codes with good nonperiodic correlation properties", *IEEE Transactions on Information Theory*, IT. -9, pp. 43-45, Jan. 1963.
- [6] B. L. Lewis and F. F. Kretschuner, "A new class of polyphase pulse compression codes and techniques", *IEEE Transactions on Aerospace and Electronic Systems*, AES-17, pp. 364-372, May. 1981.
- [7] B. L. Lewis and F. F. Kretschuner, "Linear frequency modulation derived polyphase pulse compression codes", *IEEE Transactions on Aerospace and Electronic Systems*, AES-18, pp. 637-641, Sep. 1982.
- [8] P. Z. Fan, N. Suehiro, N. Kuroyanagi and X. M. Deng, "A class of binary sequences with zero correlation zone," *IEE Electron.Letter*, 35 (10): 777-779, 1999.
- [9] P. Z. Fan and L. Hao, "Generalized Orthogonal Sequences and Their Applications in Synchronous CDMA Systems," *IEICE Trans.Fundamentals*, E832A(11): 1 16, 2000.
- [10] P. Z. Fan, "New Direction in Spreading Sequence Design and the Related Theoretical Bounds," *International Conference of Communications , Circuits and Systems*, June 29-July 1, 2002, PRC.
- [11] S. Matsufuji, N Suehiro , N Kuroyanagi and P Z Fan, "Two types of polyphase sequence set for approximately synchronized CDMA systems," *IEICE Trans. Fundamentals*, E862A(1): 229-234, Jan. 2003.
- [12] H. Torii, M. Nakamura and N. Suehiro, "A new class of zero correlation zone sequences," *Tran. Inform.Theory*, 50: 559-565, Mar. 2004.
- [13] T. Jiang, *Research on Quasi-Optimized Binary Signal Pair and Perfect Punctured Binary Signal Pair Theory*, Ph.D Dissertation: Yanshan University, 2003.

- [14] M.A.Richards, *Fundamentals of Radar Signal Processing*, McGraw-Hill, 2005.

## List of Figures

1	Periodic autocorrelation property of optimized punctured ZCZPS . . . . .	19
2	Periodic cross correlation property of optimized punctured ZCZPS . . . . .	20
3	Periodic autocorrelation property of optimized punctured ZCZPS . . . . .	20
4	Periodic cross correlation property of optimized punctured ZCZPS . . . . .	21
5	Ambiguity function of 124-length ZCZPS: (a) autocorrelation (b) cross correlation . . . . .	22
6	Doppler shift of 124-length ZCZPS (time delay=0): (a) autocorrelation (b) cross correlation . . . . .	23
7	Probability of miss targets detection (No time delay, Doppler shift less than 1): 124-length optimized punctured ZCZ sequence-pair VS. 124-length P4 code . . . . .	24
8	Probability of detection versus probability of false alarm of the coherent receiver(No time delay, Doppler shift less than 1) : 124-length optimized punctured ZCZ sequence- pair VS. 124-length P4 code . . . . .	24

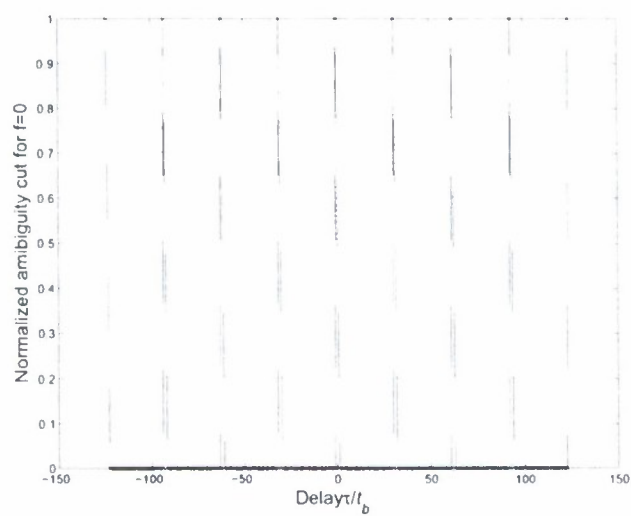


Figure 1: Periodic autocorrelation property of optimized punctured ZCZPS

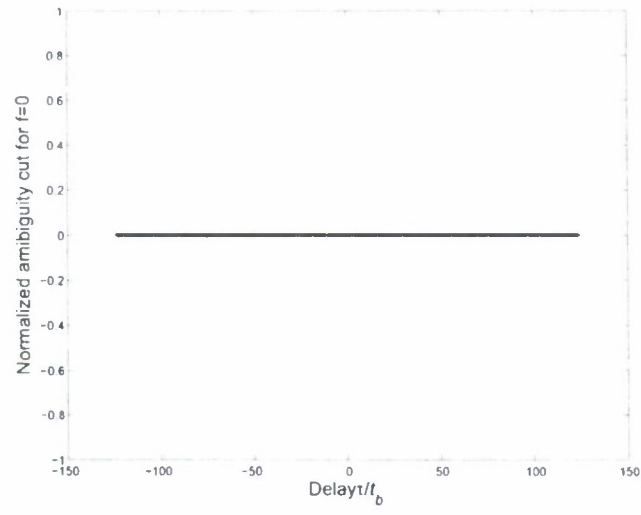


Figure 2: Periodic cross correlation property of optimized punctured ZCZPS

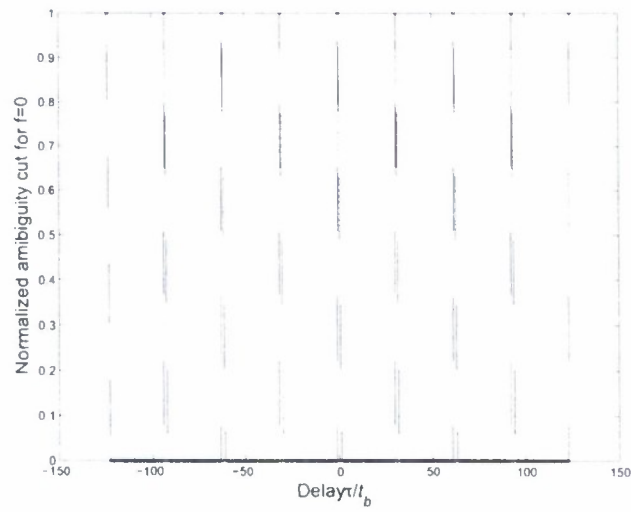


Figure 3: Periodic autocorrelation property of optimized punctured ZCZPS

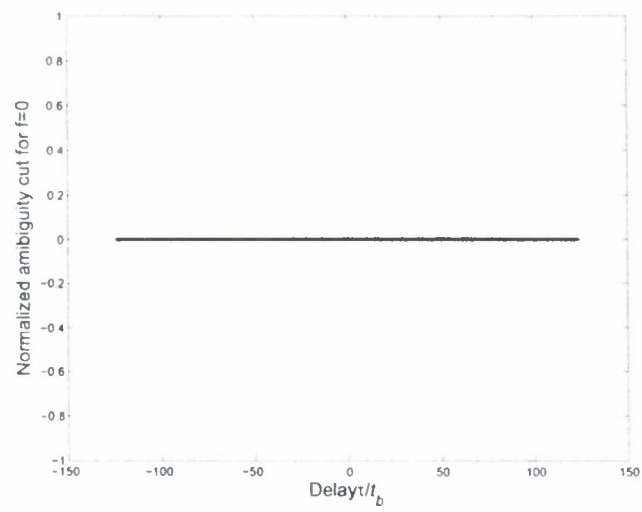
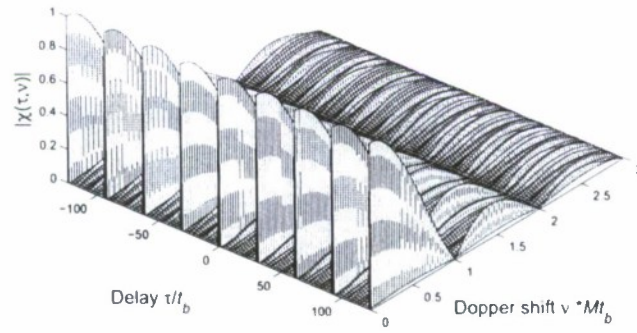
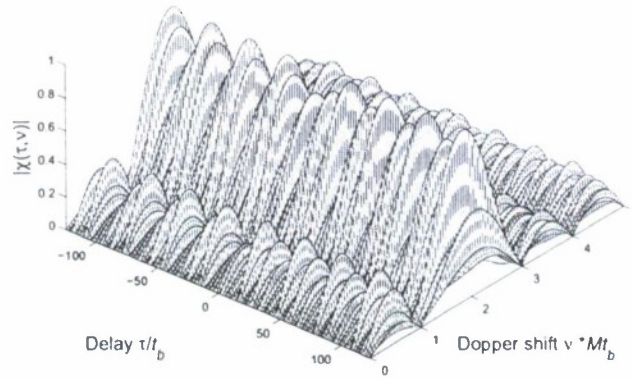


Figure 4: Periodic cross correlation property of optimized punctured ZCZPS

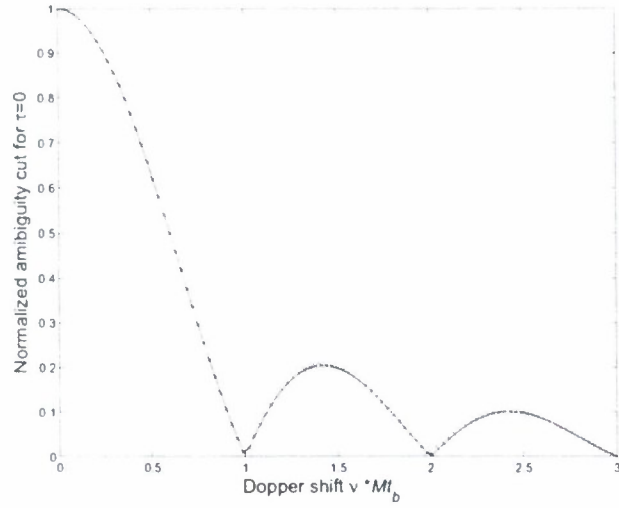


(a)

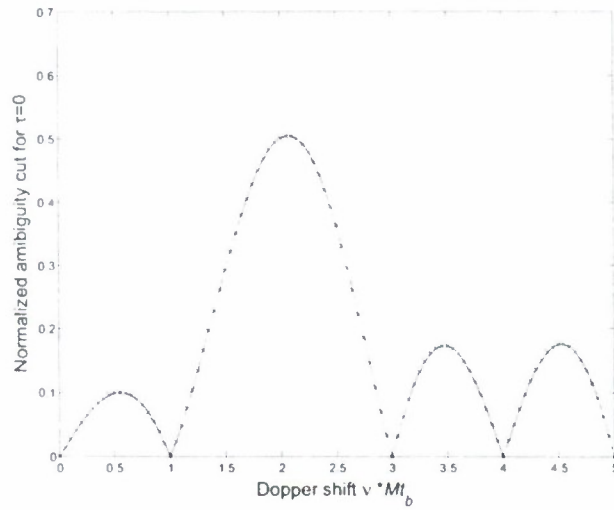


(b)

Figure 5: Ambiguity function of 124-length ZCZPS: (a) autocorrelation (b) cross correlation



(a)



(b)

Figure 6: Doppler shift of 124-length ZCZPS (time delay=0): (a) autocorrelation (b) cross correlation

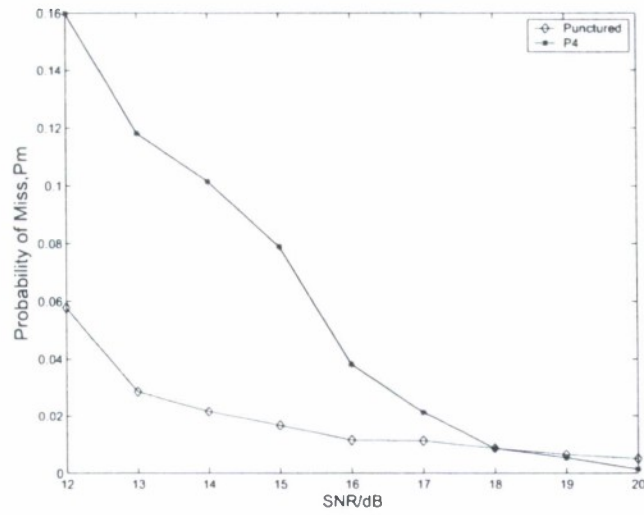


Figure 7: Probability of miss targets detection (No time delay, Doppler shift less than 1): 124-length optimized punctured ZCZ sequence-pair VS. 124-length P4 code

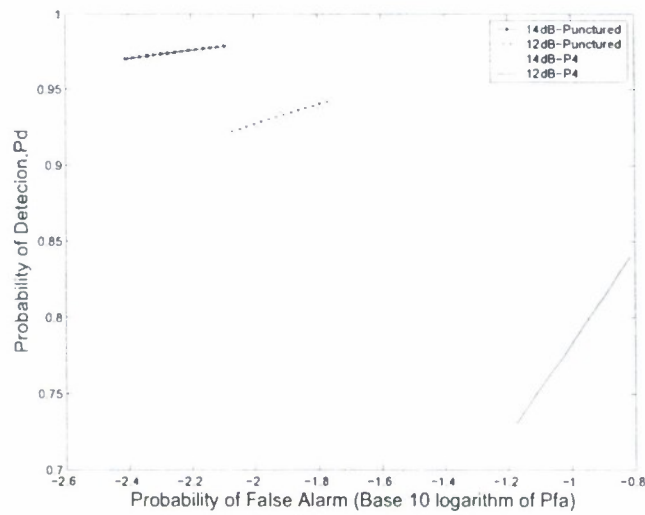


Figure 8: Probability of detection versus probability of false alarm of the coherent receiver (No time delay, Doppler shift less than 1) : 124-length optimized punctured ZCZ sequence-pair VS. 124-length P4 code

# Combined-Jamming Interference Analysis for FH/MFSK Multi-Radio Wireless Mesh Networks

Davis Kirachaiwanich, and Qilian Liang

**Abstract**—For the past decades, the performances of frequency-hopping systems under various jamming strategies have been investigated. In this paper, we consider the performance of the noncoherent slow frequency-hopping system with  $M$ -ary frequency-shift-keyed modulation (NC-FH/MFSK) under independent multitone jamming (IMTJ) and under partial-band jamming (PBJ). The exact BER expressions of the system under each jamming strategy are derived. Then, we combine the two expressions together to develop a new interference model for multi-radio frequency-hopping wireless mesh networks (MR-FH WMN). Because it takes into account both the cochannel and the coexisting-network interferences, the new interference model thus reflects a very realistic interference situation and it can be incorporated to the channel assignment (CA) algorithms to assign appropriate channels (or hopping pattern, in our case) to interfaces of the routers in the mesh network. In addition, we also compare the performances of NC-FH/4FSK system under the two jamming strategies, the numerical results have illustrated that PBJ is more effective jamming strategy than IMTJ.

**Index Terms**—Frequency hopping, MFSK, fading channel, independent multitone jamming, partial-band jamming, interferences, wireless mesh network.

## 1 INTRODUCTION

THE performances of noncoherent slow frequency-hopping system with  $M$ -ary frequency-shift-keyed modulation (NC-FH/MFSK) under various hostile jamming strategies have been widely studied in several publications in the past decades. Multitone jamming (MTJ) refers to the set of jamming strategies in which total power of jamming source is equally partitioned into multiple interference tones. The band multitone jamming (BMTJ) denotes the jamming strategy where each jammed frequency-hopping (FH) band is jammed by a specific number of the interference tones, randomly distributing within the FH band. Compared to the BMTJ, the independent multitone jamming (IMTJ) is a similar but more flexible jamming strategy. In IMTJ, there is no restriction regarding how many interference tones should be placed in each jammed FH band. The interference tones from the jamming source will randomly distribute across the entire communication bandwidth. Hence, with IMTJ, the number of interference tones in a jammed FH band can be as few as one and as many as  $M$  interference tones.

In [1], an expression for calculating the bit error rate (BER) for NC-FH/MFSK with additive white Gaussian noise (AWGN) and Rician fading under worst-case BMTJ has been derived and the BER performance of an NC-FH/BFSK ( $M=2$ ) system has been chosen to illustrate the effect of BMTJ in comparison to that of IMTJ. Later,

[2] has proposed an alternative approach to combine signal and other wideband interferences together as a single Gaussian process, which leads to a computational-effective BER expression compared to [1]. In [3], the performance of NC-FH/MFSK system with AWGN and Rician fading under IMTJ was investigated and the exact BER for the NC-FH/MFSK system has first been derived.

In contrary to the first two jamming strategies, the partial-band jamming (PBJ) is the term use to represent the jamming strategy where the total jamming power is spreaded evenly over a certain band of the entire communication bandwidth, rather than equally partitioned into certain number of interference tones. The interfering signal from the jamming source will be of similar characteristic to AWGN, except that it exists in only a fraction of the entire bandwidth. The BER performance of NC-FH/MFSK system under PBJ has previously been considered in many of the literature, for example [4]–[8].

In this paper, we derive the exact BER expressions for NC-FH/MFSK system with Rician fading channel under IMTJ and PBJ strategies. For IMTJ, we have adapted the notions in [1] and [2] for the system under BMTJ to derive a new analysis, which can be considered as an alternative approach to one used in [3]. It predicts the same BER performance as reported in [3] for NC-FH/4FSK system, but with the improvement of one numerical integration less. Then combining together the BER expressions derived for the system under the two jamming strategies, we subsequently develop a new interference model, so-called combined-jamming model, suitable for multi-radio frequency-hopping wireless mesh networks (MR-FH WMNs). As an illustration, we also provide an example application of the combined-jamming model on

• Authors are with Department of Electrical Engineering, University of Texas at Arlington, Arlington, TX, 76011.  
E-mail: davis.kirachaiwanich@mavs.uta.edu, liang@uta.edu

an MR-FH WMN where each router node in the mesh is equipped with multiple NC-FH/MFSK interfaces.

WMN has recently become a very promising alternative for establishing wireless backbone for communication networks. Our choice of FH/MFSK modulation in the MR-FH WMN not only allows multiple router nodes to access the shared media concurrently, but it also conceals the transmissions from physical layer attacks, [20] and [21], and provides ease in implementing the router nodes. As FH/MFSK modulation technique has been specified in IEEE 802.11 standard, these router nodes can be easily implemented using commercial off-the-shelf (COTS) IEEE 802.11(FH) equipment. Generally, the IEEE standard FH equipment uses ISM band (2.4GHz-2.4835GHz) as the operational bandwidth and divides it into 79 FH bands to support the FH modulation technique. And to prevent signals from collisions (cochannel interference), the FH bands are further grouped into three interleaving and non-colliding hopping patterns with 26 FH bands per pattern [16].

Obviously, if we can assign hopping patterns properly to the interfaces of each router node in our MR-FH WMN, cochannel interferences will decrease significantly; thus, the mesh capacity increases. Should we consider hopping patterns as radio channels in IEEE 802.11 a/b/g, the assignment of hopping patterns is hence equivalent to the assignment of channels to radio interfaces. Using the new interference model, we can then estimate the costs associated with assigning each hopping pattern to an interface and allow us to apply the channel assignment (CA) algorithms for IEEE 802.11 a/b/g WMNs, [12]- [15], to assign hopping patterns to interfaces in MR-FH WMN.

Additionally, this paper also investigates the degradation of the performance of NC-FH/MFSK system caused by IMTJ and PBJ. For each jamming strategy, we provide an analysis to determine the condition under which the worst system performance occurs. Then, by comparing the worst-case results obtained, we determine either IMTJ or PBJ is more effective jamming strategy.

## 2 NC-FH/MFSK SYSTEM UNDER IMTJ

All FH systems in this paper are assumed to be slow hopping systems over  $N$  non-overlapping FH bands. Each FH band is comprised of  $M = 2^K$  signal frequencies of the  $M$ -ary FSK modulation. Hence, there are  $NM$  possible frequency slots and, in each hop, one of these slots will be chosen for transmitting a signal tone. If all FH bands are contiguous, the entire communication bandwidth thus equals to  $B_T = NB_h$ , where  $B_h$  is the bandwidth of an FH band. Also, we assume that the transmission bit rate of the system is  $R_b = KR_s = K/T_s$ , where  $T_s$  is the symbol period and  $R_s = 1/T_s$  denotes the symbol transmission rate. Without the effect of fading channel, the average received power for every symbol transmitted is assumed to be  $P_s$  or equal to an average symbol energy of  $E_s = P_s T_s$ . Therefore, the received bit energy can be calculated by  $E_b = E_s / \log_2 M$ .

With IMTJ strategy, the jamming source is assumed to transmit  $q \in [1, NM]$  interference tones, which are distinct and randomly distributed over the entire bandwidth  $B_T$ . If we assume that the total interference power received at the receiver is  $P_{jT}$  and each interference tone equally contributes this power, the received power for each interference tone therefore equals  $P_j = P_{jT}/q$  or the received energy of  $E_j = P_j T_s = P_{jT} T_s / q$ .

The signal tone and interference tones are assumed to undergo independent fading channels before arriving at the receiver with noncoherent detection scheme. Besides, all fading channels in this study are assumed to be slow fading, frequency non-selective Rician processes, whose PDF is of the following form

$$f_{X_k}(x_k) = \frac{x_k}{\sigma_k^2} \exp\left(-\frac{x_k^2 + \alpha_k^2}{2\sigma_k^2}\right) I_0\left(\frac{\alpha_k x_k}{\sigma_k^2}\right) u(x_k) \quad (1)$$

where  $I_0(\cdot)$  denotes the zero<sup>th</sup> order modified Bessel function and  $u(\cdot)$  is the unit step function.  $\alpha^2$  and  $2\sigma^2$  are the average power of the LOS (Line-Of-Sight) and the scattering rays of the fading channel. We can also define another parameter to determine the Rician fading channel by using the ratio of  $\alpha^2$  and  $2\sigma^2$ , i.e.  $K_k = \alpha_k^2 / 2\sigma_k^2$  where  $k=1,2$ .  $K_1$  is the Rician factor of the fading channel for signal tone and  $K_2$  is for the interference tones.

At the receiver, the received signal is de-hopped and noncoherently detected. It is assumed that each symbol of the  $M$ -ary FSK is equally likely. The receive signal after de-hopped can be represented as

$$r_i(u, t) = x_k \sqrt{2P_i} \cos(\omega_m t + \phi_i) + n(u, t) \quad (2)$$

where  $x_k$  is a Rician random variable representing the envelope of the fading channel and its PDF can be represented as (1).  $P_i$  is the average received power of the tone if the effect of fading channel is not accounted. The subscript  $i=s,j$  denotes signal tone and interference tone respectively.  $\omega_m$ ,  $m=1,2,\dots,M$ , is angular frequency for an MFSK symbol and  $\phi$  is unknown phase.  $n(u, t)$  is AWGN with total power  $\sigma_n^2 = N_0/T_s$ .

Since the interference tones are distinct and randomly distributed, in a jammed FH band, there can be as few as one and as many as  $\min(q, M)$  interference tones. Hence, the probability of symbol error (or symbol error rate, SER) of the NC-FH/MFSK system can be calculated by

$$P_s(e) = P_0 \cdot P_{s0}(e) + \sum_{n=1}^{\min(q, M)} P_n \cdot P_{sn}(e) \quad (3)$$

where  $P_s(e)$  is the total SER.  $P_0$  and  $P_n$  are the probabilities that an FH band is jammed by zero and  $n$  interference tones, where  $1 \leq n \leq \min(q, M)$ .  $P_{s0}(e)$  and  $P_{sn}(e)$  are the SER's corresponding to the specific number of interference tones in the FH band. Then, for MFSK system, the probability of bit error (bit error rate, BER) can be calculated from the total SER by

$$P_b(e) = \frac{M/2}{M-1} P_s(e) \quad (4)$$

## 2.1 Probability of symbol error with no interference tone

If the jammer transmits  $q$  interference tones using  $q$  random frequency slots from  $NM$  possible frequency slots in the entire bandwidth, the probability that an FH band does not contain any interference tone can be given by

$$P_0 = \prod_{k=0}^{M-1} \left(1 - \frac{q}{NM - k}\right) \quad (5)$$

Generally for noncoherent detection scheme, the outputs of the envelope detector in the branch where signal tone, or interference tone (or both) is/are present will have its PDF followed Rician distribution while the other output branches with AWGN only, are known to follow just Rayleigh distributions, which can be expressed by replacing  $\alpha_k$  in (1) with zero. Therefore, the SER when an FH band contains no interference tone, given the envelope of the Rician channel of signal tone is known, can be calculated using [1] [23],

$$\begin{aligned} P_{s0}(e|no \text{ int. tone}, x_1) &= P(|S + n(u)| < |n(u)| | x_1)^{M-1} \\ &= \sum_{v=1}^{M-1} \frac{(-1)^{v+1}}{v+1} \binom{M-1}{v} \exp\left[\frac{-vP_s x_1^2}{(v+1)\sigma_n^2}\right] \end{aligned} \quad (6)$$

Multiplying the Rician PDF in (1) to (6) and integrating the resulting product with respect to  $x_1$ , we can obtain the SER when an FH band contains no interference in the form of [1],

$$\begin{aligned} P_{s0}(e|no \text{ int. tone}) &= \sum_{v=1}^{M-1} \frac{(-1)^{v+1}}{1+v(1+\frac{2\sigma_s^2}{\sigma_n^2})} \binom{M-1}{v} \\ &\quad \cdot \exp\left[\frac{-v\frac{\alpha_s^2}{\sigma_n^2}}{1+v(1+\frac{2\sigma_s^2}{\sigma_n^2})}\right] \end{aligned} \quad (7)$$

where  $\alpha_s^2$  and  $2\sigma_s^2$  are the average LOS power and the average scattering powers of the signal. These parameter can be expressed in general as

$$\alpha_i^2 = P_i \alpha_k^2, \quad \sigma_i^2 = P_i \sigma_k^2 \quad (8)$$

with the subscript  $i=s,j$ , and  $\alpha_k^2$  and  $2\sigma_k^2$ , where  $k=1,2$ , are averaged LOS and scattering powers of the channel for signal and interference tones respectively.

## 2.2 Probability of symbol error when signal branch jammed

For an NC-FH/MFSK system with  $NM$  possible frequency slots, the probability that an FH band will be jammed by  $n$  interference tones, where  $1 \leq n \leq \min(q, M)$  is given as

$$P_n = \prod_{k=0}^{n-1} \left(\frac{q-k}{NM-k}\right) \prod_{j=n}^{M-1} \left(1 - \frac{q-n}{NM-j}\right) \quad (9)$$

Provided that an FH band is jammed by  $n$  interference tones, there are two possible cases. First is the case when the signal tone is jammed by one of  $n$  interference tones in the FH band and the probability that one out of  $n$  interference tones will jam the signal is  $n/M$ . Second is when none of  $n$  interference tones is located in the same frequency slot as the signal, i.e. the signal is not jammed. The probability of the second case is  $(M-n)/M$ . The SER when an FH band is jammed by  $n$  interference tones can be expressed as

$$\begin{aligned} P_{sn}(e|n \text{ int. tones}) &= \left(\frac{n}{M}\right) P_{sn}(e|signal \text{ is jammed}) \\ &\quad + \left(\frac{M-n}{M}\right) P_{sn}(e|signal \text{ is not jammed}) \end{aligned} \quad (10)$$

To evaluate the SER when the signal is jammed, [2] has provided a computational-efficient method based on the use of phasor representations and noncentral chi squared PDF's. It can be shown for any two Rician random variables, say  $R_{01}$  and  $R_{02}$ , that  $P(R_{01} > R_{02}) = P(R_{01}^2 > R_{02}^2)$ . In (3) of [2], the probability is given as

$$\begin{aligned} P(R_{01} > R_{02}) &= P(R_{01}^2 > R_{02}^2) \\ &= Q\left(\sqrt{\frac{2K_{01}}{b+1}}, \sqrt{\frac{2K_{02}b}{b+1}}\right) \\ &\quad - \left(\frac{b}{b+1}\right) \exp\left(-\frac{K_{01} + K_{02}b}{b+1}\right) \\ &\quad \cdot I_0\left(\frac{\sqrt{4K_{01}K_{02}b}}{b+1}\right) \end{aligned} \quad (11)$$

where  $K_l = \alpha_l^2/2\sigma_l^2$ ,  $l = 01, 02$ , are Rician factor for  $R_{01}$  and  $R_{02}$  respectively,  $b = \sigma_{02}^2/\sigma_{01}^2$ , and  $Q(x,y)$  is the Marcum's Q function. Without loss of generality we can assume that the signal is present in the first output branch of the detector, as well as one of the  $n$  interference tones that jam the signal tone. And we will assume also that the rest  $n-1$  interference tones are in the next consecutive branches. Therefore, 1<sup>st</sup> to  $n^{\text{th}}$  output branches of the envelope detector will have their PDF follow Rician distributions and the output of the rest  $M-n$  branches will follow Rayleigh distributions. Furthermore, when the signal tone in the first output branch is jammed, the averaged LOS power in the branch can be expressed as

$$\alpha_{sj}^2 = \alpha_s^2 + \alpha_j^2 + 2\alpha_s\alpha_j \cos \varphi \quad (12)$$

where  $\varphi$  is the random phase difference between received signal tone and interference tone and is assumed to uniformly distributed between 0 to  $2\pi$ . So, the SER given the signal is jammed can be calculated by

$$\begin{aligned} P_{sn}(e|signal \text{ is jammed}) &= 1 - P(R_{01} > R_{02} \cap R_{01} > R_{03} \cap R_{01} > R_{04} \dots) \\ &= 1 - \prod_{k=2}^n P(R_{01} > R_{0k}) \prod_{j=n+1}^M P(R_{01} > R_{0j}) \\ &= 1 - P(R_{01} > R_{02})^{n-1} \cdot P(R_{01} > R_{0M})^{M-n} \end{aligned} \quad (13)$$

where  $R_{01}, R_{02}, \dots, R_{0M}$  represent the random outputs at  $1^{st}, 2^{th}, \dots, M^{th}$  branches of the detector. The second equality in (13) is obtained by using the fact that each output of the detector branches is independent of each other. Now, we will consider separately the first product term on RHS of the second equality in (13). For given  $\varphi$ , the conditional probability  $P(R_{01} > R_{02}|\varphi)$  can be evaluated easily by substituting the following parameters into (11)

$$\begin{aligned} K_{01} &= \frac{\alpha_{sj}^2}{2\sigma_s^2 + 2\sigma_j^2 + \sigma_n^2}, & K_{02} &= \frac{\alpha_j^2}{2\sigma_s^2 + \sigma_n^2} \\ b &= \frac{2\sigma_j^2 + \sigma_n^2}{2\sigma_s^2 + 2\sigma_j^2 + \sigma_n^2} \end{aligned} \quad (14)$$

Similarly, if we treat Rayleigh random variable as a special case for Rician random variable, we can obtain the probability for the second product term with condition on  $\varphi$  as

$$\begin{aligned} P(R_{01} > R_{0M}|\varphi) &= 1 - \frac{\sigma_n^2}{2(\sigma_s^2 + \sigma_j^2 + \sigma_n^2)} \\ &\cdot \exp\left[-\frac{\alpha_{sj}^2}{2(\sigma_s^2 + \sigma_j^2 + \sigma_n^2)}\right] \end{aligned} \quad (15)$$

Substituting (14) in (11) to obtain the conditional probability of the first product term, using (15) for the conditional probability of the second product term, and integrating (13) over  $\varphi$ , we then obtain the complete expression for the SER for the case as

$$\begin{aligned} P_{sn}(e|\text{signal is jammed}) &= 1 - \frac{1}{2\pi} \int_0^{2\pi} \left\{ Q\left(\sqrt{\frac{\alpha_{sj}^2}{\sigma_T^2 + \sigma_j^2}}, \sqrt{\frac{\alpha_j^2}{\sigma_T^2 + \sigma_j^2}}\right) \right. \\ &\quad \left. - \frac{2\sigma_j^2 + \sigma_n^2}{2(\sigma_T^2 + \sigma_j^2)} \exp\left[-\frac{\alpha_{sj}^2 + \alpha_j^2}{2(\sigma_T^2 + \sigma_j^2)}\right] \right. \\ &\quad \left. \cdot I_0\left(\frac{2\alpha_{sj}\alpha_j}{\sigma_T^2 + \sigma_j^2}\right) \right\}^{n-1} \\ &\quad \cdot \left\{ 1 - \frac{\sigma_n^2}{2\sigma_T^2} \exp\left(-\frac{\alpha_{sj}^2}{2\sigma_T^2}\right) \right\}^{M-n} d\varphi \end{aligned} \quad (16)$$

where

$$\sigma_T^2 = \sigma_s^2 + \sigma_j^2 + \sigma_n^2 \quad (17)$$

### 2.3 Probability of symbol error when signal branch not jammed

When all  $n$  interference tones in the FH band are not in signal branch,  $n+1$  output branches of the envelope detector will follow Rician distributions and the rest  $M-n-1$  branches will follow Rayleigh distributions. Similarly, we will assume that the signal tone is present in the first output branch and  $n$  interference tones are in the next consecutive branches. In this case, the SER can

be expressed as

$$\begin{aligned} P_{sn}(e|\text{signal is not jammed}) &= 1 - P(R_{01} > R_{02} \cap R_{01} > R_{03} \cap R_{01} > R_{04} \dots) \\ &= 1 - \prod_{k=2}^{n+1} P(R_{01} > R_{0k}) \prod_{j=n+2}^M P(R_{01} > R_{0j}) \\ &= 1 - P(R_{01} > R_{02})^n \cdot P(R_{01} > R_{0M})^{M-n-1} \end{aligned} \quad (18)$$

Once again, the probability  $P(R_{01} > R_{02})$  for the second equality of (18) can be calculated by substituting the following parameters into (11)

$$K_{01} = \frac{\alpha_s^2}{2\sigma_s^2 + \sigma_n^2}, \quad K_{02} = \frac{\alpha_j^2}{2\sigma_j^2 + \sigma_n^2}, \quad b = \frac{2\sigma_j^2 + \sigma_n^2}{2\sigma_s^2 + \sigma_n^2} \quad (19)$$

By the same mean, the conditional probability for the second product term is found to be

$$P(R_{01} > R_{0M}) = 1 - \frac{\sigma_n^2}{2(\sigma_s^2 + \sigma_n^2)} \exp\left[-\frac{\alpha_s^2}{2(\sigma_s^2 + \sigma_n^2)}\right] \quad (20)$$

Finally, we can combine together every equations we have derived to compute for the total SER of NC-FH/MFSK system under IMTJ in (3). Then, using (4), we can easily convert the total SER to BER.

### 3 NC-FH/MFSK SYSTEM UNDER PBJ

With PBJ strategy, we will assume that the total interference power received,  $P_{jT}$ , is being spreaded across a continuous bandwidth  $B_j$  using direct sequence spread spectrum modulation (DSSS). If  $B_T$  is the entire bandwidth then the jamming ratio,  $\rho$ , equals  $B_j/B_T \leq 1$ . Instead of interference tones, we are now considering the interference as another kind of noise, in addition to AWGN, with its power spectral density (PSD) equal to

$$N_j = \frac{P_{jT}}{B_j} = \frac{P_{jT}}{B_T} \cdot \frac{B_T}{B_j} = \frac{N_{jT}}{\rho} \quad (21)$$

where  $N_{jT} = P_{jT}/B_T$  is the equivalent PSD level of the interference noise over bandwidth  $B_T$ .

Besides, we will also assume that, if an FH band is jammed, all  $M$  frequency slots of the FH band will be jammed. The probability that an FH band will get jammed thus equals to  $\rho$  whereas the probability that an FH band will not get jammed is  $1-\rho$ . When an FH band is jammed, all of its  $M$  frequency slots will be corrupted by both the interference noise and the thermal AWGN; thus, the total noise power ( $\sigma_T^2$ ) in a jammed FH band can be expressed as

$$\sigma_T^2 = \sigma_j^2 + \sigma_n^2 = \frac{N_{jT}}{\rho T_s} + \frac{N_0}{T_s} \quad (22)$$

where  $\sigma_j^2$  and  $\sigma_n^2$  are the powers of the interference noise and the thermal noise respectively. Now, we can consider the total SER of an NC-FH/MFSK system under PBJ by

$$\begin{aligned} P_s(e) &= P(\text{hop is jammed}) \cdot P_s(e|\text{hop is jammed}) \\ &\quad + P(\text{hop not jammed}) \cdot P_s(e|\text{hop not jammed}) \\ &= \rho \cdot P_s(e|\text{hop is jammed}) \\ &\quad + (1-\rho) \cdot P_s(e|\text{hop not jammed}) \end{aligned} \quad (23)$$

### 3.1 Probability of symbol error given an FH band is jammed

When an FH band is jammed, the interference noise will superimpose AWGN and the total noise power  $\sigma_T^2$  can be found using (22). The SER given that an FH band is jammed can be calculated using (7) with  $\sigma_n^2$  being replaced by  $\sigma_T^2$ . By doing so, we can obtain the SER as

$$P_s(e|hop \text{ is jammed}) = \sum_{v=1}^{M-1} \frac{(-1)^{v+1}}{1 + v(1 + \frac{2\sigma_T^2}{\sigma_n^2})} \binom{M-1}{v} \cdot \exp \left[ \frac{-v \frac{\alpha_T^2}{\sigma_T^2}}{1 + v(1 + \frac{2\sigma_T^2}{\sigma_n^2})} \right] \quad (24)$$

### 3.2 Probability of symbol error given an FH band is not jammed

In contrary, when an FH band is not jammed, AWGN will be the only noise source corrupting the transmitted signal tone. The SER given that an FH band is not jammed can be found using (7).

$$P_s(e|hop \text{ not jammed}) = \sum_{v=1}^{M-1} \frac{(-1)^{v+1}}{1 + v(1 + \frac{2\sigma_n^2}{\sigma_n^2})} \binom{M-1}{v} \cdot \exp \left[ \frac{-v \frac{\alpha_n^2}{\sigma_n^2}}{1 + v(1 + \frac{2\sigma_n^2}{\sigma_n^2})} \right] \quad (25)$$

Then, we must substitute (24) and (25) into (23) to complete the analysis for the SER of the NC-FH/MFSK system under PBJ. Once the total SER is obtained, the BER of the system can also be calculated using (4).

## 4 THE COMBINED-JAMMING INTERFERENCE MODEL

In the previous sections, detailed derivations have been given to calculate the BER performance of NC-FH/MFSK system under IMTJ and PBJ strategies. Due to the scenarios on which the derivations base and the use of the term "jamming", the final SER expressions obtained may appear useful only to some military purposes. However, if we consider an environment where more than one NC-FH/MFSK systems/links share the same spectrum, while a transmitter is sending a signal to a receiver, other transmitters may also communicate with their corresponding receivers. A receiver may receive signal tones other than that transmitted from its intended transmitter. Thus, instead of being jammed by the interference tones intentionally transmitted from a jammer, the signal is now interfered by the interference tones from numbers of transmitters sharing the same channel, so-called cochannel interference. Because they originate from different transmitters, these interference tones are randomly distributed across the entire bandwidth. Except for their origins, the characteristic of these interference tones is very similar to that of the jamming tones in IMTJ strategy. In this circumstance, the BER

performance of an NC-FH/MFSK system can then be calculated as if it is jammed by IMTJ.

Besides the cochannel interference, in the real practice, a receiver may also receive some other interferences from external networks. Because, this paper focuses on the NC-FH/MFSK system constructed using IEEE 802.11(FH) equipment, the external interference could come from IEEE 802.11 b/g wireless local area network (WLAN), which coexists on the same area and operates on the same 2.4 GHz frequency spectrum. In this case, we can then model the coexisting DSSS-modulated interference as a partial-band interference or interference noise in the PBJ strategy. Then, to calculate the BER performance of an NC-FH/MFSK system/link under the cochannel and the coexisting-network interference, we must combine together the BER expressions for the system under IMTJ and PBJ strategies.

For ease of representation, let us define  $\mathcal{A}$  as the event that an FH band is jammed by the interference noise from the coexisting network and  $\mathcal{A}'$  as the event that an FH band is not jammed by the interference noise. Recalling from (23), we can calculate the probability of symbol error by

$$P_s(e) = P(\mathcal{A}) \cdot P_s(e | \mathcal{A}) + P(\mathcal{A}') \cdot P_s(e | \mathcal{A}') \quad (26)$$

If there are  $q$  interference tones from  $q$  interfering transmitters, the number of interference tones in an FH band will be a value within the range of  $[0, \min(q, M)]$ . For ease of representation, we then define  $\mathcal{B}_0$  as the event when an FH band is not jammed and  $\mathcal{B}_n$  as the event when the hop is jammed by  $n$  interference tones where  $n \in [1, \min(q, M)]$ . Now, if we incorporate the effect of the interference tones, (26) can then be re-written as

$$\begin{aligned} P_s(e) &= P(\mathcal{A} \cap \mathcal{B}_0) \cdot P_s(e | \mathcal{A} \cap \mathcal{B}_0) \\ &\quad + P(\mathcal{A}' \cap \mathcal{B}_0) \cdot P_s(e | \mathcal{A}' \cap \mathcal{B}_0) \\ &\quad + \sum_{n=1}^{\min(q, M)} \left[ P(\mathcal{A} \cap \mathcal{B}_n) \cdot P_s(e | \mathcal{A} \cap \mathcal{B}_n) \right. \\ &\quad \left. + P(\mathcal{A}' \cap \mathcal{B}_n) \cdot P_s(e | \mathcal{A}' \cap \mathcal{B}_n) \right] \\ &= P(\mathcal{A}) \cdot \left[ P(\mathcal{B}_0) \cdot P_s(e | \mathcal{A} \cap \mathcal{B}_0) \right. \\ &\quad \left. + \sum_{n=1}^{\min(q, M)} P(\mathcal{B}_n) \cdot P_s(e | \mathcal{A} \cap \mathcal{B}_n) \right] \\ &\quad + P(\mathcal{A}') \cdot \left[ P(\mathcal{B}_0) \cdot P_s(e | \mathcal{A}' \cap \mathcal{B}_0) \right. \\ &\quad \left. + \sum_{n=1}^{\min(q, M)} P(\mathcal{B}_n) \cdot P_s(e | \mathcal{A}' \cap \mathcal{B}_n) \right] \quad (27) \end{aligned}$$

The second equality in the equation is derived from the fact that the interference tones and the interference noise are independent, so event  $\mathcal{A}$  is independent from event  $\mathcal{B}_0$  and  $\mathcal{B}_n$ .

If the interference noise is known to spread over a bandwidth  $B_j$  of the entire bandwidth  $B_T$ , then  $P(\mathcal{A})$  equals to the jamming ratio  $\rho = B_j/B_T$  and  $P(\mathcal{A}')$  thus

equals  $(1-\rho)$ . Also, because  $N$  and  $q$  or the total number of FH bands and total number of interference tones are known parameters, we can easily calculate  $P(B_0)$  and  $P(B_n)$  from (5) and (9) respectively.

Next, let us consider the conditional probabilities in (27). Under the condition of event  $\mathcal{A}'$ , there will be no interference noise in the FH band, hence, AWGN will be the only noise corrupting the signal tone. The total noise power in the FH band,  $\sigma_T^2$ , is thus equal to the AWGN power,  $\sigma_n^2$ .  $P_s(e|\mathcal{A}' \cap B_0)$  and  $P_s(e|\mathcal{A}' \cap B_n)$  can then be evaluated using (7) and (10). Contrarily, when the interference noise exists, under the condition of event  $\mathcal{A}$ , the total noise power in the FH band now becomes the sum of AWGN power and the interference noise power, i.e.  $\sigma_T^2 = \sigma_n^2 + \sigma_J^2$ . And, to calculate  $P_s(e|\mathcal{A} \cap B_0)$  and  $P_s(e|\mathcal{A} \cap B_n)$ , we must replace  $\sigma_n^2$  with  $\sigma_T^2$  while calculating (7) and (10).

## 5 THE COMBINED-JAMMING MODEL FOR THE CHANNEL ASSIGNMENT IN MR-FH WMNS

As an example, this section will discuss how the combined-jamming model can be employed to model the interferences in multi-radio frequency-hopping wireless mesh networks (MR-FH WMNs) and aid in the assignment of channels to the radio interfaces.

Wireless mesh networks (WMNs) consist of mesh routers and mesh clients, where mesh routers have minimal mobility and form the backbone of WMNs. They provide network access for both mesh and conventional clients. The integration of WMNs with other networks such as the Internet, cellular, IEEE 802.11, IEEE 802.15, IEEE 802.16, sensor networks, etc., can be accomplished through the gateway and bridging functions in the mesh routers. Mesh clients can be either stationary or mobile, and can form a client mesh network among themselves and with mesh routers [9]. The IEEE 802.11b/g and IEEE 802.11a standards define 3 and 12 non-overlapping frequency channels, respectively. Using multiple channels in MR WMNs greatly improves the network throughput [11]. One of the most important design questions for an MR WMN is the channel assignment problem, i.e., how to bind each radio interface to a radio channel [10]. As the number of radio interfaces increases, mesh routers tend to interfere more with each other; thus, the capacity of the network drops.

To achieve the reasonable throughput from WMN, several publications, [12]- [15], have proposed algorithms, which are focused to reduce cochannel interferences by carefully managing how each node accesses to the share media. In [12], an interference-aware channel assignment (CA) algorithm has been proposed for IEEE 802.11 a/b/g MR WMN. The centralized CA algorithm was designed by taking into account both the interferences among router nodes and the external interference from coexisting network. To estimate the two types of interferences, the author developed the multi-radio Conflict Graph (MCG) and used it for modelling the

interferences among router nodes while, for the coexisting network interference, the inherited radio-sensing mechanism in the IEEE 802.11 a/b/g standards was adopted to monitor for unrecognized radios periodically. Also, in [13], the author has proposed an interference model for partially overlapped channels and, to illustrate its benefit, the model was thus used to enhance the performance of two previously proposed CA algorithms.

In this paper, we consider the channel assignment problem in an MR-FH WMN in which each router node is equipped with multiple NC-FH/MFSK radio interfaces. As previously suggested, these router nodes can be implemented cost-efficiently using COTS IEEE 802.11(FH) equipments. In spite of how they are implemented, to establish the network, we assume that the router nodes are deployed uniformly and lightly over a rural region so that the distances from any router node to its surrounding neighbors are indifferent and each node will have only a few neighbors surrounding them.

Each node is comprised of at least two different radio interfaces, one for a control channel and all the others for information channels. For an enhanced security during information transmissions, every interface designated for information are specifically chosen to be NC-FH/MFSK radio system while, for the controlling purpose, the interface can be of any radio systems other than the NC-FH/MFSK, e.g. IEEE 802.11 a. Only important thing is that the two channel types are on different frequency ranges, hence they do not interfere. We assume that the transmission power and radio parameters for every NC-FH/MFSK interface are homogenous and known and each node is perfectly aware of its own coordinate position.

In the entire bandwidth  $B_T$  for NC-FH/MFSK radio, we assume that there are  $N$  FH bands available and, to achieve the greatest benefit of having multiple interfaces a node, we divide the FH bands into  $b$  interleaving and non-colliding hopping patterns to enable concurrent links. Each hopping pattern thus has  $N_p = N/b$  FH bands, each with  $M$  possible signal frequency slots, and there will be the total of  $N_p M$  frequency slots. Because these patterns are interleaving and non-colliding, a link using one hopping pattern will not interfere with that on the other patterns. Hence, it is possible for any nodes with multiple NC-FH/MFSK interfaces to support concurrent information links without having them interfering with each other, if the links are performed using different hopping patterns.

It can be observed that the hopping patterns here is, in fact, very similar to the radio channels in IEEE 802.11 a/b/g. Hence, the decision as to which hopping pattern is suitable for a specific link can also be determined by the CA algorithm, similar to those in [12]- [15], at the setup phase of the network.

In this paper, we have adopted the interference-aware CA algorithm previously proposed in [12] and modified it to suit with the assignment of hopping patterns in our NC-FH/MFSK WMN mainly by introducing an appro-

appropriate interference model for estimating the link's BER. By doing so, it should also be noted that we have just defined the BER as a metric for measuring the severity of the interferences on the links.

Since every router node has the same transmission power and NC-FH/MFSK radio parameters, the transmission range will be the same for every router node and, in this paper, we define the transmission range to cover approximately the distance of one hop and the interference range is assumed to be twice as far as the transmission range or, roughly, a two-hop distance.

Now, let's gain some insight on the network by considering the process during setting up of the mesh. Since each mesh router is previously assumed to have a control channel, it is further assumed that the control channels of every router node are, by default, set to an encrypted common channel. After the router nodes are setup, they will immediately forward the information, such as node IDs, coordinate locations, transmission powers, and number of interfaces, to a pre-assigned center node (PAC), which will collect all the information and construct a map of the network and the MCG as defined in [12]. Then, PAC will execute the CA algorithm to assign hopping patterns to links of each routers, starting from PAC itself then moving outward to those surrounding PAC within the first hop, the second hop, and so on. It should be noted that, among those within the same hop distance from PAC, the algorithm will start at the closest node to PAC first. Once the assignment is ended, PAC then notifies the router nodes to set their radios accordingly.

When a node acquires the list of hopping patterns assigned, instead of using them directly as the hopping sequences for the designated interfaces, it will sort the FH bands associated with each pattern, one pattern at a time, and randomly shuffle the order of the FH bands to create a new hopping sequence that is distinct. But, because one link involves two nodes, only one node on the link should obviously perform the shuffling process, otherwise the hopping sequence between two nodes will not match and the link will never be formed. Therefore, we specify that the node with lower ID on the link will execute the shuffling process and then inform the new hopping sequence to the other node using the control channel. At the completion of the process, the mesh is then formed and nodes will communicate accordingly.

It is noted, however, because the main CA algorithm used in this paper is an interference-aware one, which is considered as an adapted version of the original BFS-CA algorithm in [12]. Hence, a direct information transmission between two specific neighbors may not actually exist, unless an addition topology-control code is inserted into the algorithm. But, due to the availability of the common channel for control signal, the information can then be transmitted directly between the two neighbors of interest using a temporary link on the common channel. Besides, the advantage of having a common control channel also applies in the case when a node

is required to broadcast information to its neighbors.

Thus far, we have already picked up some ideas about how the network operates and how the CA algorithm is used to assign the hopping patterns. As an illustration of how interferences can be evaluated by the CA algorithm, let us consider an example scenario shown in Fig. 1. Here, six router nodes are used to setup a simple mesh network and each node is labeled corresponding to its name and number of its NC-FH/MFSK interfaces. For example, A-2 means node A is equipped with two NC-FH/MFSK interfaces. Here, we assume that the total of  $N$  FH bands are divided into two hopping patterns and node A is the PAC node. At the time being, we assume the algorithm has been running for some times and some of the links have already been assigned with hopping patterns;  $A \leftrightarrow B$  (the link between node A and node B) and  $C \leftrightarrow E$  are assigned to pattern 1 while  $A \leftrightarrow C$  and  $B \leftrightarrow D$  are allocated to pattern 2. The algorithm is now running for  $C \leftrightarrow F$ .

First, let us consider if  $C \leftrightarrow F$  is to be assigned with pattern 1. Because the interference range is defined as the distance of two hop, every link within the two-hop radius of node C is thus considered a conflict/interfering link to  $C \leftrightarrow F$ ; namely  $A \leftrightarrow B$ ,  $A \leftrightarrow C$ , and  $C \leftrightarrow E$ . However, should  $C \leftrightarrow F$  be taken on pattern 1, the transmissions on  $A \leftrightarrow C$  in pattern 2 no longer interfere with it; hence, the BER calculation should take into account only  $A \leftrightarrow B$  and  $C \leftrightarrow E$ , which use the same hopping pattern as  $C \leftrightarrow F$ . Let's now assume information is being transmitted as NC-FH/MFSK signal tones from node F to node C and node A to node B. During the transmissions, node E has also started to transmit information to node C using another interface of node C. Therefore, as a receiver, node C will pickup not only the desired signal tones from node E and F but also undesired interference tones from A. The algorithm consider node C as a reference receiver (node C is the closer node in  $C \leftrightarrow F$  to PAC) and node F as a reference transmitter, every tone transmitted from node F is then the desired signal tone to node C while those from node A and node E are considered as cochannel interferences. Similarly, if  $C \leftrightarrow F$  is to be assigned with pattern 2,  $A \leftrightarrow C$  is thus its conflict link and the tone transmitted from node A is regarded as cochannel interference. Because the hopping sequence used on any link comes from the randomly-shuffled FH bands of the hopping pattern assigned to it, every tone transmitted will be randomly distributed on the entire bandwidth and independent of each other. Therefore, we are allowed to model the cochannel interferences as the independent interference tones in IMTJ. However, it is noted that the interference tones in IMTJ strategy are actually equal in power and, furthermore, every tone is always transmitted with different frequency slot. But, with  $C \leftrightarrow F$  being assigned with pattern 1, it is obvious that the interference tones from node A and node E will have different powers due to their different distances from node C. Besides, the interference tones from node A and node E can also be transmitted on the

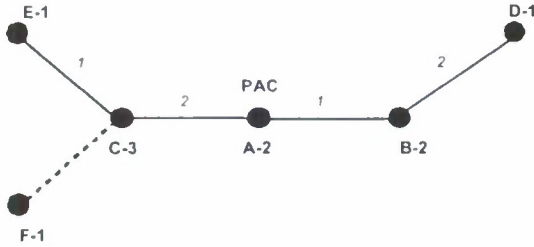


Fig. 1. An Example of Interferences in WMN.

same frequency slot because their hopping sequences are totally random and independent.

However, if we consider the practical configuration, IEEE 802.11 (FH) equipment uses 26 FH bands per pattern and 4-level Gaussian FSK modulation, i.e.  $N_p = 26$  and  $M = 4$ . The total number of frequency slots per pattern thus equal  $N_p M = 104$  slots, which is quite a lot. Besides, if we consider a lightly-deployed network, each node will be surrounded by a few neighbors and, among these neighbors, only those use the same hopping patterns are likely to introduce cochannel interferences. The number of cochannel interference tones in each pattern is hence small. In other word, there will be a lot more frequency slots than the interference tones and the probability of having interference tones being transmitted on the same frequency slot is literally negligible. Subsequently, for the equal-power constrain, since we have assumed nodes are uniformly deployed—which is usually valid with typical backbone network deployment—hence the distances between nodes will be slightly different and we can easily cope by using the average power of the interference tones received.

Now, let us cover in more detail on the case when  $C \leftrightarrow F$  is to assigned with hopping pattern 1. In this case, the total number of independent interference tones for pattern 1,  $q_1$ , is equal to two since there are two interference tones being received at node C; one from node A and the other from node E. The received powers of the signal from node F and the interference tones from node A and node E can be found using the free-space pathloss model, [25],

$$P_{kl} = K \frac{P_T}{d^2} \quad (28)$$

where  $d$  is the distance between transmitter and receiver node,  $P_{kl}$  is the received power of the signal transmitted from node  $k$  and received at node  $l$ , and  $P_T$  is the transmitted power. The constant  $K$  can be determined by the transmitting and receiving antenna gains and the wavelength of the transmitted signal. Since all these parameters are assumed to be known, we can easily calculate the received power of signal tone ( $P_{FC}$ ) and the received powers of interference tones from node A and node E ( $P_{AC}$  and  $P_{EC}$ ) using (28). Then, we can find the average received power of the interference tones at node C ( $P_{JC} = \frac{1}{2}(P_{AC} + P_{EC})$ ).

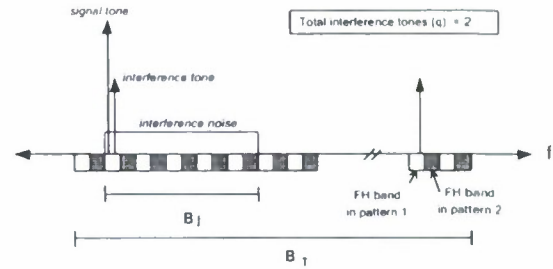


Fig. 2. A frequency-domain illustration of interference tones (cochannel interferences) and interference noise (coexisting-network interference) of an MR-FH WMNs with 2 hopping patterns available.

Next, it is assumed that a site survey has been performed prior to installation and, because the prospective site is a rural area, only an IEEE 802.11 b WLAN is coexisting on the site. The interference from the network can be modeled as the partial-band interference noise in PBJ strategy. The power of interference noise received at each node in our MR-FH WMN usually varies and depends on the distance between node and the interfering source. We can define  $\sigma_{jk}^2$  as the power of the interference noise being received at router node  $k$ . And if  $N_J$  is the number of FH bands that are jammed by the interference noise, the entire-bandwidth jamming ratio can then expressed as  $\rho = N_J/N$ . But, because hopping patterns are formed by interleaving and non-colliding FH bands,  $N_J$  jammed FH bands will be equally partitioned to each pattern. In this case, the jamming ratio of hopping pattern  $i$  or  $\rho_i$  will be the same as the entire-bandwidth jamming ratio,  $\rho$ . It should be noted that  $\sigma_{jk}^2$  at node  $k$  and  $\rho_i$  are the parameters known to PAC after the site survey is performed.

To estimate the SER associated with any hopping pattern being assigned to a link, we can use (27) of the combined-jamming analysis in the previous section to account for the effect caused the cochannel and coexisting-network interferences. Table 1 illustrates the values for some important parameters used in (27) to calculate the SER when  $C \leftrightarrow F$  in Fig. 1 is to be assigned with hopping pattern 1. Note that, in the table, the scattering ray powers for signal and interference tone are set to zero because no fading channel is assumed in this example. In general, the parameters can be set accordingly to reflect the actual characteristic of the fading channel.

Using the SER values obtained from (27) and converting them into BER by (4), the CA algorithm then compares the BER costs associated with each hopping pattern and decide the most appropriate patterns for  $C \leftrightarrow F$ .

As a numerical example of the performance predicted by the combined-jamming interference model, Fig. 3 illustrates the plots of the BER values obtained when  $C \leftrightarrow F$  is to be assigned to each hopping pattern. We assumed

TABLE 1  
Parameters for calculating SER when  $C \leftrightarrow F$  is assigned  
to hopping pattern 1

Variable	Definition	Value
$N$	Total FH bands in the pattern	$N_p$
$P_s$	Received power of signal tone	$P_{FC}$
$P_j$	Avg. received power of int. tone	$\frac{1}{2}(P_{AC} + P_{EC})$
$q$	Total int. tones in the pattern	$q_1 = 2$
$\alpha_s^2, \alpha_j^2$	Avg. LOS signal/int. power	1
$\sigma_s^2, \sigma_j^2$	Avg. scattering signal/int. power	0
$\rho$	Jamming ratio in the pattern	$\rho_1$
$\sigma_j^2$	Int. noise power at ref. receiver node C	$\sigma_{jC}^2$

that  $N = 78$  and the modulation is NC-FH/4FSK ( $M=4$ ). Since there are two hopping patterns ( $b = 2$ ) used in the example scenario in Fig. 1, thus  $N_p = N/b = 39$  FH bands per pattern.  $SIR$  (signal-to-interference-noise ratio) represents the ratio of signal power to interference noise/coexisting network interference power and  $SNR$  (signal-to noise ratio) denotes the ratio of signal power to AWGN power. Mathematically, these ratios can be expressed as

$$SIR = \frac{P_s}{\sigma_{jk}^2 \log_2 M}, \quad SNR = \frac{P_s}{\sigma_n^2 \log_2 M} \quad (29)$$

For the scenario in Fig. 1 with NC-FH/4FSK modulation,  $SIR$  equals  $P_{FC}/2\sigma_{jC}^2$  and  $SNR$  equals  $P_{FC}/2\sigma_n^2$ . In the simulation, we assume that router node F is the closest node to node C, then node A, and node E, respectively. But, because these nodes are uniformly deployed, thus their distances from node C are not so different. Consequently, we have set the powers of the signal tones received at node C as  $P_{FC} = 1.1P_{AC} = 1.2P_{EC}$ . Furthermore, it is assumed that the external IEEE 802.11 b network is operating on one of the three non-overlapping channels in 2.4 GHz band. So,  $\rho$  is set to approximately 0.3 and  $\rho_1 = \rho_2 = \rho = 0.3$  due to interleaving hopping patterns.

From Fig. 3, we can observe that, regardless of  $SIR$  value, the BER obtained when  $C \leftrightarrow F$  is assigned with hopping pattern 1 always larger than that with hopping pattern 2; the CA algorithm thus assigns hopping pattern 2 to  $C \leftrightarrow F$ . It can be observed that the interference noise contributes a very little effect on our selection for the most appropriate pattern. This is because we assumed hopping patterns are interleaving, hence the effect of interference noise appears as a constant offset on every pattern and get cancelled when the BER's for each pattern are accounted in comparison.

Now, if we drop the requirement for interleaving hopping patterns, each pattern will be differently exposed to the interference noise and, in this case, the selection can be made more accurately if the interference noise is, as well, considered. Fig. 4 illustrates the BER performances for the same example in Fig. 3 but with non-interleaving hopping patterns. To obtain the result in the figure, we

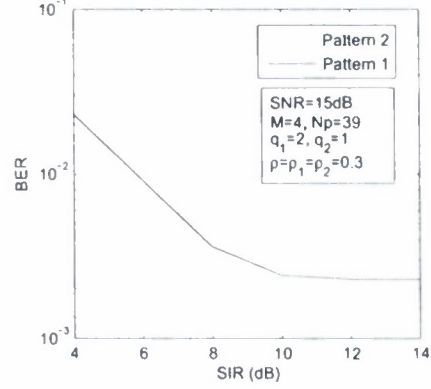


Fig. 3. The NC-FH/4FSK performances obtained from the combined-jamming interference model when  $C \leftrightarrow F$  is assigned with interleaving hopping patterns.

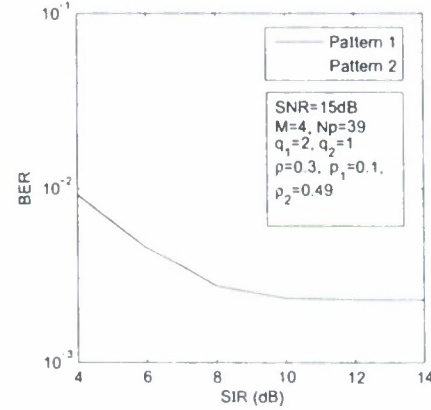


Fig. 4. The NC-FH/4FSK performances obtained from the combined-jamming interference model when  $C \leftrightarrow F$  is assigned with non-interleaving hopping patterns.

assumed the total number of jammed FH bands,  $N_J = \rho N = 0.3 \times 78 \approx 23$  is differently partitioned into pattern 1 and pattern 2; four jammed FH bands to pattern 1 and the rest nineteen to pattern 2. Obviously, we can observe that the choice of appropriate pattern is now depending not only on the interference tones but also on the external interference noise received at node C. Unless the interference noise is received with  $SIR$  lower than 8 dB, pattern 2 will be the most appropriate choice for  $C \leftrightarrow F$ . Comparing with the result from Fig. 3, we can see clearly the influence of the external interference noise on the choice of appropriate pattern when non-interleaving patterns are used.

## 6 EXTENDED STUDY: NC-FH/MFSK PERFORMANCE UNDER WORST-CASE IMTJ AND PBJ

As a direct benefit from the SER derivations in Section 2 and Section 3, in this section, we further investigate the performance of NC-FH/MFSK system with

Rician fading channels under IMTJ and PBJ strategies. First, we consider the performance of the system under each jamming strategy separately and then we compare them together to determine the most effective strategy—provided that the total power of the interference at the receiver,  $P_{JT}$ , is fixed. Starting from this point, we will define the signal-to-jamming ratio as

$$SJR = \frac{E_b}{N_{JT}} = \frac{P_s NM}{P_{JT} \log_2(M)} \quad (30)$$

Since  $B_T$  and  $E_b$  are constant system parameters,  $SJR$  is inversely proportional to  $P_{JT}$ .

### 6.1 NC-FH/MFSK performance under worst-case IMTJ

Figure 5 represents the plot of the BER performances for NC-FH/4FSK system with Rician fading channel against the tone jamming ratio or  $\gamma$ , which is the ratio between number of equal power interference tones transmitted from the jammer and the total number of FH bands in the entire bandwidth, i.e.  $\gamma = q/N$ . As  $SJR$  varies from 0 to 25 dB,  $P_{JT}$  decreases from  $2000P_s$  to  $2P_s$ ; each  $SJR$  curve then represents a fixed  $P_{JT}$ . As we initially increased  $q$  by increasing  $\gamma$ , the BER value tends to increase. This is because increasing  $q$  will increase the chance that an interference tone will get to jam the hopping signal frequency. Though increasing  $q$  will also reduce the individual interference tone power ( $P_j = P_{JT}/q$ ), but because  $P_{JT}$  is started with a value much larger than  $P_s$  (for example,  $P_j = 200P_s$  at  $SJR=10\text{dB}$ ) and, at the beginning,  $q$  is only a small number, the resulting  $P_j$  is still larger than  $P_s$  and strong enough to cause the bit error in the system.

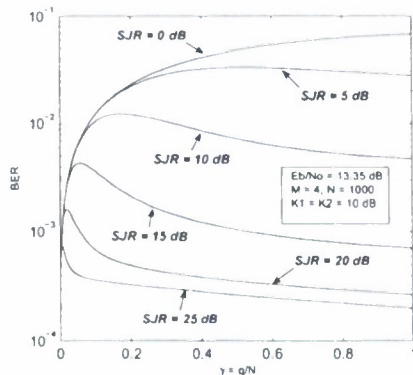


Fig. 5. BER performances for NC-FH/4FSK with Rician fading channels against the tone jamming ratio,  $\gamma$ , at various  $SJR$  values.

However, after certain values of  $q$  where individual interference tone power  $P_j$  become more critical, increasing  $q$  will now reduce the  $P_j$  even further. Although the bandwidth  $B_T$  is occupied by more and more interference tones as  $q$  increases, but these tone are now at very low power. So, the receiver can better differentiate

signal from interference tones and system BER starts to decrease; this causes the BER peaks as seen in Figure 5 for  $SJR = 5$  to 25 dB. Similar result is also reported in Figure 6 of [3]. However, it should be noted that the probability of symbol error given a hop is jammed by  $n$  interference in the signal branch was calculated in (19) of [3] using a double-integral equation while, in (16) in our analysis, the same probability is evaluated more efficiently by via a single integration.

Until now, we have seen how the total number of interference tones ( $q$ ) affects the BER of the system. To deploy the total interference power effectively, we must find the number of interference tones, which introduces the highest BER to the system, so-called worst-case number of interference tones ( $q_{wc}$ ). From Fig. 5,  $q_{wc}$  can be determined via  $\gamma$  at each BER peak and it is not surprising that  $q_{wc}$  in this case is the value of  $q$  that makes  $P_j \approx P_s$ .

Unfortunately, due to the complexity of the total SER expression, there is no closed-form formula for determining the exact  $q_{wc}$ . Besides, results from extensive simulations have shown that  $q_{wc}$  varies not only with  $SJR$ , but also with the characteristics of fading channels. To determine the exact  $q_{wc}$ , system performance must be numerically plotted every time the channels change. The procedure is time-consuming and, apparently, impractical. Nevertheless, we have observed from recursive simulations that, regardless of the channel conditions, the BER peaks for low to moderate  $SJR$  values (5dB to 20dB) are normally broad enough to allow the values in vicinity to be nearly as effective. So, if a small error is tolerable, the  $q_{wc}$  for low to moderate  $SJR$  can always be estimated instantly by  $q_{wc} \approx P_{JT}/P_s$ .

### 6.2 NC-FH/MFSK performance under worst-case PBJ

Unlike IMTJ, the performance of NC-FH/MFSK under PBJ and the closed-form expression for calculating the most-efficient jamming ratio or the worst-case jamming ratio ( $\rho_{wc}$ ) for the strategy have been widely studied in many publications. In [4], the inverse-linear relationship between BER and  $E_b/N_{JT}$  has been discovered and, without the effect of AWGN and fading channel, the condition for the worst-case NC-FH/MFSK performance has been provided. In [6], the worst-case performance of NC-FH/MFSK under PBJ has been considered with the effect of AWGN being accounted. It has been shown that  $\rho_{wc}$  is proportional to a constant that depends on  $E_b/N_0$  and inversely proportional to  $E_b/N_{JT}$ . Further in [8],  $\rho_{wc}$  for PBJ strategy on NC-FH/BFSK system with AWGN and Rician channel has been provided in a closed-form expression, which also indicates the inverse relationship between  $\rho_{wc}$  and  $E_b/N_{JT}$ .

It can be observed that, though accounts for both AWGN and Rician fading channel, the closed-form expression for  $\rho_{wc}$  in [8] is only applicable to NC-FH/BFSK ( $M = 2$ ). For the general case of NC-FH/MFSK, the

complexity of the BER expression increases dramatically and solving for  $\rho_{wc}$  from mathematical approach is nearly impossible. However, from the findings of the previous studies, it is reasonable for us to speculate also the same inverse-proportion relationship between  $\rho_{wc}$  and  $E_b/N_{JT}$  for the case of NC-FH/MFSK system with AWGN and Rician channel. In fact, the results from our simulations has actually verified the existence of the inverse-proportion relationship. So,  $E_b/N_0$  and  $E_b/N_{JT}$  are defined as signal-to-noise ratio ( $SNR$ ) and signal-to-jamming ratio ( $SJR$ ), the condition for  $\rho_{wc}$  can be expressed as

$$\rho_{wc} = \begin{cases} 1, & SJR < A \\ \min(\frac{B}{SJR}, 1), & SJR \geq A \end{cases} \quad (31)$$

For a given  $M$ , constant  $A$  depends only on  $SNR$  while constant  $B$  depends on both the Rician factor of the signal tone,  $K_1$ , and  $SNR$ . The numerical values of  $A$  and  $B$  can be found in Table 2(a) for  $M = 4$  and in Table 2(b) for  $M = 16$ . For any other values of  $SNR$  and  $K_1$ , we also provide the general expression for estimating  $\rho_{wc}$  as

$$\rho_{est\_wc} = \begin{cases} 1, & SJR \leq C \text{ or } SNR < 5\text{dB or } K_1 < 2\text{dB} \\ 0.5, & C < SJR \leq (C + 3\text{dB}) \\ 0.2, & (C + 3\text{dB}) < SJR \leq (C + 6\text{dB}) \\ 0.1, & (C + 6\text{dB}) < SJR \leq (C + 9\text{dB}) \\ 0.07, & (C + 9\text{dB}) < SJR \leq (C + 11\text{dB}) \\ 0.03, & (C + 11\text{dB}) < SJR \leq 25\text{dB} \\ 0.01, & SJR > 25\text{dB} \end{cases} \quad (32)$$

where, for a given  $M$ ,  $C$  is a constant depending on  $SNR$  and  $K_1$ . The numerical value for  $C$  is provided in Table 3.

It should be noted that  $\rho_{est\_wc}$  is only a value of the jamming ratio, which causes almost as large BER as the actual worst-case one. Thus, it may not be the same value as the actual  $\rho_{wc}$  given by (31). Also, when calculating for  $\rho_{wc}$  or  $\rho_{est\_wc}$ , one should be advised that  $SJR$  in (31) must be used in linear scale while that in (32) is proper with dB.

The worst-case BER performances for NC-FH/4FSK system with Rician fading channel under PBJ is presented in Fig. 6. Compared to broadband jamming (BBJ,  $\rho = 1$ ), the BER obtained using  $\rho_{wc}$  is higher than that obtained using  $\rho=1$ ; thus, we can see clearly the effectiveness of the PBJ strategy using  $\rho_{wc}$ , as oppose to that with a fixed  $\rho$  value. Also, it should be noted that the BER obtained from  $\rho_{est\_wc}$  is almost as high as that obtained using the actual  $\rho_{wc}$ .

### 6.3 Comparison between worst-case IMTJ and worst-case PBJ

The BER performances of NC-FH/4FSK system under worst-case IMTJ and worst-case PBJ are compared in

TABLE 2  
Constants  $A$  and  $B$  for determining the worst-case jamming ratio ( $\rho_{wc}$ )

(a) $M=4$							
$SNR$ (dB)	$A$	$B$					
		$K_1$ (dB)					
		5	7	10	13	15	100
8	3.60	7.20	4.25	2.90	2.40	2.25	2.00
10	2.14	4.10	2.85	2.14	1.85	1.75	1.60
13.35	1.50	2.85	2.15	1.70	1.50	1.45	1.35
15	1.40	2.65	2.00	1.60	1.45	1.40	1.30
20	1.25	2.35	1.80	1.50	1.35	1.30	1.20
100	1.20	2.20	1.75	1.45	1.30	1.25	1.20

(b) $M=16$							
$SNR$ (dB)	$A$	$B$					
		$K_1$ (dB)					
		5	7	10	13	15	100
8	1.65	2.55	1.80	1.40	1.20	1.15	1.05
10	1.20	2.00	1.50	1.20	1.05	1.00	0.95
13.35	0.95	1.65	1.30	1.05	0.95	0.90	0.85
15	0.90	1.55	1.25	1.00	0.91	0.90	0.85
20	0.80	1.45	1.15	0.95	0.90	0.85	0.80
100	0.80	1.40	1.15	0.95	0.85	0.85	0.80

TABLE 3  
Constant  $C$  for determining the estimated worst-case jamming ratio ( $\rho_{est\_wc}$ )

$SNR$	$M$	$C$ (dB)		
		$K_1$		
		3 to 8 dB	8 to 15 dB	> 15 dB
5 to 8 dB	2	$\infty$	8	7
	4	12	6	5
	8	8	4	3
	16	6	3	2
	32	4	2	1
8 to 15 dB	2	8	6	5
	4	6	3	3
	8	4	2	1
	16	3	1	1
	32	2	1	0
> 15 dB	2	7	5	4
	4	5	3	2
	8	3	1	1
	16	2	1	0
	32	1	0	-1

Fig. 7. Here, we obtained the BER curve for IMTJ just by taking the peak BER's at various  $SJR$  curves shown in Fig. 5. It can be seen that the worst-case PBJ always causes higher BER to the system than IMTJ, regardless of the  $SJR$  values. Hence, for NC-FH/4FSK with Rician fading channels and given the values of  $P_s$  and  $P_{JT}$ , i.e. a fixed  $SJR$ , PBJ will be more effective jamming strategy than IMTJ. On the other hand, if we compare IMTJ to the BBJ, we can observe that, at low  $SJR$ , the BBJ strategy will cause higher BER to the system than IMTJ does; but, at moderate to high  $SJR$ , it is IMTJ that introduces higher BER to the system.

## 7 CONCLUSION

In this paper, we have analyzed the BER performance of NC-FH/MFSK system with AWGN and Rician fading

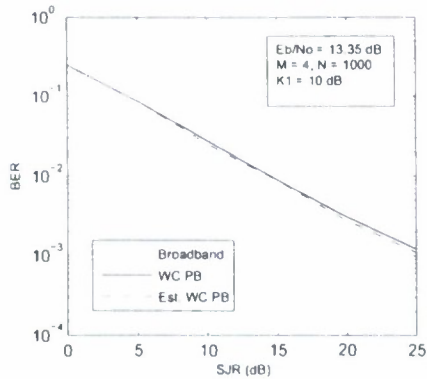


Fig. 6. Comparison of BER performances for NC-FH/4FSK under BBJ, worst-case PBJ, and estimated worst-case PBJ.

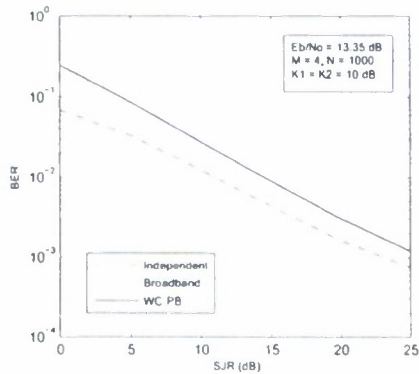


Fig. 7. Comparison of BER performances for FH/4FSK under BBJ, worst-case PBJ, and worst-case IMTJ.

under IMTJ and PBJ. The results the analyses are benefit not only to the prediction of the system performance under the jamming scenarios, but also in modeling interferences in MR-FH WMNs. We have observed that the interference tones in IMTJ strategy are, in fact, similar to the cochannel interference in MR-FH WMNs and any wideband interference from the coexisting network outside of the mesh can also be modeled as the partial-band interference in PBJ strategy. Consequently, the combined-jamming interference analysis has been developed to account for the cochannel and coexisting-network interferences in MR-FH WMNs. Next, we have illustrated the usefulness of the combined-jamming model through the channel assignment problem in a rural IEEE 802.11 MR-FH WMN. By incorporating the developed model into a CA algorithm, typically used for assigning channels to IEEE 802.11 a/b/g MR-WMNs, we have enabled the algorithm to estimate the cost associating with the assignment of a hopping pattern to a radio interface of router node and allowed it efficiently manage the shared frequency resource.

As an additional study, we also investigated the performance degradation of NC-FH/MFSK system under

IMTJ and PBJ strategies with AWGN and Rician fading channel being accounted. For IMTJ with low to moderate  $SJR$ , we can estimate  $q_{wc}$  or the worst-case number of interference tones by choosing  $q$  that makes the power of each interference tone approximately equal to the signal tone power, i.e.  $P_j \approx P_s$ . Then, for the case of PBJ, we have provided not only an expression for evaluating the actual worst case jamming ratio, but also an expression to estimate the  $\rho_{wc}$ , which is applicable to almost all  $M$ -ary FH/FSK system and fading condition. Plotted BER curves has verified the effectiveness of PBJ using  $\rho_{wc}$  or  $\rho_{est_{wc}}$  over BBJ with  $\rho = 1$ . Finally, we have compared the performance of IMTJ and PBJ strategies and it is observed that, for NC-FH/4FSK with AWGN and Rician channel, IMTJ strategy is less effective than PBJ strategy.

## ACKNOWLEDGMENTS

This work was supported in part by National Science Foundation (NSF) under Grant CNS-0721515 and CNS-0831902, and Office of Naval Research (ONR) under Grant N00014-07-1-0395 and N00014-07-1-1024.

## REFERENCES

- [1] R. C. Robertson and J. F. Sheltry, "Multitone Interference of Frequency-Hopped Noncoherent MFSK Signals Transmitted Over Ricean Fading Channels," *IEEE Trans Comm.*, vol. 44, no. 7, pp. 867-875, July 1996.
- [2] T. T. Tjhung and C. C. Chai, "Multitone Jamming of FH/BFSK in Rician Channels," *IEEE Trans Comm.*, vol. 47, no. 7, pp. 974-978, July 1999.
- [3] Z. Yu, T. T. Tjhung, and C. C. Chai, "Independent Multitone Jamming of FH/MFSK in Rician Channels," *IEEE Trans Comm.*, vol. 49, no. 11, pp. 2006-2015, November 2001.
- [4] S. W. Houston, "Modulation Techniques for Communications, Part I: Tone and Noise Jamming Performance of Spread Spectrum M-ary FSK and 2, 4-ary DPSK Waveforms," *IEEE NAECON'75 Rec.*, pp. 51-58, June 1975.
- [5] B. K. Levitt, "FH/MFSK Performance in Multitone Jamming," *IEEE Journal on Selected Areas in Comm.*, vol. SAC-3, no. 5, pp. 627-643, September 1985.
- [6] W. E. Stark, "Coding for Frequency-Hopped Spread-Spectrum Communication with Partial-Band Interference-Part II: Coded Performance," *IEEE Trans Comm.*, vol. 33, no. 10, pp. 1045-1057, October 1985.
- [7] J. S. Bird and E. B. Felstead, "Antijam Performance of Fast Frequency-Hopped M-ary NCFSK-An Overview," *IEEE Journal on Selected Areas in Comm.*, vol. SAC-4, no. 2, pp. 216-233, March 1986.
- [8] A. A. Ali, "Worse-Case Partial-Band Noise Jamming of Rician Fading Channels," *IEEE Trans Comm.*, vol. 44, no. 6, pp. 974-978, June 1996.
- [9] I. F. Akyildiz, X. Wang, and W. Wang, "Wireless Mesh Networks: A Survey," *Computer Networks*, vol. 47, no. 4, pp. 445-487, March 2005.
- [10] S. Avallone, and I. F. Akyildiz, "A Channel Assignment Algorithm for Multi-Radio Wireless Mesh Networks," *Computer Communications*, vol. 31, no. 7, pp. 1343-1353, May 2008.
- [11] A. Raniwala, and T. Chiu, "Architecture and Algorithms for an IEEE 802.11-Based Multi-Channel Wireless Mesh Network," *IEEE INFOCOM*, vol. 3, pp. 2223-2234, 2005.
- [12] K. N. Ramachandran, E. M. Belding, K. C. Almeroth, and M. M. Buddhikot, "Interference-Aware Channel Assignment in Multi-Radio Wireless Mesh Networks," *2006 Proc. of IEEE INFOCOM*, pp. 1-12, April 2006.
- [13] A. Mishra, V. Shrivastava, S. Banerjee, and W. Arbaugh, "Partially Overlapped Channels Not Considered Harmful," *ACM SIGMETRICS Performance Evaluation Review*, vol. 34, issue. 1, pp. 63-74, June 2006.

- [14] H. Skalli, S. Ghosh, S. K. Das, L. Lenzini, and M. Conti, "Channel Assignment Strategies for Multi-Radio Wireless Mesh Networks: Issues and Solutions," *IEEE Comm. Magazine*, vol. 45, issue. 11, pp. 86-95, November 2007.
- [15] A. P. Subramanian, H. Gupta, S. R. Das, and J. Cao, "Minimum Interference Channel Assignment in Multi-Radio Wireless Mesh Networks," *IEEE Trans. Mobile Computing*, vol. 7, no. 11, November 2008.
- [16] B. P. Crow, I. Widjaja, J. G. Kim, and P. T. Sakai, "IEEE 802.11 Wireless Local Area Networks," *IEEE Comm. Magazine*, vol. 35, no. 9, pp. 116-126, September 1997.
- [17] W. Ye, J. Heidemann, and D. Estrin, "Medium Access Control with Coordinated Adaptive Sleeping for Wireless Sensor Networks," *IEEE/ACM Trans. on Networking*, vol. 12, issue 3, pp. 493-506, June 2004.
- [18] A. Sheth, C. Doerr, D. Grunwald, R. Han, and D. Sicker, "MOJO: A Distributed Physical Layer Anomaly Detection System for 802.11 WLANs," *Fourth International Conference on Mobile Systems, Applications and Services (MobiSys)*, pp. 191-204, 2006.
- [19] J. Wu, and F. Dai, "Mobility-Sensitive Topology Control in Mobile Ad Hoc Networks," *IEEE Trans. on Parallel and Distributed Systems*, vol. 17, no. 6, pp. 522-535, June 2006.
- [20] W. Lou, and Y. Fang, *A Survey on Wireless Security in Mobile Ad Hoc Networks: Challenges and Possible Solutions*, a book chapter in *Ad Hoc Wireless Networking*, Kluwer, pp. 319-364, May 2003.
- [21] J. Wu, *Handbook of Theoretical and Algorithmic Aspects of Ad Hoc, Sensor, and Peer-to-Peer Networks*, Auerbach Publications, 2006.
- [22] A. D. Whalen, *Detection of Signal in Noise*, New York: Academic Press, 1971.
- [23] J. G. Proakis, *Digital Communications*, 2nd ed., New York: McGraw-Hill, 1989.
- [24] I. S. Gradshteyn, and I. M. Ryzhik, *Table of Integrals, Series, and Products*, Alan Jeffrey, editor (translated from the Russian by Scripta Technica, Inc), Boston: Academic Press, 1994.
- [25] M. Schwartz, *Mobile Wireless Communications*, Cambridge University Press, 2005.